Atomic Force Microscopy for Martian Investigations

Hanna Maria Sykulska-Lawrence

Department of Electrical and Electronic Engineering

Imperial College London

A thesis submitted for the degree of Doctor of Philosophy

6^{th} October 2008

Abstract

The Phoenix Mars Lander includes a Microscopy, Electrochemistry and Conductivity Analyser (MECA) instrument for the study of dust and regolith at the Martian arctic. The microscopy payload comprises an AFM and Optical Microscope (OM) to which samples are delivered by a robot arm. The setup allows imaging of individual dust and soil particles at a higher spatial resolution than any other *in-situ* instrument. A fully functioning test-bed of the flight microscopy setup within an environmental chamber to simulate Mars conditions was assembled at Imperial College, enabling characterization of the microscopes.

Samples are collected on small disks rotated to the vertical position for imaging, with each substrate surface promoting different adhesion mechanisms. The vertical mounting necessitates good adhesion of particles to substrates. Moreover, to achieve safe operation and good AFM scans, a sparse field of particles is required.

This work investigates models and experimental setups which consider the adhesion mechanisms of particles, including under Mars conditions. These models incorporate the forces from the AFM cantilever during scan-

ning, particle-substrate adhesion and particle-tip adhesion.

The solution offered to the problem of unstable particles is substrates with engineered features, micromachined in silicon, to trap and stabilise particles for AFM and reduce the loading of the sample to a suitable level. Various designs were investigated in a series of tests, and a final design was created for a substrate for AFM during the mission. The substrates were fabricated and incorporated on the sample wheel on Phoenix, now on Mars.

The MECA results are discussed, focusing in particular on the characterization, calibration and cataloguing of samples using the Imperial College testbed. The best ways of obtaining data from the setup were investigated. These strategies were used during the Phoenix mission.

Finally, the extant microscopy data acquired during surface operations are presented and the overall operations procedures discussed.

Acknowledgements

I would like to thank my supervisor, Tom Pike, for his continued support and for the amazing opportunity of sending hardware to space and then controlling instruments on the spacecraft. My thanks go to him for the stimulating discussions we have shared and for filling my passport with stamps.

Thanks also to my examiners Urs Staufer and Eric Yeatman.

My appreciation is also extended to people throughout the Optical and Semiconductor Devices Group at Imperial College, in particular Sanjay Vijendran for his support and being such a great colleague and friend. Also thanks to the seismometer team for useful discussions and assistance with fabrication.

Also my special thanks goes to the MECA Team, in particular Mike Hecht the instrument lead for inviting me into the team. Surface operations was a magical experience and one I will not forget.

Thanks to the University of Neuchatel where the Mars AFM was developed in collaboration with Nanosurf and the University of Basel, and to the other contributors to the MECA microscopy station including the Niels Bohr Institute at the University of Copenhagen for the magnetic substrates, and

the University of Arizona for developing the Optical Microscope. Thanks to the NASA Jet Propulsion Laboratory for running such an exciting mission and to Peter Smith - the principal investigator - for leading it.

I owe further gratitude to the EPSRC and STP (for awarding me the Jan Dzienisiewicz studentship) for funding my studies. Also thanks to PPARC (now STFC) for funding the UK involvement in the Phoenix Mars mission.

And mostly to my husband, Pete, for his constant, unwavering understanding and support. And for making me happy. And my family, to whom I dedicate this work; my parents, for their continued love and encouragement and my brother for keeping me sane.

"To see a world in a grain of sand"

William Blake

Publications

Publications arising from this work:

Sykulska, H. and Vijendran, S. and Pike, WT. Patterned Substrates for the Phoenix Microscopy Station. *36th Annual Lunar and Planetary Science Conference.* March 2005, League City, Texas.

Sykulska, H. Vijendran, S. and Pike, WT. Substrates for the Microscopy of Martian Polar Samples on Phoenix. *Fourth International Conference on Mars Polar Science and Exploration*, October 2-6, 2006, Davos, Switzerland. LPI Contribution No. 1323, p.8043

Sykulska, H. and Vijendran, S. and Pike, WT. Substrates for the Microscopy of Martian Polar Samples on Phoenix. *The UK Planetary Forum*, 2006

Vijendran, S. and Sykulska, H. and Pike, WT. AFM investigation of Martian soil simulants on micromachined Si substrates. *Journal of Microscopy.* 227 (3) pg. 236–245, 2007.

Sykulska, H. Vijendran, S. and Pike, WT. Micromachined substrates for stabilizing particles for scanning probe microscopy. *Micromechanics Europe*, Guimaraes, Portugal, 16-18 Sept., pp. 367-370 (2007)

Hecht, MH. Marshall, J. Pike, WT. Staufer, U. Blaney, D. Braendlin, D. Gautsch, S. Goetz, W. Hidber, HR. Keller, HU. Markiewicz, WJ. Mazer, A. Meloy, TP. Morookian, JM. Mogensen, C. Parrat, D. Smith, P. Sykulska, H. Tanner, RJ. Reynolds RO, Tonin, A. Vijendran, S. Weilert, M. and Woida, PM. Microscopy capabilities of the Microscopy, Electrochemistry, and Conductivity Analyzer, *Journal of Geophysical Research*, 113 (5), 2008

Contents

1 Introduction **13**

1.1 Motivation and Goals 14

1.2 Research Objectives 17

1.2.1 Phoenix Microscopy Objectives 17

1.2.2 Thesis objectives 17

1.3 Micromechanical sensing 18

1.4 Atomic Force Microscopy 19

1.4.1 Deflection Sensing 21

1.4.2 Scanning and Control 24

1.4.3 Operation Modes 28

1.4.4 AFM probes 30

1.4.5 Uses and Applications 35

1.4.6 Comparison to Other Techniques 36

1.5 Remote Sensing: the Planet Mars 37

1.5.1 Mars Exploration 37

1.5.2 Martian Dust and Soil 42

1.5.3 Mars Dust Analysis 43

1.5.4 JSC MARS-1: Martian Regolith Simulant 44
1.5.5 Past AFM work 47
1.6 The Phoenix Project 47
1.6.1 The MECA Microscopy Station 51
1.6.2 An AFM for Mars: design requirements for Space Qualification 55
1.6.3 Cantilevers for Topographical Imaging 58
1.6.4 Mars Microscopy: Imaging with the OM and AFM . . 59
1.7 Description of Thesis 65

2 Adhesion Models and Experiments 67

2.1 Particle Scanning 67
2.2 General Adhesion 68
2.2.1 The Force of Particle Adhesion 68
2.2.2 Adhesion of a Single Particle 69
2.2.3 Adhesion forces 69
2.2.4 Conclusions 94
2.3 Mechanics of Particle Adhesion 94
2.3.1 Real Particles 97
2.3.2 Further Tip-Driven Motions of a Particle 99
2.4 Tip-Particle dynamics: the lateral force from the cantilever . 100
2.4.1 AFM Forces 100
2.4.2 Background 106
2.4.3 Measuring the lateral force 111
2.4.4 The Mars AFM 123

2.5 Particle-Substrate Adhesion 125
2.5.1 Experimental Setup 126
2.6 Particle interactions 133
2.6.1 Interparticle forces 133
2.7 Summary 137
2.8 Conclusion 138

3 MECA Hardware 139

3.1 Introduction 139
3.2 Description of problem 140
3.2.1 Background 140
3.2.2 Particle Adhesion and Scanning 141
3.2.3 MECA Microscopy Operations 145
3.3 Tests of Preliminary Designs 146
3.3.1 Experimental Methods 146
3.3.2 Experimental Materials 148
3.3.3 The OM and AFM Scanning System 150
3.3.4 Designs Investigated 153
3.3.5 Results and Discussion 153
3.3.6 Conclusions from Initial Tests 167
3.4 Final Design for Flight Substrates 168
3.4.1 Substrates for MECA 168
3.4.2 MECA Substrate Design 169
3.4.3 Digital Code 173
3.4.4 Detail of Digital Code 175

3.5 Device Fabrication 177
3.5.1 Creating Substrates 178
3.5.2 Testing of Substrates 184
3.6 Summary 187
3.7 Conclusions 187
3.8 Cruise Images 189

4 MECA Testbed and Operations 190
4.1 Introduction 190
4.2 Testbed setup 192
4.2.1 Testbed at Imperial College 192
4.3 MECA Microscopy on Mars 205
4.3.1 Aims 205
4.3.2 Testbeds 206
4.3.3 OM images 206
4.3.4 Presample documentation 207
4.4 Results of Testbed Testing 210
4.4.1 SWTS motion 210
4.4.2 Backlash 213
4.4.3 Sample delivery to the Substrates 215
4.5 Summary and Conclusions 238

5 Data from Mars 240
5.1 Introduction to MECA Microscopy 242
5.2 Optical Microscopy 243
5.2.1 EDL/airfall 243

5.2.2 Mama Bear 249
5.2.3 Rosy Red 252
5.2.4 Sorceress 253
5.2.5 Mother Goose 257
5.3 AFM Imaging 259
5.3.1 The First Scan 259
5.3.2 Nanobuckets 259
5.3.3 Martian Particles 261
5.3.4 Identifying Minerals 264
5.4 Conclusions from MECA microscopy 269

6 Conclusions and Further Work 270

6.1 Contributions of this thesis 270
6.2 Thesis Objectives Revisited 271
6.3 The objectives of the Phoenix Microscopy Station 272
6.4 Conclusions 272
6.5 Further Work 273

Chapter 1

Introduction

Scope and Objectives

It is our inherent human desire to be intrepid explorers: and it is our duty as conscious creative beings. Exploration is an opportunity to encounter something perfectly unexpected and a way of advancing our civilization - to grow and expand our knowledge. Space is the next logical step for human evolution. And Mars is the next logical step for human exploration. To explore and to learn; we owe it to Galileo and Copernicus.

John F. Kennedy said it best: "not because it is easy, but because it is hard."

A scientific bonanza awaits us on Mars. This includes comparative planetology, or the science of comparing the different planets in our Solar System with the aim of understanding the origin, history and future of our own planet. For example, we need to answer important questions about the presence of water on Mars. If there used to be water, what happened to

it? Will the same happen on Earth? Why did two planets, similar in so many ways, evolve so differently? And there are tantalizingly unanswered questions beyond planetology. Is - or was - there life on Mars? Is Mars habitable by humans?

The first in NASA's Scout Program, the Phoenix Mars mission successfully landed on the North polar region of the planet in Summer 2008, where large amounts of subsurface water-ice have been detected. Since landing, scientists have been working hard to achieve Phoenix's goals to characterize the climate and geology of Mars and study the ice-rich soils of the Martian arctic looking for clues on the history of water and to determine the habitability potential. Phoenix is carrying a number of scientific instruments to analyse the soil and dust, including an Atomic Force Microscope (AFM). The AFM is a form of scanning probe microscope which comprises a sharp tip at the end of a microcantilever which moves over the surface of a sample in a raster scan.

The aim of this work has been to help prepare this AFM for a Mars mission - the first AFM on Mars - including aiding with the substrates on which samples are scanned as well as evaluating the working of the machine on Mars by testing it in an environmental chamber and preparing the software that controls it.

1.1 Motivation and Goals

The role of dust particles to the Martian dynamics and the effect of dust on equipment are critical for us to understand for planning human missions to

the surface of Mars (Mellon and Jakosky, 1993). Scattering data, generally known from remote sensing, shows dust particles observed in the lower atmosphere of Mars are in the micron-sized region (Gierasch and Goody, 1968; Kahn et al., 1992). However, there has been no imaging of individual dust and soil particles to ascertain their size distribution and shape. Existing imagers sent to Mars do not have the resolution to resolve what is on the surface.

Excitingly detailed images of the Martian soil structure direct from the surface of Mars are obtained using two types of microscope: an Optical Microscope (OM) and high resolution AFM, capable of seeing the structure of materials nearly down to the atomic level. This surpasses any capabilities of any previous instruments that have landed on Mars, by providing the highest spatial resolution of any *in-situ* instrument to date. There will be an increase in understanding of the operational parameters of these microscopes in the extreme environmental conditions that exist on the Martian surface. Such work holds great benefits for *in-situ* planetary science as the AFM a is powerful tool for obtaining fine topography on the molecular scale. Extensive earth-based testing will enable the development of new designs and methods to operate the AFM that will extend the range of space and terrestrial applications.

Cantilevers are a very versatile tool for characterising surfaces. With their very high sensitivity they provide a non-destructive means of analysis allowing a wide range of applications. Microcantilever sensing is used extensively in scanning probe microscopy. It is used in AFM for its high lateral and vertical resolution allowing us to look at surfaces on an atomic scale.

The samples delivered to the microscopy station are transferred to the microscopes via individual substrates arranged on a wheel and held in the horizontal position for imaging. Sample preparation is a critical part of successful scanning of loose micron-sized particles with an AFM. Early investigations highlight problems of tip-particle interaction, either small particles being pushed by the tip during a scan or the cantilever crashing into large particles because of the generally low aspect ratio of the tip.

Due to the finite time available for scanning with the AFM during the Mars mission, slow scan rates are not favoured, as this would greatly limit the total data returned. Likewise, reducing scan resolution is not recommended since it would reduce the detail of the image. Also, due to the very cold ($\sim -30°$C) and dry environment on the Martian surface, adhesive coatings may not be effective. Most adhesives lose their adhesive properties at such low temperatures. Even the normally present thin film of water - which is prevalent in ambient terrestrial AFM experiments - cannot assist with adhesion at these low temperatures. Therefore, it is imperative that we obtain suitable scanning conditions that allow a reasonable scan speed without disturbing the target particles.

Moreover, we have shown that flat silicon substrates cannot be relied upon to hold all the particles that are of interest for analysis by the optical and atomic force microscopes. Results show that particles with diameters greater than 150μm are unlikely to adhere to a flat substrate in the vertical orientation. Therefore, custom-designed substrates will be required for suitable sample preparation.

This work investigates a method of providing fields of particles suitable

for imaging with an AFM, and stabilizing them for scanning by developing substrates to control the forces at precisely the size scale of the particles which are being looked at.

1.2 Research Objectives

1.2.1 Phoenix Microscopy Objectives

The task of the microscopy station on Phoenix aims to characterize the dust and soil grain particles in the micrometre and submicrometre size range from the atmosphere and surface of Mars.

The official success criteria relevant to the MECA microscopy station are: for minimum mission success to acquire 'Samples of the surface soil and one depth to MECA'; and for full mission success to acquire 'Samples of the surface soil and two depths to MECA' and also to 'Use MECA to analyze 3 samples in its microscopy station.'

1.2.2 Thesis objectives

In the context of the overall aims of the Phoenix project to do with this PhD, the particular objectives of this thesis were identified.

The vertical orientation of the substrates in the sample wheel and gravity on Mars require that some form of adhesion is maintained between the soil samples and substrates. Chemical adhesion may be difficult to achieve at the low temperatures, so physical trapping may be better.

It is found that by using etched silicon substrates with patterns of particular shapes and sizes, the imaging of micron-sized Mars analog material

can be accomplished with some success. Improved designs of substrates were required that would serve both as a good surface to trap and hold particles during AFM scanning and also to provide a reference pattern in the images. An objective of this thesis was to explore the possibilities for holding particles for AFM scanning and create substrates which can adequately prepare samples for successful atomic force microscopy on Mars.

Within this objective was also the aim to study the lateral forces of AFM, in particular when considering the scanning of loose particles. This also involved an understanding of how Martian analog soils and dusts adhere to substrates of different materials and topography and thus conduct a study of all the microscopy substrates to be used during the mission. To enable this, a testbed of a functional copy of the flight microscopy station within an environmental chamber was set up at Imperial College to enable the end-to-end characterization of the microscopes under Mars conditions. Such a study was aimed at providing experience of the microscopy station valuable for mission operations.

1.3 Micromechanical sensing

Micromechanical sensors are microscopic devices with mechanical functions. They are able to detect movements or profiles on a micro- or even nanometre scale. Cantilevers, as used for micromechanical sensors, are produced by standard silicon microfabrication technology. As shown in Fig. 1.1 the microcantilevers are small rectangular or V-shaped cantilevers - typically made of silicon nitride (Si_xN_y) or silicon (Si) - with dimensions of the order

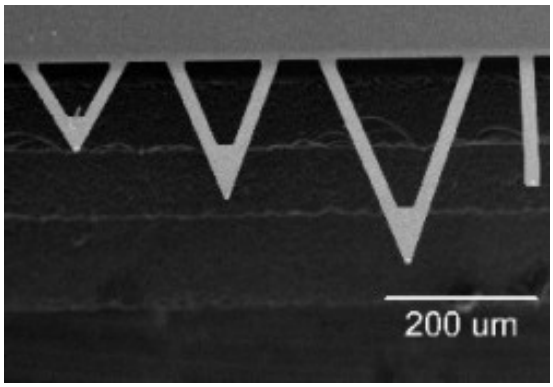


Figure 1.1: Scanning electron micrograph showing (from left to right) three V-shaped micro-cantilevers and one rectangular micro-cantilever (Cross, date accessed: May 2008).

of 400μm long, 50μm wide and 1-5μm thick.

Microcantilevers were originally designed to be used in scanning probe microscopy for surface imaging. However, microcantilevers have a variety of versatile traits. Their flexibility makes for a sensitive tool when combined with techniques to monitor bending. Forces that can cause a cantilever to bend include those acting on the tip to produce a deflection as well as tensile and compressive forces acting on an appropriately coated cantilever surface.

Whether it uses the concept of scanning with an extremely sharp tip across a surface, or coating the cantilever with another material, the technique relies upon the flexibility of the cantilever and relative movement.

1.4 Atomic Force Microscopy

Scanning Probe Microscopy (SPM) has become an important and versatile tool for the topographical study of material surfaces down to the nanometre

scale as well as providing information about material properties. In particular, the invention of Atomic Force Microscopy (AFM, or scanning force microscopy, SFM) by Binnig, Quate and Gerber (Binnig et al., 1986) in 1986 overcame the previous limitation of electrical conductivity of samples. This was a significant step in material science.

Binnig, Quate and Gerber demonstrated a new microscope with the ability to image insulators and measure forces as small as 10^{-16}N due to the small mass of the cantilever. This first AFM was a combination of an STM (Scanning Tunnelling Microscope) as discussed by Binnig in a paper earlier that same year, and a stylus profilometer (Binnig and Rohrer, 1985). Both these probe the surface by raster scanning it, with no damage to the sample, thus giving a 3D image.

In a model AFM, based on the design originally conceived by Binning, Quate and Gerber, the device comprises a cantilever-spring deflection controlling a z-regulating feedback loop. A sharp tip at the end of the cantilever moves over the surface of a sample in a raster scan. In general, the tip is scanned forwards and then backwards over the same line before stepping on to the next line. In static mode, as the tip moves, the cantilever bends in response to the force between the tip and the sample, and this deflection is measured to provide the topographic image. In dynamic mode, the change in the oscillating frequency of the cantilever due to tip-sample interaction is monitored. Feedback is used to keep the force or force gradient constant.

The Binnig, Quate and Gerber paper (Binnig et al., 1986) discusses how the AFM favours a soft spring in order to obtain maximum deflection, while also a stiff spring with a high resonant frequency to minimize the sensitivity

to vibrational noise. Piezoelectric drivers drive the cantilever at its resonant frequency and an image is obtained by measuring the force on the tip.

The original paper of Binnig *et al* also talks about 'eventual microfabrication' as an improvement to the design. The authors continue by saying that microfabrication techniques could reduce the mass of the cantilevers by several orders of magnitude. They also describe that in order to further improve the performance, operation in an ultra-high vacuum chamber would improve the stability of the system by two orders of magnitude, while cooling to below 300mK would limit the thermally induced vibrations, thus achieving the lower limit of force sensitivity of 10^{-18}N that they assert to be possible.

The paper claims that 'the interatomic forces therefore range from 10^{-7} N for ionic bonds to 10^{-11}N for van der Waals bonds and down to perhaps 10^{-12}N for some of the weaker surface reconstruction.' So the 'limiting of sensitivity of the instrument is far less than these values', as declared to be 10^{-18}N, allowing all the important forces that exist between the sample and the tip to be measured.

A description of each part of this system is given in the following section.

1.4.1 Deflection Sensing

The small bending of the cantilever in response to the interaction with the surface can be measured by various techniques, sketched in Fig. 1.2. The first AFM from Binning, Quate and Gerber used a Scanning Tunnelling Microscope (STM) tip positioned above the end of the cantilever to provide the deflection data by monitoring the tunnelling current (Binnig et al., 1986).

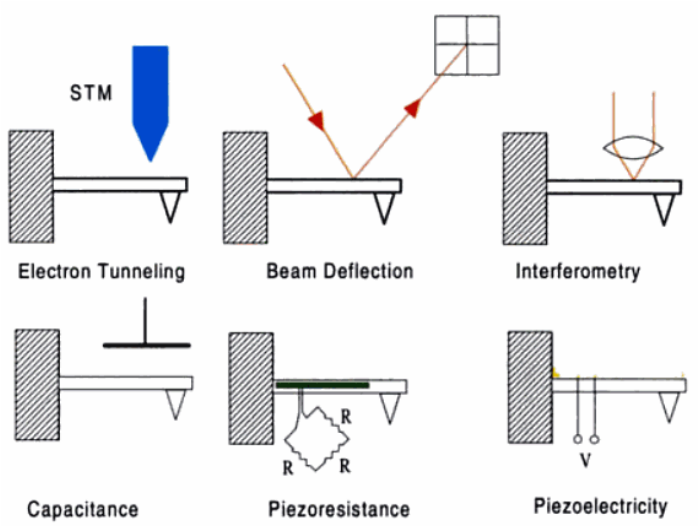


Figure 1.2: Various deflection sensors for Scanning Probe Microscopy. (Meyer et al., 2004)

Piezoresistive sensing gave the first dynamic mode images with atomic resolution. (Giessibl, 1995) Piezoresistive sensing provides an elegant form of self-sensor. The technique exploits the varying electrical resistance of materials when a mechanical stress is applied. The elements act as a strain gauge and a wheatstone bridge shows the stresses in the cantilever. However, a limitation with this type of sensor is the poor signal to noise ratio when operating in static mode due to the large *1/f* noise.

Similarly, a piezoelectric sensor uses materials that produce an electric potential in response to an applied stress. This technique can in fact provide both the sensor and the actuator for the cantilever at the same time. (Chu et al., 1997)

Another early AFM described by Gerhard Meyer *et al* (Meyer and Amer,

1988) implemented an optical scheme to detect the deflection of the cantilever. It used a technique whereby the displacement of the cantilever was detected by the movement of a reflected laser beam on a photodetector. The method involves a position sensitive detector (PSD) to detect the light reflected off the back of a cantilever. It had been demonstrated previously (Amer et al., 1986; Olmstead et al., 1983) that displacements of 10^{-4} Å could be detected. The sensitivity of this technique is better than a piezoresistive element which has a worse signal-to-noise ratio, and the optical method is limited by the thermal vibrations of the cantilever. This beam-deflection method has remained a popular technique and is currently used in most AFM systems (Meyer and Amer, 1988; Alexander et al., 1989). This 'simple and sensitive' method allows the measurement of cantilever displacement over a wide range of frequencies and distances between the tip and the sample.

An optical laser interferometer looks at the normal surface displacement as the back of the cantilever acts as one mirror of the interferometer (Rugar et al., 1989). This optical sensing technique provides another accurate method, although does not have as large a working distance as the beam deflection method.

Both the optical and electrical detection are very sensitive methods able to measure cantilever bending in the sub-nanometre, but neither is without disadvantages. Monitoring the deflection of a laser beam is popular, though the careful optical alignment of the photodiodes is critical. To align the laser beam, conventional AFMs use additional positioning equipment, often requiring tiny screws and special tools. This can make laser beams a

difficult and cumbersome approach. Although more noisy in static mode, piezoresistive sensing is attractve for remote operations or for arrayed AFM sensors (Aeschimann et al., 2007).

Another form of integrated detection scheme is to use capacitive sensing for measuring the cantilever deflection. With one stationary electrode above the cantilever and one on the rear-side, the voltage across the two plates vary as the cantilever bends (McClelland and Glosli, 1992). Again, the advantage of capacitive sensing is that the full sensor can be manufactured by microfabrication (Blanc et al., 1996). A complication of this system, as with the STM tip, is the interaction of the cantilever with the electrode above it.

1.4.2 Scanning and Control

In order to raster scan the sample with the tip, it is the relative motion of the scanning system with respect to the sample that is important. Generally, it is desirable to move the part of the system with the least mass, and to avoid moving any optics involved.

The original AFM from Binning, Quate and Gerber used a three-dimensional piezoelectric drive x, y, z-scanner to move the sample with respect to the tip, using a feedback loop to keep the force acting on the cantilever at a constant level.

Regardless of the mode of detection, a piezo-tube scanner most commonly controls the movement of the tip or sample in the x, y, and z-directions. These scanners are similar to those used in STMs. Piezo-tube scanners (Hansma and Sonnenfeld, 1989) enable positioning with a very high

precision and offer this large scan range while maintaining the stability of the scanner.

However, piezo actuators are vulnerable to thermal drift, creep and aging and may give problems with non-linearity. Further to this, piezo-tube scanners are quite bulky and brittle and require large driving voltages of over 100V in order to achieve the requirements in scan range for the instrument for the Phoenix mission. Primarily due to its low gas density (or low pressure of $\sim$7 Torr), the Martian atmosphere ionizes more easily than on Earth, thus dissipating electrical charges at a lower voltage. This Paschen electrical discharge means that voltages larger than 50V would ionize the carbon dioxide atmosphere. Therefore the large driving voltages need for piezo-tube scanners may cause electrical discharges, damaging or destroying certain electronic components, making this method of driving the scanner unsuitable for Mars.

Instead of piezoelectric actuation, an electromagnetic scanner technology with low power consumption was developed.

The technique, which is based on electromagnetic actuation, uses a driving signal of only 12V. Three actuators, sat on a platform, are arranged in a triangular configuration and each consists of an electromagnetic coil and leaf spring suspended permanent magnet. Current sources on the electronic board drive the coils. Passing a current through a coil attracts or repels the magnet. This moves the platform around an axis defined by the two opposite coils. Fig. 1.3 shows the scanning principle schematically.

For the Mars configuration an AFM 'chip' is formed of an array of cantilevers each with an integrated piezoresistive deflection sensor. The chip

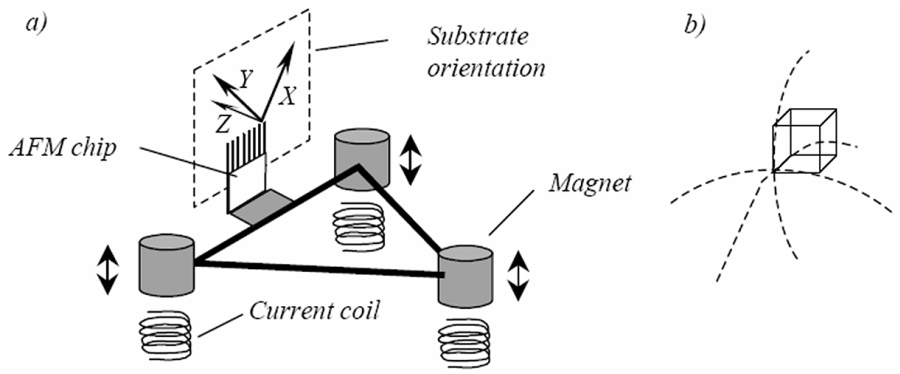


Figure 1.3: A schematic view of the scanning principle, 3 magnets are placed in a triangular configuration and are attached to a spring-loaded platform. A coil is placed under each magnet to actuate the platform. b) In a first approximation, by considering small displacements, the curved x-y-z motion produced by the platform at the AFM tip location is linear. (Nanosurf, date accessed: March 2008)

is mounted vertically on the platform with the tips facing the substrate. This microfabricated chip constitutes of 8 cantilevers, providing redundancy. This is described more in Section 1.6.2. Mounted on the backside of the chip holder is a small piezo-electric disk which vibrates the cantilevers when operating in dynamic mode.

Scanners can operate under open or closed loop control. Working using an open loop control offers no linearization. With a scanner operating at closed loop there is feedback linearization. Although open-loop control of a scanner can enable fast imaging (Lee et al., 2000) - and indeed high-speed atomic force microscopy - generally closed-loop control is preferred due to its superior linearity and force-control.

An AFM operated with feedback control allows the cantilever to main-

tain constant deflection and thus constant force on the sample when run in static mode. When the electronic feedback is on, the piezo will adjust the tip-sample separation as the tip is raster-scanned across the surface. Similarly the oscillation properties can be controlled in dynamic mode (see also Section 1.4.3. The image is generated from the position of the scanner as it moves up and down to keep the control signal constant. When the feedback is off, the microscope is said to be operating in constant height mode. As the height of the scanner is fixed in this mode, the spatial variation in deflection or vibration of the cantilever is used directly to produce the topographic image. Constant height is particularly useful for imaging very flat samples at high resolution and high speed.

For the case of most dynamic mode AFM systems, to provide the feedback signal, one of two schemes is employed: amplitude modulation AFM (AM-AFM) or frequency modulation (FM-AFM). For AM-AFM the oscillation frequency is kept constant and the amplitude of the oscillation is the feedback parameter, whereas for FM-AFM the phase shift is kept constant using a Phase Locked Loop (PLL) circuit and the frequency feeds the feedback loop. In both schemes, the user defines a 'setpoint' which is a measure of the interaction with the sample. For AM-AFM this refers to a proportion of the free oscillating amplitude and for FM-AFM it is the change in frequency that is monitored. The advantages of each mode are discussed further in Chapter 2.

The difference between the actual lever amplitude or frequency and the preset setpoint value for the chosen parameter is used to correct the tip-sample distance. This difference is labelled the error signal (or in the case

of amplitude modulation, the lever amplitude). A higher setpoint applies a larger interaction with the sample, but often means also more wear to the tip or damage to the sample.

This error signal is used to correct the tip-sample distance by applying a proportional and integral amplification and feeding it back to the scanner for adjusting the height. The gains are chosen to allow maximum response to the changing topography of the surface, but not so high that 'ringing' occurs which is a result of feedback oscillations.

1.4.3 Operation Modes

These microcantilever systems are operated in three closed-loop modes: non-contact, contact and intermediate contact or 'tapping mode'.

In contact mode or static mode the cantilever deflection, and thus the tip-sample interaction force, is held constant in a closed-loop operation. The force sensitivity is thus directly proportional to the cantilever stiffness. Hence, soft cantilevers are chosen so as to increase the deflection signal. However, this low stiffness causes the tips to 'snap-in' to the surface due to the strong attractive forces near to the surface. This means contact mode is usually operated in the contact regime - hence its name - as indicated on the van der Waals curve in Fig. 1.4, where the overall force is repulsive. The contact mode monitors the interaction forces while the cantilever tip remains in contact with the target sample; the tip permanently touches the specimen, thus also allowing the name 'constant force mode'.

In order to probe electric, magnetic or atomic forces of a selected sample, the non-contact mode is utilized by moving the cantilever slightly away

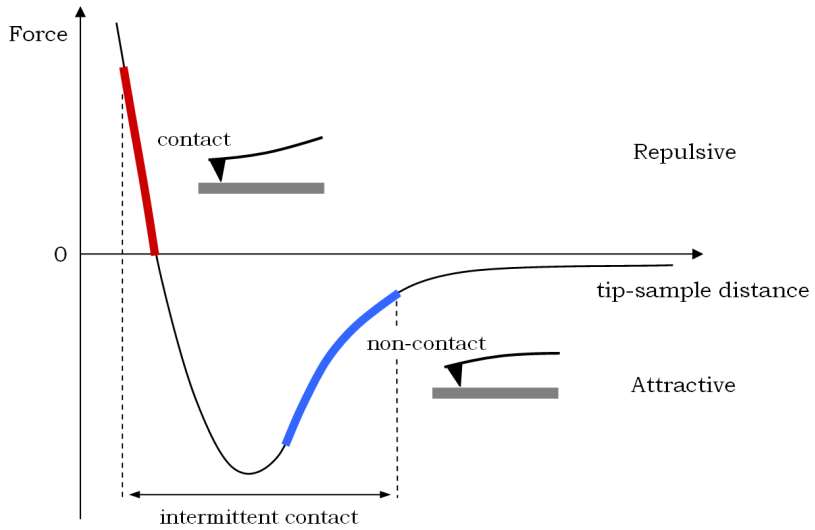


Figure 1.4: Van der Waals curve showing force as a function of the interatomic distance between the tip and the surface.

from the sample surface and oscillating the cantilever at or near its natural resonant frequency, operating in the non-contact regime of the van der Waals curve. This is particularly useful for studying soft or elastic surfaces or to protect surfaces from contamination from contact with the tip. Stiffer cantilevers are used than for contact mode so as to prevent the tip being pulled into contact.

The tapping mode of operation combines qualities of both the contact and non-contact modes by gleaning sample data and oscillating the cantilever tip at or near its natural resonant frequency while only allowing the cantilever tip to impact the target sample for a minimal amount of time.

One downside of remaining in contact with the sample during the scan is the large lateral forces that act on the sample as the tip is "dragged"

over the sample. In the case of imaging poorly immobilised or soft samples, tapping mode proves superior to contact mode for imaging, as the lateral force from the lever is reduced significantly. Similarly, tapping mode causes less damage to soft samples than contact mode AFM.

1.4.4 AFM probes

1.4.4 AFM probes - shape of tip and lever - convolution - other shapes e.g. nanotubes

For a spring constant k and effective mass m, the resonant frequency f is given by the expression

$$f = \frac{1}{2\pi}\sqrt{\frac{k}{m}} \tag{1.1}$$

It is evident from Hooke's Law that in order to achieve maximum sensitivity of the forces between the tip and sample and for the tip to exert as little force as possible on the sample, a low spring constant is desirable. In addition to this, a high resonant frequency gives a fast scan rate and minimizes the vibrational sensitivity, given that external vibrations are often in the low frequency range. It is possible to achieve both these qualities if the cantilever has a small mass. In terms of the Mars AFM, a small mass coincides with the restrictions on volume, mass and power for space instrumentation.

AFM tips are based at the end of the microcantilever, as seen in Fig. 1.5, and are the part of the instrument that directly contacts the sample to

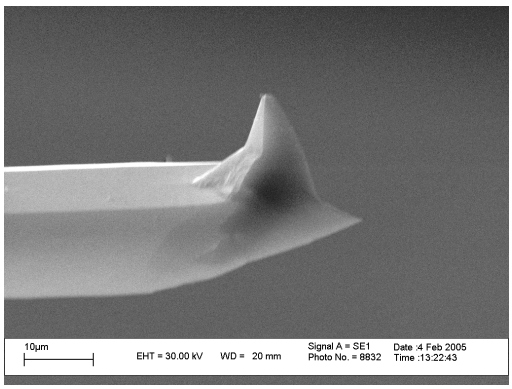


Figure 1.5: An AFM tip at the end of a rectangular cantilever.

generate the image. They are generally made of silicon or silicon nitride, and have a pyramidal shape and a radius of curvature on the order of nanometres.

It is intuitive that the sharper the tip the higher the resolution with which the sample can be imaged. AFM images are obtained as a combination of the tip and sample geometry. This leads to the imaging artefact known as tip convolution. Although this is not mathematically a true convolution, but geometrically a dilation, the images are distorted by the shape of the tip and resulting in one of the most important error sources of scanning probe microscopes. For the desired case, where the tip is much sharper than the feature, the profile of the feature is well represented. However, in the case where the tip is not as sharp as the feature, the image will be dominated by the shape of the tip and there will be broadening of the feature. The term describes the influence of the tip on the image which is generally a broadening of features with a higher aspect ratio than the tip, as in Fig. 1.6. As the tip scans over the feature, the sides of the tip make contact before the apex does, and the feedback mechanism responds to the feature.

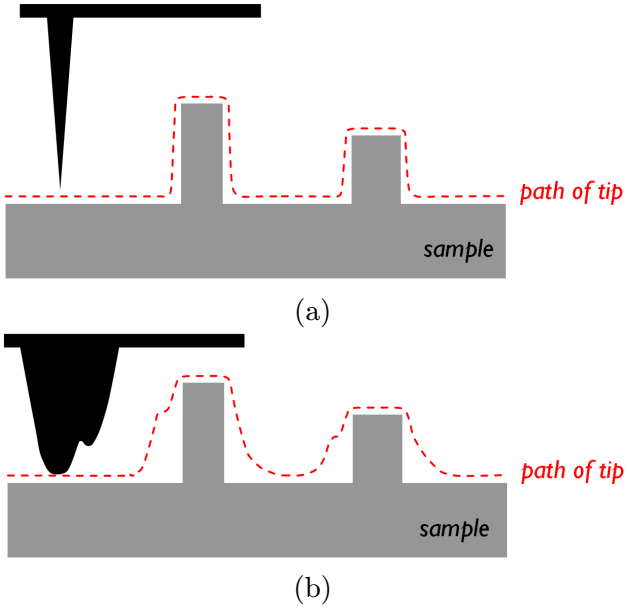


Figure 1.6: Sketches demonstrating the origin of tip convolution. In (a) a sharp tip images the sample well whereas in (b) the blunt tip is less sharp than the features it images and broadens their shape.

The true surface profile can be reconstructed by correcting for this tip artefact through using algorithms of dilation or erosion. To do this, first the tip geometry must be known. Moreover, the image cannot be reconstructed in areas where the tip has not imaged the sample, for example in corners near steep sidewalls where the tip cannot reach, so still sharp tips give more information.

In any AFM system, tips and cantilevers have a finite lifetime as they become contaminated or wear from use. Replacing cantilevers would be difficult on Mars. Therefore, an array of 8 levers was incorporated in the Mars AFM, so when one becomes damaged, or unsuitable for use, the next would be activated, as explained in detail in Sections 1.6.2 and 4.4.3.

AFM probes are usually fabricated with integrated tips using semiconductor micromachining technology (Wolter et al., 1991). The probes for the Mars AFM instrument have high aspect ratio tips. <110> silicon wafers were KOH slow-etched until the planes intersected, and then sharpened using a thermal oxidation process, giving a 50°C cone angle (Beuret, 1999), as shown in the image in Fig. 1.7.

Conventional AFM cantilever tips are about 10μm in height. While the end of the apex of the tip may have a radius of only 10nm or less, the overall pyramidal shape limits the aspect ratios to very low values. These tips are excellent for studying topography in the nm height range. However, they are extremely limited when faced with features in the micron range due to the low aspect shape. There is little evidence in the literature of work done with AFMs on 1-10μm high features, except in the area of metrology of semiconductor device processing (photoresist and trench profiling) (Ridley Sr et al.,

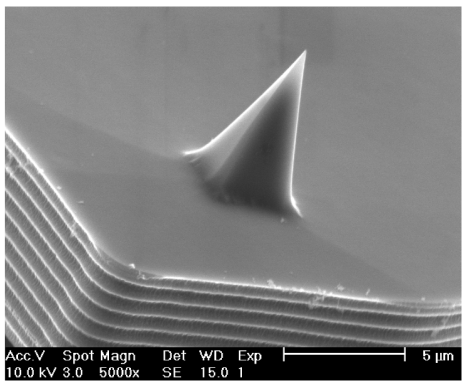


Figure 1.7: An SEM image of an AFM tip on the Mars Phoenix instrument (Hecht, 2008).

2002).

These metrology applications require special tips with high aspect ratios, including exotic tips such as carbon nanotubes (Bhushan et al., 2004). Their small radii (0.7-5nm from single-walled nanotubes), high aspect ratio, extremely large Young's modulus, and ability to be elastically buckled under large loads, make them ideal candidates for AFM tips.

The Phoenix AFM (Akiyama et al., 2001), being a space-qualified instrument, is of course limited in its range of available tip geometries, as robustness is key for space-bound hardware, and high-aspect ratio tips tend to be very fragile and more difficult to use.

Scanning probe microscopes can also obtain other information, such as a measure of the elasticity or of the friction between sample and tip as the cantilever twists as it moves across the sample.

1.4.5 Uses and Applications

The AFM system has evolved into a useful tool for a broad spectrum of applications. These range from surface characterization in material science (Nagashima et al.; Westra and Thomson, 1995; Yamamoto et al., 2000), to the study of living biological systems in their natural environment (Braet et al., 1998; Erie et al., 1994; Hansma et al., 1993; Lee et al., 1994; Ludwig et al., 1999; Yang et al., 2003) to nanolithography (Jalili and Laxminarayana, 2004). Apart from its impressive ability to perform high-resolution imaging of insulators, an AFM has the advantage of being able to operate in almost any environment, such as air, dry nitrogen (Koinkar and Bhushan, 1996), high vacuum (Carpick et al., 1996; Giessibl, 1995; Shin'ichi Kitamura, 1998), high pressures (Glezer and Mazur, 1997) or liquids (Hansma et al., 1992; Schäffer et al., 1996; Putman et al., 1994). An AFM provides additional capabilities and advantages relative to other microscopic methods (e.g. scanning electron microscopy and transmission electron microscopy) in studies of metallic surfaces and microstructures by providing reliable measurements at the nanometre scale (Westra and Thomson, 1995; Göken and Kempf, 1999; Kempf et al., 1998; Yamamoto et al., 2000).

AFMs are even finding their way into the field of space exploration. Specifically, AFM is appropriate for *in-situ* investigations of dust and soil particles from comets and asteroids or on the surface of planetary bodies (Riedler et al., 1998). Scientists and engineers have discussed a variety of potential enhancements to current AFM technology that will further expand its applications and benefits for remote planetary sensing. These include

microfabricated AFMs on a single silicon wafer (Indermuehle et al., 1994; Indermühle et al., 1995; Ando, 2004), alternative AFMs designs that do not require lasers for sensing (Manalis et al., 1996; Harkey and Kenny, 2000), and different shaped cantilevers to optimize sensitivity (Albrecht and Quate, 1987; Sader, 2003).

In summary, there are many exciting areas of further development for AFM technology. The AFMs of tomorrow will be significantly smaller, more robust, more sensitive, and better able to handle *in situ* analysis.

1.4.6 Comparison to Other Techniques

Scanning probe microscopes (SPM) offer advantages and disadvantages over other imaging techniques.

Unlike other imaging techniques, such as Scanning Electron Microscopes (SEM) which afford two-dimensional projections, SPMs provide a true three-dimensional surface profile as the cantilever follows the surface. This physical interaction with the surface means various parameters can also be measured.

A disadvantage of SPM techniques associated with this interaction is their speed. Where other high resolution techniques such as SEMs provide rapid high magnification images of any solid sample, SPMs are comparatively very slow as they raster scan across the surface and may take even on the order of an hour to produce a high resolution image.

However, SPMs benefit from their ability to image in almost any operational environment and not require a vacuum atmosphere. Measurements can be conducted for example in air, dry nitrogen, high vacuum, high pres-

sures, low temperature, magnetic fields and in liquids and gases, including through opaque fluids. The small thin cantilever dimensions can often lead to increased accessibility to the sample where, for example, beams of light cannot reach. Further to this, the small dimensions allow several sensors in an array.

Further to this, SPMs are able to image a variety of samples with high sensitivity, including conductive and non-conductive surfaces, even to the atomic level. This means minimal sample preparation which may otherwise cause irreversible changes to the sample.

Another large, and perhaps governing attribute for remote sensing, is the overall mass of the instrument. An AFM can be designed to be compact, light and compatible with the payload restrictions imposed on space missions.

The AFM attributes - high resolution, ability to provide 3D projections and measure multiple properties, robust operating environments, and predominantly its small size - compare favourably with many other common high-resolution techniques for microscopy such as SEMs and transmission electron microscopes (TEM).

1.5 Remote Sensing: the Planet Mars

1.5.1 Mars Exploration

The many missions to Mars have made much progress towards improving our knowledge of the planet, especially recently. Since the early fly-by missions, there have been three types of missions: orbiters, landers and rovers.

Orbiters tell us about the planet as a whole. They divulge a wealth of data about Mars' atmosphere, landforms, gravity, magnetic fields, elemental and mineral composition, internal structure and weather. Landers, on the other hand, provide a means to analyse the surface - both visually and chemically.

Successful landers include Viking 1 and 2 in July and August 1976, Pathfinder in July 1997, and rovers include Spirit and Opportunity in January 2004, which are still returning data today. The Viking landers each had a robotic arm that scooped up soil samples. These samples were baked and exposed to nutrients and their reactions analysed and not found to be unusual (Flinn, 1977). In addition to searching for life, the landers provided detailed panoramic views of the Martian terrain, measured atmospheric conditions on the surface, deployed seismometers and monitored the Martian weather (Klein et al., 1976; Hess et al., 1977).

Unlike the Vikings, the Pathfinder contained a mobile robot on wheels, called Sojourner. Mission control guided Sojourner around the various rocks seen at the landing site, and instruments on board measured the compositions of rocks and soil, took high-resolution photographs, and conducted spectral measurements (Bell et al., 2000; Hviid et al., 1997; Team, 1997; Rieder et al., 1997; Smith et al., 1997). The rover camera had a resolution of just below a millimetre per pixel.

More recently were the Mars Exploration Rovers (MER), the twins Spirit and Opportunity, shown in Fig. 1.8. The package of science instruments on these rovers consists of two instruments designed to survey the landing site, as well as three other instruments on an arm designed for close-up study of rocks (Benford, 2005; NASA Mars Envorinmental Rover, date ac-

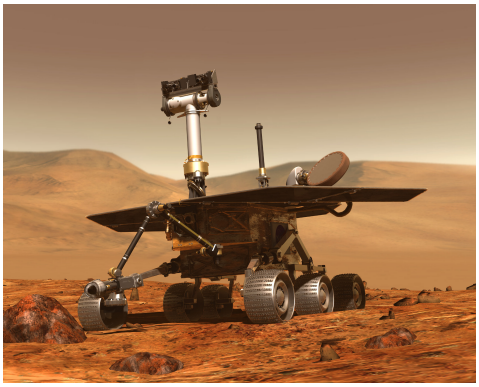


Figure 1.8: An artist's impression of the Mars Exploration Rover (NASA Mars Envorinmental Rover, date accessed: August 2008).

cessed: August 2008). The first instrument to survey the general site was a panoramic camera (PanCam) to view the surface using two high-resolution colour stereo cameras (Bell III et al., 2005). Delivering panoramas of the Martian surface with unprecedented detail, the instrument's narrow-angle optics provide angular resolution more than three times higher than that of the Mars Pathfinder cameras (Team, 1997).

On the arm is a Rock Abrasion Tool that can scrape away the outer layers of rocks acting as the rover's equivalent of a geologist's rock hammer, exposing fresh rock underneath so scientists can better determine how the rock is formed. The instruments on the rover arm are a Microscopic Imager (MI), a Mössbauer Spectrometer (designed to determine the composition and abundance of iron-bearing minerals), and an Alpha Particle X-Ray Spectrometer (to determine the elements that make up rocks and soils).

In addition, the rovers are equipped with three sets of Magnet Arrays

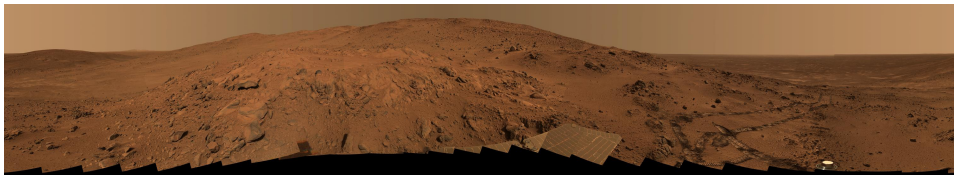


Figure 1.9: Spirit camera's panorama taken from the point informally known as "Larry's Lookout". The image was acquired on the rover's 410^{th} to 413^{th} sol on the surface and shows the summit of Husband Hill in the distance at the centre of the image (NASA Mars Envorinmental Rover, date accessed: August 2008).

that collect the highly magnetic parts of the airborne dust for analysis by the science instruments. Magnetic minerals carried in dust grains may be freeze-dried remnants of the planet's watery past. A periodic examination of these particles and their patterns of accumulation on magnets of varying strength can reveal clues about their mineralogy and the planet's geologic history.

With a camera identical to the panoramic camera, the MER microscopic imagers - one on each rover - are a combination of a microscope and a camera and provide high resolution photographs. The field of view of both instruments is 1024×1024 pixels in size, with a mosaic of panoramic images shown in Fig. 1.9. On these state-of-the-art rovers, the probes can resolve images to a spatial resolution of 30 micrometers per pixel. These detailed pictures will make other types of observations more useful as they can be associated with a visual scene.

The photograph in Fig. 1.10, taken by the microscopic imager on Mars Exploration Rover Spirit, is of a sand drift near the top of "Husband Hill", the highest of the Columbia Hills (NASA Mars Envorinmental Rover, date

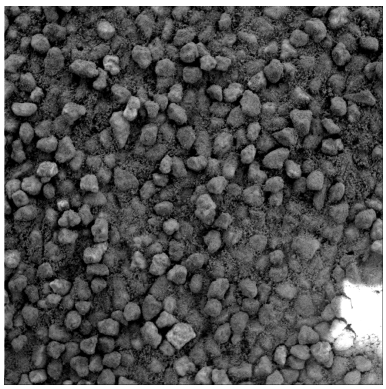


Figure 1.10: This image taken by the Mars Exploration Rover Spirit microscopic imager shows a patch of soil at the target nicknamed "Squiggle Dunes." The rover imaged this area, which measures 3cm × 3cm (NASA Mars Envorinmental Rover, date accessed: August 2008).

accessed: August 2008). Informally named "Cliffhanger" - due to its proximity to the edge of steep slopes that fringe the summit region of the hill - Spirit took the image on the rover's 607^{th} Martian day, or sol.

The image suggests that the grains have not travelled far as they are poorly sorted and are more angular and less rounded, especially when compared to sand deposits on the plains of Gusev Crater studied early in the mission, which consisted of rounded grains. Using a basic tenet of geology, these angular grains imply transport by a short distance from a nearby source.

The image is of a 3 by 3 centimetre area and, with a resolution of 30μm per pixel (Bell III et al., 2003), this allows features as small as 100μm to be resolved. On Earth, however, we are able to image at much higher resolution than this and see much more detail. It would be useful to be able to see the details of the dust and grains at an even higher resolution. High spatial

resolution of images will also help the interpretation of data gathered by other instruments.

In an article published in Nature (Catling, 2005), it was stated that 'on the basis of compositional analysis of dust captured on magnets, magnetite (Fe_30_4) is now identified as responsible'. Evidently, the dust is a mixture of basalt and oxidized minerals, but the origin of the latter is unclear. Examining the dust morphology would help, but the rovers' microscope lacks the magnification to see micrometre-sized dust or its mineral components. Fortunately, NASA's Phoenix Lander launched in 2007 and now in operation on Mars, carries both a colour optical microscope and an atomic force microscope that will open up these unseen vistas.

To put this all into perspective, the scale bar in Fig. 1.11 demonstrates the resolution capabilities of the imaging techniques on previous missions and how this compares to the superior imaging capabilities of the Optical Microscope and AFM being prepared for the Phoenix mission.

1.5.2 Martian Dust and Soil

Scientists are keen to learn about the sizes of the dust particles in the atmosphere, as they play a big role in Martian climatology. Seasonal dust storms are routinely observed, and some have even grown till they have encircled the entire planet as happened in 1998. Martian dust may also be a significant hazard to future human explorers, more so than the Moon dust was to the Apollo astronauts. Understanding the nature of the dust and surface soil will be crucial to ensuring the safety of future explorers.

The Martian atmosphere holds a significant amount of suspended dust.

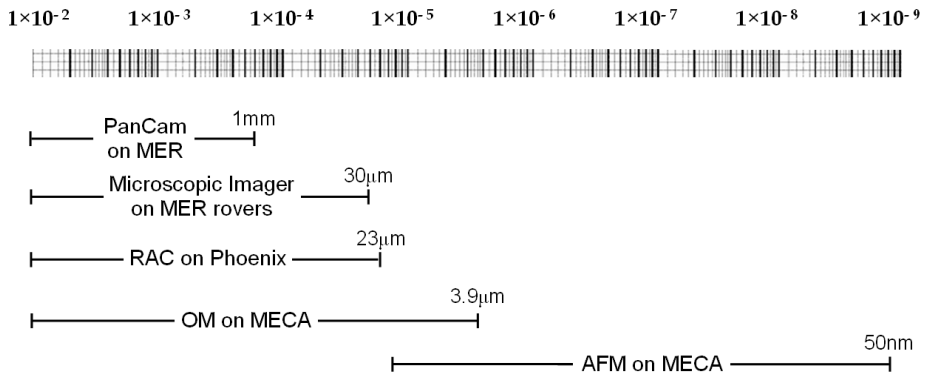


Figure 1.11: Chart showing the resolution ranges at the small scale of the various imaging systems that have returned data from Mars and of the MECA microscopy station for the Phoenix mission.

The particles have a wide range of diameters ($< 1\mu$m to 50μm) and the settling of this atmospheric dust can be a serious threat to spacecraft and to solar cells.

1.5.3 Mars Dust Analysis

Following a series of flyby missions - the first of which was Mariner 9 - Martian dust models were proposed. The first standard model was proposed in 1977 by Toon *et al* (Toon et al., 1977) and became the model to use for the following 20 years. The model consisted of a mixture of a number of different materials, such as quartz, basalt, andesite, basaltic glass, obsidian, granite and montmorillonite as simulations showed that none of these alone could account for the spectral features of the 1971-1972 dust storm.

Clancy *et al* (Clancy et al., 1995) proposed a model in 1995 that substantially improved the fit to the Mariner 9 data in the far infra red.

The Viking missions brought back a wealth of data regarding dust analysis too (Flinn, 1977). Pollack *et al* analyse and describe the use of photographs of sky brightness to obtain information on several particle properties (Pollack et al., 1977). From the observed angular variation of sky brightness close to the sun, estimates of the mean particle size were obtained. Similar data at longer distances from the sun provided information on the shape of the particles.

A number of poorly known model parameters were determined by comparing calculated brightness with the observed brightness of the sky and the ground, including the imaginary refractive index and the cross-section weighted mean particle radius $r_{\text{eff}} = 1.85\mu$m, and the variance $v_{\text{eff}} = 0.5$. From such data a further database of particles was created. This provided useful information for creating Mars soil simulants. The table in Fig. 1.12 shows a summary of dust size and composition from various spacecraft. The table was formed as part of a previous study (Gautsch, 2002) and has been added to with subsequent observations.

1.5.4 JSC MARS-1: Martian Regolith Simulant

Based on results from the Viking mission, a Mars regolith simulant called JSC Mars-1 was developed at NASA Johnson Space Center. This simulant supports scientific research, engineering studies, and education. JSC Mars-1 is a Mars soil simulant which is a sample of lava ash from the Pu'u Nene volcano in Hawaii (Allen et al., 1998a) and is composed of the <1mm size fractions of a palagonitic tephra, which is glassy volcanic ash modified at low temperatures.

Mission	Type	Size [μm] r_{eff} (v_{eff})	Shape	Composition	Source
Mariner 9	IR	1 - 4	Disks, flakes	7% Quartz 93% Anorthosite	(Aronsen et al. 1975)
Mariner 9	UV	1.0 (0.2)	Spherical	-	(Pang et al. 1976)
Viking Lander	IR	0.4	Nonspherical	10% magnetite	(Pollack et al. 1977)
Mariner 9	IR	2.75 (0.42)	Spherical	Montmorillonite	(Toon et al. 1977)
Mariner 9	UV	0.2 (0.9)	Nonspherical	Andesite, basalt, montmorillonite	(Chylek et al. 1978)
Viking Lander	Visible	2.7 (0.38)	Plate-like	-	(Pollack et al. 1979)
Viking orbiter	Visible	< 0.4	Nonspherical	-	(Clancy et al. 1991)
Phobos 2	IR	1.24 (0.25)	Nonspherical	-	(Drossart et al. 1991)
Phobos 2	UV-Visible	0.4 (0.5)	Spherical	Goethite Limonite	(Moroz et al. 1991)
Phobos 2	IR	25 km: 1.0 (0.8) 12 km: 1.8 (0.4)	Spherical	Basalt, Limonite Magnetite	(Korablev et al. 1993)
Mariner 9	IR	0.5 (0.15)	Spherical	Palagonite	(Santee et al. 1993)
Phobos 2	IR	1.7 (0.2)	Nonspherical	-	(Chassefière et al. 1995)
Mariner 9 Viking, Phobos	UV IR	1.8 (0.8)	Spherical	Palagonite	(Clancy et al. 1995)
Viking 1 Lander Viking 2 Lander	Visible	1.52 (0.5) 1.85 (0.5)	Sharp corners	1.2 % magnetite	(Pollack et al. 1995)
Pathfinder	Visible	1.0 (0.3)	-	-	(Smith et al. 1997)
Pathfinder	Visible	1.6 (0.2)	Nonspherical	-	(Tomasko et al. 1999)
Pathfinder	Visible	1.71 (0.25)	Plate-like	-	(Markiewicz et al. 1999)
Mariner 9 Pathfinder	IR	-	-	50% Andesite 10 % Sulfite 40 % mafic Si	(Grassi et al. 1999)
Global Surveyor	IR	1.5 – 1.8	Cylindrical	Palagonite-like	(Pitman et al. 2000)
Viking orbiter	Visible	1.6 (0.5) 0.2 (0.03)	Spherical Bimodal	-	(Montmessin et al 2002)
Global Surveyor	IR Visible	1.5 (0.1)	non-spherical	-	(Clancy et al. 2003)
Spirit	IR	1.47 (0.21)	-	-	(Lemmon et al. 2004)
Opportunity	IR	1.52 (0.18)	-	-	(Lemmon et al. 2004)
Spirit	IR	1.2 – 1.6 (0.4)	Cylindrical	Palagonite-like and montmorillonite-like	(Wolff et al. 2006)
Opportunity	IR	1.4 – 1.8 (0.4)	Cylindrical	Palagonite-like and montmorillonite-like	(Wolff et al. 2006)

Figure 1.12: A summary giving particles properties derived from spacecraft observations. Table from (Gautsch, 2002) and has been added to in this work.

JSC Mars-1 is yellow-brown in colour. The chemical composition has been compared to that of a typical Mars surface sample analyzed at the Viking Lander 1 site (Benford, 2005). Current data from the Spirit rover's investigation of the surface material at Gusev Crater also confirms that the JSC Mars-1 simulant is a fair match to the planet-wide dust and soil layer.

The tables in Fig. 1.13 list the major and minor oxide composition and the grain size distribution of JSC Mars-1. This can be compared to the 'blocky material' which covers 78% of the area near Viking Lander I on Mars ranges in size from 0.1-15μm (Feldman et al., 2002).

Oxide	wt%
SiO_2	43.5
Al_2O_3	23.3
TiO_2	3.8
Fe_2O_3	15.6
MnO	0.3
CaO	6.2
MgO	3.4
K_2O	0.6
Na_2O	2.4
P_2O_5	0.9

(a)

Size (µm)	wt%
1000 – 450	21
449 – 250	30
249 – 150	24
149 – 53	19
52 – 5	5
< 5	1

(b)

Figure 1.13: Chemical composition and grain size distribution of JSC Mars-1 simulant.

The Pathfinder mission in 1997 provided new data as the imager on the lander returned sequences of images of the Martian sky which could be analysed in terms of aerosol size distribution and optical refraction index by Tomasko *et al* (Tomasko et al., 1998) in the same way Pollack *et al* (Pollack et al., 1979) had done 20 years earlier with the Viking I Lander images. The good agreement of the data also confirmed JSC Mars-1 to be a good soil

stimulant.

1.5.5 Past AFM work

A study conducted by Kempe *et al.* (Kempe et al., 2004) investigated terrestrial sand with the intention of showing an AFM can recognize features which can be attributed to the presence of flowing water. The grains were glued to a macroscopic substrate with super glue to stabilize them. The successful AFM scans identified aeolian erosion and aqeous etching. The work formed a database to aid the characterization of Martian sediments.

Although Kempe *et al.* offers novel information regarding the study of materials of a Mars-like topography, in terms of the method of preparing the substrates, the paper is less informative. The 'gluing' approach adopted here, which involved revolving and positioning individual grains, is not practical for a planetary mission.

1.6 The Phoenix Project

Of the 20 full Scout Missions proposals put forward by NASA in August 2002, only 4 were selected to proceed on to the next stage. The Phoenix mission was one of them. In order to capture the low cost, low risk, and good science corner of strategy, the spacecraft built on assets created from previous missions - namely the cancelled 2001 lander. The 2001 lander had many instruments already delivered that have since been waiting for the opportunity for reflight. The objective of the Phoenix team was to develop a mission capable of meeting NASA goals for exploring Mars and exciting

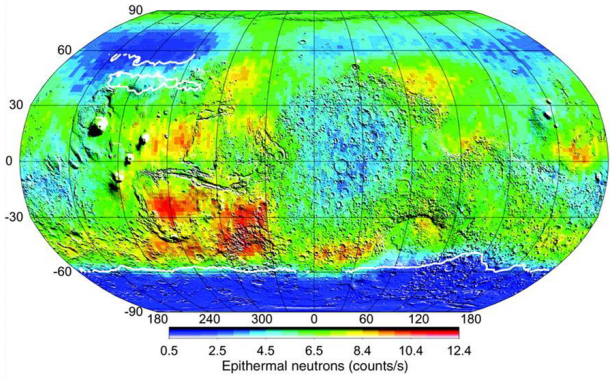


Figure 1.14: A map of Mars produced by Mars Odysseys Gamma Ray Spectrometer showing the areas of soil enriched in hydrogen as deep blue (Feldman et al., 2002; Boynton et al., 2002).

both the public and the science community.

It had been predicted by scientists such as Mellon and Jakosky, that water ice would be stable near the surface in balance with water vapor diffusion through an overburden of regolith. In the Spring of 2002, the Odyssey Gamma Ray Spectrometer (GRS) team announced the discovery of large amounts of water ice poleward of 60 degrees latitude within a few 10s of centimetres of the surface (Feldman et al., 2002; Boynton et al., 2002), shown in Fig. 1.14.

There are multiple accessible sources of water on Mars. But this near-surface icy layer seems to represent the greatest potential for hosting a habitable zone. Current work suggests that melting may produce a thin layer of water, perhaps only a monolayer, on a crystalline surface. This is enough to allow mobility and maintenance in biologic communities on Earth (Jakosky et al., 2003).

Led by Peter Smith as the Principal Investigator with a 25-member science team, the Phoenix Lander is the first Mars Scout mission and is studying the icy northern plains of the planet. Launched on a Boeing Delta II rocket in August 2007 from the Kennedy Space Centre in Cape Canaveral, Florida, the Phoenix Mars Lander began its journey to the red planet. On 25^{th} May 2008 at 23:53 GMT, Phoenix reached its landing site at 68 N, 234 E near the northern polar region in an area where there was though to be as much as 70% water-ice by volume within a few feet of the surface. The aim of the Phoenix mission is to look for signatures of potential life and for signs of frozen water. It is carrying a number of scientific instruments that are analysing the soil and dust, using a robotic arm to dig a metre deep into the soil, showing whether the surface soil has a different history to the soil a metre below. This will give clues about how the Martian climate has changed in this region over the last several million years. The arm digs through the regolith searching for the ice-soil boundary and examines it for periodic melting and thus to observe the biologic potential of this zone.

As the first scientific station in the polar region, Phoenix is also returning useful data including monitoring the weather throughout the polar summer. Measurements include temperature, pressure, and dust opacity, as well as mass spectrometer measurements of the atmospheric composition and relative humidity. Images from three cameras allow visualization of the site: panoramic images of the surrounding site through to microscopic images of the soil itself. The resolution of the panoramic camera is equivalent to the PanCam on MER, about 0.25 mrad/pixel.

Previously named the Mars Environmental Compatibility Assessment

instrument - for the 2001 Lander - and now renamed the Microscopy, Electrochemistry, and Conductivity Analyser (MECA), MECA characterizes the soil of Mars. Michael Hecht is responsible for the MECA instrument performance at JPL. The package comprises of three chief subsystems: a Wet Chemistry Laboratory (WCL), Optical (OM) and Atomic Force (AFM) Microscopes, and a Thermal and Electrical Conductivity Probe (TECP).

To analyze the soluble composition of the martian soil chemically WCL dissolves small amounts of soil in water. It then determines pH, the abundance of ions such as magnesium and sodium cations or chloride, bromide and sulphate anions, as well as dissolved oxygen and carbon dioxide. Preliminary results from the WCL experiments on Mars at the time of writing this thesis have found a significant content of soluble salts from the martian soil including perchlorate. The presence of perchlorate, the highest oxidation state of chlorine at +7, has large implications for the reactive chemistry on Mars despite itself being relatively inert. Further aqueous analysis indicate an alkaline soil; most likely due to soluble carbonates.

The microscopy station, consisting of the Optical Microscope and an AFM, analyzes the soil grains to help determine their origin and mineralogy. It produces extreme close-up views of dust and soils examined by other instruments, providing contextual information for the interpretation of composition data. Though MECA's wet chemistry experiments complement the OM and AFM, this work only involves the microscopy station, preliminary results for which are presented in Chapter 5 of this thesis.

The TECP measures wind speeds and the thermal and electrical properties of the soil that affect how heat is transferred, as well as performing

humidity and wind experiments in the air, providing scientists with a better understanding of surface and atmospheric interactions.

To summarize, the mission's goals are to understand the near surface chemistry and geology of its polar landing site. The instruments are paying particular attention to the distribution of water in all its phases.

1.6.1 The MECA Microscopy Station

The Phoenix MECA package (Microscopy, Electrochemistry and Conductivity Analyzer) includes a microscopy station comprising of an optical microscope (4μm resolution) and an AFM (Hecht, 2006) as shown in Fig. 1.15. The AFM was developed to enlarge a view of selected objects on the sample holding substrates to resolve structures at the 10nm scale, the smallest scale ever examined on Mars. The AFM is supplied by a Swiss consortium led by the University of Neuchatel. The optical microscope, provided by the University of Arizona, is a fixed-focus, $6\times$ magnification microscope capable of taking colour and ultraviolet fluorescent images. Red, green, blue, and ultraviolet LEDs illuminate samples in differing colour combinations to enhance the soil and water-ice structure and texture at these scales. The AFM and optical microscopes provide fine-scale images of the morphology of the soil samples.

As part of the lander platform equipment, a robotic arm, capable of digging up to a metre into the Martian surface, collects surface and subsurface ice and soil samples. These samples are transferred into the spacecraft from the robotic arm and delivered to the substrates on the Sample Wheel Translation Stage (SWTS). The wheel is mounted on flexures along which the

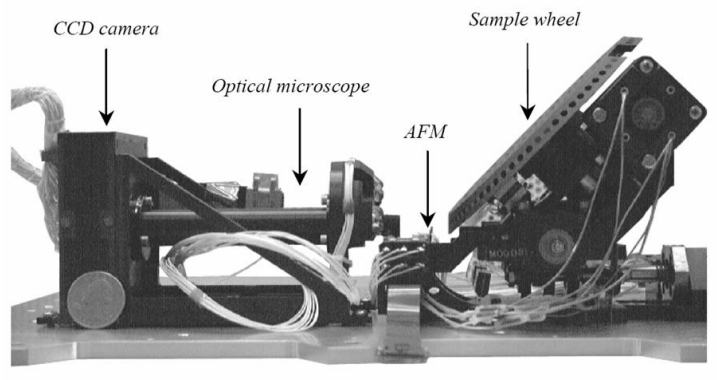


Figure 1.15: Optical microscope and AFM assembly. The sample wheel rotates and delivers the substrates holding the samples to the microscope in the vertical position. Image from JPL.

wheel translates back and forth. The wheel rotates with a 15μm step-size. The substrates are positioned around the 45° bevelled edge on the wheel, while the wheel is itself mounted at a 45° angle relative to the horizontal. Consequently, the substrates are in the horizontal position for loading and in a vertical position when being imaged. Such a design allows even a very large amount of material to be delivered from the robot arm, as the excess material will fall off under the influence of gravity, leaving a relatively sparse field for imaging.

The sample wheel holds 69 individual substrates each 3mm in diameter, six of which are revealed at once through a small slit at the top of the enclosing MECA enclosure box. Of the 69 sample substrates there are ten sets of six materials, and one utility set of nine tools and calibration standards. The layout of the substrates is shown in Fig 1.16.

The sample substrates have different properties - for example the surface

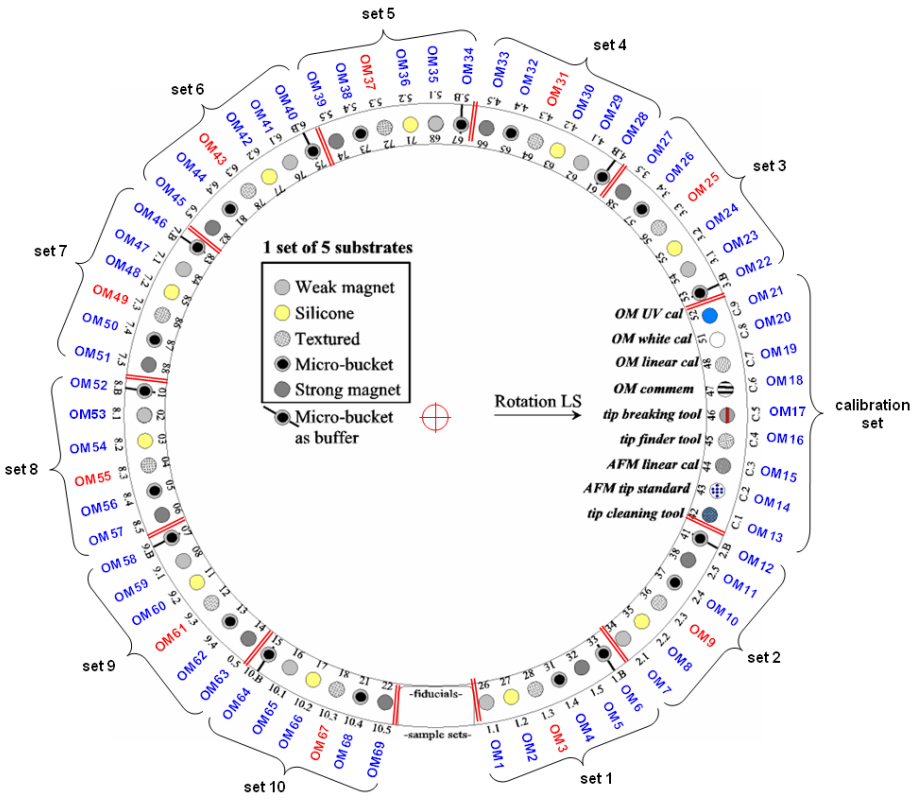


Figure 1.16: The SWTS substrate layout map showing 10 set of 6 substrates and 9 calibration substrates.

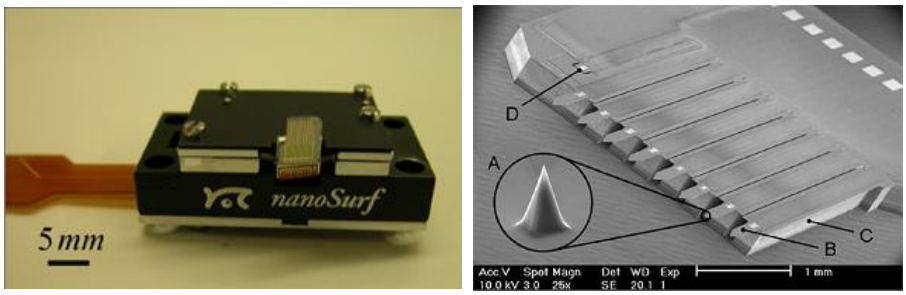
texture or patterning or the material they are made from - in order to test the composition of the dust and to distinguish different adhesion mechanisms. These 'different properties' include magnets, sticky polymers, and textured silicon for bulk and selective sampling. Any excess material 200μm above the substrate surface is removed by a scraping blade as the wheel is withdrawn into the MECA box. The samples are delivered to the microscopes by a rotation and translation of the sample wheel which consequently in turn exposes the substrates in front of the microscopes for imaging. Due to the rotation from their horizontal load positions into their vertical imaging positions, the substrates are mounted vertically (as is the AFM), so good adhesion of the particles to the substrates will be critical. The samples are first examined by the optical microscope. This allows selection of a 'clean' area for AFM - an area with features of a size within the range capabilities of the AFM. The AFM has a very limited field of view ($65 \times 65\mu$m at rtp) and height (13.8μm) range so the design of these substrates is vital for preparing the samples for microscopy. The AFM is run by a dedicated microcontroller and uses a micromachined tip array of 8 cantilevers and a low-voltage electromagnetic scanner (Akiyama et al., 2001). The AFM uses piezo-resistive detection of the cantilever deflection and an electromagnetic scanner. The frequency of operation of the Mars AFM is $\sim$35kHz, the amplitude of oscillation on the order of a few nm and the maximum scan rate is 2Hz.

1.6.2 An AFM for Mars: design requirements for Space Qualification

The Mars AFM employs an entirely different technique to detect the bending of the lever than the popular optical lever. To reduce the size of the AFM and avoid the complexity of having to align a laser beam, instead a piezoresistor, which acts as a semiconductor strain gauge, is integrated into the back of the cantilever. As the cantilever interacts with the sample and bends, the change in resistance of the piezoresistor is converted through a Wheatstone bridge circuit to a voltage which is then amplified and recorded. The piezoresistors are positioned at the base of the cantilevers as this is where the stress is the highest.

The Mars AFM chip hold an array of eight cantilevers as seen in Fig. 1.17, each supported by a thick beam. This provides redundancy in the case of a tip becoming contaminated or dull due to micro-fracture and wear. To ensure the tip of the left-most cantilever is closest to contact the sample wheel, the chip is mounted onto the scanner with two orthogonal tilt angles of 10° in relation to the substrates on the SWTS, as shown in Fig. 1.18. If this front-most cantilever needs to be exchanged, a special tool located on the SWTS is used to cleave off the cantilever and the beam, and then the next tip in the array is accessed.

The electromagnetic scanning stage to which the chip is attached, has already been described in Section 1.4.2. For the dynamic mode of operation, the entire chip is vibrated by the piezoelectric plate on which it is mounted. This excites the resonant frequency of the active lever (each lever has its



(a) (b)

Figure 1.17: (a) A photo of the Mars AFM scanner from the front with the chip in the centre. (b) An SEM image of the chip on the AFM. A shows a close-up of a sharp tip located at the end of one of the cantilevers. B is the first of the 8 cantilevers all of which are supported by beams C. A reference piezoresistor D allows for compensation of thermal drifts. Images from Neuchatel.

own unique resonant frequency).

These features of the Mars AFM design are a result of the requirements for space qualification as a part of the MECA package. The size of the scanner itself is small at $24 \times 18 \times 12$mm and together with the electronics board weighs only 190g. Further to the volume constraints, are requirements for low power - which are consistent with requirements for low voltages to prevent electrical discharge as mentioned in section 1.4.2. In fact, the total power consumption of the instrument is less than 8.5W.

Many of the AFM components for the flight model were radiation hardened to protect the components from the large doses of radiation experienced during cruise and on the surface as a result of the thin atmosphere. All the body parts of the instrument were made of a space compatible aluminium alloy which had a high resistance to corrosion. Most of the instrument was finished with black anodized aluminium to avoid light reflection towards to

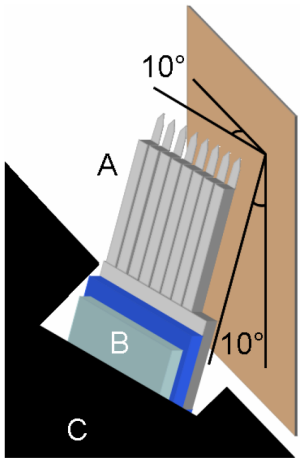


Figure 1.18: The array of cantilever (A) provide more than one sensor in case of failure of the first tip. Two tilt angles relative to the substrate ensure only the right-hand-most tip touches the substrate surface. The piezoelectric plate (B) mounted behind the cantilevers vibrate the whole chip and (C) indicates the top of the scanner. (Hecht, 2006).

OM.

Planetary protection requirements are imposed by NASA on all its space exploration to avoid the contamination of other bodies by Earth life and obscure our understanding of life elsewhere, and likewise of our own planet from forms of life that may be returned to Earth if other life does exist. As a result, all parts of the lander were assembled in a clean environment, including the AFM substrates provided as part of this work.

1.6.3 Cantilevers for Topographical Imaging

The Benefits and Challenges of AFM Remote Planetary Sensing

A critical element of a scanning probe microscope is the microcantilever as it transduces the force acting on the probe tip into a deflection. Forces as small as pico newtons can be measured (Berger, date accessed: July 2007) with such a micromechanical cantilever. This corresponds to a sub-nanometre deflection of the tip of the microcantilever, which allows us to look at surfaces on an atomic scale.

The comparison of AFM to other techniques was given in Section 1.4.6. However the AFM technique does not come without its own disadvantages. One factor that is especially significant for planetary exploration is the time taken per scan. Unlike many other imaging techniques where the image can often be made almost instantly, the cantilever must move over every part of the surface in order to image it. In addition, AFM scans can be very difficult to interpret.

The range of heights that can be achieved within a scan is also a factor. Care must be taken with scanning probe microscopes as, due to the limited range of movement in the z-axis, the cantilever may have problems with large topographical features, especially when performed at high scan speeds or when dealing with samples larger than the tip height. Similarly, there is a question of accessibility to the sample as the scan may also be disturbed by the cantilever itself being obstructed. With high aspect ratio surfaces it is important to take into account the shape and sharpness of the tip. If the sample is sharper than the tip, then the image becomes distorted by tip

artefact.

With reference again to scan speed, care must also be taken when considering the sample contact as there may be damage to the sample, or problems with moving particles, or adhesion of particles to the tip. This is a large consideration when imaging small loose particles, which is the goal of this project. Adhesion of the tip to the substrate can even cause the cantilever to twist giving false roughness measurements.

Also to consider with scanning probe microscopy is the lifetime of the probe. The tip wears out eventually so it is necessary to replace the tip after some amount of scanning. This time can depend on the sample material, topography and the speed at which it was scanned. Replacing tips manually can require some skill but pre-aligned indentations patterned into the holder guarantees the same position of a probe tip every time a cantilever is exchanged.

A final consideration is the possible effect of asymmetrical heating causing bending in the cantilever, which distorts the image, or thermal drift which can cause problems larger than a distorted image as parameters such as a shift in the resonant frequency.

1.6.4 Mars Microscopy: Imaging with the OM and AFM

The microscopy station on MECA will primarily image dust deposited by wind or altered regolith material. Shape and surface texture information will provide clues to the dominant erosion processes and transport mechanisms of the particles and so further strengthen the case for past or present water on Mars. In addition, particle size distributions provide information about

the soil porosity and tortuosity, in turn verifying the diffusive properties of the regolith with respect to heat and water vapour. These parameters help model the behaviour of the regolith material in context of the climate history. Also, information on the dust in the atmosphere will provide information regarding the radiation balance of Mars.

The expected samples to be delivered to the Phoenix AFM are dust from the atmosphere and soil particles excavated from below the surface. The particles will have a distribution of sizes from submicrometres to millimetres (Soderblom et al., 2004; Clancy et al., 1995). The microscopy station will look at particles too small in size to be imaged by the RAC. The RAC images with 23μm per pixel (Keller et al., 2006) and is preferable for imaging particles 100μm and larger. RAC images are useful for looking at the sample distribution in scoop which is more representative of the original material excavated. For the smaller particles <100μm, gravity is less important so the SWTS size distribution should give a reasonable representation of the original material.

The OM has 6 $\times$ magnification limiting the depth of focus to approximately 80μm. The OM is designed for particles 100μm and smaller, down to the resolution limit of 3.9μm per pixel. This means features or particles 10μm or smaller are barely visible. The AFM gives the next level of imaging and provides details of the microscale surface morphology of the particles.

Some work had been performed using an AFM in studying particle morphology to ascertain the roughness and surface texture of samples (Hillmann et al., 1984; Barkay et al., 2005), as well as using the AFM to look at Martian rocks in the hope of finding fossils (Steele et al., 1998). The samples

looked at in these studies were relatively smooth (<1μm roughness) and concentrated on just a small area of the overall sample.

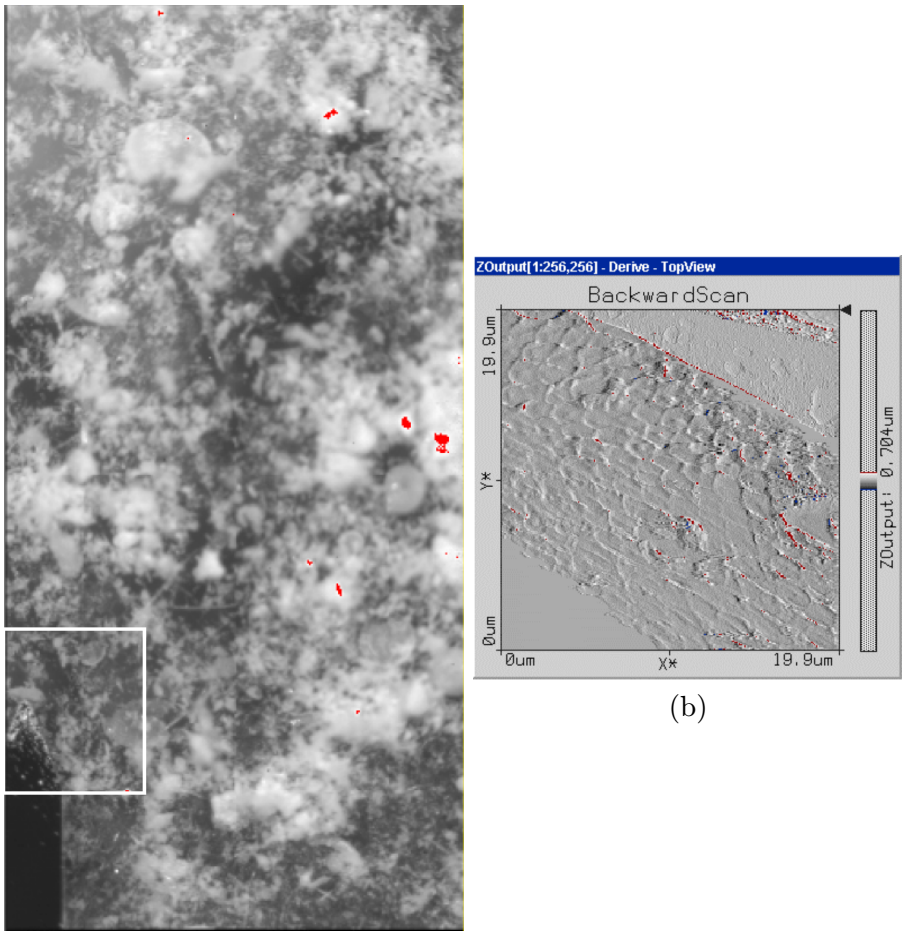
Preliminary tests were performed with the Mars AFM in 2000 (Pike, 2000) on a sample of Diatomaceous Earth held on the 'sticky' silicone substrate (silicone rubber). The tests were performed under normal laboratory conditions. The scans shown in Fig. 1.19 show the ability of the AFM to identify the subcellular structure of the material. The OM image gives no indication that the material is composed entirely of microfossils.

To prepare the samples for microscopy, as the SWTS draws in to the enclosure, the substrates pass below scraper which removes material 200μm above the substrate surface. As the wheel turns 180° to move the sample in front of the microscopes, much of the material sloughs off the surface leaving only a small sample in order to allow individual grains to be viewed. The material that remains on the surface depends on the substrate type.

Despite this preparation, how the AFM will cope with the size range is not certain. A mechanical limitation of all scanning probe microscopes, is the generally low aspect ratio of the tip. Futher to tip artefacts (which can distort and mask the actual features) as described in section 1.4.4, very rough samples are difficult for AFM even with a sharp tip. AFMs excel in imaging relatively 'flat' surfaces (<100nm height variation) and the little work performed on imaging larger features has been for metrology of semiconductor devices (Ridley Sr et al., 2002) where features are stable.

In terms of imaging loose particles, most work has been concentrated on actually trying to move particles with an AFM - nanomanipulation.

The only relevant work on the study of imaging loose individual mi-



(a) (b)

Figure 1.19: (a) An OM image of a silicone substrate covered in Diatomaceous Earth. At the bottom left of the image the back of one of the AFM cantilevers is visible, and a white box marks the area which was investigated with the AFM.(b) An AFM scan of of the diatomaceous Earth.

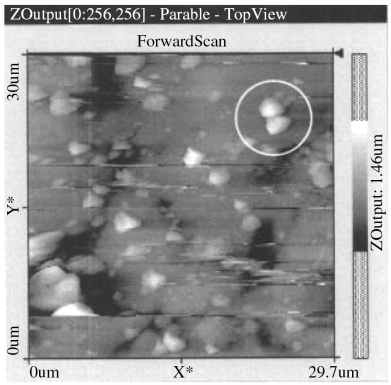


Figure 1.20: An AFM scan of quartz particles on nickel-PMMA, used as an adhesive coating, scanned at 10μm/sec. The scan direction was top to bottom. The particle highlighted by a white circle has been imaged before being flipped by the tip and being re-imaged from a new angle ref (Gautsch et al., 2002).

crometre size particles was done during early characterisation of the Mars AFM for the cancelled Mars Surveyor Project 2001 mission, which identified some difficulties as described in Fig. 1.20.

Similarly, as discovered in early experiments for this work (Vijendran et al., 2007), micron-sized particles were unable to be imaged on hard flat substrates with any success. Although the lateral force applied to the substrate during scanning can be minimized while operating in the tapping mode and using low setpoints, micron-sized particles are pushed very easily by the side of the tip, especially when scan speeds are $> 5\mu$m/s giving poor scans. An example of such a scan is shown in Fig. 1.21.

More critical is the problem of particles obstructing the AFM. Piles of particles, or individual large particles may obstruct the tip or cantilever during scanning, contaminate the tip or lever, prevent the tip from touching

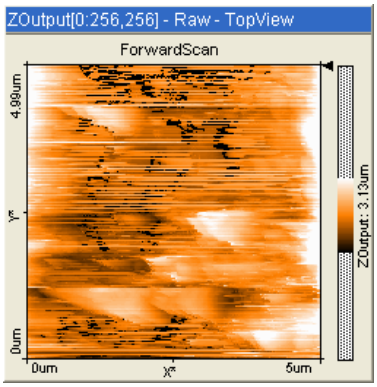


Figure 1.21: An AFM scan of an area with small iron oxide particles at 2.5μm/s. The tip-particle interaction can be very large when AFM is used to image loose, small particles and the scan is poor as the particles are moved around very easily.

the surface by giving false contact, or in the worst case break or damage the tip. So as well as for particles to be adhered sufficiently, the criteria for scanning loose particles safely with an AFM is a sparse field of particles, but for the particles to be adhered sufficiently to the surface so as not to move during the scan. Fig. 1.22 shows a cantilever in a field of particles. Sparse fields are required so individual particles can be accessed and the lever not contaminated. Moreover, due to the height of the tip, to prevent the cantilever colliding with particles, the AFM requires areas with particles smaller than 10μm.

To produce sparse fields of small particles, but also increase the particle-substrate adhesion, special substrates are required. Flat silicon surfaces are good for providing sparse fields however generally too sparse and particles are loose. This will be the discussion of the next two chapters.

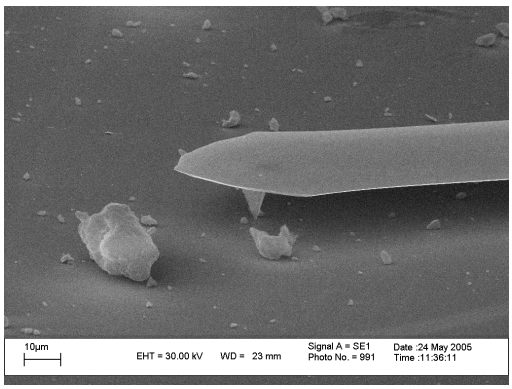


Figure 1.22: SEM image of an AFM tip in a field of particles. Despite the field being relatively sparse, the large particles provide an obstruction for the AFM as the cantilever may crash into them during scanning.

1.7 Description of Thesis

The essence of this thesis is support of the Phoenix microscopy station. The work covers two phases: pre-launch development and secondly testbed experiments and post-landing science support with analysis of the images returned by Phoenix.

Chapter 2 is an introduction to the fundamental adhesive forces of particles to substrates, and describes investigations of the lateral forces expected during AFM scanning and contains discussions of the underlying principles of the scanning motion. This gives a background of what needs to be considered when attempting to scan loose particles with an AFM. In Chapter 3 is described the final design of the Mars substrate incorporated on the spacecraft for holding particles for AFM scanning, and the experiments which led to that design.

The full Mars simulation chamber at Imperial College contains the mi-

croscopy station with an OM and AFM and SWTS complete with a sample delivery system of an articulated robot arm scoop. This enables the simulation of the extremely dry and cold Martian atmospheric conditions. Chapter 4 describes testing of the Mars substrates in context of a study of Mars analogues in the testbed inside the environmental chamber. This data contributes to an integrated dataset of microscopy images of Martian soil simulants maximizing the ability to differentiate materials from the images acquired. Chapter 5 gives more detail of mission operations describing the instruments are operated and real data acquired and also shows images - including the substrate designed as part of this thesis - acquired throughout the course of the mission to date.

Chapter 2

Adhesion Models and Experiments

2.1 Particle Scanning

As initial experiments have shown - Chapter 1, Section 1.6.4 - scanning particles with an AFM can be difficult. By definition, as an AFM scans a sample, it interacts with the surface and touches the surface it is investigating. Particles can be easily detached from the surface or pushed across the substrate with the AFM tip during the scan.

More critical is the problem of particles obstructing the AFM. Piles of particles, or individual large particles may obstruct the tip or cantilever during scanning, contaminate the tip or lever, prevent the tip from touching the surface by giving false contact or, in the worst case, break or damage the tip. The criteria for scanning loose particles safely with an AFM include a sparse field of particles in which the particles have sufficient adherence to

the surface so as not to move during the scan.

Although flat silicon substrates help to reduce the loading, they cannot be relied upon to hold all the particles that are of interest for analysis by the optical and atomic force microscopes. Observations show that particles with diameters greater than 150μm are unlikely to adhere to a flat substrate in the vertical orientation.

In order to predict the size range of the particles that will adhere to the substrate, and to understand why particles are moved during scanning on flat silicon substrates, it is important to understand the forces by which the particles adhere to substrates.

2.2 General Adhesion

2.2.1 The Force of Particle Adhesion

Particle adhesion is of vast interest scientifically and it is encountered in a diverse range of industries; from particle removal - as in the semiconductor industry (Kern, 1990, 1993; Menon et al., 1989), or particle adhesion on specific sites - as in the pharmaceutical industry (Ibrahim et al., 2000; Podczeck, 1998), to controlling the transfer of particles - as in the field of xerography (Lee and Ayala, 1985).

Particles interact with the surface giving rise to adhesion properties which are very complex in their nature. As the sample is loaded, the particles are deposited on a substrate, impinge on it, contact is established and the particles are held on the surface by gravitational settling. As the two bodies come into contact, they are both subjected to stresses linked to the

adhesion forces, causing the bodies to deform, often elastically. The deformation of the bodies is noteworthy as, due to elastic rebound, this can influence the amount of work required to remove the particle.

Though this is a much investigated field, the complexity of the adhesion forces leaves many aspects unresolved, in particular a thorough understanding on a molecular level.

2.2.2 Adhesion of a Single Particle

The adhesion forces by which a particle is held on a surface are influenced by a number of factors at and around the contact point; the topography, chemistry, size, shape, medium, relative humidity, all affect the contact of the two bodies. These forces comprise a mixture of physical attractions, chemical bonds, and mechanical stresses. Taking the simple situation of a single spherical particle on a flat surface, the various forces of adhesion, F_{ad} in Fig. 2.1, that may be present are now discussed.

2.2.3 Adhesion forces

Van der Waals

Van der Waals forces encompass the electromagnetic interactions of fluctuating dipoles between the molecules or atoms of two bodies. As the electronic structure of one body fluctuates, this induces dipoles in the other. The dipoles in the bodies interact and a force between them is generated. Though the interactions are between molecules or atoms, the force takes effect over macroscopic entities. These forces are short-range and are always

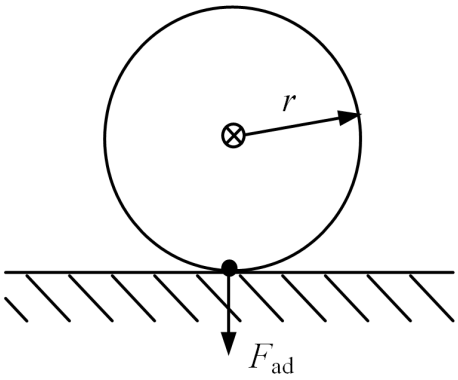


Figure 2.1: Schematic sketch of a single spherical particle of radius r on a perfectly smooth surface at normal lab conditions on Earth attracted to the surface by an adhesion force F_{ad}

attractive.

Hamaker was one of the first to explore how the van der Waals interaction related to the surface forces and - based on the London van der Waals potential energy - presented a fundamental equation for the calculation of the interatomic van der Waals potential energy (Hamaker, 1937)

$$w = -\frac{-\beta}{r^6} \tag{2.1}$$

where β is London's constant; it is the coefficient in the atom-atom pair potential and depends on the atomic characteristics of the two interacting atoms.

Thus, to find the potential energy of two bodies, all the atom pair potentials of all the interacting pairs in the two bodies are summed. Using this, Hamaker's summation method (Hamaker, 1937), the potential energy

for bodies of regular geometries can be easily found, and for the case of a sphere near a surface this integration yields the result:

$$W = -\frac{Ar}{6z_0} \tag{2.2}$$

where r is the radius of the sphere, A the Hamaker constant and z_0 the separation distance between the two bodies which is determined by Born's repulsion force (Krupp, 1967) and is usually taken as 0.4nm in air.

Following from this the van der Waals force is attained by differentiating the energy with respect to distance:

$$F = \frac{Ar}{6z_0^2} \tag{2.3}$$

The interactions described above involve the Hamaker constant A, given by

$$A = \pi^2 \beta \rho_1 \rho_2 \tag{2.4}$$

where ρ_1 and ρ_2 are the number of atoms per unit volume in each body.

In practice it is rare for the number of atoms or molecules in the two bodies to be so small that the van der Waals force could be determined definitively by using the simple pairwise addition of all the interactions.

To overcome the difficulties of the influence of interactions on neighbour-

ing molecules, which can become complex when considering a large number of molecules, the Hamaker constant is found by using the Lifshitz van der Waals theory (Langbein, 1970; Lifshitz, 1956). This technique provides a more rigorous way of calculating the Hamaker constant in terms of macroscopic properties, such that there is no direct reference to the molecular structure, and so the forces between large bodies - now regarded as continuous - are derived in terms of the bulk properties of the materials.

This use of the total macroscopic dielectric data from the component substances takes on the framework of a continuum approach (Israelachvili, 1992). The interaction energies, however, continue to be correct and the difference this method brings is simply in the calculation of the Hamaker constant. Indeed, this approach has frequently proved very accurate (Binks, 1999). Moreover, the Hamaker constant of the system can be calculated to include the presence of the medium in which the bodies interact, e.g. air. Such an expression for the Hamaker constant was derived by Israelachvili, 1992 (Israelachvili, 1992) for two bodies of material 1 and 2 across a medium 3:

$$A_{\text{Total}} \approx \frac{3}{4}kT\left(\frac{\varepsilon_1-\varepsilon_3}{\varepsilon_1+\varepsilon_3}\right)\left(\frac{\varepsilon_2-\varepsilon_3}{\varepsilon_2+\varepsilon_3}\right) + \frac{3h\nu_{\text{e}}}{8\sqrt{2}}\frac{\left(n_1^2-n_3^2\right)\left(n_2^2-n_3^2\right)}{\left(n_1^2+n_3^2\right)^{1/2}\left(n_2^2+n_3^2\right)^{1/2}\left\{\left(n_1^2+n_3^2\right)^{1/2}+\left(n_2^2+n_3^2\right)^{1/2}\right\}} \tag{2.5}$$

where k is Boltzman's constant (1.38×10^{23} JK^{-1}), h Plank's constant

(6.626×10^{-34} Js) and ν_e is the main electronic absorption frequency in the UV, typically around 3×10^{15} s^{-1}. In air $n_{air} = 1$ and $\varepsilon_{air} = 1$. For silicon $n_{Si} = 3.875$, $\varepsilon_{Si} = 11.7$ (Howatson et al., 1972)

This technique has 'full generality' and can be applied to 'any body at any temperature' (Arunachalam et al., 1998). Difficulties often arise, however, when the interacting bodies have an irregular geometry, as the interaction energies can be too complicated to be modelled analytically.

Radius of contact

So far the modelling described assumes a perfect geometry of the surfaces of the macroscopic bodies. This is rarely the case, as real surfaces are never entirely rigid and when two bodies are in contact at least one will deform. (Ziskind et al., 1995)

In the literature there are two groundwork theories which describe the adhesion between a spherical particle and a substrate; the JKR theory proposed by Johnson, Kendall and Roberts (Johnson et al., 1971) and the DMT model proposed by Derjaguin, Muller and Toporov (Derjaguin et al., 1975). Both models independently predict the nature of the adhesion-induced deformation presenting a contact area r_a as in Fig. 2.2 and a pull-off force; the JKR theory regards the interaction forces as existing only within the radius of contact, whereas the DMT theory considers the stresses that also act in a zone around the edge of this area. The principal difference between the models is that the DMT model follows the traditional Hertzian theory (Hertz, 1881) and assumes a compressive stress over the entire contact area, whereas the JKR model assumes tensile stresses at the edge of the contact

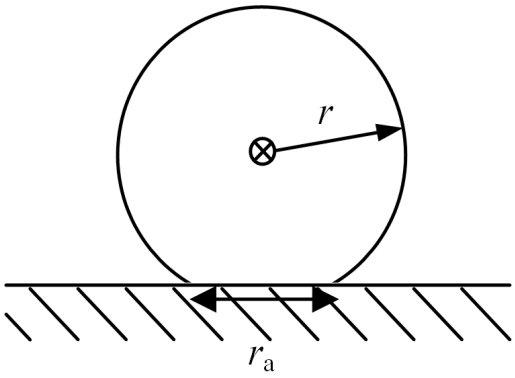


Figure 2.2: The radius of adhesion r_a of a particle r on a flat surface.

area. The pressure distribution of the applied load defines the deformed shape of the particle.

After many conflicting discussions in the literature as to which model is correct (Tabor, 1977; Derjaguin et al., 1978; Tabor, 1978; Derjaguin et al., 1980), Muller *et al* (Muller et al., 1980, 1983) confirmed both models to have a region of validity; the DMT model best determines the nature of adhesion of smaller particles with higher elastic moduli, whereas for larger and softer particles the profile is closer to that of the JKR model.

For the purpose of this study, the DMT model is found more applicable and will be used to determine the contact area of a spherical particle on a surface (Derjaguin, 1939). With this Hertzian indentor model, the van der Waals interactions yield a compressive load P_0, deforming the surface to give a radius of adhesion r_a. Under these assumptions the contact radius relates to the particle radius by

$$a^3 = \frac{3}{4} P_0 \left[\frac{1 - \nu^2}{E} \right] r \tag{2.6}$$

for a substrate with Poisson's ratio ν and Young's modulus E, where the applied load P_0 is as proposed by Hertz (Circa, 1890) so that

$$P_0 = \frac{A}{8\pi z_0^2} r \tag{2.7}$$

Taking into account this deformation of the real surface due to adhesion, the van der Waals force is amplified for this geometry. In a study (Bowling, 1988) this was found to increase the force to:

$$F = \frac{Ar}{6z_0^2} + \frac{Aa^2}{6z_0^3} \tag{2.8}$$

Retardation effects

First proposed by Fritz London (1930), who suggested how they might arise, dispersion forces or "London forces" are induced dipole-dipole forces that make an important contribution to the intermolecular van der Waals forces. These forces are always present and exist in all molecules - polar and non-polar - and are due to the transient random charges that are spontaneously produced continuously in all molecules. At any instant, there exists a momentary dipole which generates an electric field around it. This field will po-

larize neighbouring molecules and induce momentary dipoles in them. The dipoles interact and result in an attractive interaction between the atoms or molecules. The numerous transient dipoles in any material generate an attractive force on a macroscopic level.

Dispersion forces are quantum mechanical in origin and are a result of these fluctuating dipoles. If the distance from one molecule to another is significant enough, consideration may need to be given to the time it takes for the electric field generated by one atom to reach another and return. This is because it becomes appreciable in comparison with the period of the dipole; should this be the case the returning field may find that the direction of the instantaneous dipole of the first atom has changed making an attractive interaction less likely.

This retardation effect is a result of a non-instantaneous interaction of charge fluctuations. With a separation larger than 5nm the contribution of the dispersion force falls off more rapidly than the previous model suggests. No equation exists in literature which would enable calculating van der Waals forces at all separations. Moreover, the Hamaker constant is never truly a constant as it decreases gradually as z_0 increases. There are algorithms reported in the literature to compute the van der Waals force numerically through a solution of the full Lifshitz equation. (Mahanty and Ninham; Pashley, 1977)

Contact Electrification /induced electrical double layer forces

The charge equilibrium of two contacting bodies calls for their Fermi energy level to be brought into coincidence. When two initially uncharged surfaces

of dissimilar materials come into contact, their different local energy states and work functions may cause charge transfer between them. As the surfaces come into contact, electrons move from one material to the other so as to try to equalize the Fermi energy levels of these materials. The surfaces become electrified and an electric double layer at the junction is formed. This results in a contact potential difference causing the surfaces to be attracted to one another by these double layer forces.

This contact potential difference V can be calculated from the work functions of the materials using

$$eV = (\phi_1 - \phi_2) \tag{2.9}$$

where e is the electronic charge 1.6×10^{-19} and ϕ_1 and ϕ_2 are the work functions for the materials, e.g. $\phi_{\mathrm{Si}} = 4.52\mathrm{eV}$, $\phi_{\mathrm{Fe}} = 4.5\mathrm{eV}$ and even $\phi_{\mathrm{JSCMars1}} = 5.6\mathrm{eV}$ has been determined (Sharma et al., 2008), allowing us to calculate for example the contact potential difference between the surfaces of pure silicon and JSC Mars-1 as 1.08V, which is within the typical range for such a potential.

Using this potential the contact electrification force becomes

$$F_{\mathrm{contact}} = \frac{\pi e_0 r V_{\mathrm{contact}}^2}{z_0} \tag{2.10}$$

Further to this, the magnitude of the net charge Q from this contact can

be calculated using the relation (Lowell and Rose-Innes, 1980):

$$Q = eN\pi a^2 \left(\phi_1 - \phi_2\right) \tag{2.11}$$

where N is the density of states on the surface and again πa^2 the contact area. This is useful in calculating the charge acquired by a particle on contact and thus the charge the particle possess on separation.

The density of states in two dimensions is found to be (Zeghbroeck, date accessed: November 2008):

$$N = \frac{4\pi m^*}{h^2} \tag{2.12}$$

where the effective mass of an electron m^* is 9.1×10^{-31}kg and the mass for silicon is $1.08m^*$, so for the silicon surface the density of states is 2.8×10^{37} m^{-2} J^{-1}.

Image-charge effect

The second but more important type of electrostatic force expected to be dominant on Mars is the image force. This force is a classical Coulombic attraction between a charged particle and a neutral surface.

The method of images refers to a technique used to solve a particular class of problem related to the interaction of a charge with a conducting surface (Smythe, 1968). A charge near a surface induces a surface charge

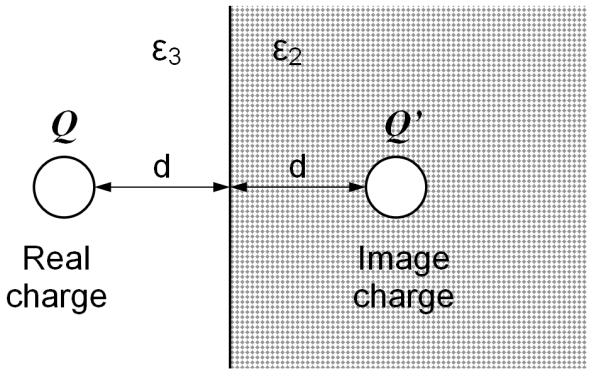


Figure 2.3: The field distribution of a charged molecule interacting with a conducting surface can be modelled as an 'image charge' below the surface, the same distance away as the source charge.

distribution in that surface. The technique calculates the charge distribution on the surface as if there where an 'image' of that charge an equal distance below the surface and of opposite sign, as shown in Fig. 2.3. The charge distribution of this imaginary charge has the same potential distribution on the surface as would be produced if the image charge were present, and maintains the boundary conditions, so can be used to model the field distribution in the space. This additional field creates a force on the source particle.

As shown in Fig. 2.3, the image charge will have a strength Q' found by $-Q\left(\epsilon_2 - \epsilon_3\right) / \left(\epsilon_2 + \epsilon_3\right)$ (Landau et al., 1984), so if $\epsilon_2 > \epsilon_3$, the charge will be attracted to the surface where ϵ_3 is the permittivity of the surrounding medium usually air. The overall force by which the charge is attracted to the surface will therefore be identical to the force between two point charges separated by a distance $2d$, giving

$$F(D) = \frac{-Q^2}{(4\pi\varepsilon_0\varepsilon_3)(2z_{sep})^2}\left(\frac{\varepsilon_2-\varepsilon_3}{\varepsilon_2+\varepsilon_3}\right), \tag{2.13}$$

Aside: charge for JSC Mars-1

For the image charge to be significant compared to other forces such as the van der Waals force, large non-equilibrium charges are needed on the particles. The triboelectric charging of dust on Mars is expected in the very dry environment and will charge due to the wind-driven particle collision and separation, and the ionizing effect of UV radiation on the dust (Sickafoose et al., 2001; Stow, 1969; Krauss et al., 2003).

Further to this, in order to use this method to calculate the image charge force of the particles to the substrate, the expected charge on each particle must be known. Publications in the literature give a number of studies of the charging of Martian particles. (Gross et al., 2001; Sternovsky et al., 2002; Gross, 2003; Sharma et al., 2008). In particular, for the JSC Mars-1 soil simulant, experiments showed an expected charge of $+1.21\mu$mC/g (Sharma et al., 2008). Based on the weight distribution given (Allen et al., 1998a) and assuming the charge on a particle is proportional to its surface area (not its volume) then charge on a particular size of particle can be simply modelled and a distribution of charge as shown in Fig. 2.4 is obtained.

Capillary force

Relative humidity (RH for water) is the relative vapour pressure defined as p_τ/p_T where p_τ is the partial pressure of water vapour in the mixture at τ-point (saturation temperature), and p_T is the saturated vapour pressure

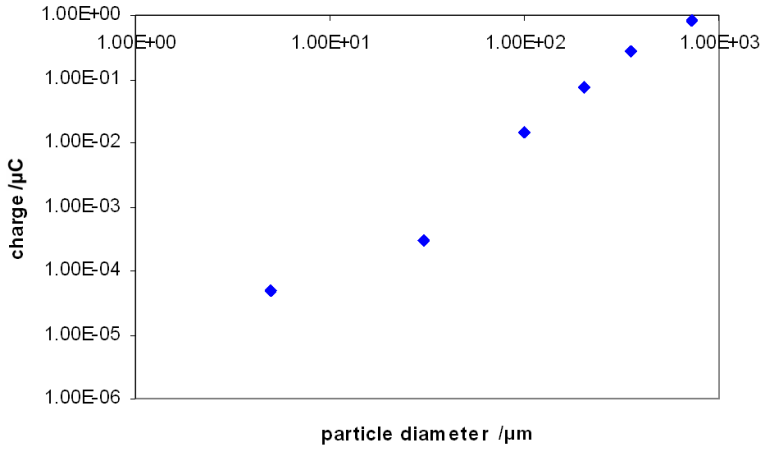


Figure 2.4: Graph for Mars JSC-1 of expected distribution of charge depending on particle size.

of water at the temperature of the mixture. The adhesion and mechanics of particles is well known for being responsive even to tiny quantities of vapour in the atmosphere (Visser, 1976). Even in ambient air the adhesive forces are much greater than in dry air (Stone, 1930; Bradley, 1932). For hydrophilic surfaces, or those exposed to a highly humid environment - RH $<$ 65% (Zimon, 1982), liquid is adsorbed creating a film at the surface. A liquid bridge may form between the particle and the substrate, resulting in a capillary force increasing the adhesion, as sketched in Fig. 2.5. This liquid bridge is a result of capillary condensation or capillary action in the space where the two bodies contact each other. Capillary forces get their energy from the surface tension, because molecules at the liquid surface have a higher energy than they have at the interior.

The force of this adhesion is determined by an intricate interplay of several parameters, but is directly controlled by the nature of the surface and

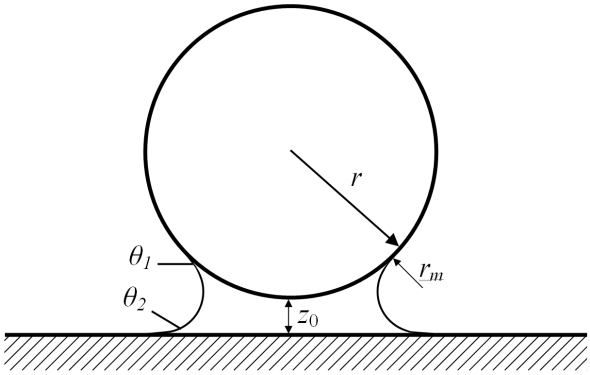


Figure 2.5: A spherical particle of radius r, at a separation z_0 from a surface, linked by a liquid bridge. The surfaces are hydrophilic, θ_1 and θ_2 are small contact angles of the liquid to the surfaces, r_m is the Kelvin radius, 0.2nm - 5nm (Jones et al., 2002) which measures meniscus curvature, γ is the surface tension of the liquid. r_m is RH dependant.

the relative humidity of the surrounding environment. These two factors control the stability of the liquid bridge and the wetting of the surface, thus determining the thickness of the adsorbed liquid film, the contact angles with surfaces and the radius of the meniscus. To complicate things further, the adsorbtion of water on a surface can in many cases change the chemical or physical properties of the surface e.g softening, solubility or phase change (Cleaver and Tyrrell, 2004) . The intricacy of the problem makes the complex behaviour very difficult to model theoretically in terms of the RH dependence in practical systems.

However, models do exist and the conventional model for the system of a spherical particle linked to a flat surface by a liquid bridge, such as in Fig. 2.5, is given by simple Laplace-Kelvin theory. For the condition $z_0 << r$, the capillary force is given by (Israelachvili, 1992; Bowling, 1988).

$$F_{\text{capillary}} = 4\pi r\gamma\cos(\theta) \tag{2.14}$$

This assumes hydrophilic surfaces with a wetting coefficient of $\cos(\theta)$ and the liquid surface tension is γ ($= 72.75 \times 10^{-3}$ Nm^{-1} for water at 293 K). The relationship has been verified experimentally by direct measurement for water down to a 5nm radius (Fisher and Israelachvili, 1981; McFarlane and Tabor, 1950). For the conditions of this model, r_m is small in relation to other dimensions, so the RH dependence disappears. This is not necessarily the case for real systems.

The work presented in the literature sees a number of conflicting reports as to the trends for the variation of adhesion with RH. The adhesive force has been reported to increase (Sugawara et al., 1993), decrease (Fisher and Israelachvili, 1981; Binggeli and Mate, 1994; Zimon, 1982), or pass through a maximum with increasing RH (Chikazawa et al., 1984; Jones et al., 2002). These final two papers suggest onset of adhesion is often not detected until RH $> 40\%$ though once a liquid bridge has been formed, it remains an adhesive force even if the RH drops.

Within the literature there is an agreement showing that hydrophobic surfaces are typically not affected by capillary forces (Bowling, 1988). The adhesion on such surfaces is generally small and constant over the entire range of RH (Jones et al., 2002).

Silicon surfaces

The hydrophilic properties of a silicon surface are very sensitive to the surface chemical condition. Bare silicon can be hydrophilic or hydrophobic but is very dependant on the treatment the surface has undergone. The literature contains evidence that hydrogen-terminated surfaces, or those with a layer of carbon bonded to oxygen, are hydrophobic, while surfaces with an oxide- or hydroxide- layer, often OH-terminated, are ordinarily hydrophilic. (Zhang, 2001). Treatment with dilute HF solution produces a hydrophobic surface (Bhushan, 1997), while alcohol generates a hydrophilic surface (Iyer et al., 2002).

Surfaces with a native oxide - albeit just a monolayer - are hydrophilic (Arai et al., 1996). At temperatures below 200°C, the surface is covered by an absorbed film of water (Tas et al., 1996) and typically offers a contact angle with water and air of 10-15°. (Iyer et al., 2002).

Magnetic force

When a magnetic material is placed in a magnetic field the external field H induces a magnetic flux in the material. Broadly, three types of magnetism exist: diamagnetism, paramagnetism and ferromagnetism.

Diamagnetism is the result of the individual contributions from the orbital electrons aligning their magnetic moments leaving no magnetic dipole at the atomic level. This material tends very weakly to expel magnetic flux and it has relatively small and negative susceptibilities in the range $-10^{-5} < \chi_m < 0$. Quartz and salt exhibit diamagnetic properties. Super-

conductors are sometimes referred to as ideal diamagnetics (cancelling the field inside altogether).

Paramagnetic materials, on the other hand, weakly increase the magnetic flux. Paramagnetism is associated with materials with elements with an odd number of orbital electrons. These atomic dipoles align with the external magnetic field. The response of the magnetic dipoles is a function of field, but also temperature, so that above a given temperature, known as the Curie temperature, paramagnetism is no longer observed. In a paramagnet the susceptibilities are small and positive, commonly $0 < \chi_m < 10^{-3}$. Aluminium and chromium are examples of weakly paramagnetic materials.

Ferromagnets strongly increase the magnetic flux. These materials can be thought of as an extension of paramagnetic behaviour where the large number of unpaired inner-shell electrons gives an additional very large internal field due to this magnetization. By means of a quantum effect called exchange coupling, the spins of neighbouring atoms align, resulting in domains - a favourable configuration in terms of magnetic-field energy. The domains form in such a way that they are magnetized in different directions so that the net magnetization of the material is zero. These domains are commonly in the nanometre region (Withey and Nuth, 1999; Schwarz et al., 2004; Kucharczyk et al., 1994), but have been occasionally found to be up to tens of micrometres large (Hubert and Schäfer, 1998). Once these domains form, they remain, even once the field has been removed. When exposed to an external field, the magnetization within the domains magnetized in the directions almost parallel to the field shifts direction to align perfectly with the field. These domains aligned with the field grow as the field increases,

at the expense of the less favourably aligned domains. If the field is large enough, the material becomes saturated by a single grain. These materials are strongly magnetic, but not very common and are typically ferrites or artificial alloys. Like paramagnetic materials, they also have a Curie temperature, and have large positive susceptibilities, approaching thousands or even more.

Fig. 2.6 shows a classic B-H curve for a hard ferromagnetic material. Some magnetic flux remains in the material even when the field is removed. This residual magnetism retained is known as the remanence B_r and, for hard ferromagnetic materials, this is close to the saturated flux density B_S. These materials are useful as permanent magnets due to the large coercive force, indicated in the figure by $-H_c$ as the field required to cancel the magntic flux. Soft ferromagnetic materials, e.g. annealed low impurity iron, have a high magnetic susceptibility but low or no magnetic remanence. This gives them no permanent magnetism, so when the field is reduced the magnetization returns to zero, along the path from B to A. Such materials are required, for example to make the cores of electromagnets. In practice, even soft materials will always have some remanence which - even if small - may produce detrimental effects on the performance. On the other hand, in applications such as magnetic cores of direct current machines, even a small remanence is sufficient and essential to produce self-excitation of the generator.

When a magnetic particle is placed in a magnetic field in a non-magnetic medium, it experiences a force from the field around it. The general equation describing the force on a piece of magnetizable material of volume V in a

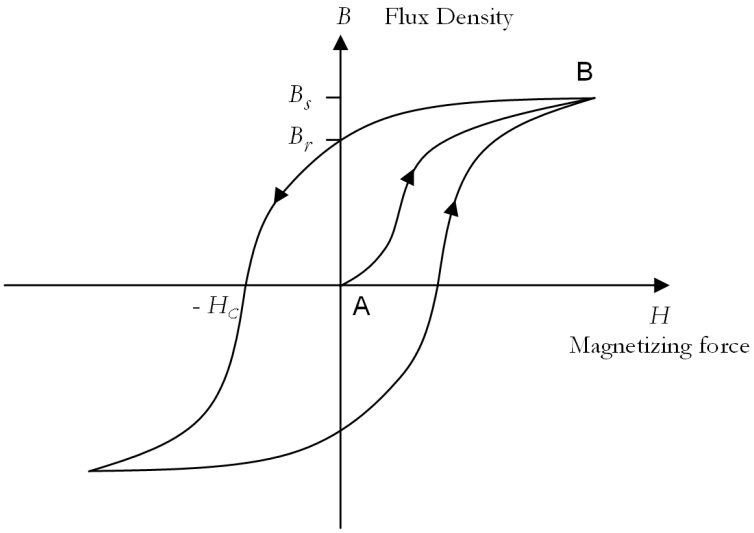


Figure 2.6: A *B*-*H* characteristic curve for a ferromagnetic material.

magnetic field is:

$$F = \int_V \mu_0 M \nabla H dV + \oint_S \frac{\mu_0}{2} M_n^2 df \tag{2.15}$$

where H is the magnetic field within the particle and M is its magnetization with the normal component of the magnetization M_n over its surface S. df is the normal component of the fractions of area of the surface. This forms the anisotropic term in the equation.

For small magnetic particles the gradient of the field strength is often assumed constant across the diameter, and the susceptibility taken as being independent of the field (Fujita et al., 2007).

$$F_{\text{sphere}} = V\mu_0 H_0 \nabla H_0 \left(\frac{\chi}{1 + \frac{1}{3}\chi} \right) \tag{2.16}$$

$H_0$is the magnetic field strength of the applied field.

Paramagnetic materials follow this linear trend of increasing magnetic flux with field, as more of the atomic dipoles align to the field, until they are all aligned and the material is saturated. For very low magnetic susceptibilities $\chi << 1$, the second term in equation 2.15 is of the order χ^2 and becomes insignificant compared to the first integral. With a negligible demagnetization, $M\nabla H$ is equivalent to $\chi H \nabla H$, allowing the approximation:

$$F_{\text{weak}} = \mu_0 \chi V H \nabla H \tag{2.17}$$

This result is consistent with previous derivations using magnetostatic energy (Henjest, 1994).

For particles with $\chi >> 1$ the second term of equation 2.15 becomes more significant than the first integral and the resulting magnetic force is (Henjest, 1994)

$$F_{\text{strong}} = 3\mu_0 V H \nabla H \tag{2.18}$$

Thus, when a particle of high permeability material is placed in a magnetic field, the magnetic field strength inside is amplified; assuming a uni-

form field and a spherical particle, this amplification is by a factor of three. Other shapes will have a slightly different factor (for example for a long cylinder the factor becomes 2). This amplification is also limited by the saturation properties of the non-linear magnetic characteristic, the saturation magnetisation shown as point B in the figure. This result is consistent with equation 2.16, when assuming high χ and a linear relationship. Soft ferromagnetic materials, such as iron, are often assumed to have no magnetic remanence, and thus no hysteresis. Moreover, the increase of magnetic flux with field is often modelled to a linear approximation.

As hard ferromagnetic particles exhibit permanent magnetization, they are usually assumed to have a constant magnetization M. The force they experience depends on the applied field. From equation 2.15 the second integral, which becomes constant is no longer included in the force equation (Henjest, 1994). The surface integral also does not contribute and the force is given by the expression

$$F_{\text{ferro}} = \int \mu_0 M_j \nabla H_{oj} dV \tag{2.19}$$

This expression for the force experienced in a magnetic field is independent of the susceptibility of the particle, as the particles are in saturation.

The MECA wheel includes a set of magnetic substrates as the material on the surface of Mars is expected to be highly magnetic (Bertelsen et al., 2004; Hviid et al., 1997). In this section the effect of the particle adhesion to magnetic substrates will also be considered. The magnetism found in

particles on Mars will mostly be of material of the ferromagnetic class, which indeed is often natural minerals, commonly iron oxide compounds.

Gravitational force

Finally, for a spherical particle of radius r the force of gravity is given by

$$F_{\text{gravity}} = \frac{4}{3}\pi r^3 \rho g_{\text{mars}} \tag{2.20}$$

In the orientation of the MECA wheel, as the substrates are mounted vertically, this force acts to pull the particles away from the surface, or rather slide them parallel to the surface. On Earth $g = 9.81\text{m/s}^2$, whereas with the reduced Mars gravity $g_{\text{mars}} = 3.7\text{m/s}^2$ particles have a smaller force pulling them off.

Vibration force

As the substrates rotate around from the loading position and translate in to the viewing position, the SWTS motors (described in more detail in Section 4.2) create a vibration felt throughout the system. This vibration is speed dependant and tests performed on the system have established maxima and minima for the amplitude of the movement at various speeds. This force determines which particles remain on the substrates once they are in the viewing position. During AFM scanning the wheel is not in motion so the vibration force is not present. Nonetheless, this force will be discussed briefly here.

The vibration force acts on the wheel to produce a displacement. Approximating to a sinusoidal motion, then displacement $x = x_0 \sin(\omega t)$ gives a max acceleration of -$\omega^2 x_0$. The frequency at which the wheel is operated is $\omega = 2000\text{rads}^{-1}$, so estimating the displacement for the vibration as 50μm, then the maximum acceleration is 200ms^{-2}, or 20g on Earth. The relationships between the applied vibrational force and the mass of a particle can be calculated by

$$F = ma = -\frac{4}{3}\pi r^3 \rho \omega^2 x_0 \sin(wt) \tag{2.21}$$

Again, this force will be proportional to r^3.

Measurements of this displacement have not been performed, though it must be noted that the performance of the testbed systems may differ considerably from the flight model in this regard due to even very minor differences in the way the systems were manufactured and assembled.

Adhesion variation with radius

Having discussed the suitability of each of the models in each section, and how they might be used to model an appropriate system for this work, the graph in Fig. 2.7 shows the relative magnitudes of these forces and how they vary with respect to each other with varying particle size. The values are calculated assuming spherical particles of materials similar to those expected on Mars. The graph includes all the forces investigated, and all are presented on the same plot, even though not all these forces will be present for any

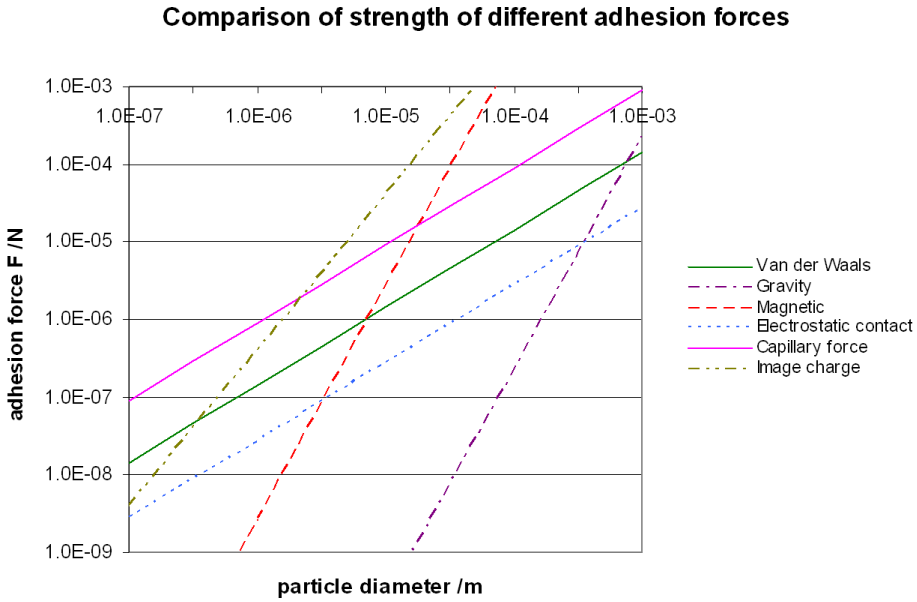


Figure 2.7: A graph showing a theoretical estimate for the relative magnitudes of various adhesive forces as they vary with particle size.

particular system. Of course the trend can not be extended to apply for much larger particles as the forces no longer act in the same way when the bodies are large. However for the region of interest for MECA microscopy - 1μm to 200μm - the trend should follow this shape.

As previously reported, van der Waals forces are indeed found to dominate for small particles on a surface. (Eichenlaub et al., 2004; Cooper et al., 2001). Image charge effect has the largest degree of uncertainty. It appears to dominate for larger particles. This is of course not as great an effect in a humid environment. The capillary force is strong and a dominant effect under normal atmospheric conditions on Earth.

The graph suggests that the sum of the adhesive forces far outweigh the

force of gravity and show that on a flat silicon substrate particles up to 1mm in size would be expected to adhere. This does not of course consider any effects of vibration of the wheel as discussed above. Certainly at a small size range the force from gravity can be negligible due to the dominating van der Waals force.

Magnetic particles on a magnetic substrate have different considerations. Van der Waals is an isotropic interaction, whereas the magnetic interaction is anisotropic. Further to this, van der Waals forces are a function of r/z_0^2, while the magnetic force has a dependence on the particle volume. This shows that with increasing particle size, the magnetic contribution to the attractive forces becomes relatively more important. Specifically, the number of particles 20μm or larger would be expected to be significantly greater on the strong magnet than for non-magnetic substrates, whereas for smaller particles, as van der Waals forces dominate, the number of particles is expected to be more comparable.

Adhesion on Mars

In an ambient terrestrial environment, a thin film of water on the surface of the bodies assists with adhesion. In the low humidity Mars environment the capillary force is not present so the other mechanisms of particle adhesion become more important. Some of the MECA substrates utilize other adhesion mechanisms eg. the magnetic substrates and silicone and these are described in more detail in Chapter 4.

2.2.4 Conclusions

It has been shown that for particles in the Mars environment, the major adhesion forces to be considered are Van der Waals, electrostatic and magnetic (in the case of magnetic particles). Conversely, both gravity and vibrational forces from the motion of the sample wheel act to promote de-adhesion. In the absence of significant topography on the substrates holding the particles, the balance of forces depends critically on the size, shape and electromagnetic properties of the material.

Two parts to the force balance can be considered further; (i) the vibration during translation and rotation which can 'shake off' particles - this determines what is left in front of the OM to be viewed - and (ii) the lateral force applied during AFM tip scanning itself which can move particles during a scan. The vibration force is proportional to r^3 so is more important for large particles, whereas the AFM lateral force, which depends only on the scan speed, is independent of particle size. In light of this, it might be expected that the large particles would be the particles of choice for AFM investigation (as long as they are within the physical range of the AFM) as they would be more stable against the tip lateral forces. However, it is only the small particles that will not have been removed by vibration, and therefore be available for AFM scanning.

2.3 Mechanics of Particle Adhesion

The forces which hold particles onto surfaces have been investigated, so in order to immobilise these particles, a good understanding of the mecha-

nisms involved in particle adhesion to surfaces is required. There has been considerable work on the removal of particles from substrates by fluid flow, often motivated by control of particle contamination in the semiconductor industry. (Kern, 1993). The numerous theoretical models developed to estimate particle detachment from surfaces take a range of approaches; these models can be based on energy balance (Reeks and Hall, 1988), force balance (Soltani and Ahmadi, 1993; Wang, 1990) or momentum balance models (Ziskind et al., 1997; Soltani and Ahmadi, 1993; Wang, 1990).

Work by Ziskind *et al* (Ziskind et al., 1997) which looked at the moment balance models, recognised that consideration of the equilibrium between normal adhesive forces and lift-off forces (Wang, 1990) is inadequate in explaining the detachment of particles from substrates. In particular, it is much easier to detach particles than such a force equilibrium suggests; the hydrodynamic lift force is smaller than the adhesion force by a few orders of magnitude, yet is able to cause particle detachment.

The adhesion of a particle is dependent on the number of points of the particle touching the surface of the substrate and will result in movement if the torque from an AFM tip is high enough. The adhesion moment model was introduced (Ziskind et al., 1997) based on detachment by rolling of the particle under a shear force. In this model, detachment will occur when the applied moment is greater than the adhesive moment at the point of contact. Expressions for the adhesion moment for both rough and smooth surfaces were derived.

This model can be readily applied to the stability of particles under both substrate tilting and AFM scanning, where the applied moment, rather than

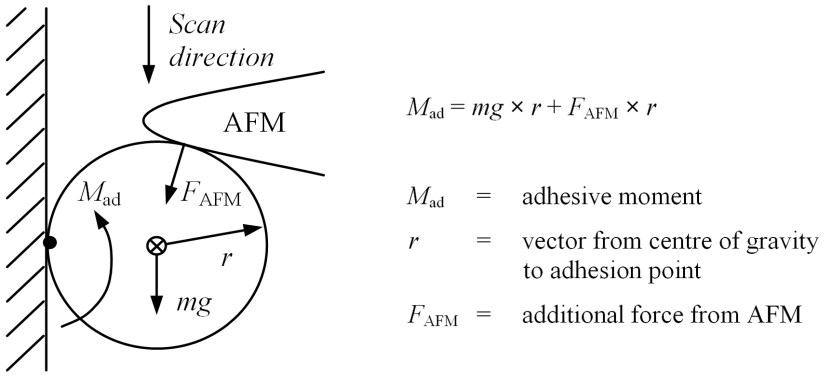


Figure 2.8: Balance of moments in equilibrium for a spherical particle interacting with an AFM tip.

due to fluid flow, is produced by the weight of the particles and the lateral forces of the AFM tip. For the particle to remain in equilibrium the adhesive moment must be large enough to counteract the sum of the AFM lateral force moment and the moment due to the particle weight, all taken about the pivot point for particle breakaway at the bottom of the contact area. The balance of moments (in the configuration of this study) for a spherical particle of radius r and density ρ is shown in Fig. 2.8, where the force from the AFM tip is in the same direction as the gravitational force thus representing the 'worst case' scenario.

As the SWTS rotates the substrates from the horizontal loading position to their vertical viewing position, the particles on the substrate experience an increasing force acting perpendicular to the substrate normal, due to their weight. This force increases to a maximum when the substrates are vertical. The largest particles fall off - assisted by vibration of the SWTS - and the smaller ones remain adhered by the forces described in Section

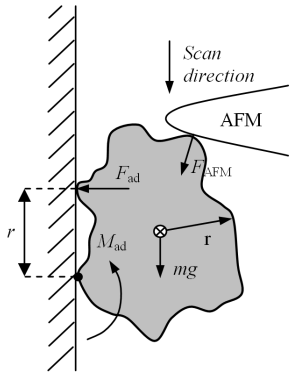


Figure 2.9: Balance of moments in equilibrium for a particle of an irregular shape interacting with an AFM tip.

2.2.3.

2.3.1 Real Particles

Real particles are not accurately modelled by perfect spheres and a more realistic model considers other shapes. During deposition of the loose sample, particles tend to occupy stable positions. Real particles are irregular, and, on a flat substrate, will often have multiple contact points with the surface. Fig. 2.9 shows a possible model for such a configuration. A number of assumptions have been made; for a particle of average radius r, the average distance apart between the contact points is said to be r; the contact points each have a given radius that does not increase as the particle size increases.

For the particle to remain adhered to the substrate once rotated to the vertical, the shear moment $\frac{4}{3}\pi r^4 \rho g_{\text{mars}}$ must be matched by a restraining adhesive moment at the contact points. Further to this the additional force for the AFM tip must not move the particle. The moment model describing

this configuration may be constructed by taking moments about the lower contact point, giving rise to the expression

$$M_{ad} = mg \times r_1 + F_{\text{AFM}} \times r_2 - F_{\text{ad}} \times r_3 \tag{2.22}$$

where $|r_1| = |r_2| = |r_3| = r$

To quantify a little further, particle stability when the substrate is vertical requires a balance of the gravitational moment about the contact points and the moment due to the adhesive forces at the contact points. The moment due to gravity about the contact points must be less than the maximum adhesive moment at yield. The difference between the two gives a margin for any additional moment due to the AFM tip forces. If the margin is sufficient, the AFM scan should be repeatable. Otherwise particle motion or loss will disrupt the AFM image.

With more than one contact point, the balance of the forces changes, as each force varies in size based on the difference in their interaction with the surface. The forces dependant on the contact area will vary differently to those more dependant on the overall size of the particle. The size of the contact point may not increase with increasing particle size for example. Taking the number of contact points as 3 for example, all of a similar average radius, the van der Waals is simply 3 times the force at one point and will not vary with particle size.

The moment model above in equation 2.22 shows two unknown parts to the problem; the true magnitude of the particle-substrate adhesion and the

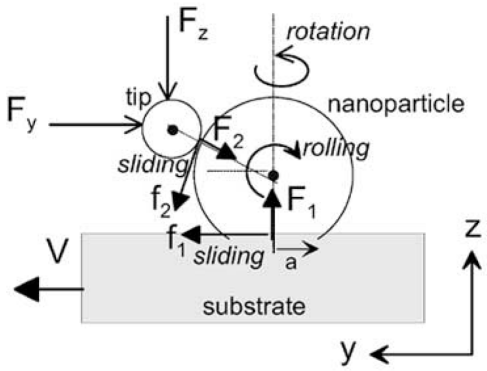


Figure 2.10: A description of tip particle interactions such as sliding, stick-slip, rolling, sticking and rotation.

lateral force from tip. Having offered a theoretical model of the adhesion of particles to surfaces, the next section describes the practical experiments that were performed to investigate this further.

2.3.2 Further Tip-Driven Motions of a Particle

Further to 'pushing' of the particle by the tip, the tip can pick particles up from their location. This is different to pushing as it involves adhesion of the particle to the tip, and possibly contamination of the tip. This is especially likely in a dense field of particles.

Other phenomena that can be observed other than lift off involve rolling and sliding. Sitii (Sitti, 2004) looked at the various mechanisms of particle detachment shown in Fig. 2.10, but also considered mainly pushing from the tip.

2.4 Tip-Particle dynamics: the lateral force from the cantilever

As the particles are being imaged the AFM tip touches the particle as it moves back and forth in a raster scan across the surface. The success of the scanning depends upon the relative stability of the particle compared to the lateral force exerted on it. This section describes work done to quantify the lateral forces produced when scanning with an AFM.

2.4.1 AFM Forces

Since the invention of the atomic force microscope, it has been utilized in ways other than imaging down to nanometre resolution. The AFM has since become a useful tool as a nanomanipulator capable of positioning objects on the nanometre scale (Schaefer et al., 1995), a device for cutting (Junno et al., 1995; Stark et al., 1998), and nanolithography applications (Ahn et al., 2002).

As the cantilever moves over a feature, the reactive force is normal to the plane of the surface where the interaction happens. Part of the reactive force on the cantilever goes into producing an upward deflection in the cantilever, and the rest into twisting of the tip producing torsion in the cantilever. The force experienced by the feature is equal and opposite.

In order to understand the mechanics of the cantilever and tip interaction with the surface, it is instructive, as a first step, to consider friction force microscopy (FFM) - a system usually used to examine the material-specific friction coefficient - but it is also important to remember that it is very

different to dynamic mode AFM.

A paper by Haugstad *et al.* (Haugstad et al., 1993) describes the use of a FFM to observe how topography-induced transitions can affect the friction measurement. Fig. 2.11 shows the illustration of their model. The authors describe how a sudden surface elevation or slope can be measured by an AFM/FFM as the friction trace follows the first derivative of the topography, as demonstrated by the equation for the torque about the principal axis of the cantilever:

$$\tau_n = F_n L \sin\theta = F_1 L \tan\theta = F_1 L \frac{\mathrm{d}z}{\mathrm{d}x} \tag{2.23}$$

Where $F_1 = F_n \cos\theta$ and F_n is the force applied to the tip which acts normal to the surface at the point where the spherical tip contacts the surface. θ is the angle of the surface to the vertical at this point.

The tangential torque associated with the tangential force F_t, given by

$$\tau_t = F_t \left(L + \frac{R}{\cos\theta} \right) \cos\theta \tag{2.24}$$

Where $F_t = \mu F_n$. As shown later in this section, the relevant bit of this model considers only the F_n.

The torque on a cantilever as it scans over a feature is further discussed by Sitti (Sitti, 2004) where various methods for measuring such forces are described. The analytical analysis describes how to extract a measurement

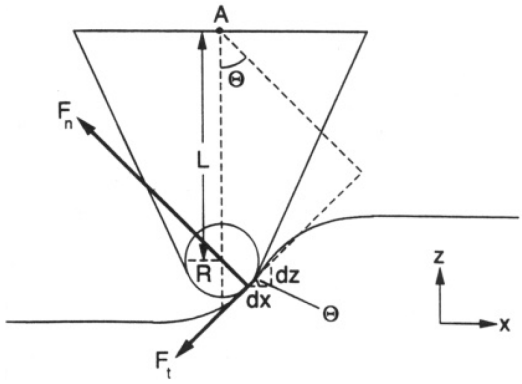


Figure 2.11: A = principal cantilever axis, L = distance of cantilever from the vertex of spherical tip of radius R, F_n and F_t are the normal and tangential reaction forces respectively, θ the angle fo the surface at the point of contact to the z-direction.

quantifying this associated torque which acts around the principal cantilever axis when the cantilever moves with a constant speed. The measurement technique suggested to directly find the lateral force, involves a static mode of operation and uses a friction measurement. The geometry of Fig. 2.12 describes how the friction measurement is extracted, where F_y and F_z are provided from the $\Delta\theta$ and $\Delta\zeta$ deflection data and can be found by using the relationships

$$f_1 = F_y = F_2 \cos\beta - f_2 \sin\beta \tag{2.25}$$

$$f_2 = F_z \cos\beta - F_y \sin\beta \tag{2.26}$$

$$F_z = F_1 \tag{2.27}$$

The second method is for one dimensional force sensing systems, Fig.

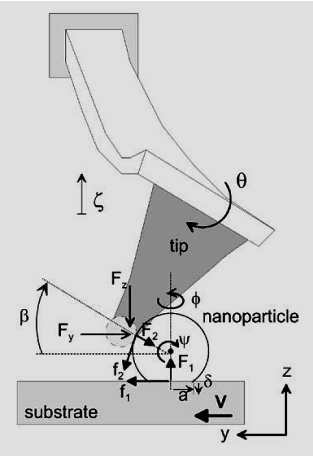


Figure 2.12: This is a technique whereby the force sensing is in two dimensions allowing a direct measurement of friction. $\Delta\theta$ and $\Delta\zeta$ are measured to give F_y and F_z.

2.13, systems without the ability to measure the friction force, such as the Easyscan or Mars AFM.

The relationship between the parameters has the following correlation

$$\Delta\zeta = \frac{F_z \cos\alpha - F_x \sin\alpha}{k_z} - \frac{F_z \sin\alpha + F_x \cos\alpha}{k_{xz}} \tag{2.28}$$

The same sensing system can be modelled in the perpendicular case simply by swapping F_x for F_y in the equations.

A paper by Sriram Sundararajan (Sundararajan and Bhushan, 2000), also advocates the relationship between the slope of surface topography and friction measurements. Again, using a FFM/AFM to measure the effect of topography on the apparent friction of surfaces, the authors at a first

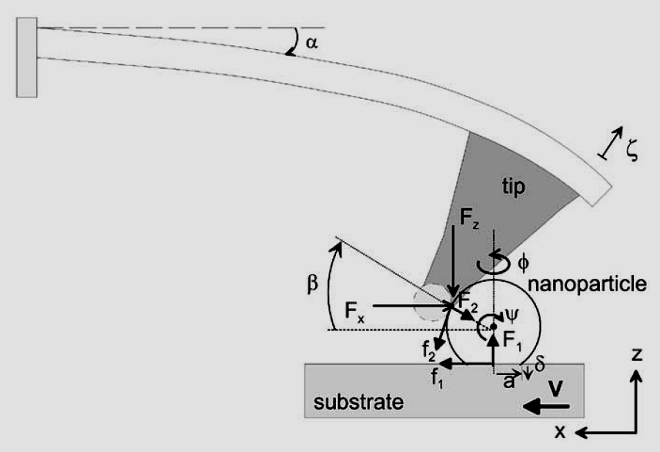


Figure 2.13: one dimensional sensing allows the indirect measurement for force sensing. Only $\Delta\zeta$ is measured, a parameter which depends on both F_x and F_z.

approximation confirm the findings of previous studies and show the friction force trace relating to the first derivative of the topography of a surface, but develop this idea further.

The authors study surfaces by looking at the friction force of the forward and backward scan - which the authors refer to as a 'trace' and 'retrace' - over samples of homogenous material, thus removing any non-topographic friction measurements. They closely study the traces and subtract the trace and retrace (T-R) showing that this does not eliminate the topographic contribution to the friction trace. In Fig. 2.14, data presented in their paper, we see how point A is a much higher peak than Point B is a trough, similarly for the retrace, leading to the friction force T-R.

The authors attribute the increased friction measurement when experiencing an increasing slope to a 'collision' force as the cantilever impacts the

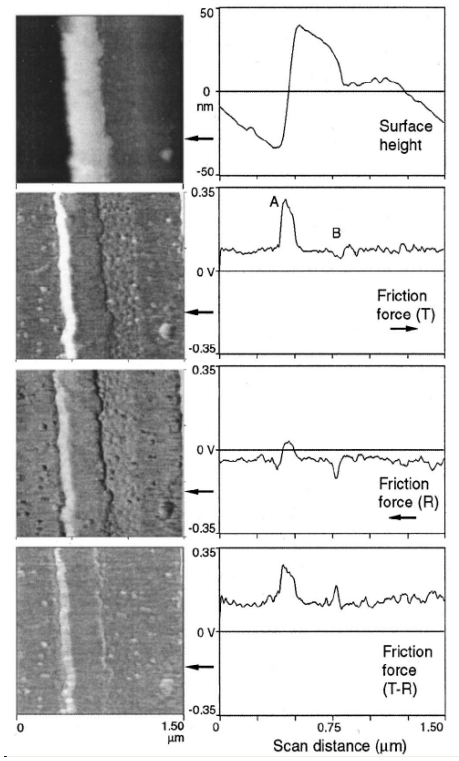


Figure 2.14: Two dimensional profiles of surface height and friction forces scanning a gold-coated ruler with a 70nm height over a 1.5μm scan size.

feature and experiences a larger torsion about the tip. As the leading edge of the tip approaches a feature and contact between the two is established, the linear momentum of the tip which moves at a constant speed is transferred to an angular momentum producing torsion in the tip. This process occurs only for positive gradients, and not as the tip scans down the feature, thus the peaks remain in the T-R traces. In addition to this, depending on the speed of the tip and the bandwidth of the feedback loop of the system, the scanner may produce a brief increase in the normal load applied to the feature. This in turn increases the contact area and thus friction between the two surfaces.

The measurements in the work described above investigate small topographic features affecting friction measurements leading to effects such as the 'ratchet mechanism' as the tip moves with a stick-slip motion. Although these findings are not directly applicable to the Mars AFM scanning system, some ideas are relevant. The work described shows measurements performed over relatively small features in comparison to those the Mars AFM is expected to encounter. Having identified this 'collision' force, it is clear that this force is a dominant interaction to consider that is most relevant to scanning large features, as a larger horizontal component is produced when the edge height is comparable to the tip radius and the torque contributed by the normal force is respectively larger. This is discussed in the next section.

2.4.2 Background

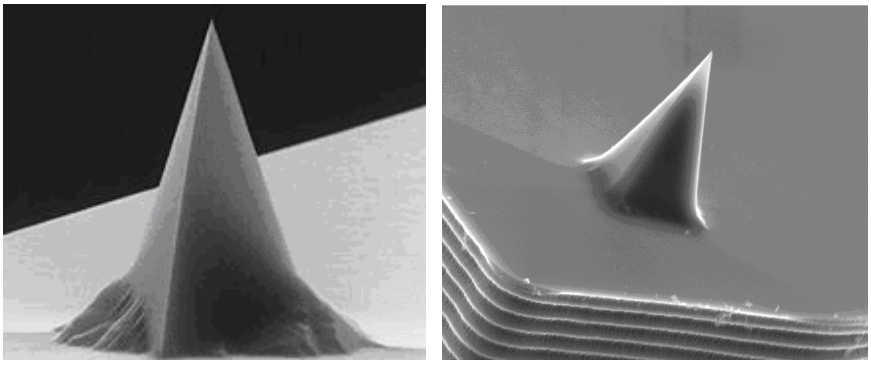
Expecting a relatively large impact force, and understanding that it is the maximum force which will remove a particle from the surface, this section

describes a somewhat different model of the forces expected as the tip scans over features comparable in size to the tip itself. For these tests the Nanosurf Easyscan system was used (Nanosurf, date accessed: March 2008).

The EasyScan - described in more detail in later sections - uses a conventional optical lever to detect the position of the cantilever. This method, used by most AFMs, involves shining a laser beam off the back of a cantilever. The reflected beam is detected by a photodiode, in the case of the EasyScan a two-quadrant diode, and the difference in signal identifies the position of the lever. As the tip is scanned over the surface, the cantilever deflection is recorded giving 1-dimensional optical data but from the scanning position a three-dimensional topographic image of the surface is obtained.

When scanning large features in comparison to the tip radius (quoted as <10nm) shown in Fig. 2.15, the tip can be modelled as a perfect point and the angled surface of the tip contacts the features first, rather than the tip apex.

The AFM tries to maintain a constant deflection of the cantilever throughout the scan. As the deflection of the cantilever is directly proportional to the vertical force, in a perfect ideal scan the deflection (error signal) should be constant (due to operation in constant force mode). In reality though, the way the probe reacts to the surface is by sensing a change in deflection, it then tries to change the scanner height as quickly as possible to return the deflection signal to normal. The time it takes to do this is controlled by the gains (P and I) with higher gains roughly corresponding to quicker response times. As high a gain as possible should then be used to make sure the probe reacts as quickly as possible, however if these are set too high you



(a) (b)

Figure 2.15: An SEM scan of a AFM sensor tip from a) Nanosurf (Nanosurf, date accessed: March 2008) and b) the Mars AFM chip. Image from Neuchâtel.

get undesirable effects such as ringing.

Despite there being a feature in the surface, the lateral component of the speed of the probe should not, in theory, change. However due to some lateral twisting action of the cantilever as it is dragged up the step, the true horizontal speed of the tip apex will probably slow a little and then snap back as it reaches the top. This is a passive action and cannot be fully controlled, although the effect will be minimized by slowing the scan rate or increasing the gains to allow the probe to more quickly react to the step.

Though the feature may be completely vertical, it will take some time for the tip to rise over the surface, due to the pyramidal shape of the tip. There will be an increased force for all this time. The initial 'collision' of the tip produces a maximum force. the force is used to deflect and bend the cantilever. This deflection corresponds to a potential energy which stems from a reduced kinetic energy of the scanner motion. A certain deflection is

needed until the feedback loop reacts; this corresponds to a force which is proportional to the compliance of the lever. Thus, a stiffer tip will produce a larger force.

The 'collision' expected when a rapid increase in elevation occurs is the largest force the particles experience and therefore is most likely to move or remove the particles. However, this force acts momentarily until the feedback loop closes, and the force continues at a more constant magnitude as it moves up over the whole feature, as shown in the schematic sketch in Fig. 2.16. In the EasyScan system, the horizontal movement in x is not controlled by a feedback mechanism, as the vertical z direction is. So as well as the lateral speed of the tip apex, the lateral scanner speed may not remain constant across the line.

The work described in the previous section suggests that the peak force can be obtained by performing a friction mode scan over a step edge, giving the maximum force that the tip could apply to a particle for a given set of conditions (speed, feedback settings etc). The magnitude of the collision force is a function of the tip radius, the applied normal load (determined by the scanning parameters) and the feedback of the system and scanning velocity. However, the methods described to measure the lateral force require friction mode, which the Easyscan and Mars AFM do not have.

Using a similar setup to one suggested by Sitti (Sitti, 2004), the Easyscan system can be used to scan over a step edge, and the lever signal - which provides a direct measurement of the deflection (and hence, force) on the cantilever - can be overlaid with the z-output image, to observe how the force varies from the point of first contact until the tip is over the edge.

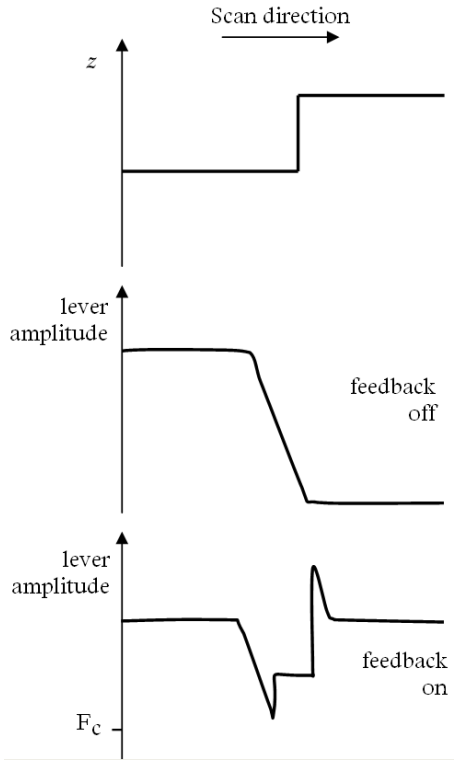


Figure 2.16: A schematic sketch showing the predicted lever amplitude as the cantilever scans forward over a step.

Such scans over a 5μm tall and 5μm wide ridge are shown in Fig. 2.17.

From the scans it is evident how at the faster speed the lever is not able to stay in contact with the surface as the feedback is not fast enough. For the slower speeds the tip appears to remain in contact with the surface. In all the traces the impact from the 'collision' force is evident in the large lever amplitude signal when the tip first contacts the step edge. For the forward scans this is the left hand trough and for the backward scans, the right hand trough. As the tip goes down the ridge, a peak appears as the lever amplitude increases as the lever is moving further from the surface.

From this data it is possible to compare the trace-retrace as suggested by Sundararajan *et al.* (Sundararajan and Bhushan, 2000). Fig. 2.18 shows such a comparison for a scan at $50\mu ms^{-1}$.

The trace-retrace does indeed not cancel to zero, showing the topographic contribution to the lateral force. The impact force is clearly evident as the peak in lever amplitude as the tip first contacts the feature.

2.4.3 Measuring the lateral force

The deflection of the lever is an indirect measure of the lateral force applied against the tip as it is sliding up the step. The first impact is the collision force which is greater than the constant force during the sliding up once feedback has kicked in. Deflection data was compared for different scan speeds. Speed was chosen as the controlled parameter, as it is the most useful practically for our purposes, and also it has been used by other friction studies (Mailhot et al., 2001), though with a different AFM system.

In order to calibrate the amplitude deflection of the easyscan system,

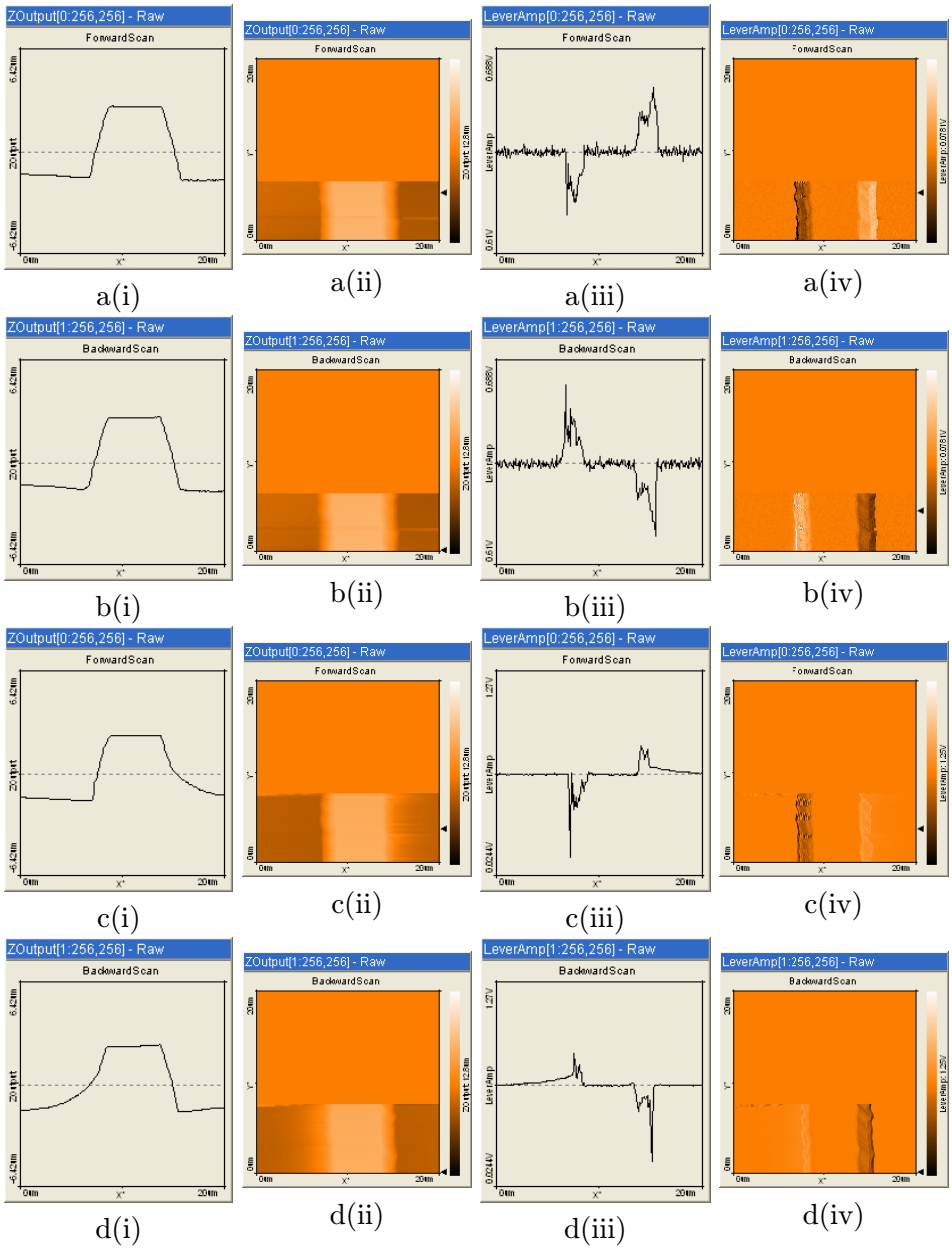


Figure 2.17: Scans performed at two different speeds over a 5μm tall and 5μm wide ridge. (a) shows the forward scan (left to right in x) at the slower speed of 5μms^{-1}, (b) the backward scan (right to left in x) at 5μms^{-1}, (c) the forward scan at the faster speed of 50μm s^{-1}, and (d) the backward scan at 50μm s^{-1}. For each scan the 4 windows show (i) a linescan of the z-output, (ii) the topview of the z-output, (iii)a linescan of the lever signal, (iv) the topview of the lever signal. The scans were all 'up' and stopped after approximately 1/3 of the scan.

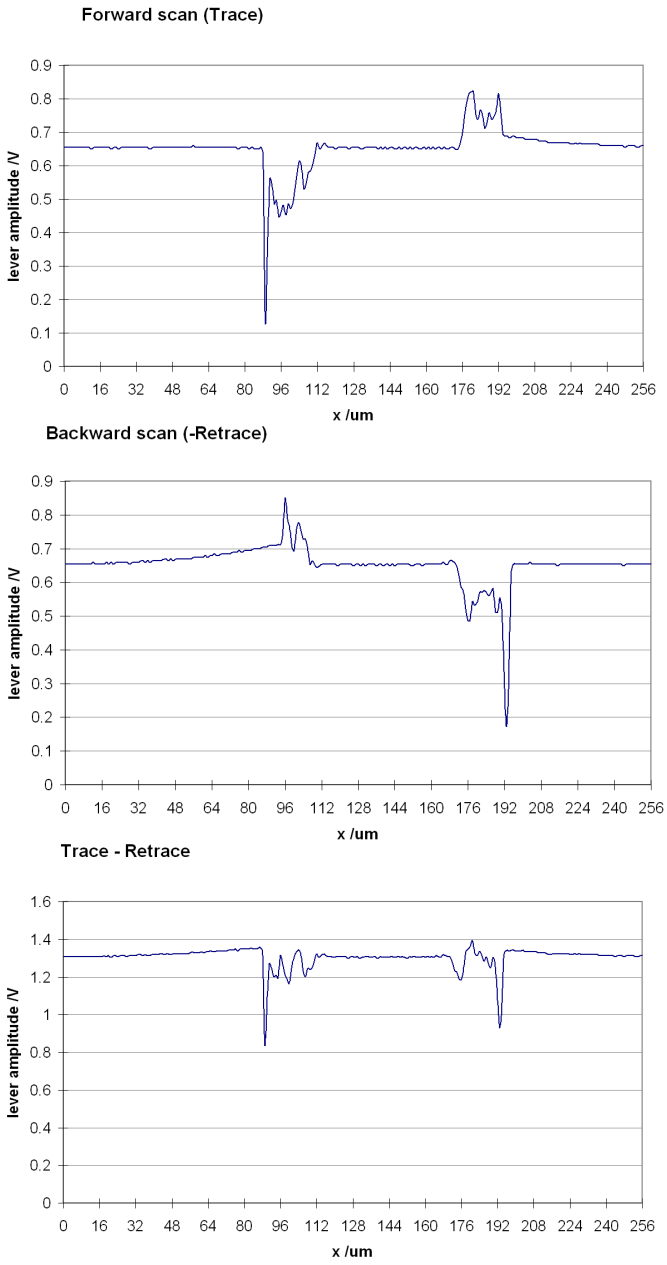


Figure 2.18: A forward scan and a backwards scan for a scan over a 5μm tall and wide ridge at a speed of 50μms^{-1}.

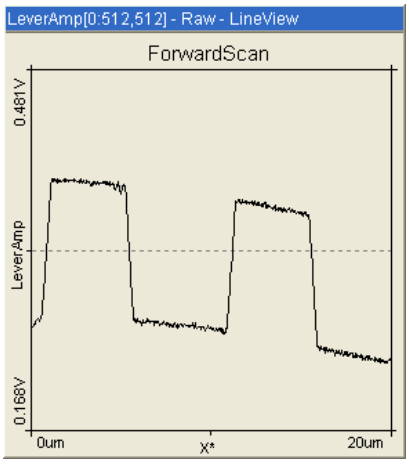


Figure 2.19: A scan of a grid with features 110nm high with the feedback off. The z-output signal was flat for the entire scan, only in the lever signal do we see features.

two methods were used. The first involved scanning over a ridge of known step height with the feedback off. This gave a direct calibration of V/nm for the lever signal vs. deflection. A step height of 110nm was used (no larger so as not to bend the cantilever too much). This technique calibrates the photodetector with respect to the nominal position of the cantilever, therefore it depends only on bending and not on other things like gain, speed, setpoint, etc. Such a scan is shown in Fig. 2.19. This calibration gave a value of $1.00\mu\mathrm{mV}^{-1}$.

The force on the cantilever can also be determined using another technique in which the force calibration of the scanner converts the voltage measurement to a force; the Amplitude signal calibration is to use an amplitude-distance spectroscopy measurement. This required a hard clean sample of silicon, a high free vibration amplitude and a sharp tip. The amplitude-

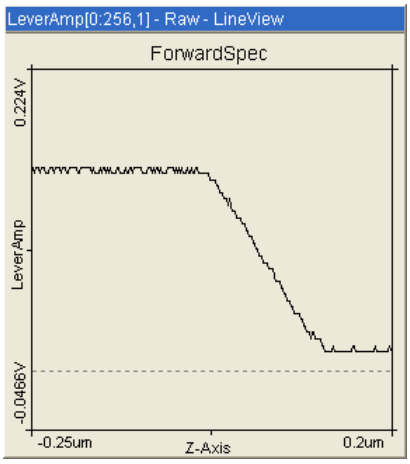


Figure 2.20: Amplitude-distance spectroscopy measurement scan.

distance measurement was performed and the slope determined in nm/V the results of which are shown in Fig. 2.20. This calibration gave a value of $1.01\mu\mathrm{mV}^{-1}$.

Once the amplitude deflection of the scanner had been calibrated, the measurement of the maximum force produced by the scanner as it scans over a ridge could be performed. For each speed the maximum lever amplitude was found which, using the calibration, gave the maximum force exerted by the scanner during the scan.

Estimating the tip-sample interaction force

Quantitative theory of amplitude-modulation AFM is very complicated and in particular the interaction force is difficult to measure. It is the maximum interaction force which occurs at the lower reversal point of the oscillation cycle at the closest tip-sample distance which is of interest in this work. In

order to provide an estimate of the tip-sample force, existing models and measurements have been used to guide calculation for this work.

Anczykowski *et al* (Anczykowski et al., 1996) investigate the cantilever dynamics of the tip-sample interaction with experiment and numerical simulation. They model the amplitude, phase and force and how they each vary with tip-sample distance, as shown in Fig. 2.21. These numerical simulations are shown for excitation frequencies above, below and at the resonance frequency f = 299.95 kHz. The models were verified with experimental values. The force they describe is the force at the lower reversal point of the oscillation cycle. The measurements in this work used a microscope which operated at 160.151 kHz just below the resonance frequency of 160.671 kHz, so the appropriate model was used.

The oscillation amplitude for the Easyscan setup was found by amplitude vs. distance spectroscopy to be 160 nm peak to peak. Although a large amplitude, it is within the usual operation amplitude range of 10-100 nm from the centre position. The phase measurement results are not delivered by the Easyscan system.

The force on the cantilever depends on the force constant. The large oscillation amplitudes of such dynamic SPM systems mean the effective spring constant k_{eff} can no longer be approximated by a linearized model where k_{eff} is a result of the cantilever spring constant k coupled with the spring constant of the tip-sample interaction k_{ts}. This is because the oscillations are much larger than the usual width of the surface potential (< 10 nm) (Anczykowski et al., 1996).

However, spring constants are still found to be lower than the static

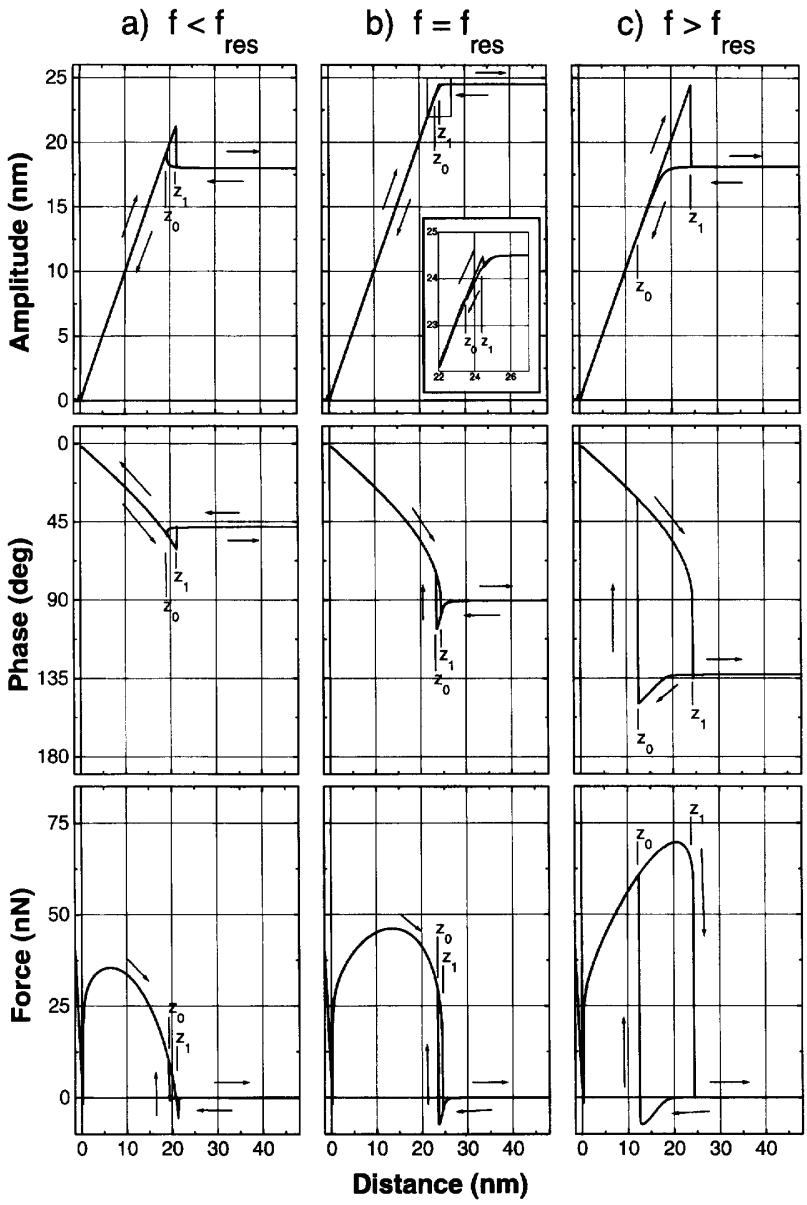


Figure 2.21: Oscillation amplitude, phase and force diagrams for excitation frequencies (a) below (f = 299.45 kHz), (b) at (f = 299.95 kHz) and (c) above (f = 300.45 kHz) the resonant frequency f_{res}. The force shown is the interaction force at the closest tip-sample distance. (Anczykowski et al., 1996).

cantilever spring constant alone. Examination of experimental force curves, such as performed by Schirmeinsen *et al* (Schirmeisen et al., 2005), shows that if the curve is approximated by a simple linear fit, a stiffness of the interaction in the repulsive region drops by two orders of magnitude compared to that reported for static mode.

The magnitude of the force can be estimated for the experiments in this work by using the assumptions and values found in the literature as a guide. The tip-sample force with the cantilever oscillating at 60% setpoint - as used in the vibration amplitude calibration - is calculated as just over 30 nN. The other point used in the calibration, which is at the top of the step (100nm high) while in open loop, gives a force of over 50 nN. These values assume a reduction in the spring constant of two orders of magnitude, which in static mode is 48 Nm^{-1}.

If these values are compared to those found by Anczykowski et al they appear of very similar magnitude. Although the amplitude of modulation for the Easysan setup in this work is much larger, the excitation frequency is smaller, perhaps contributing to the similarity of the values. The spring constant of the lever for Anczykowski *et al*'s work is quoted as 29 Nm^{-1}.

Another work by Garcia *et al* (García and San Paulo, 1999), also studies the tip-sample interaction regimes for AM-AFM. They perform numerical simulations to estimate the average repulsive forces which they find to be in the 0.2 - 2 nN range, and find peak forces to be 10 - 40 nN. They model a cantilever of spring constant of 40 Nm^{-1}, a working frequency of 350 kHz operating at amplitudes of 10, 30 and 60 nm.

For this thesis, the values of force calculated with the values from the

vibration amplitude calibration give forces on the order of 30 - 50 nN. These are similar to those modelled and calculated elsewhere in the literature, which have been confirmed by experiment, suggesting a similar situation. The conclusion is that the interactive force must be in this range and is a reasonable estimate.

The lateral force when scanning over a step edge

Following from this, the lateral force F_x can be extracted from the deflection data. The resolution of forces is calculated considering the shape of the tip to give lateral force. This is done from using the spring constant to find the normal force on the surface from $F = kx$, where k for the tip used is 48.1Nm^{-1}. This was reduced accordingly as explained in the previous section. The lateral force is then calculated by resolving this force using the angle of the tip edge to the vertical which is 15^o.

A study of the lateral force using the EasyScan to perform scans perpendicular and lateral to the cantilever axis. The results are given in Fig. 2.22. The axial scan direction produced a larger lateral force than scanning in the perpendicular direction as the lever is not able to 'twist'.

As far as it can be determined from the literature, this is the first measurement of the lateral forces produced by AFM tips as they scan over high aspect ratio features.

The lateral force when scanning over a sphere

The particles we will be scanning will not likely have the shape of a 5 μm step, but likely a more spherical shape. In order to see the lateral force over

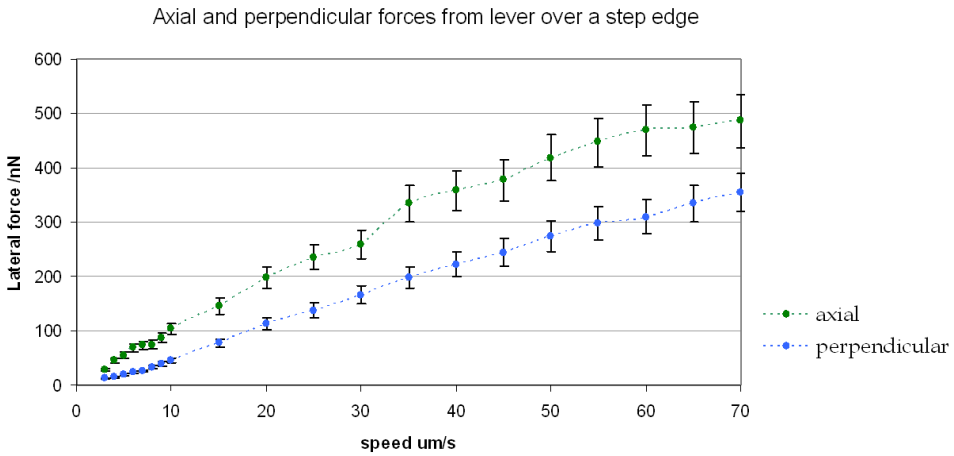


Figure 2.22: A graph showing the forces from axial and perpendicular scanning, as resolved from the vertical force into the substrate.

a curved surface, 5 μm glass spheres were stuck to a flat silicon substrate and similar scans performed. The measurements were performed using the scanner in the perpendicular direction - as will be scanned on Mars. The traces are shown in Fig. 2.23.

As with scanning over a step, scanning over a sphere produces a larger 'collision' force as the tip first comes into contact with the sphere. Note the difference in profile of the interaction force as the tip scans over the sphere.

In Fig. 2.24 the magnitude of the lateral force produced on a 5 μm spherical edge to that produced on a 5 μm step edge can be compared.

For a spherical particle of radius 5 μm, on a planar surface, even at the very slow speed of 5 μm per sec, 17 nN is a rather substantial force.

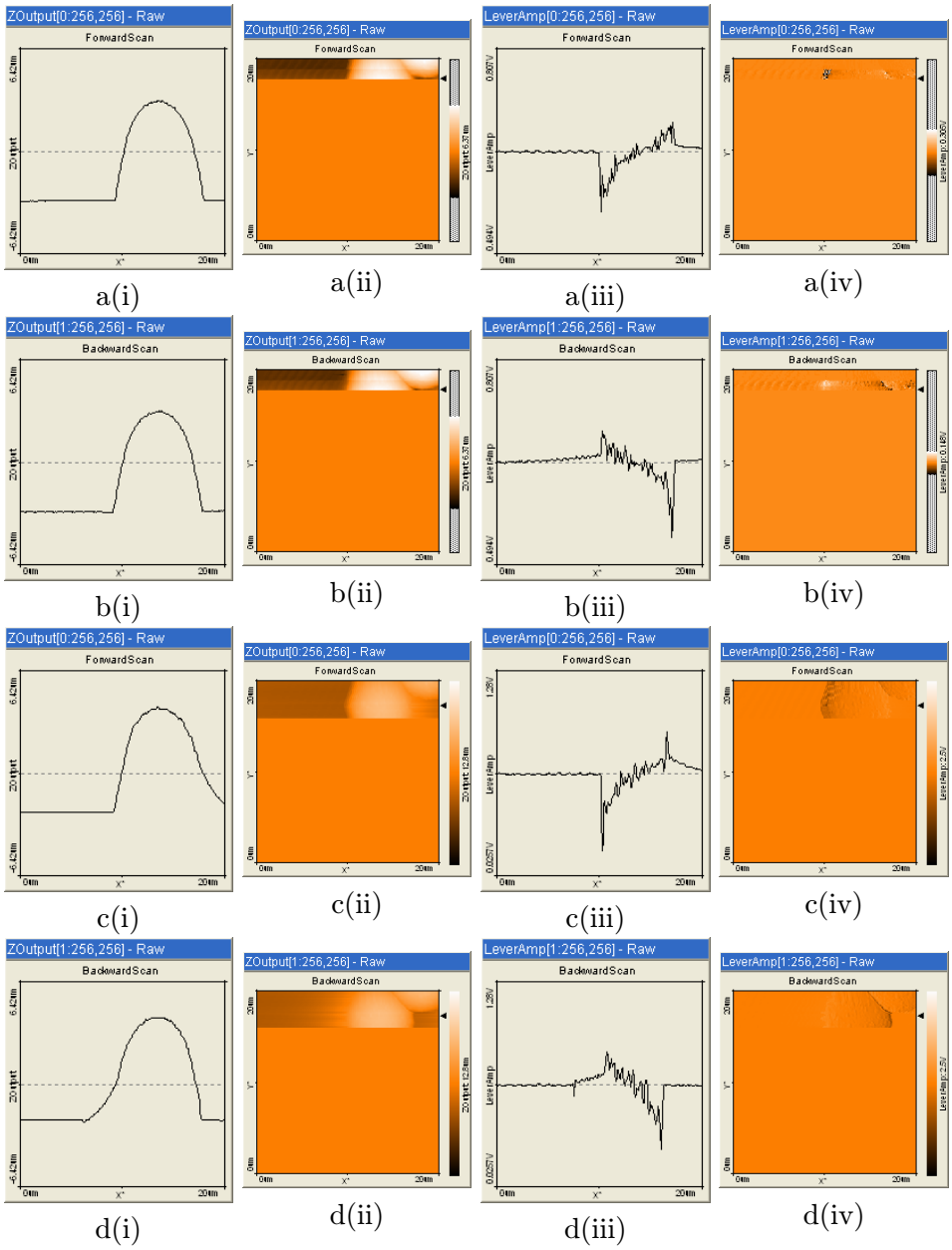


Figure 2.23: Scans performed at two different speeds over a 5μm sphere. (a) shows the forward scan (left to right in x) at the slower speed of 5μms$^-$1, (b) the backward scan (right to left in x) at 5μms$^-$1, (c) the forward scan at the faster speed of 50μm s$^-$1, and (d) the backward scan at 50μm s$^-$1. For each scan the 4 windows show (i) a linescan of the z-output, (ii) the topview of the z-output, (iii)a linescan of the lever signal, (iv) the topview of the lever signal. The scans were all 'down' and stopped after approximately 1/3 of the scan.

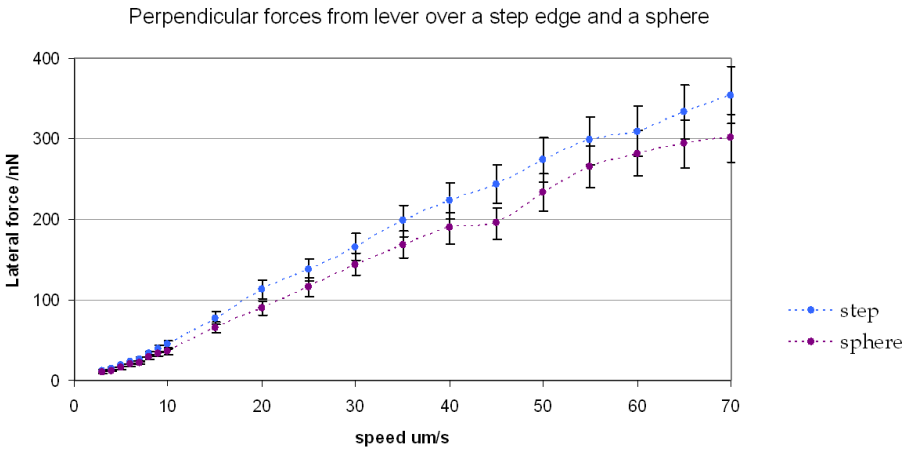


Figure 2.24: A graph showing the forces from axial and perpendicular scanning, as resolved from the vertical force into the substrate.

Summary and conclusions

General result is: even at the slow speeds we will be scanning, the force from the tip is of the order of 60×10^{-9}N.

Looking at the magnitude of the force, it is not an insignificant force in the moment model, which may then lead to particle detachment, as found in experiments.

This force can be added to the graph of adhesion forces for a sphere that was drawn in Fig. 2.7 to provide a comparison of the magnitude of this lateral force from the scanner. The graph shown here in Fig. 2.25 shows the lateral force from the scanner as being independent of the size of the particle. This representation is likely to hold for most particles we are interested in as it is the angle of the side of the tip that is important. For small particles of the order of 10nm - comparable to the radius of the

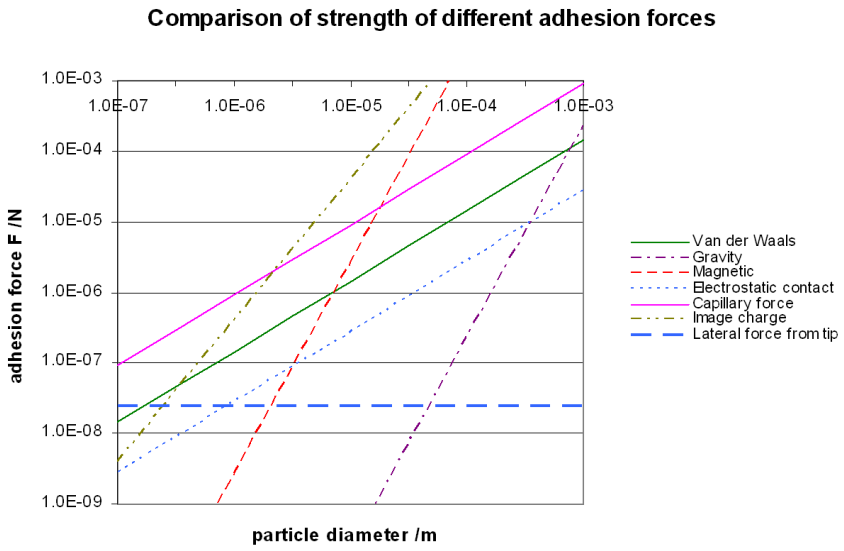


Figure 2.25: A graph showing a theoretical estimate for the relative magnitudes of various adhesive forces as they vary with particle size as well as the lateral force produced by the AFM tip.

tip - this force will probably decrease. Further, for particles larger than the tip, the force may be much larger as it will be the cantilever colliding into the side of the particle rather than the tip, so the motion will be to bend the cantilever sideways rather than twist it. The AFM is not intended to measure particles at these extremes.

2.4.4 The Mars AFM

To understand how these tests performed on the Nanosurf EasyScan system relate to the Mars AFM, a comparison of the two systems is required.

Nanosurf AG (a spin-off company from University of Basel) worked with the Jet Propulsion Laboratory to develop the FAMARS instrument. The

company went on to build portable high resolution microscopes such as the Easyscan DFM scanning system used as part of this research work. The EasyScan system is versatile, portable and compact and similar in many respects to the Mars instrument. The principal difference between the microscopes is the method of detection of a beam deflection, but this factor is not important for comparing the above results as - since for both, whether 1-D optical or piezoresistive deflection data, only delta zeta is measured - it is the control of the scanning system that is important.

The cantilever's dimensions are the same; length 225μm, width 38μm, thickness 7μm and tetrahedral tip shapes with opening angles of 30^o typical of fabrication by anisotropic etching in a KOH solution.

For both microscopes the scanner is controlled by a very similar platform which uses electromagnetic actuation, as described in Chapter 1. The principal difference between the experiments described above which use the Easyscan system and the Mars AFM, is operation of the Easyscan under amplitude modulation rather than frequency modulation. As discussed in Chapter 1, in the amplitude mode of operation, the cantilever is oscillated outside contact with a surface (free oscillation) by an excitation voltage and this sets the free amplitude of oscillation just above its resonant frequency. The excitation voltage which drives the oscillation is the voltage applied to the piezoelectric drive element on the AFM chip holder. The fixed free oscillation amplitude of a cantilever is somewhere between 10-100nm. When the tip is brought into contact, the feedback loop closes when the oscillation amplitude reduces to a certain fraction of that, defined by the 'setpoint' (for the experiments here this is set as 65%). The topographic signal is then

obtained from the z-position of the scanner which shifts to maintain the setpoint amplitude.

When operating in frequency modulation mode, the cantilever is also driven into oscillation with a set amplitude close to its resonance frequency. However, when in contact with a surface, the feedback loop closes when the shift in the cantilever resonant frequency from the free oscillation frequency (the oscillation frequency when not in contact with the surface) is equal to the setpoint. The feedback loop adjusts the scanner's z-position to maintain the frequency shift. It is the spatial dependence of the frequency shift, which converts to a spatial dependence of the z-position of the scanner that is the source of the topographic signal.

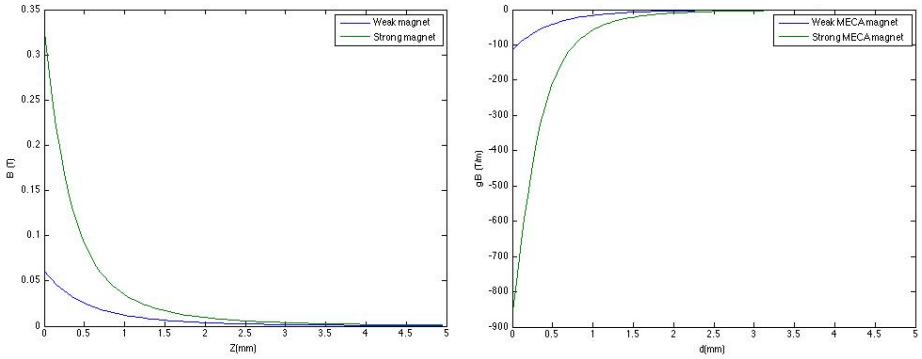
2.5 Particle-Substrate Adhesion

Earlier in this chapter, the adhesion force between the particle and the substrate were examined theoretically. However, thus far it remains an unmeasured factor in the adhesion equation. It has been demonstrated that the adhesion force of small particles to silicon substrates is not strong enough to withstand the large lateral force produced by the AFM scanner, which in the last section was measured as 60×10^{-9}N at the slow scanning speeds of 5μm per second that will be used on Mars. One method to experimentally estimate this force would be to use this measured force from the scanner, and try to remove particles that are experiencing an additional known force of adhesion, such as a magnetic force.

2.5.1 Experimental Setup

The MECA magnets are well characterized, and Fig. 2.26 shows graphs of both the field strength and the field gradient in the centre of the magnets projecting upward from the surface. The magnets are built into an aluminium housing structure giving the appropriate dimensions for the SWTS. For investigating the adhesion of particles to silicon, the surface of the magnet substrates can be overlaid with a surface of flat silicon. This means that magnetic particles on the surface of the silicon are adhered by the usual adhesion forces, and by an additional magnetic one. Using the previously described equation 2.19 for the force acting on a ferromagnetic particle in a magnetic field $F_{\text{ferro}} = \mu_0 M_j \nabla H_{oj} V$ the force acting on a 5μm sphere of iron on the surface of the strong magnet is of the order of 6×10^{-8}N. This force is much smaller than other expected adhesion forces and its contribution to the overall adhesion force is not enough to keep particles in place during scanning. Increasing the size of the sphere would increase the force proportionally by r^3, where r is the radius of the sphere and the magnetic adhesion force would quickly reach the necessary value. Particles larger than 14μm, however, cannot be scanned by the AFM in their entirety due to the limited z-range.

Fig. 2.25 can be understood as a plot of the adhesion forces acting on an iron microsphere while sat on a silicon surface on a magnet. In order to immobilize particles with a known magnetic force (Sigma-Aldrich, date accessed: January 2008), and thus investigate adhesion to a substrate, a different experimental setup was investigated. The plot in Fig. 2.25 shows



(a) (b)

Figure 2.26: Graph showing (a) the magnetic field strengths and (b) the gradient of the strong and weak MECA magnets. The graphs show these values as a function of height above the centre of the magnet.

the lateral force produced by the scanning tip on a graph showing the other adhesion forces. It appears that even with particles only a little over a micrometre, the van der Waals force alone should hold the particle down well enough for scanning, contrary to the experience of scanning such particles.

With a larger magnetic force, it may be possible to hold small particles on a substrate for scanning.

The following describes a technique designed to investigate the adhesion forces between a particle and a substrate. The method involves measurement of the detachment force by the AFM scanning of iron particles held down on a magnet. A silicon substrate loaded with iron particles was placed above a solenoid with a known magnetic field. An appropriate iron sphere was identified and scanned with the AFM, with a large field holding the particle in place. Once the scan was complete, the current through the solenoid was decreased by a set amount, and another scan performed. This procedure

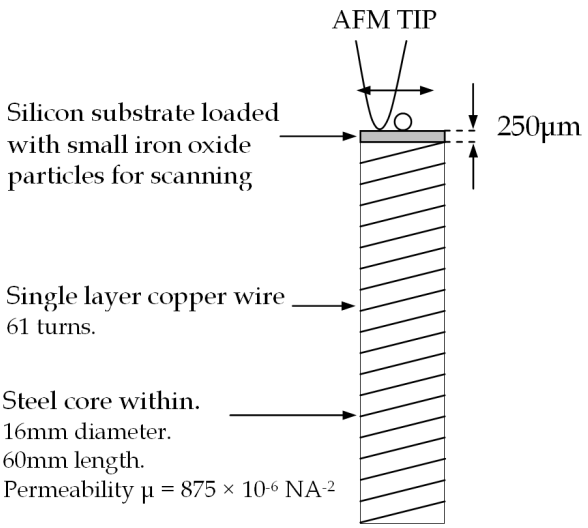


Figure 2.27: A schematic of the setup designed to apply varying magnetic fields to small 5μm Fe particles on a flat piece of silicon substrate.

was repeated reducing the current each time. When the force of detachment (in this case equivalent to the force from the scanner) exceeded the forces of adhesion between the particle and substrate, the particle moved. From the balance between the forces of detachment and adhesion the force between the particle and substrate could be determined, from which the non-magnetic interactions could be found. This setup is potentially a very controllable and useful experiment. A first trial of such a configuration is described in Fig. 2.27.

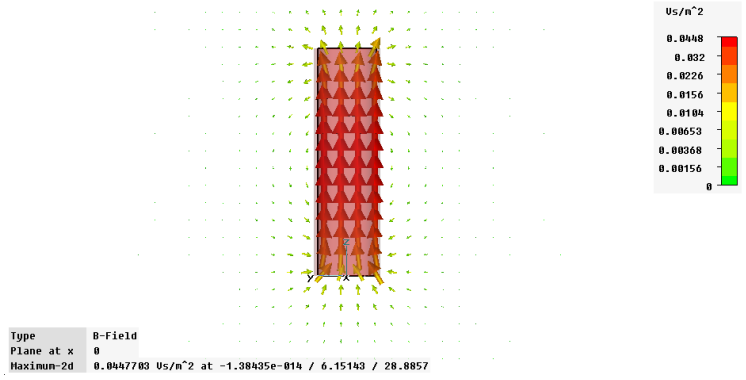
Modelling this setup analytically is complicated - in fact no such solutions were found except for the trivial case of the field inside an air-cored solenoid (of no relevance here), but even then it is only the inner field which is easy to calculate, not the values away from the top edge needed for this

experiment - thus the best way to determine the field around the solenoid is using a numerical model. The electromagnetic simulation software CST Microwave Studio (Technology, date accessed: April 2008) provides computational solutions to electromagnetic designs. The setup was modelled in three dimensions and numerical solutions for the strength of the field and the field gradient were obtained for various currents. The current through the coil was modelled as a sheet around the core. The solution for a 2A current through the coil is shown in Fig. 2.28.

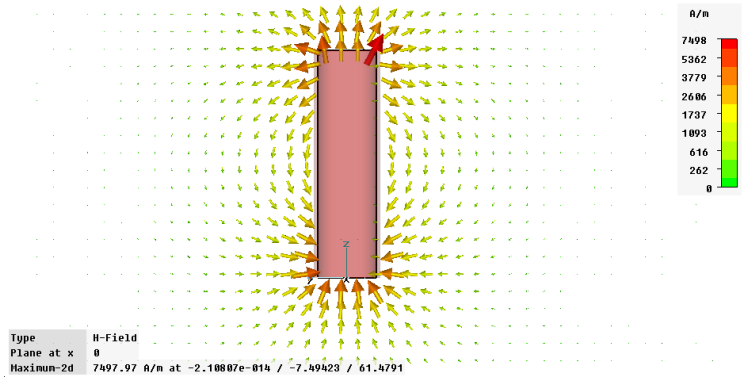
The magnetic flux density for the point at the centre of the surface of the silicon substrate is plotted for a range of currents in Fig. 2.29.

The gradient of the field can be easily calculated from extrapolated values of the field and thus the force on a 5μm particle computed, again using equation 2.19. The force for a 2A current was found to be very small at 6×10^{-11} N.

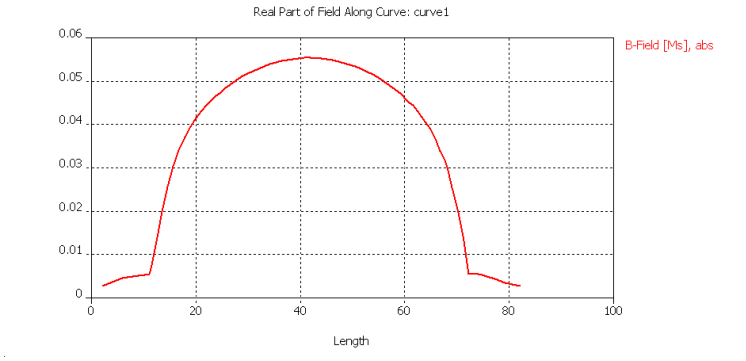
Despite applying large currents to the solenoid, the field produced outside the solenoid or within the core was not large enough. This is a consequence of the large reluctance outside the solenoid and the relatively very low reluctance within the core due to its high permeability (which is interestingly the opposite case to the air-cored solenoid, where the H field is mainly driven by the reluctance of the space inside the winding, while the influence of the outside region can be neglected - which incidentally makes the computation for this case so much simpler). The inner magnetic core is of course useful, it was found (through numerical modelling) that the fields in the solenoid and just outside were about five times those of an air-cored design.



(a)



(b)



(c)

Figure 2.28: Graphics showing (a) the B-field, (b) H-field and (c) a line showing the B-field along the axis of the centre of the steel rod.

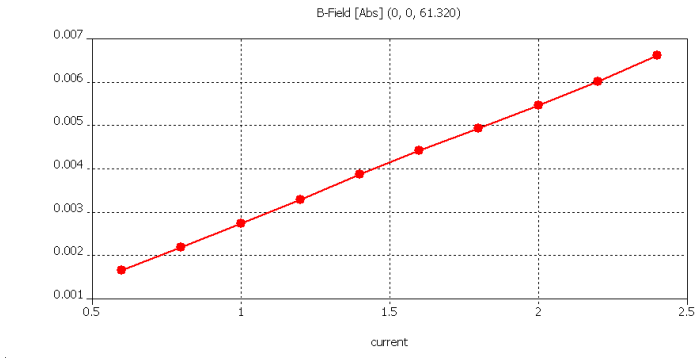


Figure 2.29: The magnetic flux density B for the point at the centre of the surface of the silicon substrate.

The field close to the end of the solenoid is shown in Fig. 2.30. It demonstrates that the simple arrangement of this magnetic excitation system might not be ideal for the purpose of this experiment because, not only high values of the field, but also a high field gradient are needed.

The setup was investigated practically, but it was found that, as the current through the coils was increased, the magnetic field produced by the solenoid began to interfere with the AFM scanning system. The scanning head contains electromagnets and, due to the proximity to the solenoid, at currents larger than 3A, scans became unstable and the scanner could not keep track of the surface. Shielding the scanning head would have been complicated because the microscope must contact the surface to take images. Thus even if the excitation system were able to produce fields of sufficient strength and gradient, such fields could not have been used in combination with the AFM system anyway, unless they could be produced in a somewhat more localized geometry.

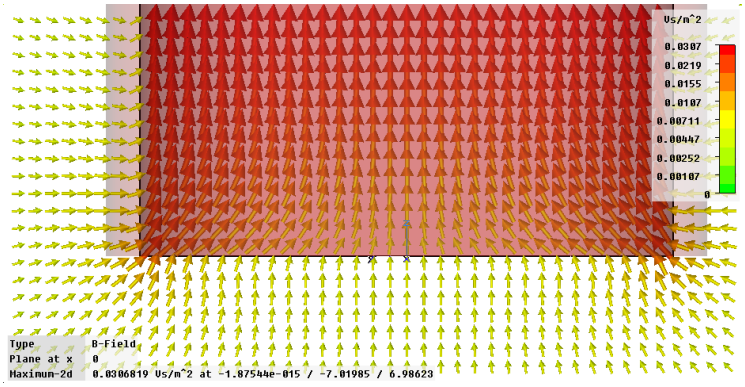


Figure 2.30: Details of the magnetic flux distribution at the edge of the solenoid in the region (just outside) where a magnetic particle could be positioned. Apart from the field not being strong enough, its variation is not sufficiently pronounced.

It was concluded that a larger attractive force to hold the particles is required, at the same time an arrangement to protect (screen) the AFM system from the influence of strong magnetic fields is required. Since larger particles cannot be scanned by the AFM in their entirety, an idea to use much larger particles to increase the force - which otherwise would have been a very plausible solution - is not helpful either. The experiment clearly requires a configuration with a stronger and more localized field with a larger field gradient. Such a system would no doubt require a complicated magnetic circuit, probably resembling a C-shaped core, with a winding on one side and carefully designed overhanging 'poles' on the other side, so as to try to focus the field on to a very small volume. The conflicting constraints for such a design would be to achieve high concentrated fields and prevent them from entering the space where AFM equipment is present. Designing and building such a system would require a considerable effort both in time and

cost. The purpose of the attempted design described above was to establish if a simple design could achieve the same purpose and a straightforward answer to this question is that it does not.

2.6 Particle interactions

Most sample delivered to the microscope station will be from the robot arm. Therefore it is important not only to consider how the particles interact with the substrates but maybe more important is how particles interact with each other.

The forces between a particle and a flat surface were discussed in some detail in Chapter 2. Here the forces that may exist between particles will be described briefly, though some adhesion mechanisms will be the same as already discussed.

2.6.1 Interparticle forces

Various factors affecting inter-particle adhesion exist and the main ones will be briefly outlined below.

Photoelectric emission induced by solar UV radiation Fig. 2.31(a) is more common in an environment with a low surface humidity combined with a high UV flux. It is recognized to be the dominant process for charging of the lunar dust (Abbas et al., 2006) and changes the properties of the soil in terms of its cohesion. These changes on the surface material may lead to aggregates forming sufficiently large for Aeolian transportation (Towner et al., 2004).

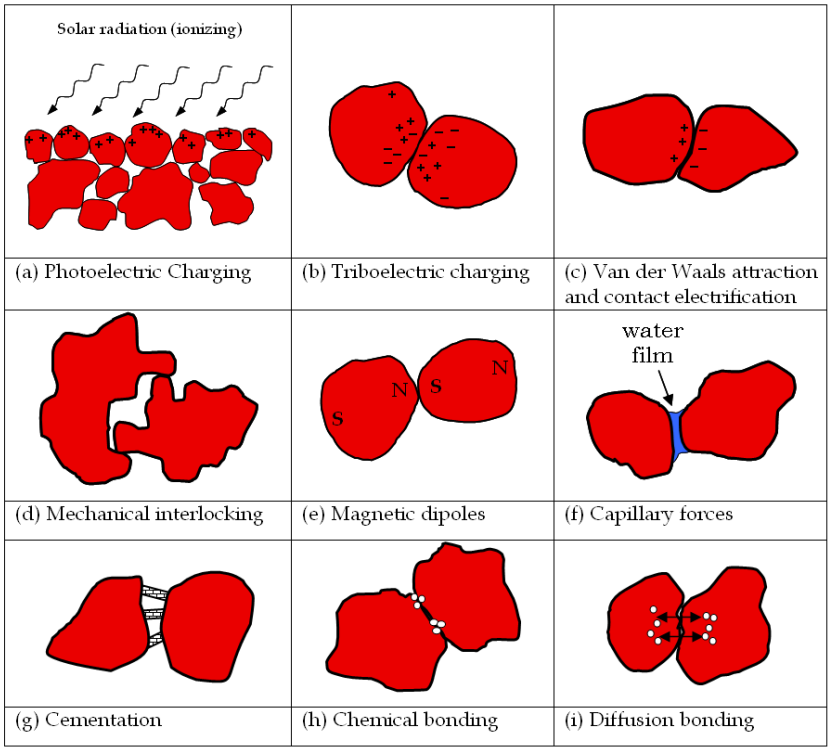


Figure 2.31: Various mechanisms for particle-particle adhesion.

Triboelectric charging is a common phenomenon experienced when two materials come into contact and are subsequently separated, shown in Fig. 2.31(b), and electrons exchange. The word originates from the Greek for 'rubbing', *tribos*. Although it is enough that the materials touch, the effect is larger when the materials rub and contact each other repeatedly. It is a type of contact electrification in which on simple touch or sliding one body over the other, a charge transfer of electrons occurs from the material with a high work function to one with a lower work function, to equalize their electrochemical potential. The magnitude and polarity of the resulting charges will depend upon the materials, their surface roughness, temperature, strain, as well as other properties. This effect may be large for 'sprinkled' samples, rather than 'dump-delivered' onto the microscopy substrates.

Van der Waals forces, Fig. 2.31(c), arise due to temporarily fluctuating dipoles which induce dipoles in other bodies. They have been discussed in more detail in Chapter 2. These forces are optimally active at 0.4nm separation (effective contact) and without the liquid bridge, they dominate the adhesion of fine particles.

Mechanical interlocking of macromolecular and particle shape effects can occur between molecules and chain branches, interlocking by overlaps of surface roughness contacts and interlocking of hook-link bonds, Fig. 2.31(d). Magnetic dipoles, Fig. 2.31(e), are a stable adhesion force that can increase the cohesion of a material.

Described so far are long-range interactions which attract particles to a surface and form the adhesive contact area. The contact area between particles can also be established by interfacial reactions, such as diffusion,

where forced molecular bonding occurs due to cold welding, sintering, pressure solution Fig. 2.31(i), or the formation of liquid and solid bridges Fig. 2.31(g) such as cementation - crystalline interstitial growth from ice, salts, silica, carbonates, etc.

In a terrestrial environment, capillary forces, caused by liquid films between grains can occur when the adhesive forces between the grain and the film are greater than cohesion between film molecules, Fig. 2.31(f). The presence of a capillary force can reduce the effect of other adhesion forces, such at the van der Waals force, as the liquid bridge between the bodies results in the bodies being further apart.

Short range interactions also contribute to the adhesive force, but only once the contact area is established. These are forces such as chemical bonds Fig. 2.31(h) and intermediate bonds for example hydrogen bonds.

Some adhesion types originate from mechanisms inherent to the particles, some are non-inherent and originate from the environment or handling of the material, and some are mediated by aiding processes.

The forces we expect to see on Mars differ to those seen on Earth due to the Martian environment; the cold dry climate is conducive to the electrostatic charging of materials; the seasonal winds good for stirring things up; and the dust storms provide turbulent motion further mixing particle in a different way.

The grain size distribution of the material also effects the cohesion of he soil. Large grains have few bonding points, whereas the 1-2

The interaction of particles with each other will affect important parameters modelling the behaviour of the soil. As well as the distribution of the

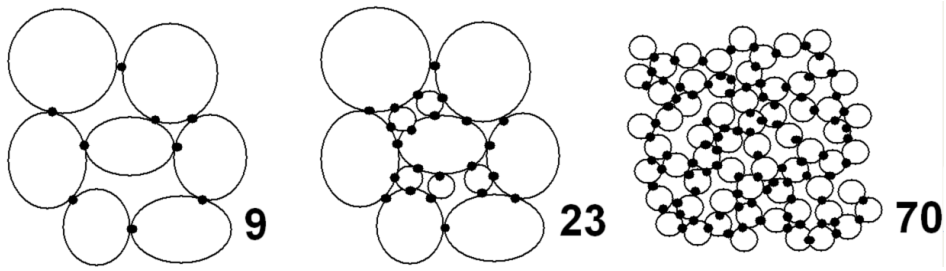


Figure 2.32: Demonstration of the effect of grain size distribution in a sample. The black dots indicate where particles contact each other. The centre image shows that even the addition of a small number of grains, greatly increases the number of contact points. The material on the right, composed entirely of the smaller size of grain, as a very large number of contact points. Schematic courtesy of John Marshall, SETI Institute, NASA Ames.

soil on the microscope substrates, factors such as the angle of repose are important, for example when material is delivered from the robot arm.

2.7 Summary

The work described in this Chapter is focused on understanding the mechanics of scanning loose particles with AFM. A theoretical study of the adhesion forces of a single spherical particle to a substrate showed the relative magnitudes of the interactions between the two bodies.

A model in terms of moments was used to describe the system of a particle being scanned by an AFM tip. The lateral force from the scanner was unknown and not quantified in the literature on AFM. Experiments to estimate the lateral force from a scanning tip for this system were performed as part of the study, and an analysis of the force profile described.

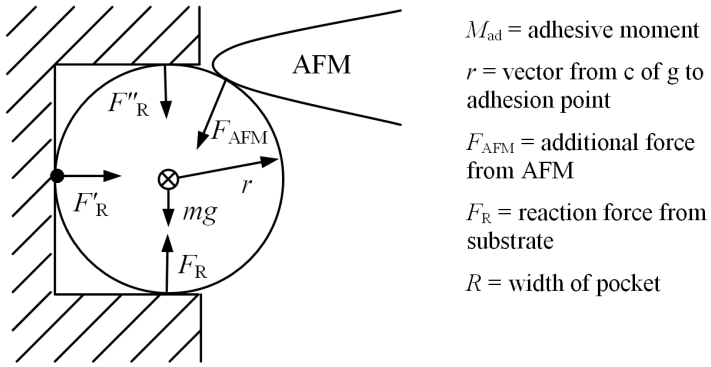


Figure 2.33: Balance of torques for equilibrium for a spherical particle (for simplicity) with an AFM.

2.8 Conclusion

Even scanning particles very slowly with an AFM produces 'large' forces that remove the particle. In the absence of adhesives - most of which are not effective at the low temperatures of the Martian arctic, one solution to this problem would be to stabilize the particles with mechanical trapping.

In the case of a substrate that has 'steps' or 'pockets' for the particles to fall into, the situation changes, as we see in Fig. 2.33. The weight of the particle and the force from the AFM are balanced by the reaction force and the particle remains on the substrate and is no longer dependant only on adhesion forces. Since on Mars we do not know the adhesion forces we do not want to rely on knowing the adhesion moment.

This will be investigated in the next chapter.

Chapter 3

MECA Hardware

Substrates for the sample wheel on the MECA microscopy station are required to hold samples that will be imaged by the optical microscope and scanned by the AFM. Micromachined features can be used to aid microscopy, and in this chapter the utility of such substrates in preparation for *in-situ* experimentation during the Phoenix mission is demonstrated. Moreover, this chapter contains a description of how the substrates - which were incorporated in the Phoenix spacecraft - were designed, fabricated and tested.

3.1 Introduction

Here a discussion of the development, design and manufacture of substrates for the mission, the problems encountered in development and how such problems can be resolved is offered.

It has been shown in Chapter 2 how flat silicon alone cannot hold particles sufficiently for scanning with AFM. Substrates on the MECA wheel

such as silicone and strong and weak magnets help to keep particles in place. Often, however, these produce very dense fields of particles which are not suitable for AFM scanning. Therefore another way had to be found to stabilize particles, yet maintain a field sparse enough to be able to scan with the AFM.

The idea of micromachined silicon with high aspect ratio topography was investigated and developed to enhance the adhesion of particles for AFM measurements.

3.2 Description of problem

3.2.1 Background

The AFM and the OM on Phoenix are intended to be used together to study particles in the micrometre size range. The samples are collected on 3mm diameter disks, which include ten sets of six standard substrates. Each disk is designed to promote different types of particle adhesion and has a particular purpose to aid with microscopy. The set includes: two micro-buckets for bulk sampling, a strong and a weak magnet, a sticky silicone flat disk and a micro-machined silicon target referred to as a nano-bucket or textured substrate - primarily intended for aiding AFM imaging. Based on the testing described in this chapter, this micro-machined target was designed and manufactured here at Imperial College. (A fuller description of the SWTS and microscopy station is given in Chapter 1 Section 1.6.1.)

Using the MECA microscopy setup, we want to image at a high spatial resolution. The first level of data yielded for each sample delivered to the

microscopy station is the images from the Robot Arm Camera (RAC). These provide us with an overview of the sample to be tested. The microscopy instruments available to us, both OM and AFM, are limited by the maximum particle size that can be measured; the OM has depth of field of 80μm and the AFM has a maximum z-range of 13.8μm. For this reason a scraper, which removes material over 200μm above the surface, is used to control the height of piles on substrates. Between them, the OM and AFM can image particles at various levels. As images are taken at different focus positions software tools can be used to form a through-focus composite image. Constrained by this limited sample preparation, consideration was required on how well the AFM can image this range of particle sizes on Mars.

3.2.2 Particle Adhesion and Scanning

As discussed in chapter 1, investigation of loose micrometre sized particles with AFM is a poorly studied area, likely due to the difficulties encountered during imaging. These arise due to two main reasons; i) the similar size of the particles to be imaged and the AFM tip and ii) the lateral force applied by the tip, even when scanning in tapping mode. This results in the generally poor quality of images of particles obtained so far.

A mechanical limitation of all scanning probe microscopes is the generally low aspect ratio of the tip. Tip-particle interaction can be very large when AFM is used to image loose, small particles (Gautsch et al., 2002), as demonstrated in Chapter 2. Although the lateral force applied to the substrate during scanning can be minimized while operating in the dynamic (tapping) mode, we have still found that micron-sized particles are pushed

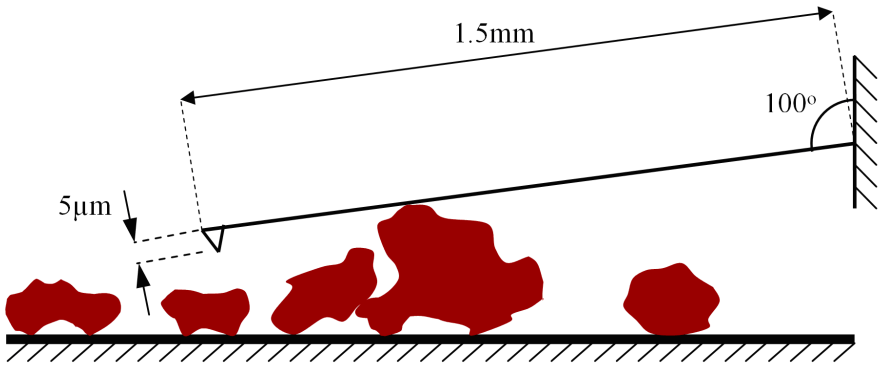


Figure 3.1: Schematic drawing of the cantilever in a field of large particles with the lever causing false contact and the tip still far from touching a surface.

very easily by the side of the tip, especially when scan speeds are $> 10\mu$m/s. This gives poor quality scans, as particles are moved during the scan, sometimes re-scanned again in a different place, but most often are pushed outside the scanning area completely.

In order to image particles with the AFM, a sparse field ($\sim <$ 60000 particles cm^{-2}) of small ($< 10\mu$m) particles is required. This allows individual particles to be scanned without resulting in cantilever or tip contamination, false contact or movement of other particles. Fig. 3.1 shows a schematic of some of the risks involved in AFM scanning with too much sample on the substrate.

Although flat silicon substrates help reduce the loading, results described in Chapter 1 show that flat silicon substrates cannot be relied upon to hold all the particles that are to be gathered for analysis by the optical and atomic force microscopes. Tests show that particles with diameters greater than

150μm are unlikely to adhere to a flat substrate in the vertical orientation due to removal by gravity.

For good AFM imaging it is important that particles do not move during scanning. Controlling the adhesion of particles to the substrates is a major problem. By scanning very slowly or at a lower resolution it is possible not to disturb the target. This is not favourable during Mars operations though, as due to the finite time available for scanning with the AFM, the aim is to perform as many scans as possible at as high resolution as is practicable in the time available. As such, considerably slowing down the scan rate would greatly limit the amount of data returned. As an example of our operational limitations, to perform a 40μm by 40μm sized scan with 512 lines and scanning at 5μm per sec requires significantly more than 120 minutes. (Added to this is also the time of rotating the wheel to the correct position above the sample and then slowly approaching the substrate with the AFM tip, so this overhead on each scan is not negligible.) The Microscopic Imagers (MI) on the MER rovers at times acquire many tens of images per day, whereas we might expect a maximum of 60 AFM images in total during the 90 day mission. It is important to remember that because the MECA AFM images are 3D microscopic images and of much higher resolution than anything before from Mars, they are of a different scale of measurement to previous data. This is a strong case therefore not to reduce resolution. During the mission, the number of scans that can be performed by the AFM per day is highly limited by operating time available for all the instruments, so a balance of all the factors must be maintained in order to maximize the scientific utility of the instrument without compromising the quality of the

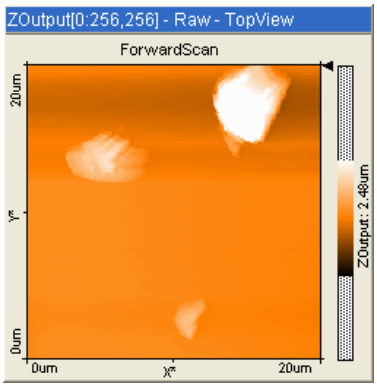


Figure 3.2: A flat Si substrate coated with 1μm of photoresist on which particles of JSC Mars-1 simulant were deposited. Successful scans of particles were achieved with speeds up to 6.5μm/s without any evidence of particle movement.

data; this will be discussed further in Chapter 5.

In a laboratory setting on Earth, a possible solution would be to stick the particles on to the substrate with a careful choice of adhesive. An example of a thin adhesive assisting with this is shown in Fig. 3.2 where particles are stuck down with photoresist which allows successful scanning. However this cannot be done on Mars. Due to the very cold ($\sim -50°$C) surroundings - the kind of temperatures we expect to be operating at during flight - and the dry environment on the Martian surface, adhesive coatings may not be effective as most adhesives lose their adhesive properties at these low temperatures, making them unable to fix particles in place.

Furthermore, even the thin film of water present on Earth is not able to assist on Mars. The adhesion of particles must then rely upon other mechanisms mainly Van der Waals at the very small particle level. These were discussed in detail in Chapter 2.

The magnetic substrates on MECA, although perhaps providing some opportunity for AFM imaging, generally attract piles of particles much too large for AFM imaging. Further to this, the piles are not adequately stable due to the vibration from wheel motion making it unsafe to approach with the AFM. This is further discussed in Chapter 4.

In addition, we expect most, though not all, of the Martian material to be magnetic. So the magnets give a selective representation of the Mars dust, at least for larger particles as for smaller particles other forces are more dominant, as shown in Chapter 2 section 2.2.3.

The silicone substrates - which are essentially a 'sticky' face of silicone rubber - could potentially also be useful to AFM, but would be expected to be of reduced adhesion at Martian temperatures. The PIT and testbed data give an indication of what to expect, and this is discussed in the following two chapters.

In light of these issues, a proposed method to collect targets suitable for AFM imaging was the patterning of substrates with features of a similar size to the particles of interest by etching into a silicon substrate. In the next section the initial tests of small micromachined features are described and their prospect as a solution is demonstrated.

3.2.3 MECA Microscopy Operations

During mission operations the planned procedure for microscopy consists of two days of operation for each sample delivered by the robot arm. These two microscopy days are known as canonical sols A and B; on the first of these days an OM survey of a loaded substrate set is acquired; on sol B having

used the sol A data for target selection - AFM imaging of the chosen targets is performed. These targets are chosen by the science team - principally the geology theme group who will have identified scientifically interesting areas for high resolution scanning, which are also safe for the AFM.

3.3 Tests of Preliminary Designs

In order to understand how particles behaved, various substrates of different topography were created. This led to particular custom-designed substrates to prepare samples adequately for successful microscopy on the Mars mission.

3.3.1 Experimental Methods

All the materials used for the testing described in this chapter, including the substrates, were dehydrated in an oven at 150°C for at least 1 hour before use. A clean silicon substrate was used for each test. To simulate the mechanical handling of the robot arm delivering the sample to the MECA substrates, the samples were dropped with a spatula from a small height (2-3cm) under normal laboratory conditions. This resulted in a pile of material a few millimetres high on the substrate. The quantity of material was sufficient to cover the substrate completely. Material was not pressed onto the substrate. The substrate was then turned through 90° to simulate the vertical imaging position of the substrates on the SWTS while the samples will be analysed with the microscopes. Any loose material was allowed to fall off the perimeter of the substrate. For these preliminary tests, the sub-

strates were returned to the horizontal position for analysis, with the notion that the remaining particles are the same as those available for analysis had the substrate remained in place in the vertical position.

The configuration for these initial tests differs from the conditions and procedures expected during the Phoenix mission in three important ways.

First, these preliminary tests were performed under normal room temperature and humidity conditions. Although the material was dehydrated, it will have been damper than is expected on Mars. Also the adsorbed water layers on the silicon and particle surfaces will have led to increased adhesion. It was discussed in Chapter 2 that relative humidities of even trace amounts of water in the air increase the adhesion of particles (Israelachvili, 1992).

The second way these experiments differed from the actual conditions during the mission is the absence of the scraper blade that removes all material greater than 200μm above the substrate while the SWTS is brought into the MECA enclosure for imaging as detailed in Chapter 1. As this blade removes the large particles, it pushes towards a smaller size range. Larger particles often form larger aggregates which pry themselves off the substrate surface under their own weight when the substrate is rotated through 90°.

The materials in these experiments have the vast majority of particle sizes below 200μm, so not much abrasion should be expected while the SWTS is brought in under the blade; thus the primary mode for depopulation of the substrates will be during tilting.

Both the higher humidity and the lack of scraping indicate that the loading of the substrate observed is likely to be an upper limit for these materials, i.e. under flight conditions more material would be expected to

fall off the substrates while they move under the blade and are tilted to vertical.

The final difference between this experiment and the conditions during mission is the reduced Martian gravity, g_{mars}. This will allow larger particles to adhere during tilting of the substrates to the vertical. For a spherical particle of radius r and density ρ the shear moment acting against the adhesive moment is $\frac{4}{3}\pi r^4 \rho g_{\text{mars}}$, hence Martian gravity has the effect of increasing the radius of the largest particles that will adhere to the substrate by a factor of $(g/g_{\text{mars}})^{0.25}$ or around 27%. Therefore, although the quantitative particle size distribution is affected by the difference in gravity, we would not expect the loading of the substrates to be much increased due to this factor alone unless the Martian material has a very narrow particle size distribution.

These factors mean the initial tests can only be taken as a qualitative analysis of the size distribution and number of particles.

Finally, to try to understand the effect of laboratory humidity on the adhesion of particles to substrates, dried samples were compared to those with normal laboratory humidity. As before, dust was dried by placing in the oven at 150°C for at least 1 hour. The dried and undried samples were placed on flat silicon substrates and rotated though 90°. This was repeated with substrates that had not been dehydrated. The particles retained were compared under an optical microscope.

3.3.2 Experimental Materials

The features designed to hold the samples were loaded with a range of loose particles of various materials, with differently sized and shaped particles,

concentrating on those similar to those expected on Mars. Since no sample-return missions have been achieved thus far, three Martian soil simulants were employed in the form of JSC Mars-1, aluminium oxide particles and Diatomaceous Earth. Small samples of each are shown in Fig. 3.3.

JSC Mars-1 is a simulant used for terrestrial studies that aim to evaluate the suitability of Martian soil for materials processing (Allen et al., 1998a). While closely matching the reflectance spectrum, the material is a favourable and prevalent simulant as it also approximates the mineralogy, chemical composition, grain size, density, porosity and magnetic properties of Martian soil (Allen et al., 1998b). JSC Mars-1 is an altered volcanic ash from Puu Nene cinder cone on the Island of Hawaii (Mauna Kea). The material is the $<$ 1mm size fraction of a palagonitic tephra of basaltic composition, taken from the tephra layer 1 metre beneath the organic layer. The fresh tephra is altered to palagonite via dissolution, oxidation and addition of water. It has undergone passive enrichment, not by transport. The chief chemical composition of JSC-1 is silica 43.5%, alumina 23.3% and iron oxide 15.6%. Si_20_3, Al_20_3 and Fe_20_3. The material ranges in size from $\sim 1\mu$m to 1mm and does not stick well to flat silicon; after rotating a substrate through 90°, most of the material fell off leaving only a sparse field of $\sim$ 3000 particles cm^{-2}.

Diatomaceous Earth is a naturally occurring, soft, chalk-like sedimentary rock composed of the microscopic skeletal remains of diatoms (Dolley, 2001; Survey). It is a type of hard-shelled algae and is easily crumbled into a fine white to off-white powder, with particles mainly in the micrometre size range. It is mined mainly for use as abrasive polishing material or for filters

(Kogel; Fulton, 2000). When placed on flat silicon and turned through 90°, $\sim$ 20% of the sample remains adhered, though the distribution of this remaining sample is very irregular, often with a fine spread. The typical chemical composition of Diatomaceous Earth is 86% silica, 5% sodium, 3% magnesium and 2% iron. The Diatomaceous Earth was supplied by Carolina Biological Supply Company.

In addition, two aluminium oxide samples were used: one larger and one finer grained. The first sample of Al_20_3 powder was in the size range 5-50μm, and is of unknown provenance. After depositing on a substrate and tilting by 90°, $\sim$ 50% (<100000 particles cm^{-2}) of the sample remained. The other sample of Al_20_3 powder was $< 10\mu$m, 99.7%, supplied by Sigma-Aldrich (Sigma Aldrich, date accessed: March 2008). This finer sample had a coverage of $\sim$ 30% on flat silicon, but often in large clumps. Fine particles are left behind where large clumps have fallen away.

3.3.3 The OM and AFM Scanning System

The micromachined designs were first investigated using an optical microscope with a 6$\times$ magnification - similar to that of the Phoenix microscope. SEM images also provided a means of studying the adhesion patterns of the particles on a higher magnification scale, often examining areas of interest that were subsequently studied with the AFM.

For initial testing with an AFM a commercial system called the Nanosurf EasyScan was used. The EasyScan and the Mars AFM have common scanning systems - including similar scanning mechanisms and limits - and common software control. However, unlike the Mars AFM, the Easyscan system



(a) (b)

(c) (d)

Figure 3.3: Small samples of (a) JSC Mars-1, (b) Diatomaceous Earth, (c) aluminium oxide 5-50μm and (d) aluminium oxide $< 10\mu$m, 99.7%.

does not have an inbuilt optical microscope, hence a stand-alone OM was required.

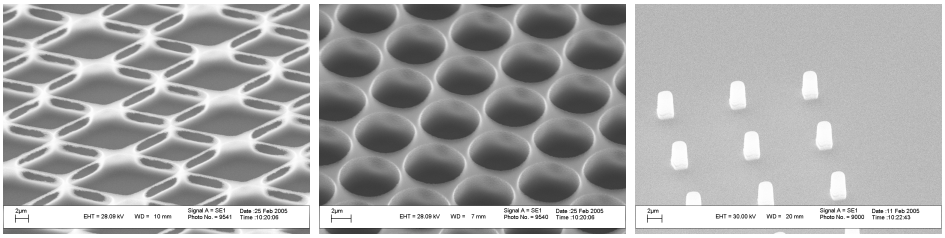
The Mars AFM cantilevers are inclined at 10° in two dimensions relative to the surface. The levers used here were silicon tip cantilevers from Nanoworld sensors type (PPP-NCLR) with the following average dimensions: length 225μm, width 38μm, thickness 7μm and tip height 10-15μm. These were inclined 10° at only one dimension. The Mars AFM lever dimensions are the same apart from a tip height of 5μm.

An important difference in the properties of the levers is that the tip on the Mars cantilevers is much smaller, meaning that the Mars levers are more limited in the aspect ratio of the topography they can image.

All AFM images were taken in dynamic mode. The Mars AFM dynamic mode is different to that of the EasyScan system as it operates under frequency modulation rather than amplitude modulation, as used by the Easyscan. This means that the setpoint defines a shift in resonant frequency, rather than a change in oscillation amplitude. For the Easyscan, the scanning conditions used deviated insignificantly from speeds of 5μm per second and setpoint of 60% with a tip amplitude of 1V. The Mars AFM uses frequency modulation when operating in dynamic mode, whereas the EasyScan uses amplitude modulation since it is not operated in a vacuum. This point was discussed in Chapter 2 Section 2.4.4.

3.3.4 Designs Investigated

RIE and Deep reactive ion etching (DRIE) was used to create substrates with a range of topographies in order to trap particles and to mitigate the problem of poor particle adhesion for AFM scanning. A variety of aspect ratios and geometries, consisting of both regular and irregular shapes, were tested, some of which are shown in Fig. 3.4, each having different effects.



(a) (b) (c)

Figure 3.4: SEM images of various Reactive Ion Etched patterns on silicon substrates. (a) An array of rhombuses, (b) 5μm diameter pits and (c) 2μm pillars at 10μm spacing. Etch depth 4μm.

3.3.5 Results and Discussion

The etched patterns that proved most effective and appropriate for the MECA setup were regular patterns of pits and pillars. Each of the test materials behaved in different ways on the etched features, but the pits and pillars had the greatest ability to manage and regulate the material. The more irregular shapes proved not as effective because their results were more variable.

Sorting of Particles

It was at once clear that closely-spaced pits had the ability to filter particles; areas with etched pits demonstrated reduced loading, particularly of larger particles. After turning the substrate through 90°, most particles larger than the size of the features fell away. Some stayed, but overall on the etched region there were significantly fewer particles larger than the feature size. These results are shown in Fig. 3.5.

This observation was most significant for the large Al_20_3. However, each material responded differently to the features. Mars JSC-1 does not adhere well to flat silicon, so a reduction in the number of particles on an etched region was not obvious. Diatomaceous Earth is sufficiently irregular so as to stick everywhere - even areas etched with pit features. The finer Al_20_3 showed some increased adhesion on pillars, but often stuck in clumps spread over the entire substrate, although at times the areas where the clumps fell away were exactly where a pattern of pits was etched into the silicon, further demonstrating how pits might help to make areas scannable with the AFM.

To demonstrate clearly the interaction of the pits with the large Al_20_3 particles, Fig. 3.6 depicts material loaded over two regions: flat silicon and etched features of 10μm pits.

The much lower loading and smaller particle size of the material on the closely spaced 10μm pits is apparent. By looking in more detail at the effect of the pits, it was discovered that particles appeared either to fall into the pit if their diameters were identical to or smaller than that of pit, or - if their diameters were larger - then they fell off altogether due to the reduced

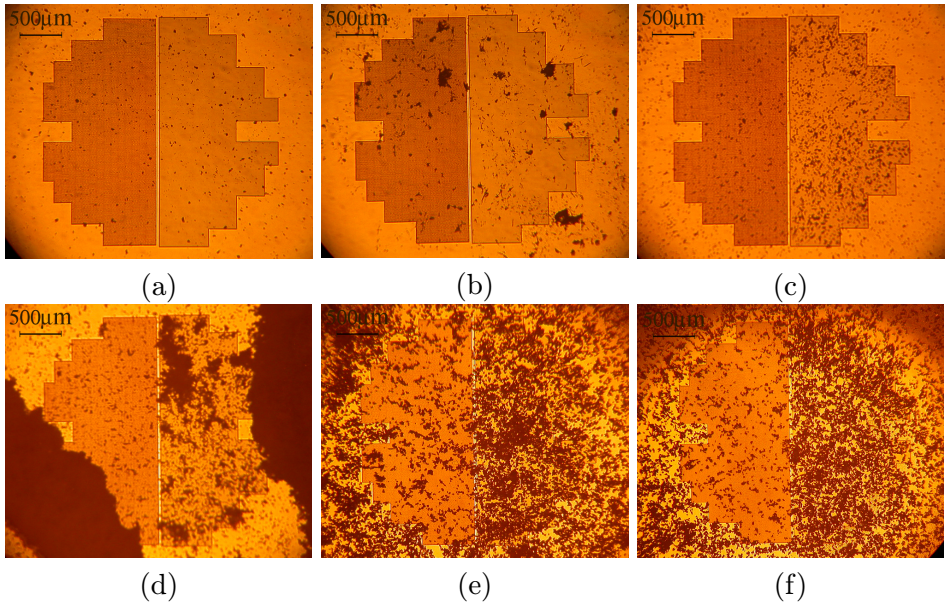
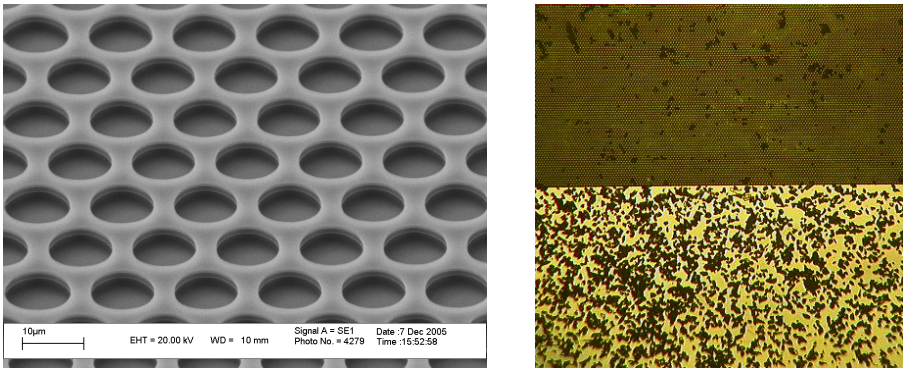


Figure 3.5: Various samples on a substrate of pits (left shaded semi-circle), pillars (right shaded semi-circle) and blank silicon (light bachground). (a) JSC Mars-1, (b) Diatomaceous Earth, (c) and (d) aluminium oxide $< 10\mu$m, 99.7% and (e) and (f) aluminium oxide 5-50μm.



(a) (b)

Figure 3.6: (a) An SEM micrograph of a substrate at a 45° angle of closely spaced 10μm circular pits at 14μm pitch, etched 3μm in deep in silicon. (b) An optical image of Al_20_3 larger 5-50μm particles on an array of these same 10μm closely spaced pits showing the reduced adhesion of particles on the etched area (top half of image) compared to flat silicon (lower half of image), showing pits provide a sparsely populated region of particles more suitable for AFM scanning.

top surface area to which they could adhere.

Particle Density Statistics

Table 3.1 summarizes the effect of the pits on adhesion of the different materials, showing the rough size distribution observed after tilting through 90°.

On the etched pits, the remaining particles are sufficiently small and sparsely distributed - closer to the desired $\sim$ <60000 particles cm^{-2} - so that it is possible to attempt scanning with the AFM. This demonstrates how the pits could be very useful for samples that would otherwise have too many particles on the substrate for safe AFM operation.

Material	Substrate	
	Flat Silicon	Pits
JSC Mars-1	< 3000 particles cm^{-2} Sparse	< 3000 particles cm^{-2} The field on flat silicon is so sparse that there is little difference in the loading.
Diatomaceous Earth	$\sim 20\%$ (< 40000 particles cm^{-2}) Irregular	$\sim 20\%$ (< 40000 particles cm^{-2}) Irregular
Al_20_3 powder 5-50μm	$\sim 50\%$ (< 100000 particles cm^{-2})	$\sim 5\%$ (< 10000 particles cm^{-2})
Al_20_3 powder $< 10\mu$m, 99.7%	$\sim 40\%$ (< 200000 particles cm^{-2}) Overall coverage due to clumping of material. $\sim 20\%$ (< 100000 particles cm^{-2}) In areas where clumps had fallen away.	Irregular loading due to clumping. A small reduction on average observed in areas where clumps had fallen away: $\sim 15\%$ (< 75000 particles cm^{-2})

Table 3.1: Summary of the effect of etched pits on the adhesion of different materials.

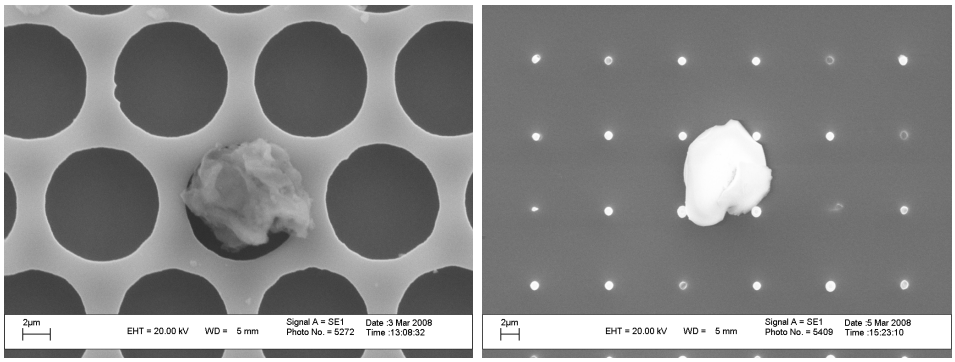
Gripping of Particles

Pillars demonstrated a different way of controlling the adhesion of particles than did pits. Pillars helped with the overall gripping and adhesion of particles, often helping more material stick. As with the pits, pillars also had the tendency of holding down individual particles and preventing them from moving during scanning, but this applied at all shapes and sizes of particles and to all materials.

It was found that the aspect ratio of depth of etch to the size of the particle was important. An appropriate ratio ensures that the particles of interest are not hidden or distorted but are gripped enough for scanning with the AFM cantilever. It was favourable for the particle to be gripped with the top half protruding above the surface of the etched features, so the particle surface could be approached with the AFM without touching the features. In general an aspect ratio of 2:1 was found to be effective. This meant the features were deep enough to grip but allowed the particles to be

imaged by the AFM.

This is particularly important for particles of sizes smaller than 10μm, shown trapped in Fig. 3.7, as they are of a size such that the whole particle can be imaged by the AFM. The pits were likewise good for trapping and holding for AFM and preventing particles being moved by lateral forces from the tip.

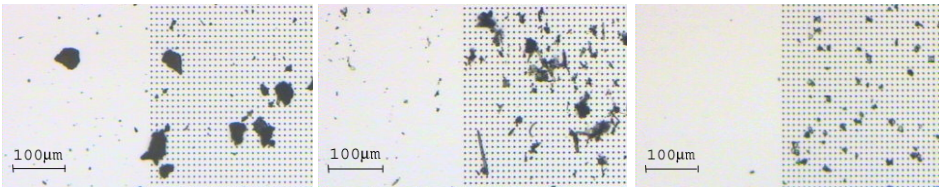


(a) (b)

Figure 3.7: SEM micrographs of (a) a particle of JSC Mars-1 immobilized in a 5μm diameter, 7μm pitch pit with 5μm depth, and (b) a particle of the finer $< 10\mu$m Al_20_3 wedged between 1μm diameter, 8μm pitch pillars with 5μm height.

Pillars are also good for improving general adhesion, including large particles (up to 200μm in the case of the MECA microscopy station) which would otherwise fall off the flat silicon - even under reduced Martian gravity - when turned through 90° due to their own weight.

The optical micrographs of Fig. 3.5 show clearly how the adhesion of Al_20_3 larger 5-50μm particles is increased - see the previous section. Fig. 3.8 shows increased adhesion of other materials to the etched region compared to flat silicon.



(a) (b) (c)

Figure 3.8: Optical micrograph of 4μm diameter etched silicon pillars with 10μm pitch and 5μm height showing increased adhesion of particles in the patterned regions due to the gripping action of the pillar structures.

It can be concluded that the pillars - which are etched in the opposite areas to pits - behave in exactly the opposite manner to pits, with etched regions holding more large particles than does flat silicon.

With irregular samples - such as Diatomaceous Earth - the particles are often aligned with the directions of the pillars. We can see many examples of this in figure Fig. 3.9. The reason the particles align is likely to be due to these particles being best gripped by the patterned substrate. These were therefore the most strongly held in place and the most likely to remain once the substrate has been turned. They will therefore be good potential candidates for AFM scanning and they may be the most stable and least likely to move during scanning.

AFM Imaging of Small Particles

Pits and pillars allow a wide range of particle sizes to be collected and immobilised. This therefore provides better targets for AFM scanning, offering the next level of detail.

The 5-50μm micron-sized Al_20_3 particles best demonstrate how the pits

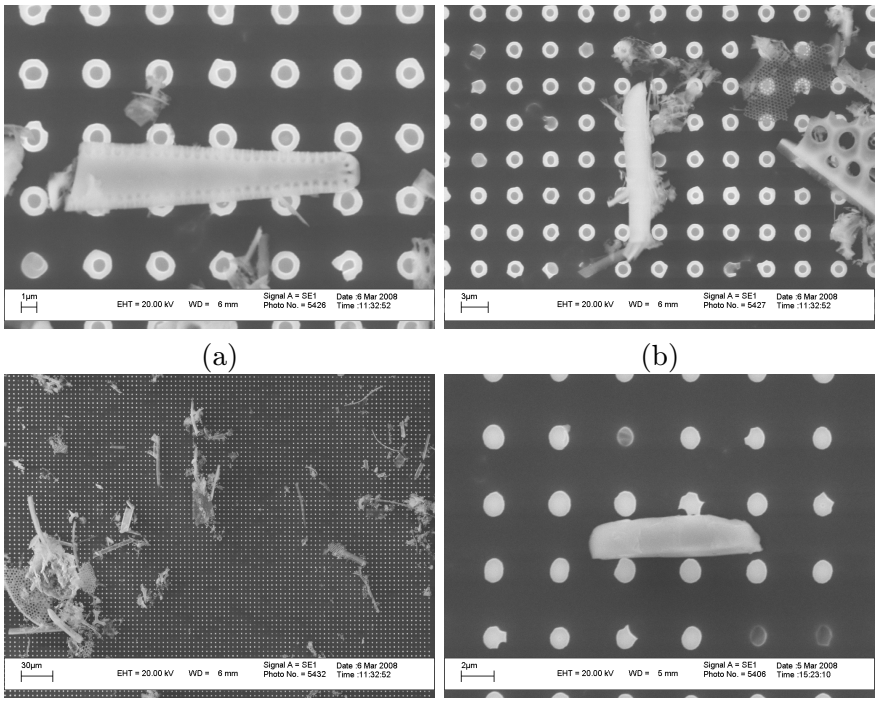
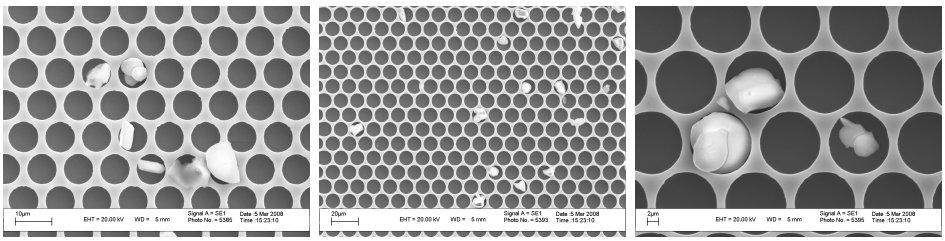


Figure 3.9: (a) - (c) are SEM scans at various magnifications of Diatomaceous Earth on 4μm and 2μm spaced pillars. (d) is an SEM scan of a long Al_20_3 particle on 4μm pillars. These images demonstrate how successfully the pillars collect irregular shaped particles and that the particles often align with the pattern because this is the position in which they are best 'gripped'.

and pillars operate usefully on a sample overall. However, on a smaller scale, the SEM shows how the materials arrange themselves on an individual particle scale.

When looking at the finer $< 10\mu$m Al_20_3 particles, there are large clumps in some areas as seen in the optical image of Fig. 3.5(d). In areas where the large clumps fell away, only fine particles were left. Of what is left, it is evident that a large selection of particles lodged in pits and that these would be suitable for scanning, as we can see in Fig. 3.10.



(a) (b) (c)

Figure 3.10: SEM images of Al_20_3 on 10μm and 12μm pits. Small particles have fallen into pits and are available for scanning.

The AFM has a 13.8μm max z-range. In the context used here, 'small' describes particles of 10μm and smaller; those that can be easily scanned by the AFM in their entirety. Closely spaced pits provided the most opportunities for the AFM to scan such small particles by: (i) collecting such particles, (ii) ensuring the area around them is free of obstructions in the form of large particles and, (iii) immobilizing the target particles so that they are not moved when subjected to the lateral force from the scanning tip. A number of suitable targets have been observed as we see in Fig. 3.11.

A demonstration of the pits holding particles for AFM scanning is shown

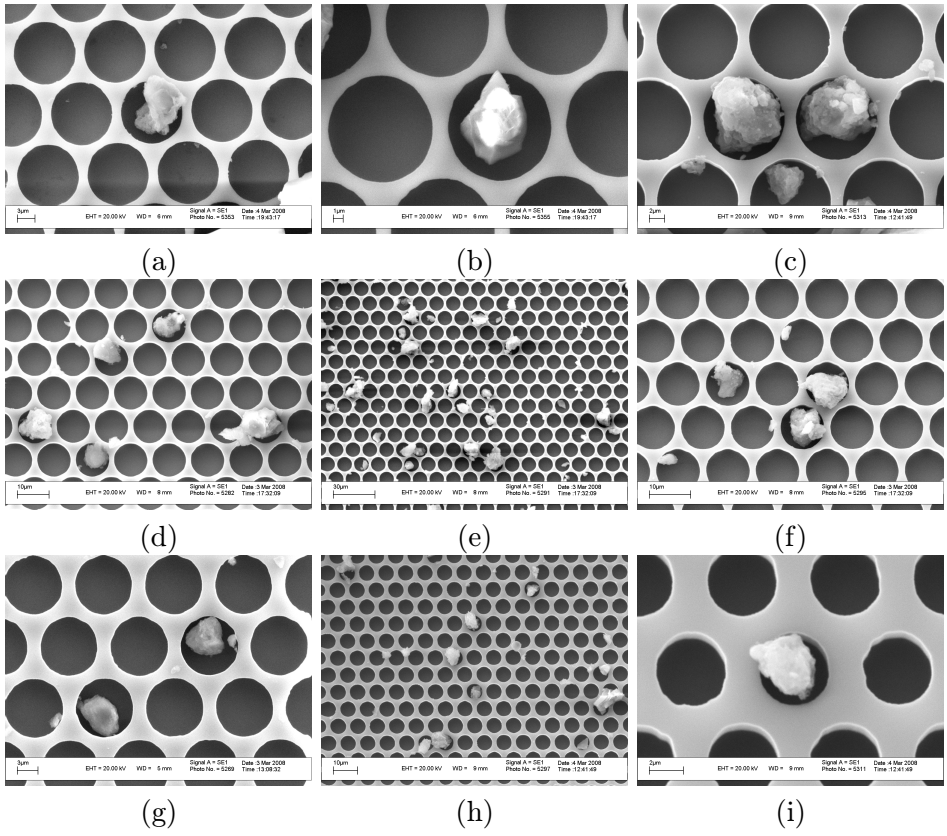
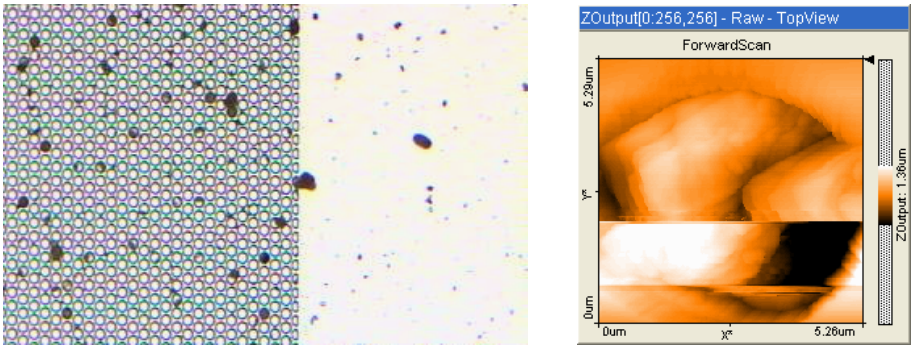


Figure 3.11: SEM images of (a) - (b) Al_20_3 5-50μm on 10μm pits and (c)-(i) JSC Mars-1 particles in 10, 8, 6 and 4μm pits. Small particles have fallen into pits and are available for scanning.

in Fig. 3.12. An etched region of 5μm pits covered in JSC Mars-1 particles was viewed by an optical microscope - as seen in Fig. 3.12(a) and an AFM scan of a particle in and around one of the pits performed - Fig. 3.12(b). The scan was performed from the top of the image downwards at a low speed of 1.5μm/s. First the particle held firmly in the pit is viewed, then the particle perched on the top surface comes into view. Roughly halfway through the scan this particle on the surface appears to be moved by the lateral force from the tip, and rescanned in a new position, until finally, near the end of the scan, the tip pushed the particle away altogether. This shows very well how pits are able to pin down particles firmly enough to be scanned by an AFM and evade being shifted by the tip.



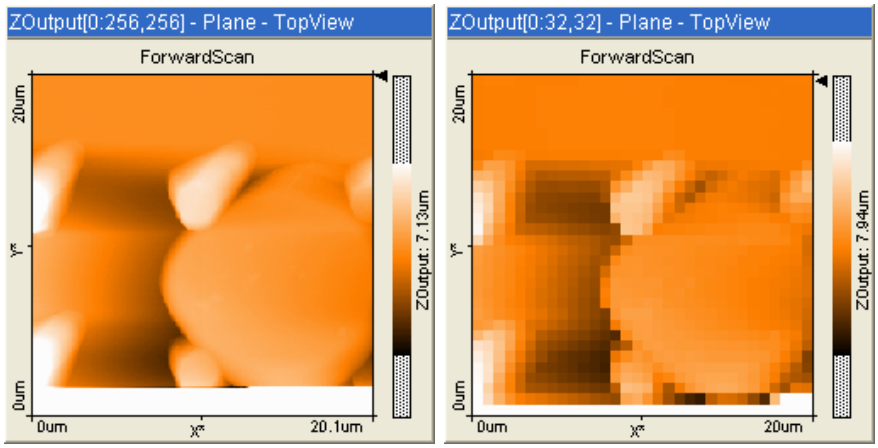
(a) (b)

Figure 3.12: (a) An optical micrograph of an area of 5μm pits covered in JSC Mars-1 particles. (b) An AFM scan of a particle in, and a particle sat on top of, one of the pits. The dashed line shown aids to outline the pit. The scan direction for the image was from the top downwards. Whilst the particle within the pit is immobilized, the particle perched on top of the pit is moved easily and repeatedly by the scanning tip. Remembering the 4μm per pixel resolution of the MECA OM, a 10μm particle would be almost invisible at this scale.

Fig. 3.13 shows a particle of JSC Mars-1 gripped by 5μm tall 10μm pitch pillars making it possible to scan it with an AFM. The scan shows the particle to have a 14μm diameter, 7μm height and a fairly smooth surface. Despite a scan speed of 7μm/s - relatively fast - the particle still does not move, suggesting the particle is tightly held in place. Towards the end of the 20μm downward scan, a large particle - larger than 14μm - is encountered by the cantilever and the scanner becomes out of range. This was confirmed by a subsequent scan performed at a lower resolution of 32 lines per scan and further inspection under an optical microscope. This demonstrates well the ability of the AFM to scan particles held in place and within the scan range, and the importance of creating fields of particles within this range for the AFM. Moreover, particles which are 10μm or smaller would be barely visible with the OM which has a resolution limit 4μm per pixel.

AFM Imaging of Larger Particles

All AFM systems - due to their high resolution - are limited in their scan range. The Phoenix AFM and the Easyscan have a relatively large height range of 13.8μm, which is larger than some even higher resolution AFMs which can sometimes only image a 2μm range (Agilent Technologies, date accessed: May 2008; Veeco, date accessed: May 2008; Nanosurf, date accessed: March 2008; Advanced Surface Microscopy, date accessed: July 2008). This limit in range means that large particles cannot be imaged in their entirety. It is however still interesting to see their surface structure close-up. This is useful as it can give information on weathering processes (Aeolian or water) or transport history as described by Kempe *et al* (Kempe et al., 2004).



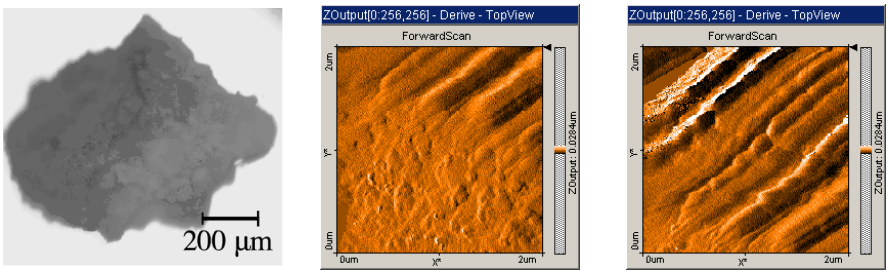
(a) (b)

Figure 3.13: (a) A JSC Mars-1 particle trapped between 10μm spaced pillars. The scan direction is top to bottom and appears to drop out at the end of the scan as the cantilever encounters a large particle causing the scanner to go out of range. (b) A re-scan of the same area performed directly after the first scan and at the same speed. For both scans the scan direction was up.

The information obtained from imaging parts of larger particles in detail can be combined with data from OM images to help collect information on dust and soil particle sizes, shapes and weathering processes.

Fig. 3.14 shows an example of the detail of the surface of a large particle where an AFM scan 2μm $\times$ 2μm of a 1mm particle may be seen. An area was selected for scanning from the optical micrograph. The OM image gives little indication or hint of the texture of the surface itself as it is limited by the 4μm per pixel resolution and also by the depth of focus which is restricted by the high magnification of the microscope. The AFM scan however shows a high level of the fine detail over a very small 2μm by 2μm area. The surface texture can be observed to the level that the surface

roughness was measured at 200nm. As a first inspection of these features they can be assessed together with the OM image to provide contextual data. The combination of the optical and the AFM images in this figure suitably demonstrates the complementary capabilities of these two microscopes in imaging from the millimetre down to the nanometre scale.



(a) (b) (c)

Figure 3.14: (a) An Optical microscope image of a 1mm particle at the high magnification of 4μm per pixel - the same resolution as that of the MECA OM. The optical microscope is unable to resolve the finest features on the surface of the large particle. (b) and (c) are a 2μm by 2μm scan of the 1mm particle from the AFM showing the derivative of the topography image demonstrating the fine structure that is resolvable for particles. This is a good example where the AFM can give us a much better insight into the texture and therefore history of the particle.

Adhesion due to Humidity and Electrostatic Charging

Consistent with previous studies (Jones et al., 2002), preliminary experiments on the effect of adsorbed water on the samples and substrates suggested - albeit qualitatively - that the adhesion of the sample to the substrate is enhanced by the presence of adsorbed water.

Samples and flat silicon substrates dried in the oven at 150°C were tested with undried sets. Substrates dried prior to deposition of a dried sample re-

tained the fewest number of particles, especially in the larger (<100μm) range. In this case of a dried samples and substrates, triboelectric charging of the particles might be expected to lead to electrostatic effects that enhance adhesion between particles and substrates. However the above experiments show that dry samples appear to hold fewer particles than damp ones, suggesting any effect of electrostatics in assisting adhesion is probably weaker than that of surface tension. As discussed in Chapter 2, it is not expected that capillary forces will be present on the cold dry atmosphere of Mars, however triboelectric charging is expected to be significant (Gross et al., 2001; Merrison et al., 2004).

Chapter 4 describes further experiments using the MECA microscopy testbed at Imperial, which simulates the low humidity, pressure and temperature environment of Mars. This provided a better understanding of the adhesion mechanisms that dominate between the particles and substrates and also particles and AFM tips.

3.3.6 Conclusions from Initial Tests

In summary, the initial findings have shown that sample preparation for the Phoenix microscopy station is essential to guarantee return of useful scientific data. Flat silicon, having been turned through 90° to the imaging position of the substrates on Phoenix, holds a very sparse field of unstable particles. Highly adhesive substrates hold too much material for the AFM to scan safely. Further, in the case of the Phoenix mission, chemical adhesives are not appropriate as most are unable to remain pliable at the low temperatures on Mars.

The initial tests have demonstrated that micromachined pre-patterned silicon substrates with high aspect ratio topography allow substantial control of the sample arrangement and are useful in both sorting and fixing particles in place, making it possible to study sand-like material with large aspect ratios with an AFM. The AFM has been shown to be versatile in imaging micron-sized particles in their entirety as well as areas of detailed surface texture on larger particles. Thus the combination of optical and atomic force microscopy allows observation of particle features from the millimetre to the nanometre scale, and will help provide more clues about the history of water and ice on and below the Martian surface.

The general concepts learned from these initial tests were then applied to the design and fabrication of the Phoenix MECA flight substrates. By considering the difficulties in scanning that were experienced during these tests, as well as looking at what did and did not work successfully in terms of adhesion to the substrate and sorting, an optimised set of features were produced for the Mars-AFM.

3.4 Final Design for Flight Substrates

3.4.1 Substrates for MECA

In the design for the Phoenix Mars microscopy station, the substrates are 2.9mm diameter round silicon disks that hold the material for scanning. The optical microscope (OM) has a field of view of 2 $\times$ 1mm, so three side by side images are required to see an entire substrate (it should be noted that the OM has no vertical positioning movement), as shown in Fig. 3.15. The

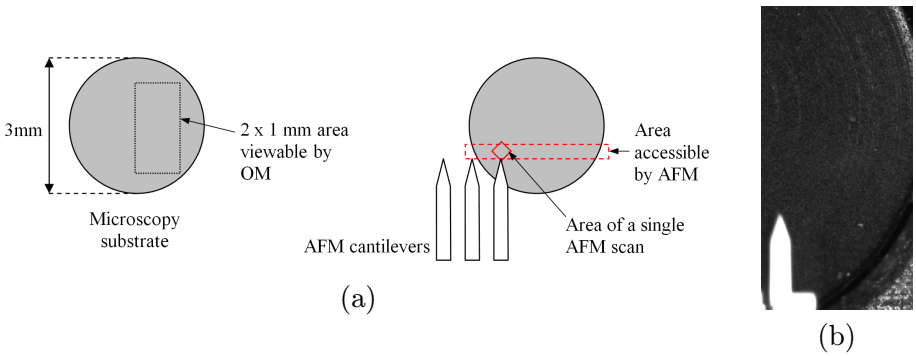


Figure 3.15: Schematic showing the substrate area that the OM can view and the area the AFM can view. (b) an OM image from the testbed showing with the AFM strip drawn in red.

resolution of the MECA-OM is 4μm per pixel.

Each patterned substrate was used as part of a set of six substrates on which a single sample was analysed. It is important to be consistent between samples and not bias the sample collected on any particular set by using different designs of micromachined feature to collect the particles. However, it was observed that different features were useful for different purposes and these can be used for gripping and sorting of a particular size of particle. Therefore it would be useful to use more than one design of feature - each to serve a different purpose - for each of the samples collected. Therefore a number of feature designs were incorporated onto each substrate.

3.4.2 MECA Substrate Design

Features were chosen based on results from the last section which showed that closely spaced pits were effective in both reducing the number of larger particles and gripping smaller ones while pillars helped generally with the

Design	Description	Purpose
5μm pits	5μm diameter pits, 8μm pitch, close-packed arrangement.	- To reduce surface area on top of substrate for large particles to adhere to. close-packed arrangement. - Good for immobilizing particles for scanning e.g. airfall samples.
20μm pits	20μm diameter pits, 24μm pitch, close-packed arrangement.	- To reduce surface area on top of substrate for large particles to adhere to. - To trap and immobilize particles with sizes within the range of authority of the AFM.
5μm pillars	3μm pillars, 8μm pitch, square arrangement.	- Increase general adhesion for particles with limited adhesivity. - To trap particles, including those irregularly shaped, and immobilize them for scanning.
20μm pillars	3μm pillars, 23μm pitch, square arrangement.	- Traps a range of particle sizes and wedges them in place as the wheel rotates. - To trap particles, including those irregularly shaped, and immobilize them for scanning.
Tear drops	Teardrops.	- To catch particles of various sizes that may be of interest and immobilize them for scanning.

Table 3.2: Substrate design philosophy. Each pattern is designed with a different purpose aiding microscopy. N.B the designs were named in accordance with the spacing into which particles fell.

gripping of particles of all sizes. The limit to how small and closely spaced our features were was mainly determined by the resolution of the mask printing. The limit in depth of the features was governed by the size of the AFM tip - which is a little over 4μm.

While it was necessary to incorporate a variety of the designs it was also important to get a substantial enough coverage of each on the substrate. In order to do this, four main strips each of a different pattern were chosen. To determine which patterns to use, it was necessary to consider which particles we would most like to image with the AFM within the operating constraints mentioned earlier and, of course, which would be of the highest geological interest. Table 3.2 shows the final designs chosen with a brief description of their intention.

For good AFM images particles up to 13.8μm tall can be scanned. Particles of 5μm and below are of interest but need to be stabilized for scanning. Therefore to provide the best opportunities for safe AFM scanning of such

particles, 5μm pits were chosen with the intention of catching particles 5μm and smaller in a safe region with few large particles.

20μm pits were chosen to trap particles of 20μm and smaller. These particles would stick out above the pit in order that the AFM could image them - quite possibly in their entirety - as this is still within the aptitude of the AFM.

5μm and 20μm pillars would increase the adhesion of materials which did not adhere well to flat silicon - as we found with sample such as JSC-1 and also trap particles with irregular shapes. The 5um pillars particularly would also trap particles holding them in place for AFM scanning.

On either side of the strips an additional feature was incorporated named here as 'teardrops'. These were an addition, thought to aid by generally trapping particles of interest of various sizes. Though not the primary target area, they may provide interesting targets that the other features do not catch.

The diagram of the mask used for micromachining the substrates in Fig. 3.16, shows the arrangement of the features on the substrate.

On the mask the light grey area in the figure is that which undergoes a shallow etch (often 5μm) to produce the features. Note that the pillars protrude from the (new) surface of the flat silicon, whereas the base of the pits is at the same level as the flat silicon, so pit features are produced by small raised walls on the substrate. On the mask may be seen a ring around the substrate; this is where a through-wafer etch is performed and this 40μm wide trench is used to release the substrates from the rest of the wafer. The outer diameter of the trench is 2.98mm, and the inner diameter is 2.90mm.

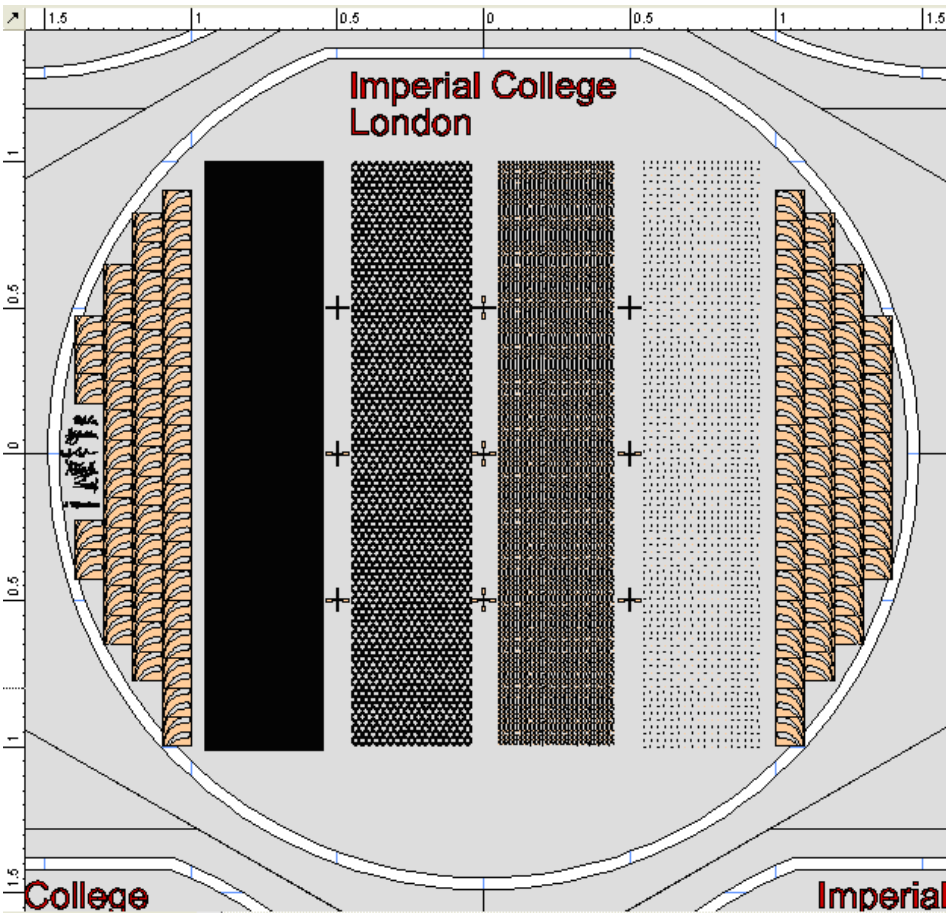


Figure 3.16: VectorWorks CAD file of the mask design for the Mars substrate showing its layout. All dimensions are in mm. The final mask itself contained around 300 substrates allowing them to be produced on a large scale for later testing. They were arranged in a honeycomb formation. The edge of some of the other substrates can be seen in this figure. There are four main central strips approximately 400μm wide of different designs of pits and pillars in the range of 2 to 20 micrometers in diameter. In addition the teardrop features on the extreme left and right trap particles of various sizes that may be of interest.

The large crosses between the strips were included as fiducial markers which are easily visible in the OM. Some flat silicon was left around the strips to allow comparison of adhesion to that on the features and other substrates. And finally, the small features on the left of the substrate seen among the teardrops are signatures of group members who helped out with the substrate fabrication.

As all the features are on the same piece of silicon substrate, and since the tips in the Mars AFM are only 4μm high, all the features on the substrate have been etched to the same depth of 5μm.

3.4.3 Digital Code

The resolution of the optical microscope is 4μm per pixel and with this it should be possible to see the individual patterns on the substrate except the very smallest ones. The AFM has a maximum field of view of $40 \times 40\mu$m and can see well below the resolution required to distinguish the individual pattern markings.

The masks used to transfer the patterns to the silicon wafer were drawn using the program Vectorworks (Vectorworks, date accessed: April 2008), and manufactured by Delta Mask (Co., date accessed: March 2008) who are able to laser print masks to a 1.5μm resolution limit.

In the initial designs the substrates had regular patterns over the etched regions. The patterns were only irregular if the edges of the patterned areas were scanned. With this design, it was not possible to register the position of each AFM scan on the optical image by looking at the AFM image alone. The challenge therefore was to design a way to determine the exact position

on the substrate, using information from the AFM scan alone to eliminate the necessity for comparative analysis with an optical image. Although the OM image will usually be available, this check can be time consuming and often difficult due to the difference in resolution.

In order that the markings are effective, at least one position marker should appear within every $40 \times 40\mu$m scan area, which is the maximum scan range of the AFM. This creates a system for recognising the scan area using *in-situ* registration marks. In order to ensure that at least one mark appears in each $40 \times 40\mu$m scan, the code must have a periodicity of 40μm or less. This is relatively frequent considering that the etched features themselves have a periodicity of between 8μm and 24μm. Hence, care should be taken to ensure the code markings are small, similar in size to the original marking, so as not to disrupt the functioning pattern on the substrate. The markings also need to be simple, regular and logical. The approach to achieving these requirements was to use a digital code across the substrate giving a form of numbering to the position.

The design ensured minimal disturbance to the pattern design, but was still within the lithographic resolution. Moreover, the design is useable even if the code markings are only partially on the scan e.g half of one marking showing on the right of the scan and part of another towards the left of the scan.

The code was designed to replace or partly displace one or a number of pits or pillars of the individual pattern on each $40 \times 40\mu$m area of substrate. A different design was created for each substrate pattern. It took into account the spacing of the markings on each pattern and the area available to

create a code marking.

The code varies horizontally across the substrate, not vertically down. This helps to determine the horizontal position of the scan but not the vertical because the vertical position of the AFM (and the OM) relative to the wheel is fixed.

The digital code on each marking was designed to be as logical and intuitive to read as possible. The position markings were created using a combination of displacements, rotations and changes in the shape of the original markings. The code across the substrate is a form of a binary code using least significant bits (LSB) and most significant bits (MSB).

3.4.4 Detail of Digital Code

Table 3.3 describes the digital code for the 4 strips of pattern. The code markings are made either by changing the position of the markings and not the shape, or replacing a marking with a small shape to give the digital code.

And Fig. 3.17 shows a section from the mask design showing each strip with an example of a position marking.

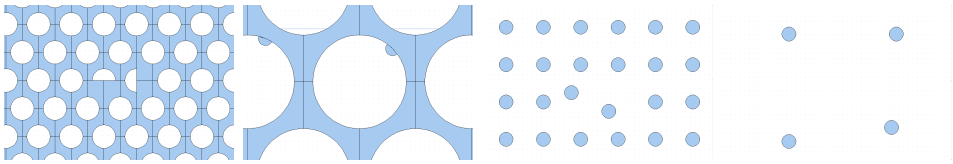


Figure 3.17: Picture from mask detail of each strip showing markings.

The markings on the 20μm pillars have a pitch greater than 40μm, so

Design	Description	Number of markings across the width of the strip	Form of code marking	Description of code
5μm pits	5μm diameter pits, 8μm pitch, close-packed arrangement. Total width of strip 399um.	9 markings in total at 42 micron pitch, starting at distance 31.5um from edge of strip. Vertical pitch 36um.	Two semicircles replace horizontally adjacent two pits. Semicircle has 4 positions at 90^o rotation to each other.	Right semicircle is LSB and left is MSB.
20μm pits	20μm diameter pits, 24μm pitch, close-packed arrangement. Total width of strip 408um.	17 markings at 24 micron pitch, starting at 12um from each edge of the strip. Vertical pitch 40um.	Small notch inside the pit rim at hour positions on a 16-hour clock. First and last marking same at the midnight position.	Notch moves round the rim of the pit clockwise, round like on a clock.
5μm pillars	3μm pillars, 8μm pitch, square arrangement. Total width of strip 392um.	10 markings at 40 micron pitch, starting 28um from right hand edge of strip, finishing 4um from left hand edge Vertical pitch 40um.	Two horizontally adjacent pillars are displaced about their original position (0,0). Each is displaced by $\pm$2um in the x-y plane; position 1 is (-2,2), position 2 (2,2), position 3 (-2,-2) and position 4 (2,-2).	Right semicircle is LSB and left is MSB, and the pillars move from positions 1 to 4.
20μm pillars	3μm pillars, 23μm pitch, square arrangement. Total width of strip 391um.	9 markings at 46 micron pitch, starting 23um from right hand edge of strip, finishing 0um from left hand edge Vertical pitch 46um.	Displaced pillar. 16 positions from original position; first is (-3, 3), next (-1,3) then (1,3) then (3,3) then (-3, 1) then (-1,1) and so on	16 possible positions...

Table 3.3: Description of code marking on each of the 4 different strips of pattern on the substrate.

it is not guaranteed that a marking will be viewed in such a scan. Taking into account the width of the pillars, this means there is a 6.5% chance that the scan will not show a marking horizontally. This design was chosen as it was thought important not to disturb the overall pattern too greatly. Furthermore the 20μm pillars are designed to trap large particles for the AFM to scan a small area of their surface, meaning the substrate surface will not be approached anyhow.

The markings on the other strips all fall within a 40μm pitch.

3.5 Device Fabrication

The AFM samples were made using standard Micro-Electro-Mechanical Systems (MEMS) processing techniques. MEMS are mechanical or electrical sensors and actuators micromachined in silicon using planar processing similar to semiconductor processes such as surface micromachining and bulk micromachining. The devices generally range in size from a micrometre to a millimetre. These devices are fabricated on a wafer surface using compatible micromachining processes that selectively etch away parts of the silicon wafer, or add new structural layers, to form the mechanical and electromechanical devices. The processing involves material deposition, lithography and etching processes.

The fabrication of the Mars silicon substrates requires high aspect ratio micromachining. A variety of processing issues were addressed to develop a recipe that achieved the geometry of the substrates that was required.

The substrates were manufactured from a 100mm n-type 100 single crystal silicon wafer 525μm thick, which required an etch through the entire wafer to release the individual 3mm diameter substrates, whilst maintaining a vertical profile of the sidewalls thus requiring a highly anisotropic etch.

Deep Reactive ion Etching (DRIE) is often used to create microsystems devices (Clerc et al., 1998). The process involves the formation of ions in a gas plasma under low pressure being accelerated by an electric field and physically bombarding the target atoms to remove them. The wafers were etched using a Surface Technology System (STS) Multiplexer ICP DRIE system (Surface Technology Systems plc, date accessed: March 2008).

To achieve an anisotropic etch of silicon, the well established BOSCH process (Laermer and Schilp, 1996) was employed. This achieves its directional etching by alternating between an etching and a passivation cycle, which shields the wafer from further chemical attack. Etching occurs by the bombardment of the ions generated from an SF_6 plasma, and passivation involves the deposition of a monomer produced from the dissociation of the polymer octafluorocyclobutane (C_4F_8).

3.5.1 Creating Substrates

The manufacture of the substrates is a two-mask process for a 100mm silicon wafer. The first mask is used to etch the shallow pattern features on the substrate into the silicon. The second is a through-wafer etch which releases the individual 3mm substrates from the overall silicon wafer. The chart in Fig. 3.18 shows the micromachining processing procedure that was developed. DRIE was used for both the shallow and the through-wafer etch. The etch rate for the system was approximately 2μm/min, hence requiring over four hours to completely etch through the wafer.

Careful processing of the substrates was required throughout the procedure due to the very small features on the mask. Further to delicate handling and keeping the processing very clean, the fine balance between hardening the photoresist enough for DRIE etching and losing resolution of the fine features was considered. A successful recipe was found ultimately producing good features.

The process recipe used to prepare the wafers for etching of the oxide layer is described in Fig. 3.19. The shallow etch uses a thin photoresist and

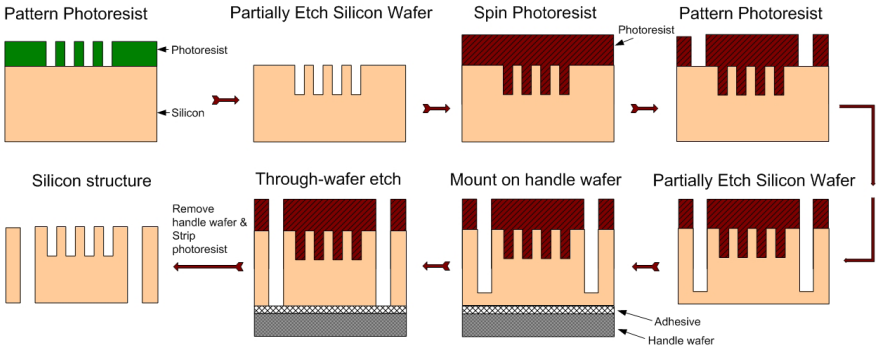


Figure 3.18: The complete etch process flow for fabrication of the MARS AFM substrates.

no hard bake before etching so as to preserve the resolution of the small features. During the through wafer etch, however, the thick photoresist acts as an extra layer shielding the silicon during DRIE processing. It is critical that this layer can withstand the long etch period. An intricate procedure was developed to successfully deposit an adequate thickness. As the substrate outline is a large circle with no fine detail, unlike the patterned features, a thicker photoresist and hardbake can be used. The thick photoresist however requires an overnight sit so as to prevent any bubbling during exposure of the resist to the UV light when patterning the resist. With such a long etch through the wafer, precautions are taken not to burn the resist. The etch passivation cycle employed to ensure vertical etching of the wafer also allows the surface of the resist to cool between etch steps. Other measures include the evaporation of a thin layer of aluminium on the backside of the wafer before etching, and mounting the wafer onto a handle wafer towards the end (last 40 minutes) of the etch.

PROCESS FOR ETCHING THE PATTERN FEATURES

This is the process recipe used to etch the shallow pattern layer:

1.1µm expected thickness S1813 spin, bake, exposure and develop

Wafer Preparation
Clean: Acetone/ IPA/ DI and blow dry
Oven bake, 150C, 30'
Spin HMDS onto hot wafer
Oven bake, 150C, 5'
Allow wafer to cool down ~ 5-10'

Spin Parameters
Resist: S1813
spin - 500rpm/1000rpm/s/10sec/Open Lid (C)
EBR - 1500/5000/60"/Close Lid (C)
Soft bake 120oC, 1' (Hotplate)
15' before exposure
Exposure – 25''
5.6A, 20mW/cm2
Develop (MF–319 undiluted, room temp)
time ~ 22''

Descum 60sccm O2, 100W, 50mTorr, 20C, 30''

Oven bake, 110C, 30' (Oven)

DRIE etch
Recipe name: 'Dark 3s', total run time: 2 min 3 sec
Etch-passivation cycle:

SILICON ETCHING PROCESSING

This is the process recipe used to etch through the silicon and release the substrates:

10.6µm expected thickness AZ9260 spin, bake, exposure and develop

Wafer Preparation
Oven bake, 150C, 30'
HMDS, bell jar, 15' (immediately after oven while wafer is still hot)
Oven bake, 150C, 2'
Allow wafer to cool down ~ 5-10'

Spin Parameters
Pre-spin - 500rpm/500rpm/s/10sec/Open Lid (O)
Spin - 600/600/60"/Close Lid (C)
EBR - 4000/4000/2/C

Cool down the oven, set temp to 90C
Place wafers and switch the oven "ON"
Set countdown timer to 45' when oven reaches 90C
Open the oven doors and allow wafer to cool down ~10'

Overnight stay before exposure
Exposure - 90" (50" + 5' delay + 40")
5.6A, 20mW/cm2

Develop (4:1 DI (distilled):400K, room temp)
time ~ 13'

Evaporate 300nm Al.

DRIE etch
Recipe name: 'Dark 3s', total run time: 3 hrs 30 min
Etch-passivation cycle:

Remove wafer and mount on handling wafer
(handling wafer Spin Parameters
Resist: S1813
spin - 500rpm/1000rpm/s/10sec/Open Lid (C)
EBR - 1500/3000/60"/Close Lid (C)
Mount wafer
Soft bake 120oC, 1' (Hotplate))

Complete DRIE etch: approx 40 min (with monitoring)

Figure 3.19: Description of the process recipes for the shallow and through wafer etching.

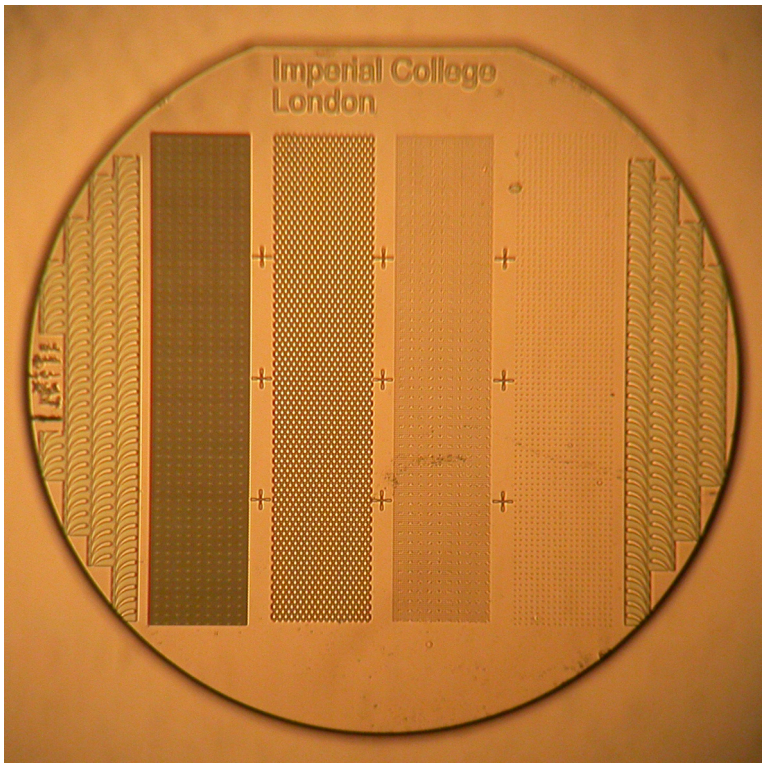


Figure 3.20: Our reference: MARS10(substrate19) - A Mars Phoenix microscopy substrate viewed at 5× magnification - one on its way to Mars now. It has a diameter of 3mm

On completion of the through-wafer etch - which was visually indicated by the bright aluminium layer shining through the trenches - the wafer was removed from the STS, the substrates were released from the handle wafer and were cleaned by soaking in hot 1165 resist stripper, and further washing in acetone, IPA and DI water. A final clean with an oxygen etch ensured all the organics on the surface had been removed. The optical micrograph in Fig. 3.20 shows a substrate patterned and released from the wafer after DRIE. This is one of the substrates that is now on the Phoenix spacecraft.

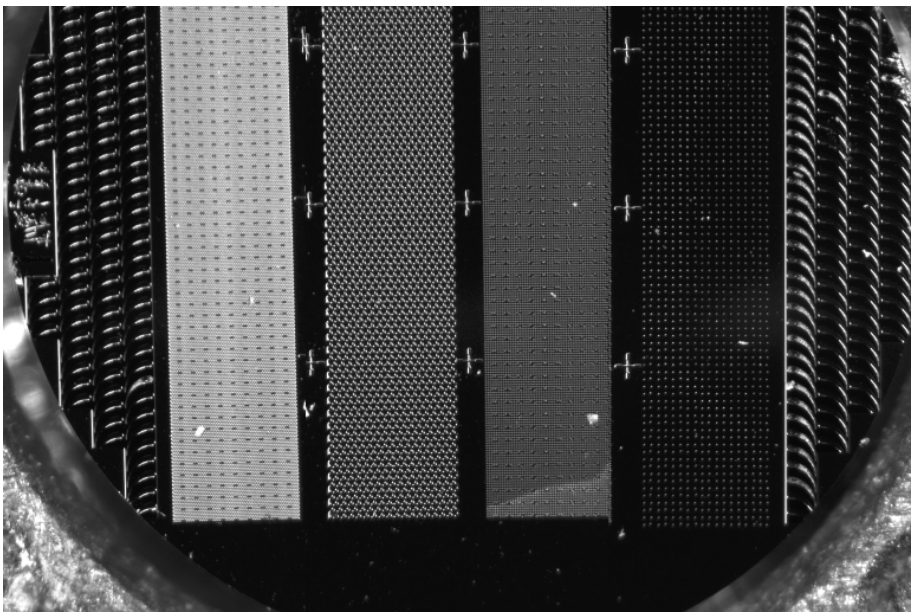


Figure 3.21: Mosaic image of a MECA substrate as viewed through the MECA OM.

Fig. 3.21 shows a mosaic of a substrate imaged through the MECA OM. Three 2mm$\times$ 1mm images were required to produce the mosaic image. Note that the side by side images are at an angle of 1 degree relative to each other since the wheel has to rotate between images to acquire the mosaic.

These SEM scans in Fig. 3.22 show the patterned regions where the irregular features are part of an encoding scheme built into the pattern to help with scan field location. This is in the form of a digital code describing the position on the substrate.

Fig. 3.23 shows AFM images where again the code markings may be seen. In each 40μm scan we can tell where we are on the substrate. OM to AFM registration is very important for targeting samples and the markings

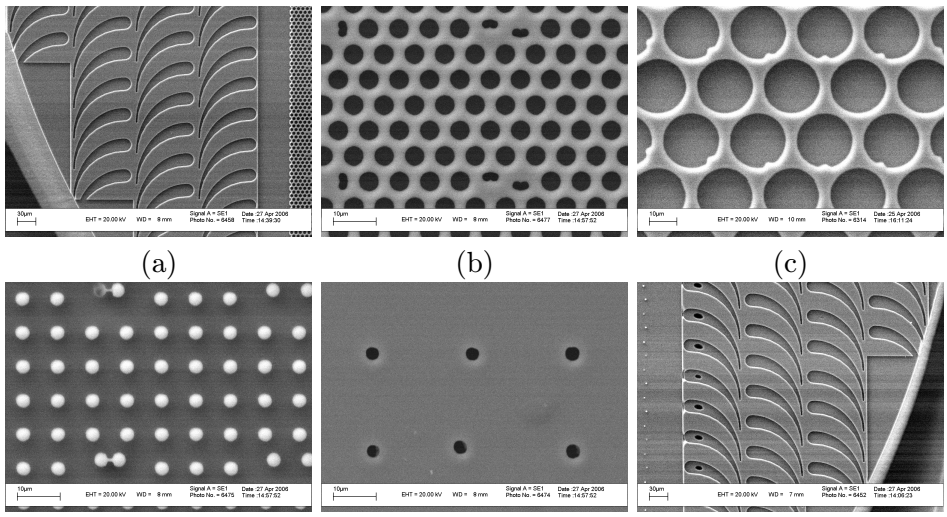
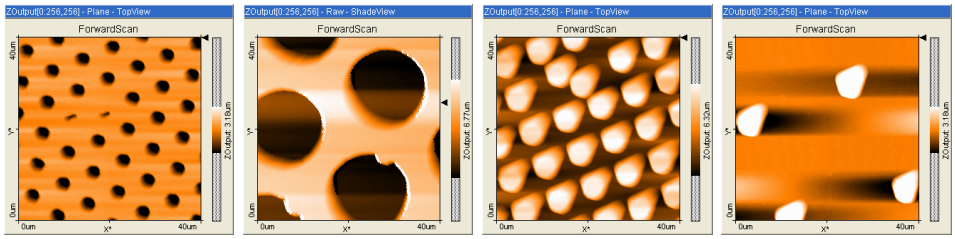


Figure 3.22: SEM images of areas on Mars microscopy substrate; (a) left tear drops, (b) 5μm pits, (c) 20μm pits, (d) 5μm pillars, (e) 20μm pillars and (f) right tear drops. See table 1 for more detail.

provide valuable engineering data to aid with these flight activities. So not only will the exact location of the scan on the substrates be obtained, engineering data on the performance of the sample wheel rotation system is also returned from the scan. This may be important as it may save repeating positioning scans which would require taking more AFM images - using time which is a very valuable resource during microscopy AFM days. As well as being a confirmation of the scan position, it also may help to understand any scans that did not return results as expected, as at least the position will be known; for example we could then determine whether particles were moved during or before the scan.

This registration is a feature that the other substrates used to collect the sample are not able to provide. As well as this, the features provide an



(a) (b) (c) (d)

Figure 3.23: AFM scans of the different etched features of a Mars substrate. a) 5μm pits, b) 20μm pits, c) 5μm pillars and d) 20 μm pillars. On each scan we can see a coding feature allowing identification of the particular position of the scan.

in-situ calibration for scale and orthogonality of the scanning system.

3.5.2 Testing of Substrates

The substrates were first tested under similar conditions to the initial tests with JSC Mars-1 soil, as in fig. 3.24. Some diatoms were also deposited to examine their alignment to the grid of pillars.

The next stage of testing was to perform some AFM scans of such particles demonstrating their stability during scanning. Fig. 3.25 shows a scan of some JSC-1 particles immobilized in a pit. The particles stick out just above the substrate at 6μm tall. A larger scan of the area shows no other particles in the area only this one trapped by the pit and no other particles are sat around the pit. Even at this much faster speed of the second scan, the particle did not move. From the markings it is found the image is 26μm from left hand edge of strip as this is a 40 $\times$ 40μm scan.

The AFM scan in Fig. 3.26 also shows an image of a particle in a pit demonstrating the fine structure that is resolvable for an 8μm diameter par-

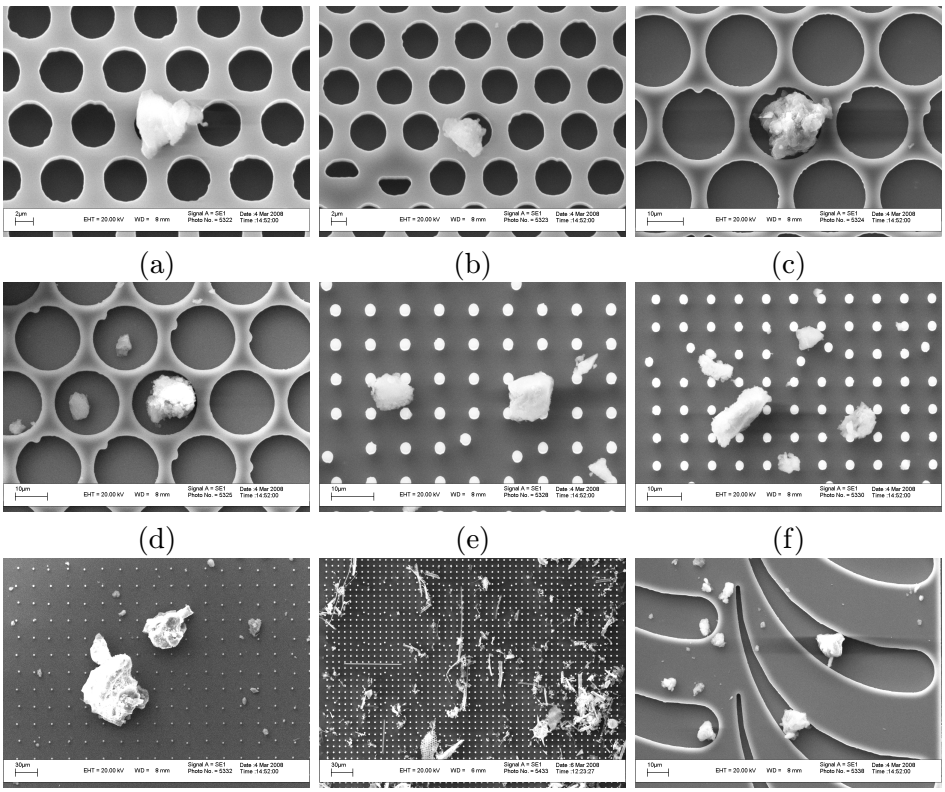
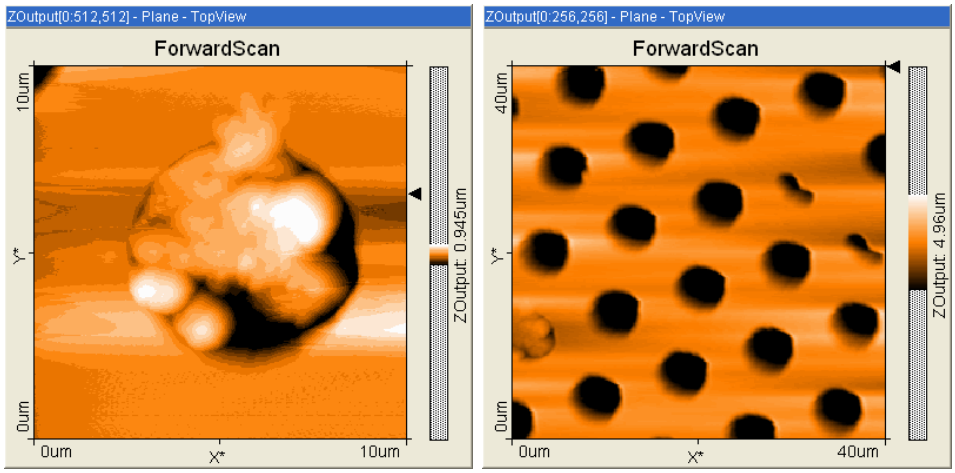


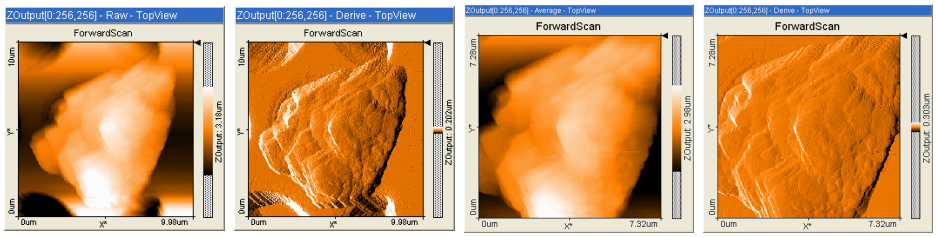
Figure 3.24: SEM micrographs of areas of a Mars substrate holding or trapping particles; (a) and (b) 5μm pits with individual particles of JSC-1 immobilized; (c) and (d) particles trapped in 20μm pits; (e) and (f) particles wedged between 5μm spaced pillars and (g) Diatomaceous Earth with particles aligning between 5μm pillars; (h) larger particles sat on 20μm pillars; and finally (i) some particles trapped in teardrops. The substrates were all etched to give features 5μm deep in silicon.



(a) (b)

Figure 3.25: (a) shows a scan of a particle - or small cluster - of JSC Mars-1 sat nicely in a 5μm pit scanned at 5μm/s. (b) a second scan performed immediately after looking for other particles in the area surrounding the pit performed at 10μm/s.

ticle. Such a particle would be visible in the MECA OM merely as a couple of pixels, but the AFM data allows the determination of the particle size (1.3μm high above the substrate surface, and 8μm wide), shape and surface roughness (850nm). Furthermore, the observed surface texture, which includes a number of parallel linear features, may be the imprint of an aqueous environment on this particular grain, as suggested by the work of Kempe *et al.* (Kempe et al., 2004). This clearly demonstrates the importance and utility of the AFM in investigating particles in this size range.



(a) (b) (c) (d)

Figure 3.26: (a) the raw scan and (b) the derivative of a topography image from the AFM of an 8μm diameter particle on a 5 μm pit. (c) and (d) is a repeat of the scan over a smaller area.

3.6 Summary

Our testing has demonstrated that one method to sort and immobilize individual grains of a sample is the use of deep reactive ion-etched substrates with arrays of microscale pit and pillars features. As well as helping with gripping or sorting of particles, the features are able to hold the particles in place during AFM scanning.

Based on these results, a number of patterns and aspect ratios that were particularly good at isolating and fixing down particles for AFM imaging were identified. The pattern described in this section was chosen for the substrates to be used as part of the microscopy package for the Phoenix mission.

3.7 Conclusions

The NASA Phoenix mission, which landed in the Martian arctic north on May 25th 2008, motivated this work, and aims to demonstrate the viability

of using the MECA AFM to far extend the imaging resolution of planetary science imagers into the submicrometer regime. The AFM will operate in combination with an OM to image micometre-sized and larger particles, harvesting data on particles on and below the Martian surface in terms of their size, shape and transport history.

Adequate sample preparation is essential for the study of loose particles using the AFM. The technique illustrated in this chapter, and consequently incorporated into Phoenix, is the stabilization and segregation of individual particles using features micromachined into a flat silicon surface. The etched features grant a degree of control over the sample distribution, providing fields of particles that can be successfully imaged with an AFM. Moreover, with unknown adhesion factors on Mars, the patterned topography retains a greater range of particle sizes and shapes for analysis with the microscopes.

As a limited range of materials were used here, increased confidence in the ability to image Martian material awaits the much more extensive characterising and cataloguing campaigns described in the next chapter. This work, as well as using a wider range of materials, will also involve experiments at Martian temperature and pressures and the use of a scoop and environmental chamber to best represent the flight sample preparation. Of course the ultimate proof of the ability of the AFM to image Martian material at an unprecedented resolution is proved during flight operations, data from which will be presented in Chapter 5.

3.8 Cruise Images

Here are some pictures of our substrates taken from over 100 million miles away, Fig. 3.27.

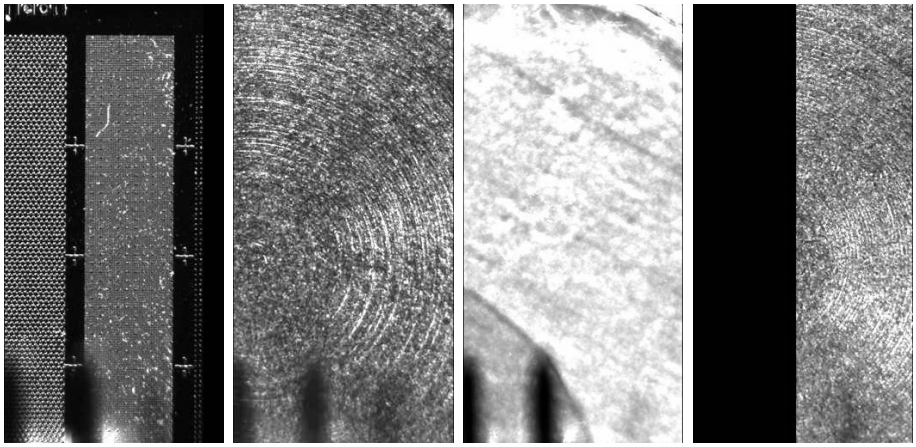


Figure 3.27: This shows four OM images from the OM Cruise checkout on 17th September 2007. Phoenix had travelled 125 million kilometres since launch on its trip to Mars. Shown are the 4 images as part of the checkout; (left to right) the nanobucket substrate, the weak magnet, the silicone substrate and a partial image of the strong magnet. OM images are 1mm wide and 2mm tall.

The substrates are not perfectly clean - they achieved some contamination during mounting, and it is clear that the pillars are very good at trapping particles.

Chapter 4

MECA Testbed and Operations

In this chapter is investigated the information obtainable about material delivered to the MECA microscopy station by looking at its behaviour and what can be deduced from the imaging. Within this, the performance of the nanobucket design described in Chapter 3 is analyzed, in particular observing how the substrates contribute to and function as a part of the complete set of six substrates. The tests are performed in the environmental chamber assembled at Imperial College and under both Earth and Mars ambient conditions.

4.1 Introduction

The microscopy station will receive samples of dust and soil from the surface of Mars delivered by the robot arm, as well as collect samples from the airfall.

There are many challenges of using an AFM to study Martian soil and dust particles. To begin with, studying loose and irregularly shaped particles is a challenge for AFM. Further to this, the broader challenge of operating an AFM autonomously is made even more difficult by the reduced flexibility associated with space operation, especially as an AFM needs the ability to exchange used, damaged or contaminated tips.

At Imperial College work has been done to understand and limit these problems. Studies performed on the testbed aim to understand how the material deposited on the substrates behaves with particular focus on suitability for the AFM and then how the AFM can be operated in this environment.

The intention of only one uplink of commands to the spacecraft every sol, necessitates that the science instrumentation be pre-programmed to operate autonomously. For the purposes of looking at features of interest in more detail a day between microscopy sols will allow identification of suitable targets for the AFM to image.

Knowing the mode of operation and the intended surveying of the material with the OM and AFM, the system at Imperial was developed to simulate the imaging and the conditions. Labview software is used for the autonomous operation of the microscopy station for the control interface of the OM, AFM and the associated electronics with the environmental chamber. This allowed for end-to-end tests using a flight copy of the AFM and OM model (which simulates the flight model) and the sample wheel which will hold the substrates.

The conditions for the experiments are very important. Most AFM measurements will be dynamic mode acquired at Mars pressure ($\sim$ 7 mbar

under N_2 or CO_2 gas) and room temperature down to $\sim -20°C$.

4.2 Testbed setup

The work in this section is largely focused on testing using the testbed setup in order to prepare the AFM for the mission and for autonomous operation on Mars. The AFM is rarely used to characterise dust particle properties, therefore testing is of great importance. The full Mars environmental simulation facility set up at Imperial College integrates the AFM and is used for testing of Martian soil simulants.

An aim of the testing was to acquire AFM and optical microscope images of Martian soil simulants, to understand the capability of the instrument to differentiate materials in the images acquired from Mars. Further, it allows to explore different imaging parameters. A range of materials such as soils, clays and volcanic rocks were tested under a range of environmental conditions that simulate the Martian surface.

4.2.1 Testbed at Imperial College

The testbed, which was setup at Imperial College and used as part of this work, is a copy of the flight setup but with some differences. The following section describes the setup, also describing the important differences and similarities between the two systems.

The main difference between the systems is how they are driven; in flight, the Flight Software (FSW) and electronics drive the system, whereas the testbed uses Labview and Nanosurf Easyscan AFM software and a commer-

cial stepper motor controller. The tesbed is therefore assembled of discrete components rather than all on one board. In flight, such a board is called the CME board and it provides control and power for whole system, with exception of the OM as this used the Robot Arm Camera (RAC) electronics.

Another difference of course is the environment of the setup. In order to simulate Mars, the tests at Imperial College are conducted in a closed chamber within which many of the Martian conditions are created.

Hardware

This section describes the hardware used at Imperial College (Testbed Model - TB) describing any differences to that used in flight (Flight Model - FM, but also represented by the Engineering Model - EM).

Sample Wheel Translation Stage

The SWTS consists of a wheel on flexures which rotates and moves forwards and backwards in front of the OM and AFM allowing the substrates to move into the viewing position, as in Fig. 4.1. Mechanical microswitch limit switches are included which to enable the identification of the position of the wheel along its travel. The configuration of TB models is the same as the EM, though as this is a mechanical system, small differences in positioning may lead to slight differences in the Limit Switch positions.

Stepper motor controller

The SWTS is controlled by two motors - one that translates the wheel back and forth, towards and away from the microscopes, and the other to control

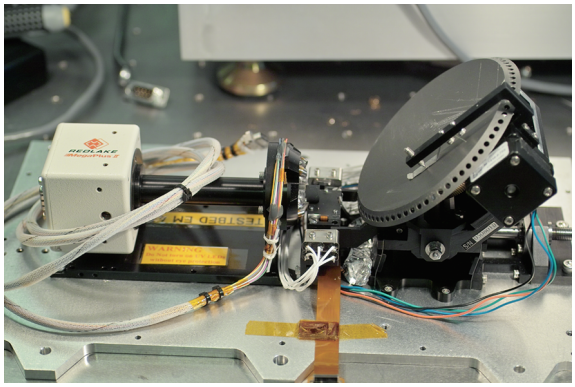


Figure 4.1: The Sample Wheel Translation Stage (SWTS) with the OM and AFM positioned in front of the wheel. Image from JPL.

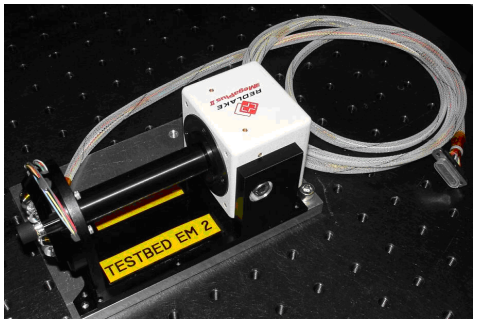
rotation. The difference between the two models is in the gearing in the translation motors as the TB has $1/8^{\text{th}}$ μm per step whereas for the EM it is $1/4^{\text{th}}$ μm per step. Both the FM and TBs have the same rotation stepsize of 15 μm. The motors are driven using 2 phase drive mode, the same as during flight. However, the TB model has more torque than flight so the TB sees no lost steps, whereas on Mars there may be some. The stepper motor controller is an AML SMD2.

Limit Switch board

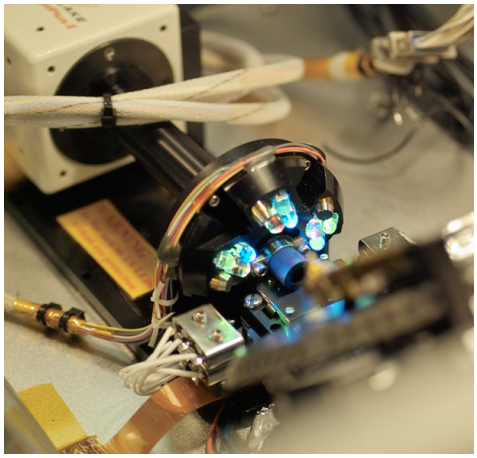
The Labview interface is used to command the SWTS motion, which is controlled by the limit switches, the electronics for which were built by JPL. This control is the same as is the flight software such that the stage is stopped whenever it goes onto, or comes off a limit switch. The AFM also feeds into this providing the AFM near signal which acts as a limit switch also.

There are 7 limit switches in total. 6 are mechanical switches; 2 in rotation (ROT A and B, one required and one for redundancy); and 4 in translation (Focus Position, Safe to rotate A and B (one redundant), and OUT Position. AFM near is an additional electronic limit switch for the translation to halt the stage when the AFM detects the surface of a substrate during the AFM approach.

Optical microscope



(a)



(b)

Figure 4.2: (a) The Engineering Model of the optical microscope. There is no apparent physical difference to the testbed model. A 12-bit analogue-to-digital converter reads out the chip creating an image data range of zero to 4095 DN (b) A front view of the camera lens and LED arrangement on the OM showing the three banks of LEDs - each cluster contains one in red, blue, green and unltraviolet (the UV are in the small metal cans). the UV LEDs irradiate at 375nm with a visible light blocking filer and are used for fluorescence measurements only.

The testbed OM model (TBOM) performs very similarly to the flight

model (EMOM). The optical design and physical layout are the same for the two models Fig. 4.2(a). A black and white CCD is used to acquire the images, while the samples are lit with a combination of LED lamps as instructed by the user. The primary way the two systems differ is in the Camera specifications, as the different CCDs have a different resolution and response for RGB.

The TBOMs use a Kodak KAI 2001 12 bit 1600×1200 pixels CCD supplied by Redlake. This is different to the 528×256 Loral CCDs of the EMOM. Despite a different array and pixel size, the TBOM images can be altered using simple software in order to mimic the OM used on flight. A Matlab program processes the raw 1600×1200 12 bit images and bins the arrays into a 3×3 array, with centering and cropping, producing 12 bit images with a resolution close to that of the 528×256 Loral CCDs.

The other difference is the spectral response of the CCDs. The Loral CCDs work effectively from 350 - 1100 nm, whereas the Kodak CCDs are shifted towards the blue and are cut off before the infrared, giving a narrower range and relatively skewed response which is in fact non-linear.

LED Controller

The LED illumination of the samples is the same for the two models in hardware and control. The LED lamps are arranged in groups of three around the lens in the configuration shown in Fig. 4.2(b). Each group contains 1 red, 1 blue, 1 green and 1 UV LED. For the EMOM, the MECA electronics powers the LEDs. For the TBOMs a switch box allows manual operation of the individual LED lamps, however the box will accept computer control

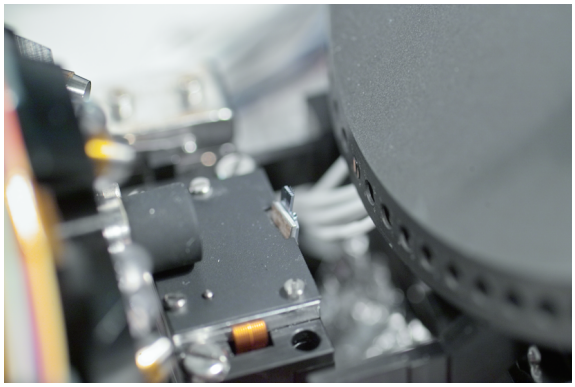


Figure 4.3: A close-up of the AFM when placed in its position in front of the wheel with the OM behind it.

via the parallel port connector as provided by the LabView software and this allows flight-like control of the LED lamps.

Atomic Force Microscope

The AFM, as seen in Fig. 4.3, has the same electronics, though the TB models do not have radiation hard components. The scanner and AFM board microprocessor are same. The control of the instrument is similar, although the TB uses EasyScan software to control the microscope. As a result the high level commands, such as those which start and stop a scan and approach onto a surface, are the same.

Mars Environmental Chamber

This chamber, shown in Fig. 4.4, is how the testbeds simulate the Mars environment. Being sealed off from the surrounding atmosphere, the chamber allows operation of the microscopy station under Mars pressure, temperature

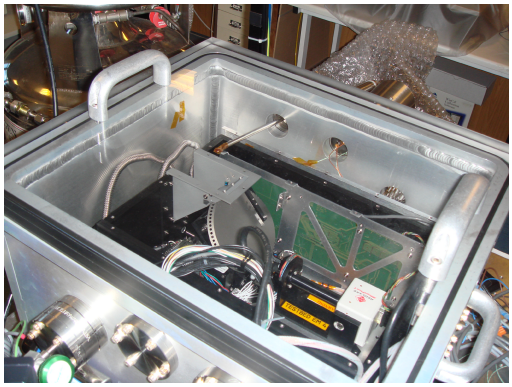


Figure 4.4: The Mars Environmental Chamber.

and low humidity environment.

A vacuum pump is used to take the pressure down to 4 mTorr - a similar pressure to which is expected on Mars. The chamber is dried and filled with dry N_2 gas for which there is an inlet. The cooling is provided by liquid N_2 running through piping, while the temperature is controlled by a large sheet kapton resistive heater at the base of the chamber. The heater power is provided by a thyristor and a constant temperature is maintained by a Eurotherm PID controller. To achieve a stable cool temperature is a process which takes a couple of hours.

Sample Scoop

To simulate the robot arm scoop depositing the sample material onto the substrates, the testbed at Imperial College uses a small sample holder as shown in Fig 4.5. This scoop allows us to deposit material that has been dried within the chamber and then control the method of delivery - whether it is all at once deposited on the substrates or sprinkled over.

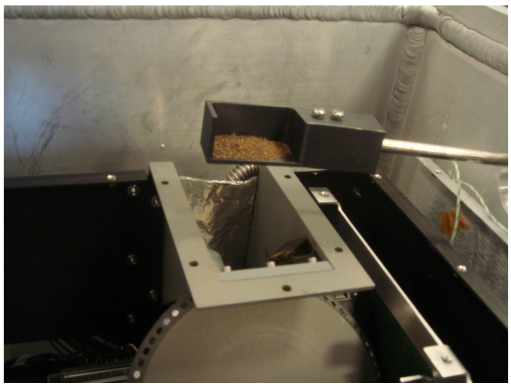


Figure 4.5: The sample scoop in the testbed which simulates the robot arm scoop.

Sample Heater

In order to ensure the sample deposited on the wheel is completely dry, a 'light bulb' heater is used to locally heat the sample. This light bulb heats the sample in the chamber to approximately 200°C in order to remove all the humidity. The heater for the sample material also uses the PID controller. This again is powered through the thyristor.

Software

The flight system is controlled by the flight software which is written in the vml programming language. The testbeds are controlled by a custom version of the commercial Easyscan software and Labview Virtual Instruments. The main difference in the control is the user interaction. The .vml files are pre-written sequences that run as a whole 'block', whereas using the Easyscan and Labview allows for control and feedback by the user for each command, although this is at the discretion of the user.

There are similarities in control, for example that the AFM near signal is sent from the Mtest2 board - one of the AFM electronics boards - into Labview and acts as a limit switch. Also, as in flight, the system is only sensitive to AFM near being asserted whenever we translate the stage inwards.

Labview GUI

The Labview software GUI for operating the TBs was written and developed by JPL. A display of the tool is shown in Fig. 4.6. The interface allows the user to; control the individual SWTS motors changing the speed and number of steps commanded, turn on and off LEDs (individual control of all 12), acquire and save OM images while controlling the shutter speed which controls the time of exposure, observe the limit switches (with the ability to chose to ignore them where desired), and run macros allowing commands to be executed as routines in a pre-written 'block' of instructions.

Mars EasyScan GUI

The Mars EasyScan software developed by the University of Neuchatel and Nanosurf AG, controls the TB AFMs, and is a special version of the commercial EasyScan software, Fig. 4.7. The user loads the parameters and initializes the AFM, finding the operating frequency and applied voltage that is optimal for each of the cantilevers, after the appropriate calibrations are performed, the sample can be approached (this is in fact done by also using the motors controlled by Labview) and the AFM near limit switch will be asserted. The scan parameters can be set - choosing feedback settings

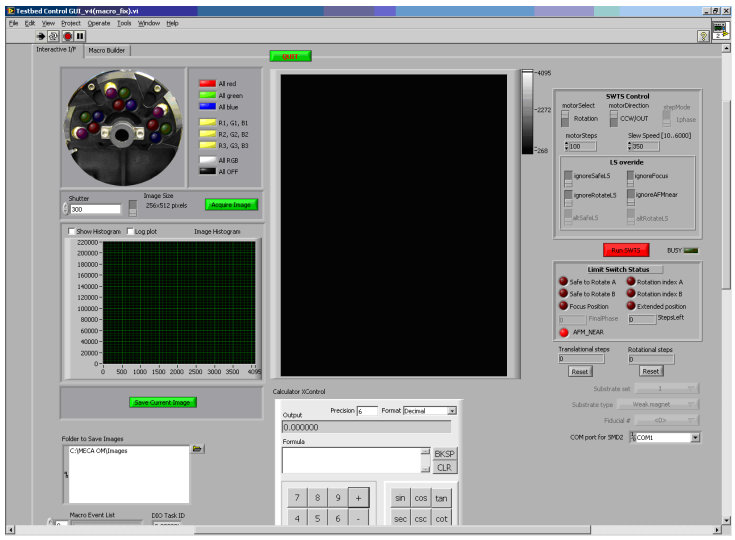


Figure 4.6: Window of the Labview showing the control interface.

such as the P- and I-gains (usually 9 and 8 respectively are used for scanning) and the setpoint (often +1V for dynamic mode). The x- and y-slopes are then adjusted so that the sample surface lies in the x-y plane of the scanner.

For imaging, the user has control of the x-y scan range, the number of lines per scan, the speed of the scan, the z-range, autoadjust z-offset on/off (which can adjust the scanner position using information from the previous line scanned), the form in which the data is presented on the screen, as well as other control parameters and display options.

Stage approach

When operating the TB, during the approach of the stage to bring the AFM to the surface, the two signals V_{shake} (the excitation signal) and V_{sig}

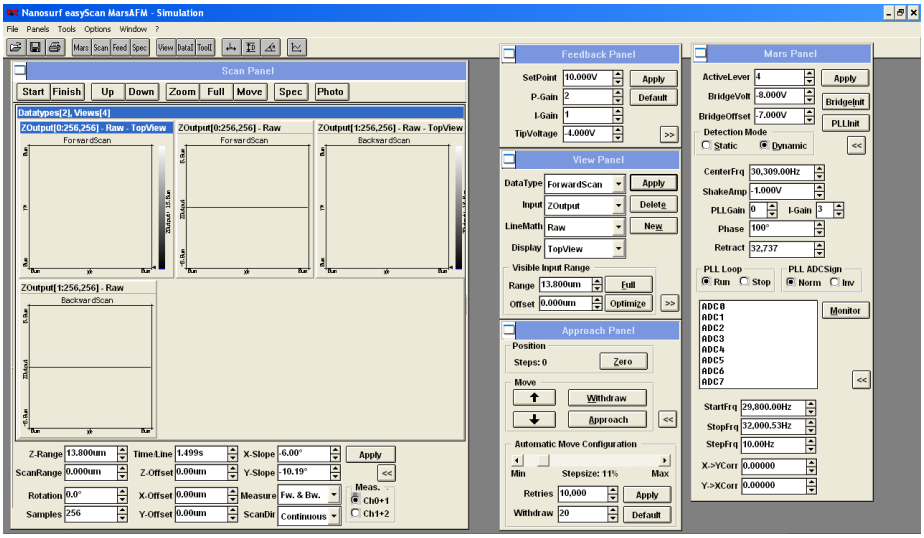


Figure 4.7: Window of the Mars EasyScan with a view of the different panels.

(the response of the lever to the excitation) are monitored on an oscilloscope directly from the AFM electronics board. This shows the quality of the AFM signal and the change in the vibration of the lever as it touches the surface.

Humidity Control Procedure

The processes developed to ensure a low humidity environment within the chamber are:

1. pump down to base pressure
2. cool chamber down to allow frost to collect on the liquid N_2 piping
3. allow to warm but continue to pump down to remove moisture
4. backfill with dry N_2 gas to just below atmospheric pressure (to around

600Torr)

5. pump down to base pressure

6. repeat this pumping/backfill procedure three times

7. pump down to Mars pressure ~ 4 Torr

Confirmation that the humidity is low is obtained from observing for signs of frosting on the liquid N_2 inlet tube in the chamber which is the coldest part of the system. If no frosting is observed, the atmosphere is extremely dry.

Temperature Control Procedure

The processes developed to create the cold environment of Mars within the chamber are described below. The N_2 liquid flowing through the base plate remains constant, while the current through the heater controls the temperature. Two thermocouples are used; one at the AFM itself, and another underneath the base plate directly next to the capton heater. This latter thermocouple is used for PID control of the temperature. The thermocouple at the AFM is not used for this purpose due to its large temperature lag.

Procedure:

1. Before cooling down to a stable Mars temperature, an initial cooling of the system is performed.

2. Having pumped down to base pressure with a dry environment, liquid nitrogen is allowed to flow through the base plate.

3. As the system cools, frosting appears on the nitrogen inlet tube as the tube acts as a cold trap for all the remaining humidity in the system. Once the frosting has appeared, the flow of nitrogen is stopped and the system is allowed to warm up while the chamber is being pumped. This lasts about 20 minutes.

4. When the frosting has cleared, the pump is then closed, dry nitrogen allowed into the system bringing it back up to Mars pressure, and then the system is cooled to Mars temperature.

5. Once the temperature of the base plate reaches $-100°$C, the flow of liquid nitrogen through the base plate is stopped. The kapton heater switches on to warm the system until the thermocouple on the base plate reads $-70°$C.

6. Again, liquid nitrogen is allowed to flow through the base plate to cool the system to $-100°$C and so on.

7. Due to the large lag of temperature lag of the system, throughout this procedure the system is slowly cooling down and the thermocouple on the AFM shows a slowly decreasing temperature.

8. The cooling-heating procedure of the base plate is repeated until the temperature at the AFM reads the desired value. (n.b. below $-30°$C the image from the CCD of the optical microscope drops out - the system is therefore often operated at $-20°$C)

4.3 MECA Microscopy on Mars

4.3.1 Aims

The aims for the microscopy station on MECA are to establish the characteristics of the soil and dust. It will look at grain size, grain size distribution, shape (this refers to grain surface curvature), colour, surface texture, and the magnetic properties of the soil, as well as characteristics such as colour, homogeneity and particle-particle interactions (aggregation). The aim of AFM is to capture the finest features of the material and analyse its size, shape and texture. It is expected that the AFM will be especially valuable in examining airfall particles in the 1 - 3μm size range. For all AFM scans executed an OM image will also be acquired as documentation of the substrate as well as to provide context of the scan.

Studies in the testbeds have looked at the amount of material retained by the different substrate types and the manner in which it is distributed, as well as the capacity of the microscopes to distinguish particles aggregates or the parasitic attachment of finer grains to larger ones. Also investigated were techniques to coalesce information from AFM and OM imaging.

The testbeds have also been useful to study cross-contamination from earlier samples, as material may transfer between substrates. Also important is the stability of samples as affected by the SWTS motion, from individual particles - important for AFM targeting - to material that piles up on substrates - relevant if obtaining a through-focus series of such a pile.

The MECA wheel is equipped with 5 different types of substrate, each with a different purpose, to investigate a given aspect of the soil. The sub-

strates do this by promoting different modes of adhesion; the microbuckets are 3mm in diameter and 2mm deep and thus are designed to perform a type of 'bulk sampling' catching particles up to a couple of millimetres in diameter. The remaining substrates aim to catch submillimetre particles. The strong and weak magnets will investigate the magnetic properties of the soil, and a uniform 'sticky' silicone disk which is expected to remain pliant under Martian conditions and finally the micromachined silicon target or 'nanobucket' substrate for holding material for AFM imaging. These final two substrates have been included specifically for AFM use.

4.3.2 Testbeds

The testbed used a variety of test materials and Mars soil simulants for measurements. These include: JSC Mars-1, aluminium oxide, iron oxide, Diatomaceous Earth, glass beads, and a number of soil simulants supplied by the Johnson Space Centre.

Cataloguing of these OM images acquired by the testbed provides a basis to distinguish between the mineral types by observing the parameters such as shape, colour and combinations.

4.3.3 OM images

The OM 512×256 pixel CCD provides portrait images of 2×1mm in size, resulting in 3.9μm per pixel. This provides an adequate overlap with the field of view of the AFM to enable the registration of common features. The 2×1mm field allows most of the substrate to be viewed and a rotational shift of 1mm at a time allows a 'mosaic' to be captured i.e. three adjacent

images show a whole substrate. The OM takes images in red, blue and green and the UV LEDs can allow fluorescence measurements.

The depth of field of the OM is between 50 to 100μm, larger than most particles liable to be imaged. To acquire a focused view of a pile of particles larger than the depth of field, the SWTS is translated inward to the microscope between images, thus obtaining a series of several images all with the optimal focus on a different part of the pile until the substrate surface is in focus. This will allow three dimensional images of the piles to be constructed.

4.3.4 Presample documentation

In preparation for sample delivery, the substrates on which material will be collected are first imaged in a presample survey in order to examine their cleanliness. This allows identification of which features should not be ascribed to the newly deposited sample.

Six substrates (a complete set) are exposed outside the enclosure when the wheel is extended, as we see in Fig. 4.8. A scraper blade at 200μm above the surface of the substrates removes the excess material. The exposed substrates are then translated and rotated into the vertical imaging position for examination by microscopes.

Characterization of the OM (as performed after landing on the surface) involves imaging of a few selected calibration substrates. This includes an image of the commemoration substrate (which contains text to help ascertain the focus position for the microscope and determine whether it had changed during launch, cruise or EDL) and a white substrate (to calibrate

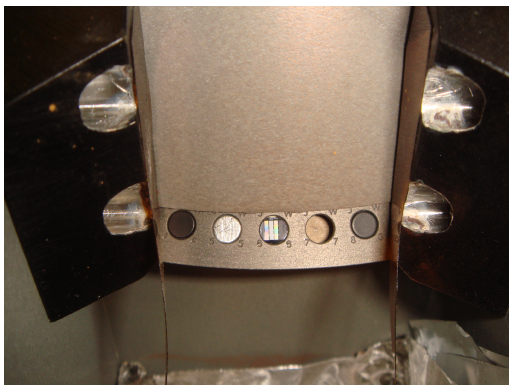
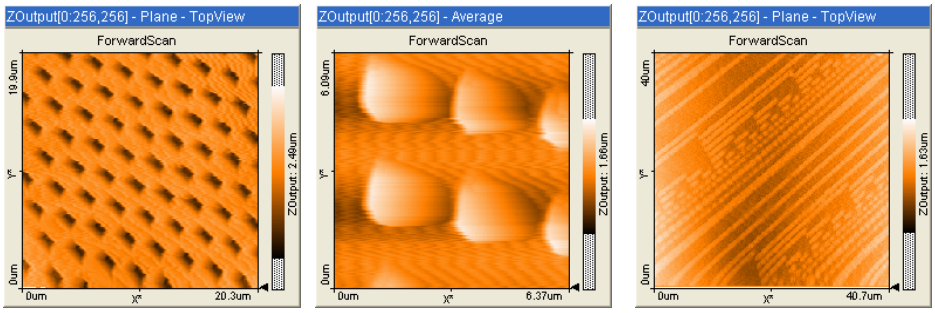


Figure 4.8: A picture of the sampling chute viewed from above showing the SWTS extended revealing a set of six substrates exposed and ready for sample acquisition. The substrates are flush to the top of the wheel around them and the scraping blade rests 200μm above the surface of the wheel.

the intensity and uniformity of each red, green and blue LED and enable producing true colour composites based on this calibration - also imaged as regular checks during the mission).

Similarly, the AFM calibration involves scans of three substrates performed in situ, such scans are shown in Fig. 4.9. First is a scan of a linear grid. This is used to correct for the saddle distortion typical of this type of AFM drive. It also establishes the absolute length of the scan area, since the scan size is reduced at lower temperatures.

Second is the tip standard substrate which is a 'pincushion' consisting of a field of sharp tips 0.3 to 0.6μm high with a curvature of less than 10nm. All AFM scans are a dilation of the substrate and AFM tip shape. These pins, however, have a higher aspect ratio than the AFM tip itself, so the scan is dominated by the AFM tip shape. The shape of the AFM tip is determined by scanning these sharp pins. Such a scan will be useful to perform regularly



(a) (b) (c)

Figure 4.9: The AFM calibration targets. (a) The linear calibration grid, (b) the tip standard substrate or 'pincushion' and (c) the tip finder tool with a digital code for determining the position of the tip.

- before and after imaging samples - to determine the condition of the tip in terms of contamination or wear.

The third calibration substrate, called the 'tip finder' tool, which is a coded substrate, has features visible to both the OM and the AFM. It registers the position of the AFM scans within the OM image, giving information vital for AFM target selection.

For the final stage of the calibration the Wheatstone bridge is initialized and the unique resonant frequency used to excite each tip to its maximum deflection is found. This frequency is measured each time the instrument is initialized.

A number of other tools are available on the SWTS to assist the AFM. These include a blank silicone pad to clean contaminated tips, and a tip cleaving tool that is used to break damaged cantilevers exposing the next cantilever in the set.

4.4 Results of Testbed Testing

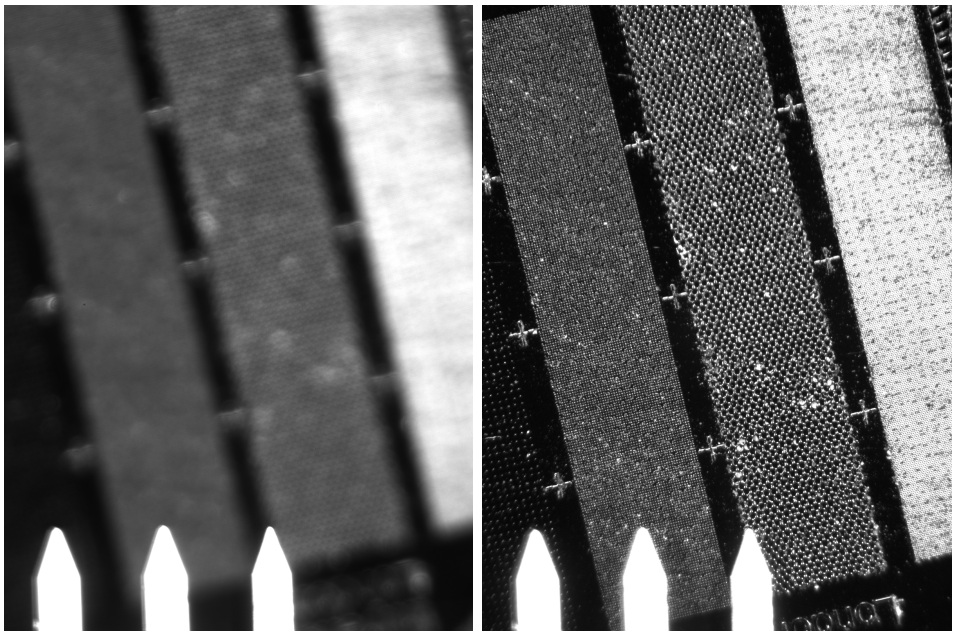
This section discusses the main findings of the experiments performed at Imperial College using the testbed and environmental chamber. These observations investigated the motion and behaviour of the SWTS and the nature of the material that sticks to the substrates. The findings show new limiting operational constraints for running the system and have developed procedures for operating the microscopy station on Mars and in some cases resulted in changes in the hardware on the spacecraft.

4.4.1 SWTS motion

During translation motions (for example a through-focus series) the substrates appeared to shift as the SWTS translated inwards. This motion is attributed to the SWTS being mounted on flexures, so as it translates back and forth it dips downwards at the extremes of its motion. Quantifying and understanding this motion was important to the accuracy of the imaging, especially for AFM.

40 images were analyzed while translating inwards in 100 step increments. Images taken at two different positions are shown in Fig. 4.10; the first at the safe to rotate Limit Switch (LS) position (step count 82106), and the second at optical focus (step count 85006). For the purpose of this analysis the images were not clipped or binned to the flight dimensions as the higher resolution would increase the accuracy of the study.

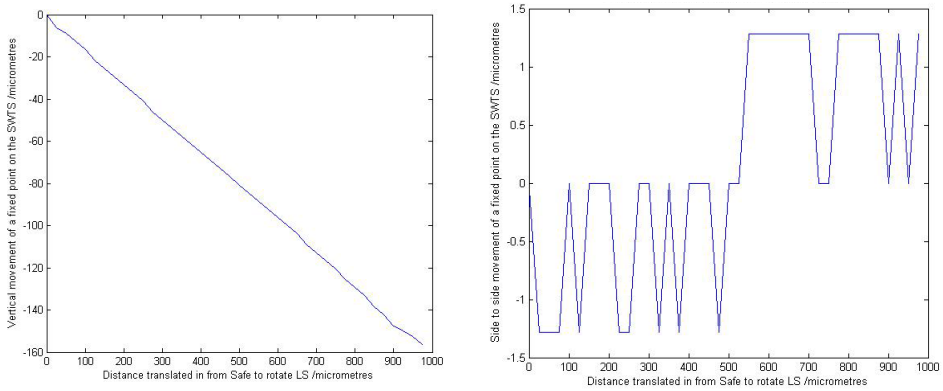
The graph in Fig. 4.11 summarizes the lateral and vertical motion of the wheel for the region in which the OM is commonly used. The lateral



(a) (b)

Figure 4.10: OM images from the testbed of the SWTS at (a) the safe to rotate LS and (b) the focus position. The substrate has appeared to shift down as the SWTS translates closer to the microscope. The images are taken with all LEDs on ('white' images) and have not been cropped and binned to preserve resolution.

side-to-side motion of the wheel is small and shows the SWTS to be very stable in this configuration as it translates in. The vertical position of the substrate clearly changes as the SWTS translates in. The vertical motion appears linear over this region, but is expected to follow a parabolic shape if monitored for the full motion from the position of fully exposed substrates through to the other extreme in front of the microscopes, as the motion is on flexures.



(a) (b)

Figure 4.11: Shown are two graphs showing (a) the vertical and (b) the side-to-side motion as the wheel translates towards the AFM. The plots show how the vertical and horizontal displacement varies at the wheel translates in by 100 step (25μm) increments. The motion appears smooth and consistently down as the wheel approaches the AFM from the safe to rotate LS to AFM touching the surface, but there is little lateral motion.

An advantage to be gained from this motion was associated with AFM imaging. As the substrate appeared 'higher' in the view of the OM, the area that would be below the tip at the AFM near position, was visible at the focus position of the OM. In particular, the distance between the OM

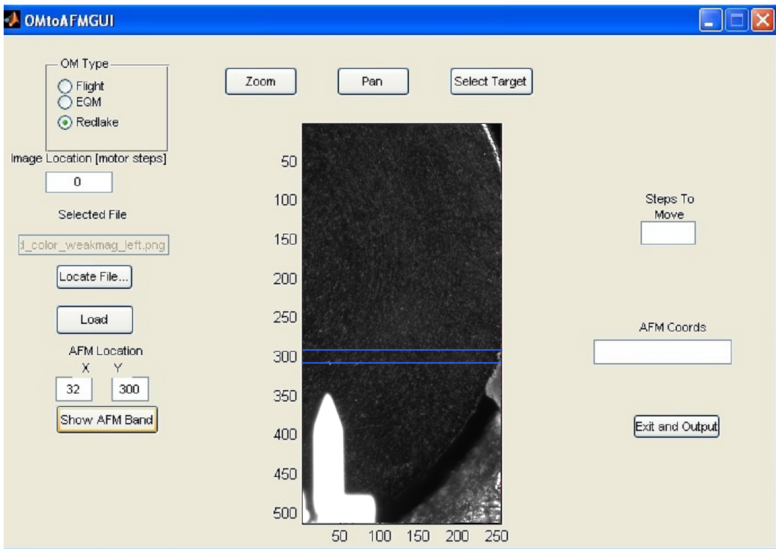


Figure 4.12: A snapshot of the AFM targeting GUI from Matlab. At the focus position, the AFM scan region is shown (between the two blue lines) and is above the AFM tip.

focus position to AFM scanning position is 3500 steps or 875um, thus the substrates drop by approximately 140um. A program built in Matlab allows the AFM band to be located on an OM image, as in Fig.4.12. The region accessible to the AFM is between the blue lines.

4.4.2 Backlash

Clearance between mated gear teeth is often used to allow for angular misalignment. The backlash or play in the SWTS system refers to the amount of slackness when the SWTS movement changes direction and contact between the gear teeth is re-established. On the Imperial College system the backlash was ascertained to be 32 steps in the rotation gears - thus, for ex-

ample, when doing a large (<32 steps) motion clockwise and then changing direction to the anti-clockwise direction by commanding 32 steps, the SWTS would appear not to move.

To account for this, backlash compensation is applied in the form of the SWTS always approaching its final position from an assigned direction. This may involve over-shooting the target and returning to the correct position from the assigned direction.

On the Imperial College testbed the more reliable rotation direction was found to be anti-clockwise (the asymmetry of the wheel is attributed to the vibration arm fixed on one side of the wheel.)

However, another phenomenon observed occasionally is 'drift' into the backlash region during translation motion. This occurs as when the wheel rotates is one direction, the teeth of the gears of the 'driven' cog are flush against those of the 'driver' (the driving gear), preventing the 'driven' cog to move any less than this rotation. The 'backlash region' in which the driven cog could turn is in front of it - i.e. in the forward direction to the direction it is moving. When the wheel translates, the vibration caused by this translation can cause the wheel to 'drift' into this backlash region, by a maximum of 32 steps. So for the case of anti-clockwise backlash compensation, after large translations the wheel appeared to have moved an even larger distance anti-clockwise. This phenomenon of drifting into the backlash region was greatly reduced by the vibration arm. Nonetheless, for the tip breaking procedure which involves many and large translations, this was an important consideration as such a drift of 32 steps is equivalent to 480μm - and the pitch of the levers is 350μm with a distance of between them of only 50μm.

To reduce the risk to the already very daunting procedure of breaking tips it was important to use clockwise backlash compensation so any drift would move the tip breaking tool away from the next lever to be exposed if the SWTS were to drift.

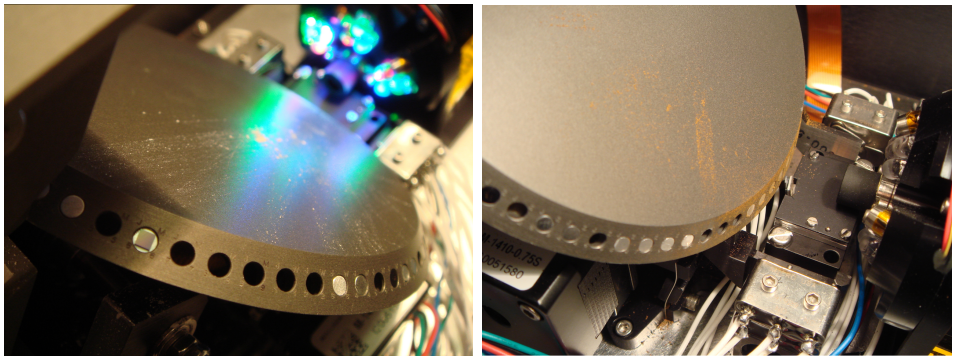
4.4.3 Sample delivery to the Substrates

Delivery to the substrates was performed using the sample scoop to simulate the scoop on the robot arm. After delivery, the SWTS was retracted into the MECA enclosure and the microscopes used to analyze the remaining material. In the most part, as the substrates move to the vertical position for imaging, the excess deposited material sloughs off under the influence of gravity and what remains is a much finer, less aggregated layer. This vertical orientation was used as a means to create sparse fields of particles which are modestly well adhered to the substrate surface.

Cross-contamination study

When material was delivered to a particular exposed substrate set and the SWTS withdrawn into the chamber, much of the material ($< 200\mu$m in size) fell away spreading over the face of the wheel and over adjacent substrate sets thus 'contaminating' them with this sample. Examples of these experiments are shown in Fig. 4.13 where aluminium oxide and JSC Mars-1 were deposited.

Fig. 4.14 shows two OM mosaic images of the strong magnet on a substrate set at the opposite side of the wheel to the substrates loaded with sample (so sat 180° rotation away and thus in front of the OM and AFM).



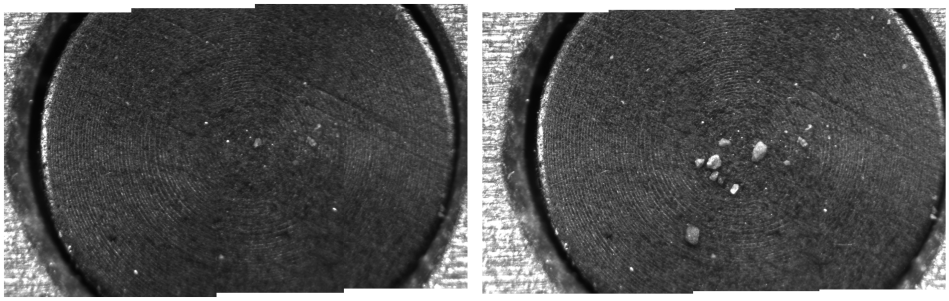
(a) (b)

Figure 4.13: Images of the SWTS and microscopes after delivery of material and then rotation of the loaded substrates by 180° in preparation for imaging. (a) A shows trail of fallen Al_2O_3 particles which tumbled across the wheel after rotation. (b) JSC Mars-1 particles fallen onto AFM scanner. In both cases both the wheel and AFM scanner were clean of visible particles before delivery of the sample.

The first image is taken before any loading of sample. The second is acquired after delivery of JSC Mars-1 onto the exposed substrates and translating the wheel in to safe to rotate, then rotating by 180° (as if bringing the loaded substrates round to be imaged), and then returning by rotating 180° to view the 'opposite' substrate. It is evident that a number of large particles had fallen across the wheel and in front of the AFM.

The implications of cross-contamination extend to concerns about safety for the AFM as even small particles falling on the chip may damage or contaminate the levers making them unusable, especially after repeated sample deliveries.

However, it was observed that most material fell sideways around the wheel when the wheel was in motion. Even the small gap under the side



(a) (b)

Figure 4.14: The strong magnet on opposite side of wheel to loaded substrates (a) before soil deposited and (b) after JSC Mars-1 was deposited and wheel translated. A number of large particles had fallen across the wheel.

slots allowed a significant amount of material to escape into the enclosure. As a result kapton 'wings' were added to the side slots on the flight and testbed models of the MECA boxes, shown for the flight model in Fig. 4.15, in order to try to limit the amount of material falling down the sides once the sample is acquired.

Of course, some cross-contamination is expected and material will move in under the 200μm slot and later fall away inside the chamber. To mitigate the effect of this contamination, strategies for imaging sample sets with preserving the unused 'clean' substrates were developed. The direction in which the SWTS is rotated after delivery to the substrate sets is carefully considered. As contamination of the leading set may occur during the translation or during the subsequent rotation, the direction of rotation of the wheel was chosen to rotate towards substrates which have been previously used or towards the slot in the wheel. Also, limiting the vibration of the wheel by choosing an optimum translation speed may reduce the lateral motion of

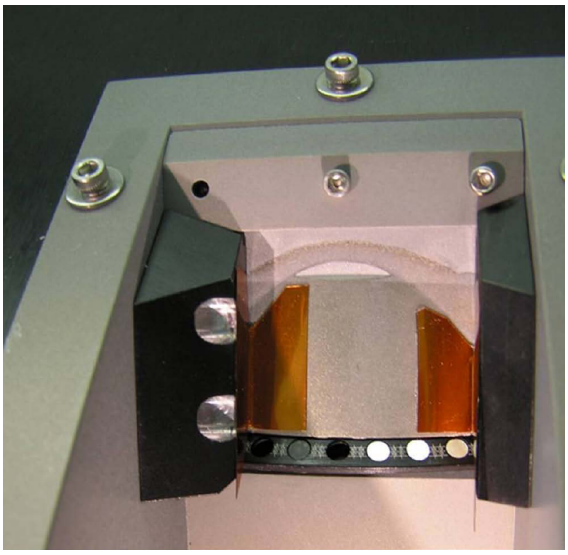


Figure 4.15: This picture of the extended SWTS was acquired just before final installation of MECA on the flight deck. Baffling was added in the form of Kapton tabs (orange-coloured flaps protruding forwards) to intercept particles that would otherwise escape sideways onto adjacent substrates. Image from JPL.

the material.

Also performed is pre-sample imaging, where the substrates are all examined with the OM, and in some cases AFM, before material is deposited. In that way if the substrates are already contaminated, the new material can be distinguished from what was already there.

Testbed Data

The OM data produced at Imperial College contributed to Calibration, Characterization and Cataloguing experiments required for the instrument. The SEM at Imperial allowed an independent assessment used for comparison where needed. The aspects investigated included for example the ability of the system to reconstruct known particle shapes (sphericity and roundness), textures, and structures such as aggregates in a wide range of samples.

Presented here is a study of JSC Mars-1 within the environmental chamber under vacuum conditions, the images for which are shown in Fig. 4.16. Material was collected on 4 types of substrate: nanobuckets, silicone, weak and strong magnets. No visible material was observed in the microbuckets. As the substrates were tilted from the horizontal to the vertical, if the adhesive moment of any particle is less than the gravitational moment, it fell off the substrate. In addition, vibration of the sample wheel during motion produced forces on the sample that were several times that of gravity. This caused additional removal of the sample from the non-magnetic substrates if the vibration forces were greater than the adhesion forces: loss of contact and consequently adhesion between sample and substrate led to

sample sloughing. The sample on the magnets also underwent redistribution under vibration, as the magnetic adhesion force only falls off gradually with sample-substrate separation giving the possibility of readherance during each vibration period.

Nanobuckets

Studying the sample delivered to the nanobuckets, Fig. 4.16(a), the 5μm pits (first strip) hold some selection of small particles (<20μm) and a few large ones. Larger particles (~50μm) appear on the 20μm pits and 20μm pillars (the second and forth strips respectively), which even hold some small clusters of particles. The 5μm pillars (third strip) hold a very large selection of small particles but few large ones.

The nanobuckets are a substrate primarily designed for AFM imaging, not for OM. However, the flat silicon between the features holds only a very sparse field of particles. The dark background and separation of particles provides good conditions to perform a size distribution analysis of the sample, as the individual particles can be seen. As the particles are small, this techniquie may be more useful on an airfall sample on Mars. From presample images, the material on the nanobuckets is all JSC Mars-1.

Weak Magnet

The pile of material on the weak magnet is estimated as 300μm high. Due to the stronger magnetic adhesion forces compared to the van der Waal forces of the silicon micromachined substrate, larger magnetic particles adhering to this substrate, up to 300μm in lateral diameter, with dimensions probably

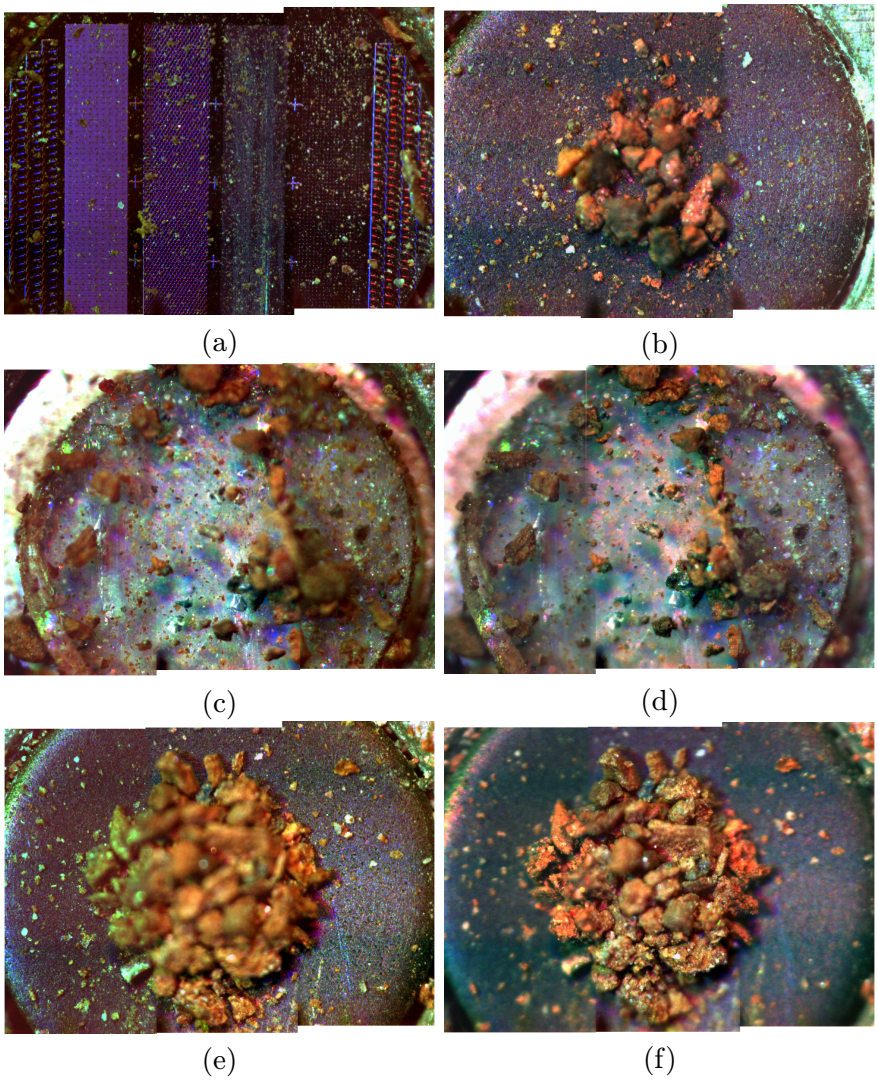


Figure 4.16: For each of the 4 substrates, mosaic of images were taken - centre, left and right - at various focus positions. The RGB images were composited from images in monochrome using the red, green and then blue LEDs. All OM images at 12 bits per pixel. (a) is the nanobucket, (b) the weak magnet, (c) the silicone focused on the substrate surface, (d) the silicone focused 160μm above the substrate surface, (e) the strong magnet focused on the substrate surface, (d) the strong magnet focused 240μm above the substrate surface.

more limited by the 200μm height of the loading slot than the strength of the adhesion forces.

Silicone

For this sample, a large amount of material adhered to the substrate, suggesting it is far more 'sticky' as a surface than the silicon of the nanobuckets, or aluminium surface of the magnets. Particles up to 250μm in diameter have adhered so leaving fewer opportunities for AFM scanning.

Strong magnet

The pile of material on the strong magnet is estimated as 600μm high, with particles even as large as 400μm lateral diameter. These larger particles of the sample are redistributed during sample wheel motion (see Fig. 4.16(e) and (f)), an indication that the magnetic forces are comparable to the vibrational forces for these larger particles, while the smaller particles show no redistribution, with adhesive forces dominating.

Analysis of testbed sample

Looking at the nanobucket substrate in Fig. 4.16(a), particles that were able to adhere to the substrate ranged between about 4 - 60μm, of silt size on the Wentworth Scale (Wentworth, 1922), with mass fractions fairly evenly distributed throughout the size range. The lack of particles above 60μm suggests that this limit is the size range above which the van der Waals forces are smaller than the gravitational pull assisted by the vibration of the wheel, suggesting that the sample may also have had larger grains that

were lost from the substrate. The particles are very small in terms of detail with the OM and the relatively sparse fields mean there are many good candidates for AFM.

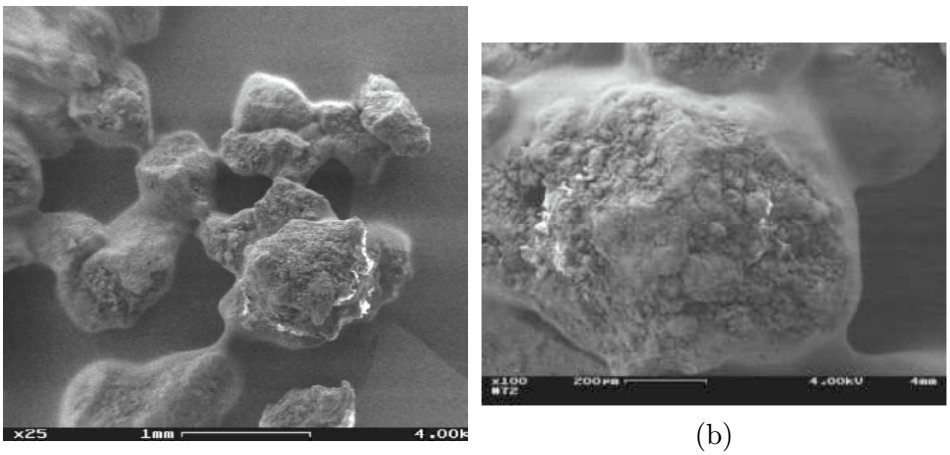
The presence of this additional material on the magnets is due to the strength of the magnetic force, indicating that these larger particles, at least, are magnetic - this confirms that these larger particles were indeed lost from the nanobucket substrate. The volume fraction is dominated by 250 to 350μm sized particles (fine to medium sand) though smaller particles are also present including a volume fraction of silt. By cross comparison with Fig. 4.16(a), this silt is very similar in appearance to the sample seen on the nanobuckets.

The grains are overall quite angular with some rounded grains, but the texture of the surface seems quite rough. When considered on the Krumbein particle roundness/sphericity chart these particles are estimated to rank 0.5 for roundness and 0.7 for sphericity (Drevin and Vincent, 2002).

The material on the silicone substrate seems very similar in shape, size distribution and colour to that on the magnets indicating that the material seen on the silicone is magnetic.

Considering the overall sample, there appears to be a continuous size range of particles, from 4 to 400μm, the complete range observable by the optical microscope. The sample has an overall reddish to pink colour with many white, grey, orange and brown blends. Small white particles can be seen with some large fairly rounded black particles evident on the silicone and the magnets.

Fig.4.17 shows SEM images of JSC Mars-1 material. Comparison to the



(a) (b)

Figure 4.17: SEM images of JSC Mars-1. From JPL document 'Characterization and Cataloguing Preliminary Report, Phoenix MECA Optical Microscopy'.

SEMs shows the ability of the OM to recognize the round/angular grains.

Pile heights on magnets

Pile heights are not always limited to 200μm heights above the substrate surface by the scraper. The magnetic substrates retain larger particles, as they scavenge material that has not adhered to other substrates during sample wheel translation and rotation. The through-focus series in Fig. 4.18 provides evidence of such pile heights using JSC Mars-1 deposited on a weak magnet substrate. The images show the stage being translated out, away from the AFM beginning from focus on the substrate through to focus of the top of the pile of particles, in 40μm iterations. In this case the height of the pile of particles is 400μm, given the number of iterations that were required to focus from the substrate to the top.

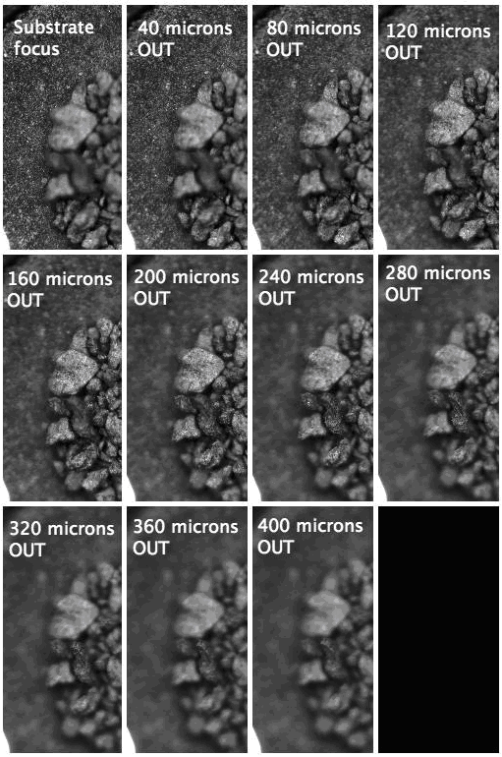


Figure 4.18: A through-focus series with the OM of JSC Mars-1 deposited on a weak magnet substrate. the series begins at the substrate surface and translated out until the top of the pile is in focus.

On the strong magnet piles nearly 1mm high have been observed. With the sample of HWMK11, as shown in the single image in Fig. 4.19, the strong magnet at the safe to rotate position with the top of the pile still not quite in focus. The pile is therefore over 800μm tall. This has implications for safety in regards to the AFM. The distance from the AFM on the surface to optical focus is 875μm on the Imperial College testbed. This distance means that piles of this height could touch the tips when the wheel is at the position for focus on the substrate surface. The height of the piles on Mars may be taller - for example due to reduced gravity. This means rotating past piles - even during a survey of a sample set - has some risk involved. Therefore all rotations between substrates should occur at the safe to rotate positions. The AFM near signal, which acts as a limit switch, should also be switched on during imaging - especially during a through-focus series.

Moving piles on magnets

The tall piles seen of material delivered to the magnets and 'scavenged' as the wheel moves have been observed using through-focus series. While creating such a series, the movement of particles was often observed as the wheel translated. This suggested that the piles were not stable as the vibration from the motors was enough to disturb the particles as the wheel moved in, but that the magnetic force holding the particles was great enough that the particles did not fall away completely. In Fig. 4.18 we see in the through-focus series that simply by translating in with the wheel by 40μm, there has been a shift in the position of some of the large particles - most easily seen on the bottom left of the pile. Although these may not seem like a large

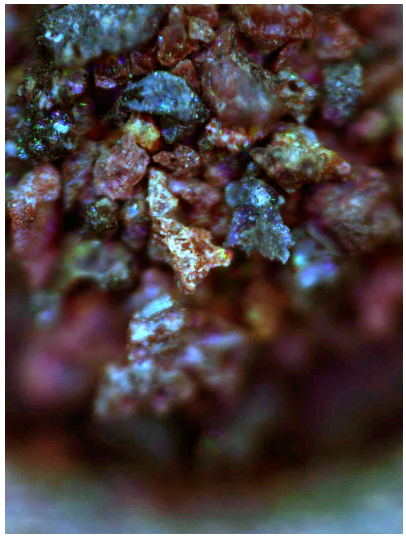


Figure 4.19: An OM image of the sample HWMK11 on a strong magnet with the wheel at the safe to rotate position.

movements, in terms of AFM they are huge and this is simply too dangerous for the tips.

Airfall on magnets study using AFM

To use the AFM to scan the material deposited by the scoop on the magnetic substrates would be at large risk to the AFM. The magnets are generally heavily loaded collecting large particles in dense fields and piles which are unstable when the SWTS moves. This makes finding a particle of a suitable size tricky and the targeting of particles difficult, as well as posing a threat to the tip.

One opportunity for AFM scanning on magnets may be provided by the airfall samples which are collected. Such substrates were provided by

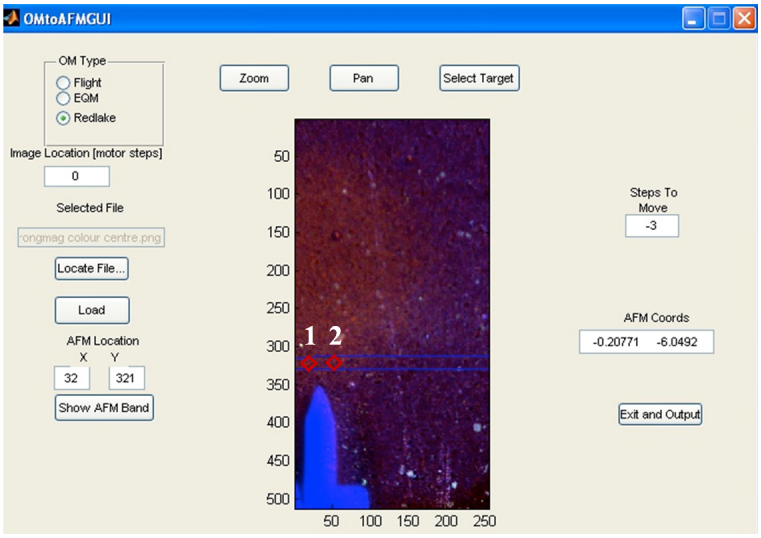
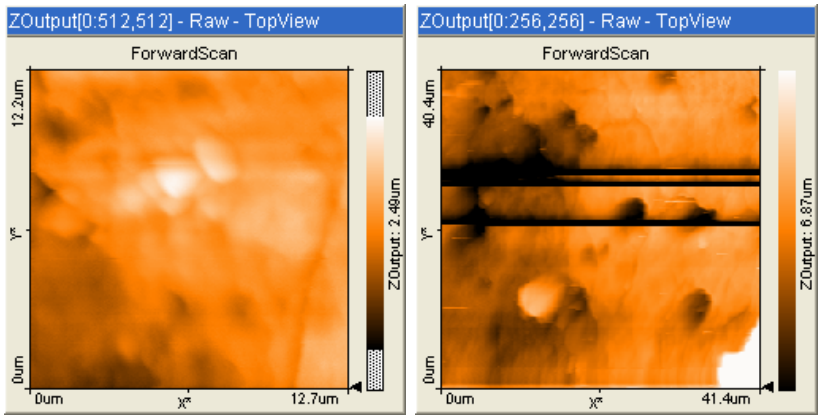


Figure 4.20: A snapshot of the Matlab OM to AFM targeting software showing two areas targeted with the AFM on a dustfall sample of Salten Skov on a strong magnet.

the University of Copenhagen and were analyzed on the testbed. The OM showed sparse fields allowing safe targeting on the substrates - as shown in Fig. 4.20 for the a sample with the material Salten Skov deposited on a strong magnet.

Two of the AFM scans of this sample are shown in Fig. 4.21. The first shows a small cluster of particles and the second a single 8μm particle.The scan in (b) shows the magnets to have pitted surfaces which can hold particles in much the same way as the nanobuckets. But the pitting is not regular and thus difficult to know which particles are in a pit. Nonetheless, these experiments show that the magnets, under certain circumstances, may be appropriate for AFM scanning.



(a) (b)

Figure 4.21: AFM scans of a strong magnet with a Salten Skov dustfall deposit. (a) shows particles of 2-3μm in size and (b) shown a single particle of 8um. Also in this second scan we see holes appearing in the substrate surface from the anodized aluminium casing of the magnets.

Tip breaking

Part of the work on the Imperial College testbed involved determining routines for procedures such as tip-breaking for heavily contaminated or damaged tips. The procedure of cleaving off a beam to expose the next could be fatal for the AFM if not conducted correctly.

The tip to be broken is placed in front of the cleaving tool as in Fig. 4.22. Alignment of the chip with the tool is critical and thus requires ground in the loop. Two images are returned from the OM during the procedure; the first is of the cantilever (if still attached to the beam) with the tip breaking tool in focus. For cantilevers 0 and 1, the alignment can be checked directly. For 2 to 7 the beams are outside the OM field of view so calculations based on what is in the image are performed to verify if the positioning is correct. Fig.4.23(a)

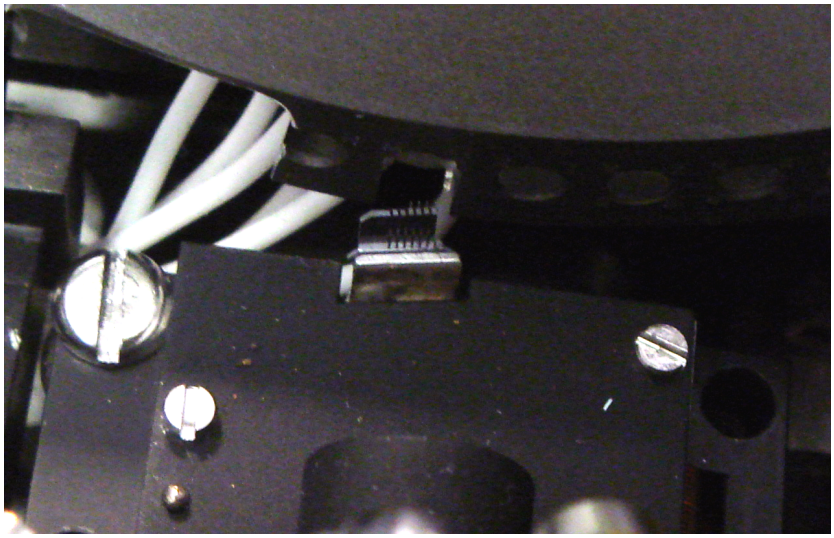
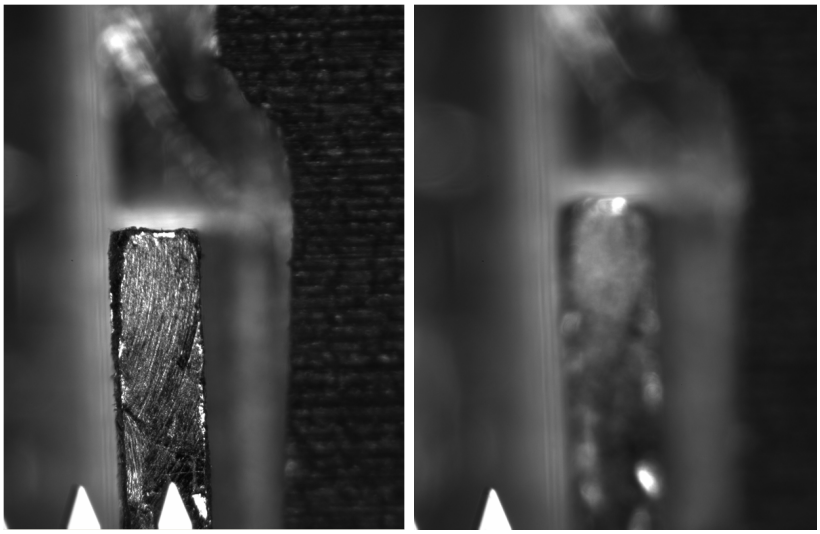


Figure 4.22: Camera image of tip 0 in front of the tip breaking tool.

shows the alignment of tip 0 against the cleaving tool. Confirming the focus of the surface also confirms that the distance from the AFM to the surface is known.

The second OM image returned to ground is confirmation that the beam (or at least the cantilever) has been broken. Although this does not provide a full confirmation as the beam may still be in place, in the case of breaking tip 0, it is possible to see that tip 1 is still intact.

Although ground is in the loop to check the alignment, the rest of the procedure is fully autonomous. At Imperial College the tips were broken in a semi-automated fashion - as much as the system would allow - by using macros to run some of the commands. A description of the procedure developed is described in Fig. 4.24. From the focus position to breaking the beam a distance of 3392 steps (848μm) was required. This meant the lever



(a) (b)

Figure 4.23: The two images returned during the tip breaking procedure; (a) at optical focus on the tip breaking tool before the beam has been broken - here showing tip 0 aligned with the tool; (b) after tip breaking - showing tip 0 missing.

- **Parameters: ROT pos= (-5929 + 24 x [tip no.+ 1] =) -5881 from CW and XLT pos= (91600 + 247x [tip no. + 1] =) 92094**

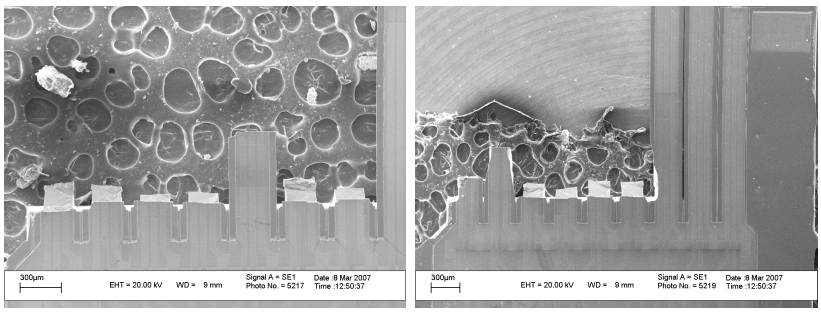
- First find extended position off as zero for translation.
- Translate out 65000 steps at speed 1000. Safe to ROT LS off at XLT pos=-2086.
- Continue translating out 65000 steps then 20000 steps at speed 1000. Extended LS on at XLT pos=-83360.
- Translate in 5000 steps at speed 1000. Extended LS off at XLT pos=-82639.
- Reset translation counter.
- Translate in 65000 steps then 20000 steps at speed 1000 to Safe LS on. XLT pos=82076.
- Rotate 7000 steps CW at speed 350. ROT1 LS on at ROT pos=5837. ROT2 LS on at ROT pos=5909.
- Reset counter.
- Rotate CCW 6000 steps at speed 350 to position past tip breaking tool.
- ROT2 LS off at ROT pos=-91. ROT1 LS off at ROT pos=-122
- Continue CCW (6000-122=) 5878 steps at speed 350 past tip breaking tool. ROT pos=-6000
- Rotate CW (6000-5881=) 119 steps at speed 350 to position tip 1 above tool. ROT pos=-5881
- Translate in (92094-82076=) 10018 steps at speed 350.
- Stopped by Focus position LS on at XLT pos=88702.
- Acquired image 'Tip1_256x512_shutter100_tip1breaking_atfocusLS_notip1'
- (N.B cantilever broken. Looked inside chamber - beam not broken.)
- Distance left to break beam is (92094-88702=) 3392 steps.
- Translate in 3392 steps at speed 350. XLT pos=92094. Beam broken.
- Move out to safe to rotate at speed 350. Focus LS off at XLT pos= 87983. Safe LS off at XLT pos=80537.
- Moved further 1000 steps at speed 350. XLT pos= 79537.
- Moved in 5000 steps at speed 350. Safe LS on at XLT pos=82723.
- Acquire image 'Tip1_256x512_shutter100_tip1breaking_afterbreaking_atsafe'

Figure 4.24: An example log of the procedure used. In this case for breaking beam 1.

was bent by approximately 3055 steps (764μm) from when it touched the surface.

Testing included breaking the beams from an entire chip from zero through to 6, until exposing tip 7, the last tip. Figure 4.25 shows SEM images of chips with the beams broken.

In the image in Fig. 4.25(b) beam 1 was broken not at the base of the beam, meaning that due to the 10° tilt of the chip, tip 6 and 7 were not able to reach the surface for scanning and the chip became unusable. The



(a) (b)

Figure 4.25: SEM scans of chips with broken beams. (a) shown the chip shown in Fig. 4.23 above. (b) shows a chip where beams 0 to 5 were broken.

problem is shown in Fig. 4.26. Although we have little control of how far down the beam breaks, it is important to realize that the risk of the later cantilevers being obstructed exists.

AFM Targeting

The accuracy of targeting samples with the AFM was important to understand in terms of the capability of placing the AFM within a lateral and vertical distance of a point identified in an OM image. The section below demonstrates the ability of the AFM in terms of targeting a particular feature.

Using the tip finder tool calibration substrate described in Section 4.3.4 (above), the actual tip location relative to the OM field-of-view was determined as 32 pixels from the left edge of the OM image, demonstrated in Fig. 4.27. By starting from an arbitrary start position, the wheel proceeded to move to a precise location.

First the SWTS was rotated to position the active lever over the sub-

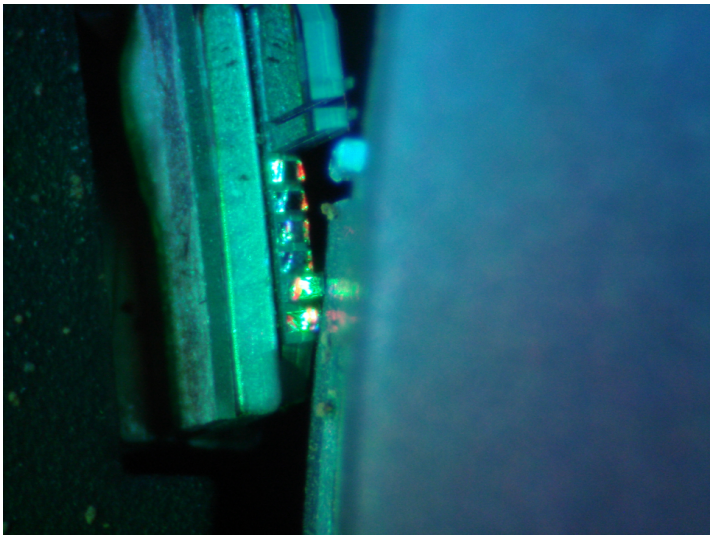
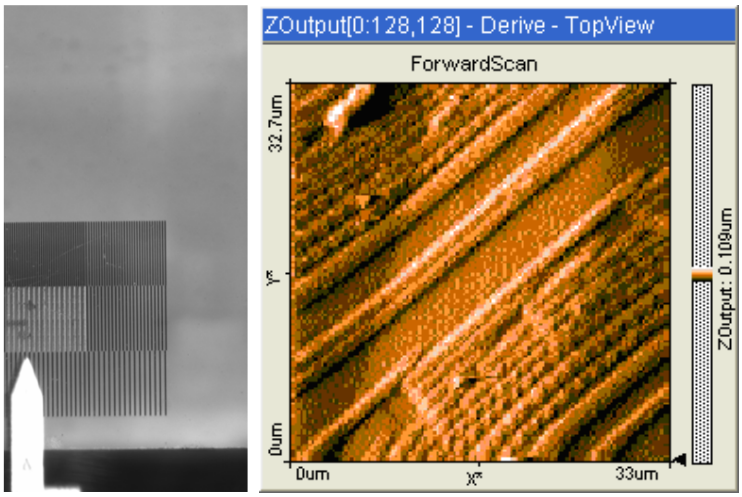


Figure 4.26: A camera image looking down on the AFM chip showing the remnants of beam 1 touching the SWTS and preventing tips 6 and 7 from reaching the surface.



(a) (b)

Figure 4.27: (a) An OM image of the fip finder substrate with the AFM tip ready to perform a scan. The coded area is just above the tip - the area with lightest stripes. (b) an AFM scan of the coded area.

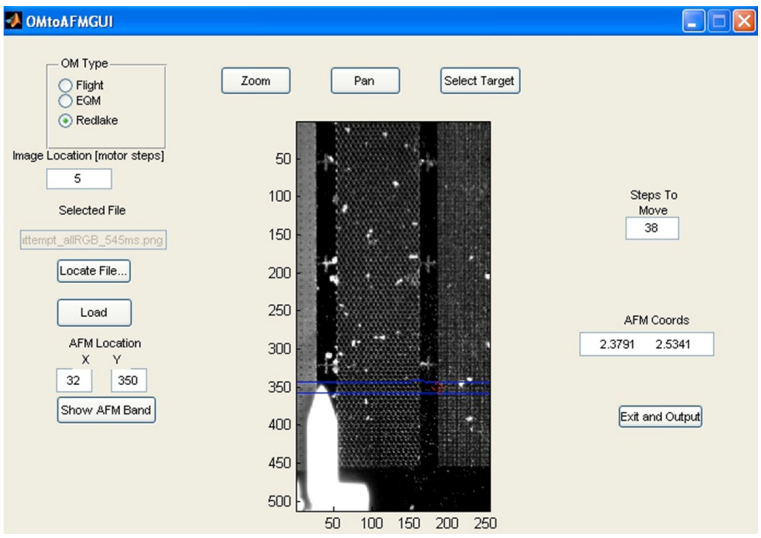


Figure 4.28: AFM GUI for target selection showing the target to be the left hand edge of the 5μm pillars.

strate of interest (one of the nanobucket substrates in this case) and an OM image at the optical focus position acquired. This image was input into the OM to AFM GUI Matlab utility to identify the region of the substrate accessible to the AFM - shown in the blue band Fig. 4.28.

A suitable target for the AFM to scan was identified, in this case, a pillar on the edge of the strip of the 55μm pillars (half the strip is visible on the right side of the image). A close-up of the targeted region is shown in Fig. 4.29 inside the red diamond. The Matlab utility then indicated the number of steps the sample wheel needs to be rotated to position the tip above the target region. In this case, 38 steps CW were required.

To avoid backlash errors, the wheel is rotated 100 steps CW, then 62 steps CCW to end up in the position shown in Fig. 4.30.

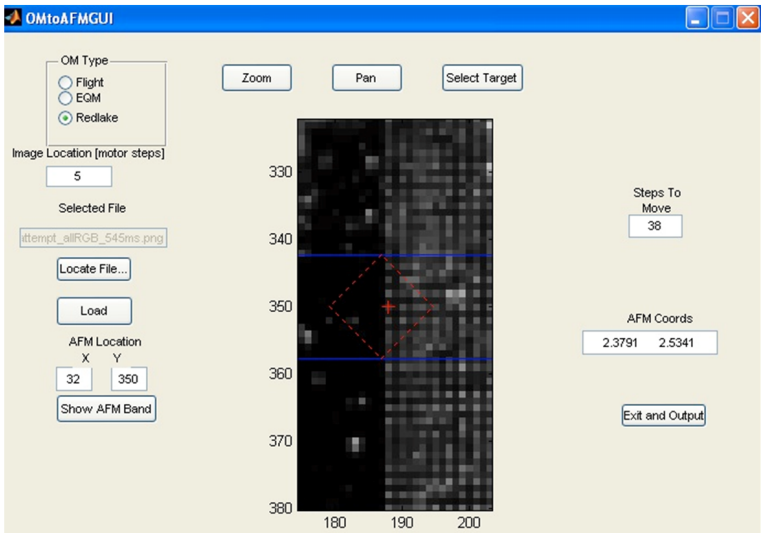


Figure 4.29: Close-up of the targeted region at the left hand edge of the 5μm pillar strip. The OM to AFM Matlab GUI indicates a move of 38 steps clockwise is required.

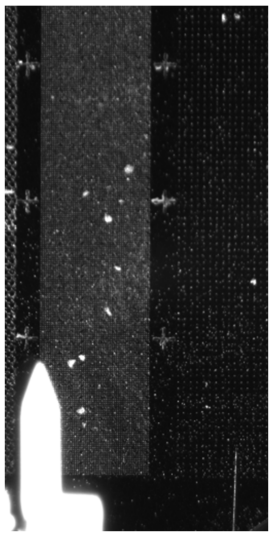


Figure 4.30: An OM image of the AFM positioned with the correct rotation ready to begin the approach for the AFM scan.

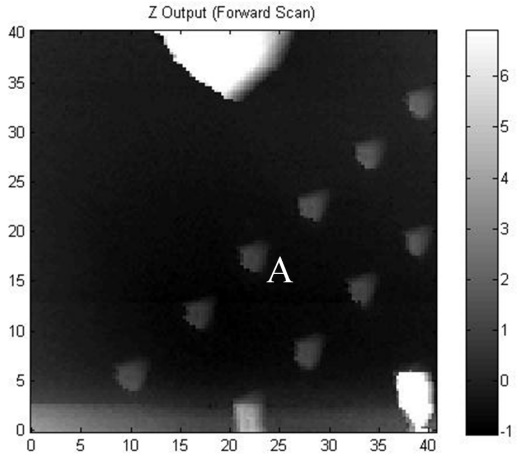


Figure 4.31: The AFM image shows the edge of the strip of 5μm pillars. The targeted region (measuring from the centre of the image to the centre of the pillar marked 'A') is within 3μm of the centre of the scan field. The bright regions are particles on the substrate which exceeded the z-range of the scanner. Note that the AFM co-ordinates are rotated 45° relative to the OM image. Dimensions are in micrometres.

An approach with the AFM was performed and a $40 \times 40\mu$m scan successfully executed shown in Fig. 4.31 (Time/line = 7s, channel gain = 0, x-offset = 2.375μm, y-offset = - 2.535μm, setpoint = 1.5V, P/I gains = 9/8) demonstrating the OM to AFM targeting capability to 3μm laterally.

For the vertical direction, we have no control of the AFM position using the sample wheel and the AFM tip will end up in a location determined by the vertical motion of the sample wheel on the flexures during translation from the optical focus position to the AFM contact position. The difference in the vertical position of the AFM tip over the substrate between these two translational positions has been determined as 140um.

4.5 Summary and Conclusions

The testbed at Imperial College is the only complete microscopy testbed outside JPL. The testing on this testbed provided invaluable experience in end-to-end testing in preparation for the mission. The main aspects investigated presented above which fed through to surface operations were:

i) The up and down motion of wheel. This will benefit AFM imaging as it provides to opportunity to see the region accessible to the AFM in the OM image without being obscured by the AFM cantilevers.

ii) Backlash compensation. The problem was quantified and demonstrated on how best to operate in order to avoid misalignment, especially when cleaving tips.

iii) Cross-contamination problems. This led to further kapton baffles being installed on the flight system which protect adjacent sets from becoming contaminated, with exception of the magnets which scavenge loose particles.

iv) Capabilities of the OM to characterize samples. This was done by comparison to SEM images and many samples were tested in the testbed under vacuum and non-vacuum conditions and the data catalogued which will provide a reference for images from Mars.

v) Piles of material on magnets. This was found to be much higher than the

expected 200μm scraper limit. The implications for AFM were examined and found to require extra precautions to protect the AFM from rotating past large piles and contacting them.

vi) Moving material on magnets. Particles moving on the magnets during the translation of the SWTS were observed. As a result the idea of attempting to image small areas of the large particles adhered to magnets was dismissed.

vii) AFM imaging on magnets of airfall samples. It was demonstrated that the magnets provide a good surface for AFM imaging when only a dustfall of sample has been deposited. This may be considered during the mission.

viii) Breaking cantilevers. Routines were developed and procedures for tip breaking examined and executed, identifying the further risks involved, such as a beam breaking too high and obstructing further tips from touching the surface.

ix) AFM targeting. This was practiced and demonstrated to within a 3μm accuracy.

Chapter 5

Data from Mars

The material in this Chapter is all from 350 million kilometers or 220 million miles away, acquired during Phoenix surface operations.

Phoenix's successful landing on 25th May 2008 was photographed by NASA's Mars Reconnaissance Orbiter's High Resolution Imaging Science Experiment (HiRISE) camera which caught Phoenix on it's descent shown in Fig 5.1.

The spacecraft quickly began to explore Mars and characterize the area around it. The robot arm was deployed and began to dig below the surface around the lander. An annotated image showing the dig sites for the primary mission of 90 sols is presented in Fig. 5.2 .

The material visible in the scoop from digging, shown for sol 007 in Fig. 5.3, can be imaged by the RAC and appears to be uniformly reddish-brown in colour and have a large particle size distribution, but with some white material perhaps ice or salt precipitates. The microscopy station has the ability to further analyze such material and determine more closely its



Figure 5.1: A HIRISE image of Phoenix descending towards Mars with a back drop of the Heimdall crater 10km in diameter. The full resolution image of the lander and its parachute is inset on the left. Image from NASA.

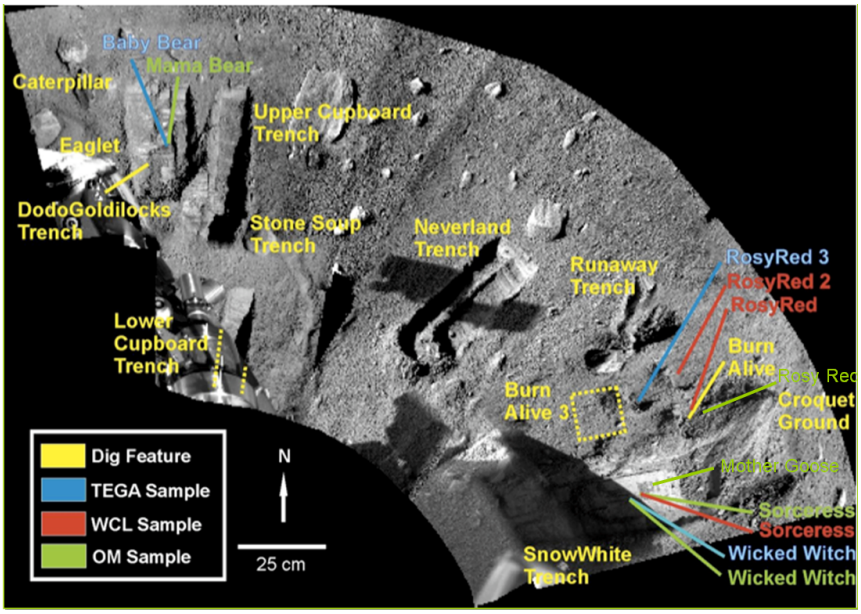


Figure 5.2: An annotated image showing the dig sites around the lander. Image from strategic planning during surface operations.



Figure 5.3: RAC image of the inside of the RA scoop on Sol 007 from the 'Knave of Hearts' as part of the first dig and dump trial.

composition.

5.1 Introduction to MECA Microscopy

The speed of electromagnetic waves means that signals take between 8 and 22 minutes to travel between the Earth and Mars. The spacecraft will therefore not be operated in real time. To run the AFM autonomously on Mars, strategies for acquiring data and operating procedures had to be developed. Imaging strategies spanning over many days were employed to give ground in the loop so as to decide whether proceeding would be safe for the instruments. Also, there are another ten instruments onboard, and tactical and strategic timelines create operational limitations and constraints.

A summary table of the RA deliveries to various instruments is shown in Fig. 5.4, as well as a schematic marking the samples collected on the SWTS

Instrument	Sol	Trench	Sample Name	Type of Sample
MECA OM	017	Goldilocks	Mama Bear	Surface
MECA OM	026	Rosy Red	Rosy Red	Surface
MECA OM	038	Sorceress	Sorceress	Scrape pile above ice
MECA OM	067	*Unknown*	Mother Goose	*Unknown*
MECA OM	075	Snow White	Wicked Witch	Scrape pile above ice
MECA OM	099	DodoGoldilocks	Golden Key	Scrape pile above ice
MECA OM	101	Stone Soup	Golden Goose	Subsurface
MECA WCL	027	Rosy Red	Rosy Red	Surface
MECA WCL	041	Sorceress	Sorceress	Scrape pile above ice
MECA WCL	066	Rosy Red	Rosy Red (redelivery)	Surface
MECA WCL	096	Stone Soup	Golden Goose	Subsurface
MECA WCL	102	Stone Soup	Golden Goose (redelivery)	Subsurface
TEGA	012	Goldilocks	Baby Bear	Surface
TEGA	064	Snow White	Wicked Witch	Scrape pile above ice
TEGA	072	Rosy Red	Rosy Red	Surface
TEGA	084	Burn Alive	Burning Coals	Surface

Figure 5.4: Overview of the dig samples delivered to MECA from the RA.

for imaging in Fig. 5.5.

5.2 Optical Microscopy

At the time of writing, over 2,300 images have been acquired by the OM. In the following section only a selection of the results are presented so as to describe the main findings and show what is achievable with the OM.

5.2.1 EDL/airfall

The first sample analyzed by the microscopy station was the EDL/airfall sample collected from the tongue out during landing as material is 'kicked up' by the retro rockets and also from the airfall during the first 4 sols of surface operations after which the wheel was retracted into the MECA box.

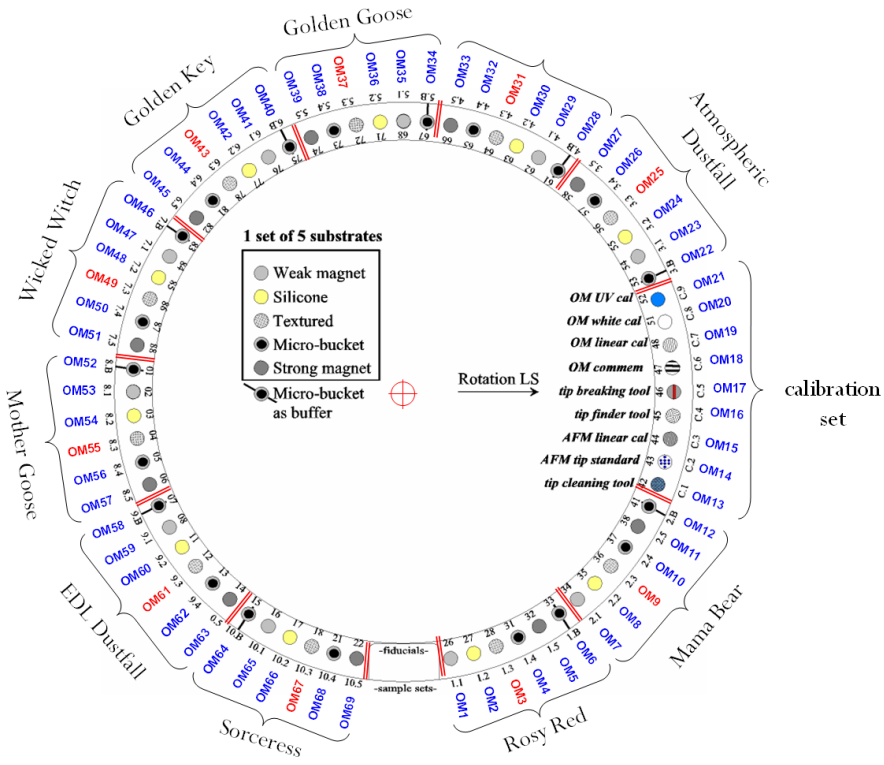


Figure 5.5: The SWTS wheel as it is populated to the date of writing this work. One set remains unused, and further material can be distributed over already used sets.

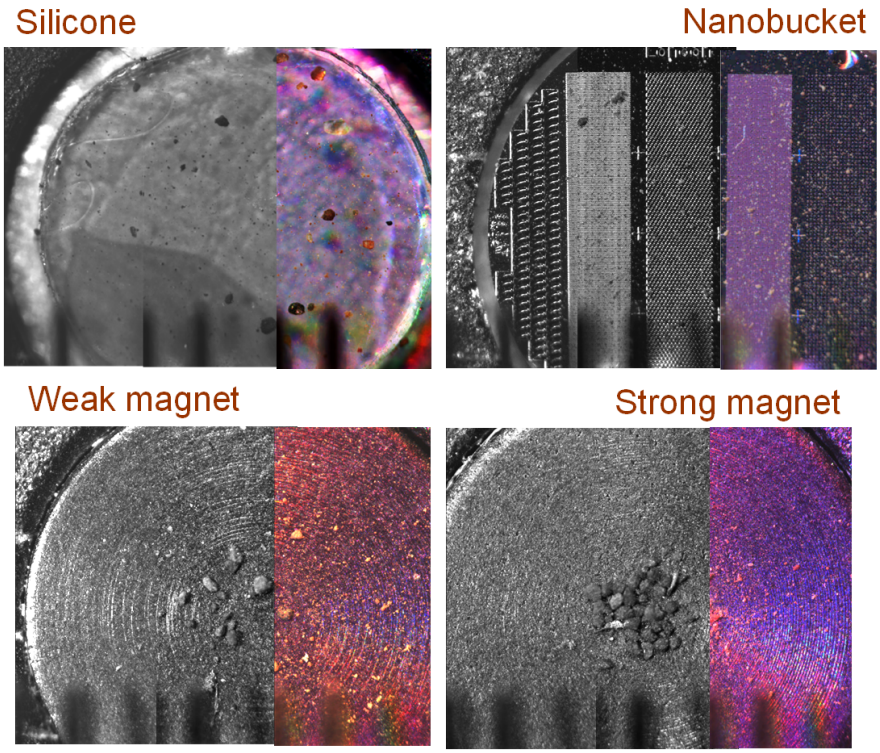


Figure 5.6: Blue mosaic and RGB composite OM images from sol 009 of the material redistributed by the landing jets and then further dustfall from the following 4 sols. At the bottom of the image, shadows from the AFM cantilevers are visible.

The four images in Fig. 5.6 taken on sol 009 of this sample are the highest resolution images of dust and soil yet acquired on Mars, or any other planet. For each substrate shown are three side-by-side OM images - one of which is a colour composite. The pre-sample images for this set are the cruise images shown at the end of Chapter 3 in Fig. 3.27. and cross-comparison shows most of the material collected is 'new' and of Martian origin.

The intention of this first experiment was to gain a 'first look' to char-

acterize the microscope, as well as an insurance policy to observe a sample early in the mission before delivery of a sample from the robot arm.

The images reveal grains as large as 150μm and down to the limit in resolution of the microscope. The material clearly has a magnetic component as the particles aggregate in the centre of the magnetic substrates where the field gradient is highest. There does not appear to be a larger presence of the finer material on the magnets, suggesting these finer particles are not as strongly magnetic.

The images demonstrate the diversity of mineralogy on Mars at high resolution revealing grains of a range of shape and colours, as seen in Fig. 5.7, in a material that otherwise looks just reddish brown when observed by the other instruments.

The sample collected on the nanobuckets show a distribution of particles up to 50μm in size. Some of the larger particles are highlighted in Fig. 5.8. Although the 5μm pillar strip (the one holding a small fibre) was already contaminated in the cruise images, there was a large increase in the number of particles suggesting most are from Mars. The particles do not seem to aggregate into 'clumps' on this substrate, giving a good opportunity for a particle size distribution analysis.

The silicone substrate also lends itself to give information about the particle size distribution. Two analyses are shown in Fig. 5.9, show excellent agreement with similar mean particle sizes of 11.2μm and 11.4μm, and a well matched profile of the size distribution plot shape. The analysis is limited as it will be unreliable below 2-3 pixels due to undersampling and JPEG artifacts, both of which cause problems for determining the size and shape

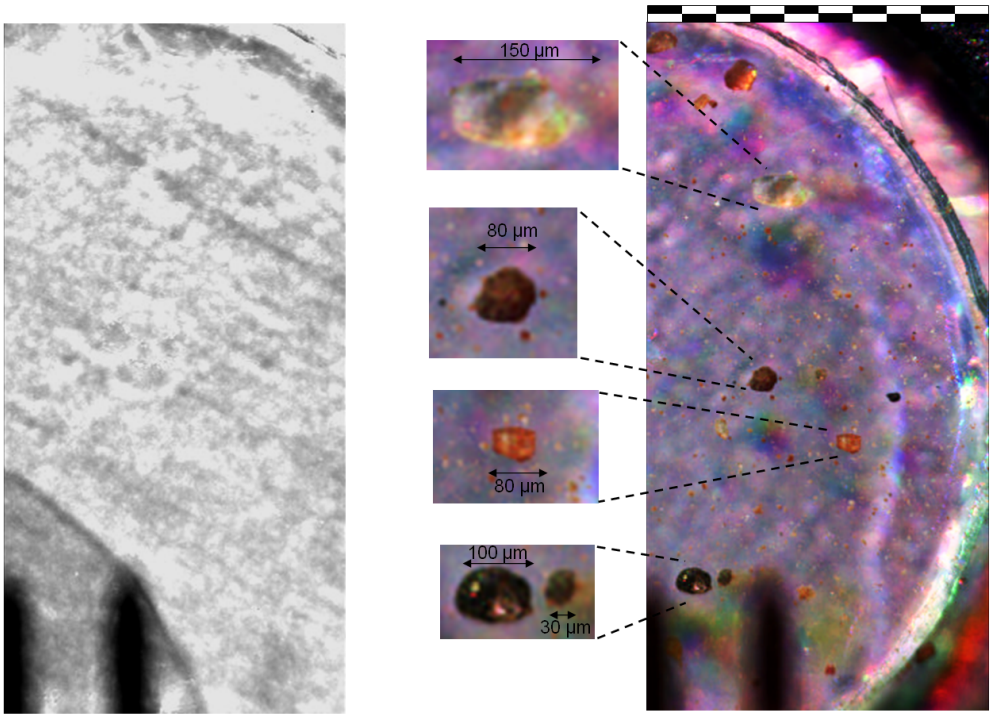


Figure 5.7: The silicone RGB composite holding the EDL/airfall sample. Sizes reach up to 150μm and some particles are reddish brown as typically expected from the Martian surface, while others appear translucent.

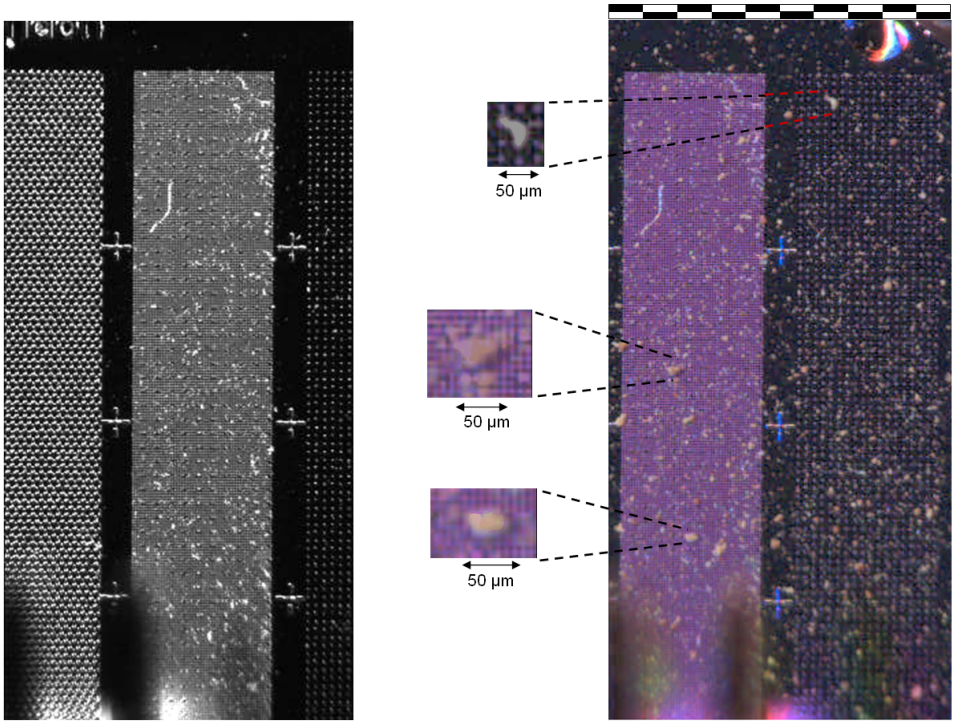
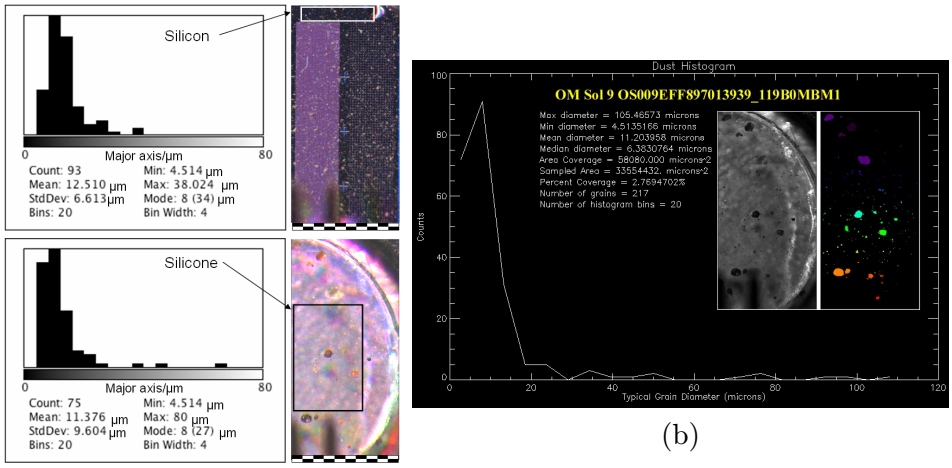


Figure 5.8: Comparison of the material on the nanobucket substrate before and after landing.



(a) (b)

Figure 5.9: Size distribution analyses of the EDL/airfall sample. (a) is of the silicone and a part of the silicon on the nanobucket substrate using the 'image J' software (from private communication: Tom Pike) and (b) an independent size distribution analysis of the silicone substrate by Brent Bos.

for smaller particles.

5.2.2 Mama Bear

The first dig sample delivered to MECA was Mama Bear - a surface sample from the dig cite 'Goldilocks'. This was the first surface sample analyzed by Phoenix, and the first sample collected from the surface and analyzed by any instrument since the Viking missions in 1977.

A view of the content of the scoop shortly before sample delivery is seen in Fig. 5.10. The sample was 'sprinkled' over the substrates by using the RASP to gently dust material over the exposed substrates. The deposition of the sample from the scoop is documented by the SSI camera in order to assess the success of the delivery. The three such images of before, during

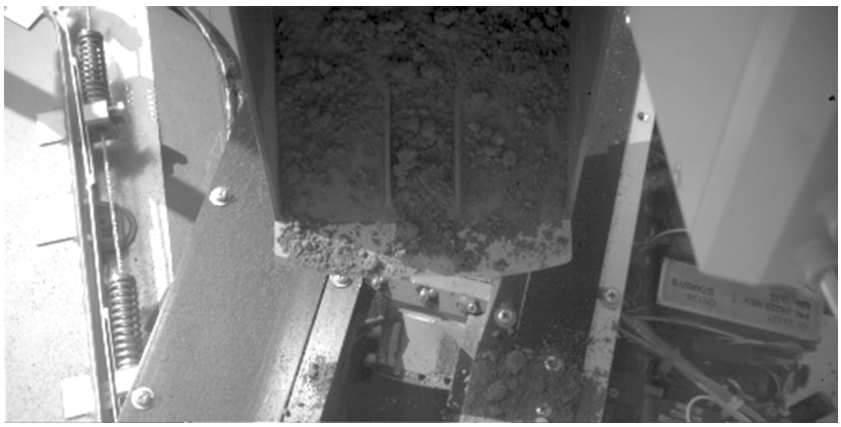
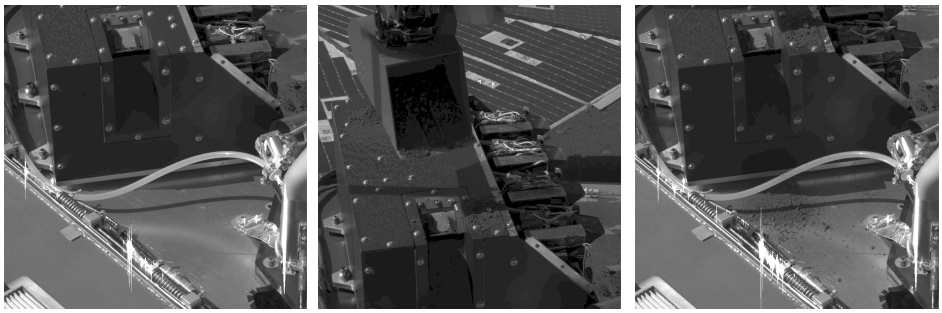


Figure 5.10: A RAC image of RA Scoop with sample poised over the MECA box.

and after sample delivery are shown in Fig. 5.11. The result is shown in Fig. 5.12.



(a) (b) (c)

Figure 5.11: SSI documentation of the sample delivery of Mamma Bear. Shown are (a) pre-delivery, (b) during delivery and (c) post-delivery images.

The nanobuckets hold a sparse field of particles with no large particles - as per their design. Also, as noticed in previous experiments, the 5μm pillars are most successful at collecting the small particles. The weak magnet

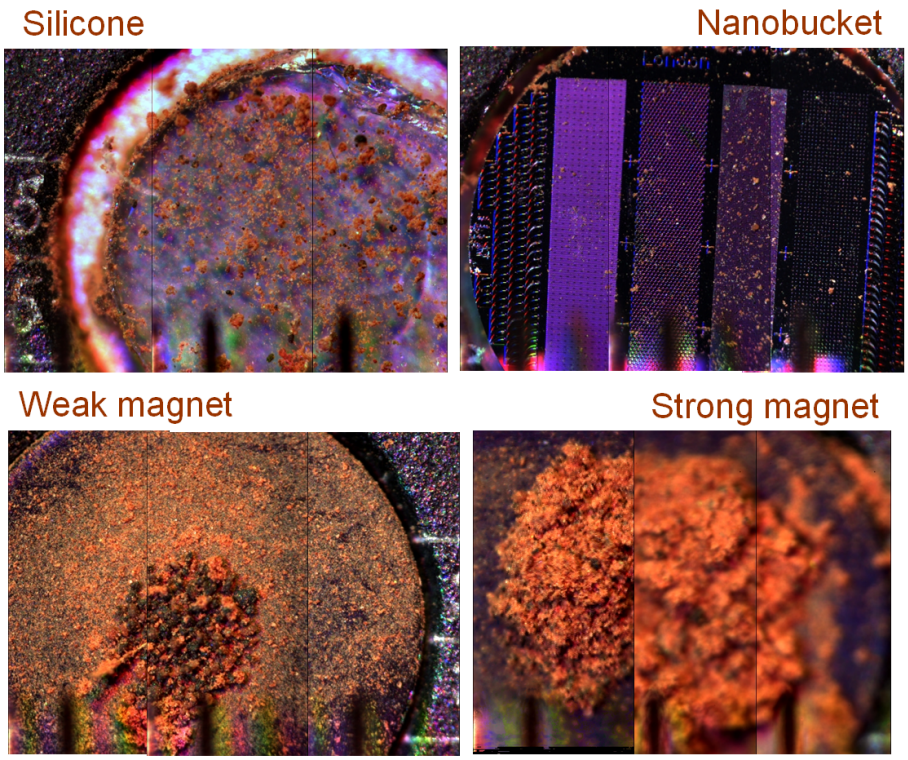


Figure 5.12: Full RGB mosaics of the Mama Bear sample delivered to MECA on sol 017. The left hand image of the strong magnet is a synthesized focused image created by using the in-focus parts of a number of images taken at different focal positions.

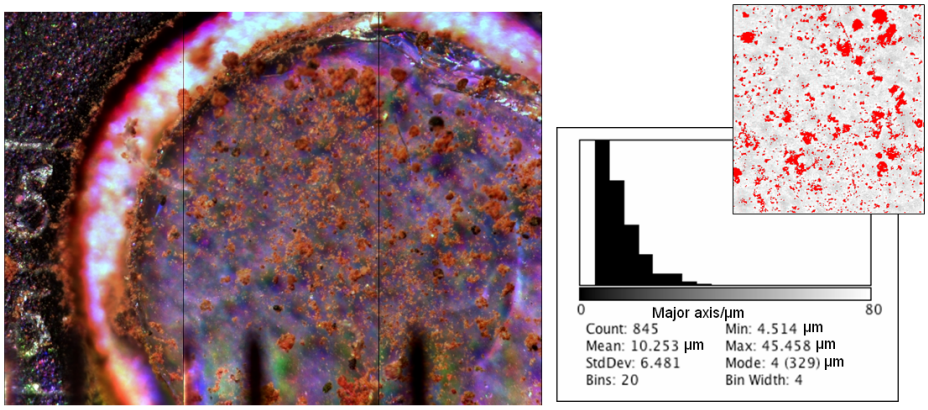


Figure 5.13: A particle size distribution for the silicone substrate of Mama Bear showing a mean particle size of 10.2μm (from private communication: Tom Pike).

collected many large red and black particles in the centre giving an indication that the particles are being pulled in.

The material on the silicone substrate is dominated by small clumps of fine particles close to the resolution limit of the microscope. Some large dark particles seem rounded and glassy resembling those seen on the EDL/airfall sample. The particle size distribution of Fig. 5.13 shows most of the material to be <30μm and continues until reaching the microscope's resolution limit. The particle size distribution may be weighted even more to the smaller particles than the analysis shows, as many of the small particles clump together appearing as one larger particle.

5.2.3 Rosy Red

The next sample delivered to the microscopy station was Rosy Red. This was another surface sample, but the material was quite different to that

seen from Mama Bear. The material was similar in that it also contained larger dark particles and fine red ones, as shown in Fig. 5.14. This time the material appeared much more sticky and stayed as a slab of material stuck to the substrate despite the vertical orientation. As a result the substrates were 'caked' in material - especially on the strong magnet. It is possible that the large magnetic particles act as 'pins' holding up the finer red matrix. In fact the huge clumps on the strong magnet required more than one through-focus image to see the entire pile.

This 'caked' material may be more representative of the soil as it is not biased by those particles more likely to stick in the vertical orientation. However, it is hard to get a size distribution of such a dense field. Also, the finer material appears so fine it is below the resolution of the Optical Microscope.

As the wheel rotates it vibrates and performs some selection on the particles. The large particles move towards the centre and the small ones fall off achieving an equilibrium energy orientation eventually. The time lapsed images in Fig. 5.15 show the same sample - with no new material delivered - of the Rosy Red strong magnet imaged with the OM 48 days apart.

5.2.4 Sorceress

Of the further samples analyzed, some interesting observations include the material on the sample Sorceress. From the 'smear' of material across the magnets seen in Fig. 5.16, it is difficult to discern whether there are any of the larger dark particles which have been observed in other samples. There

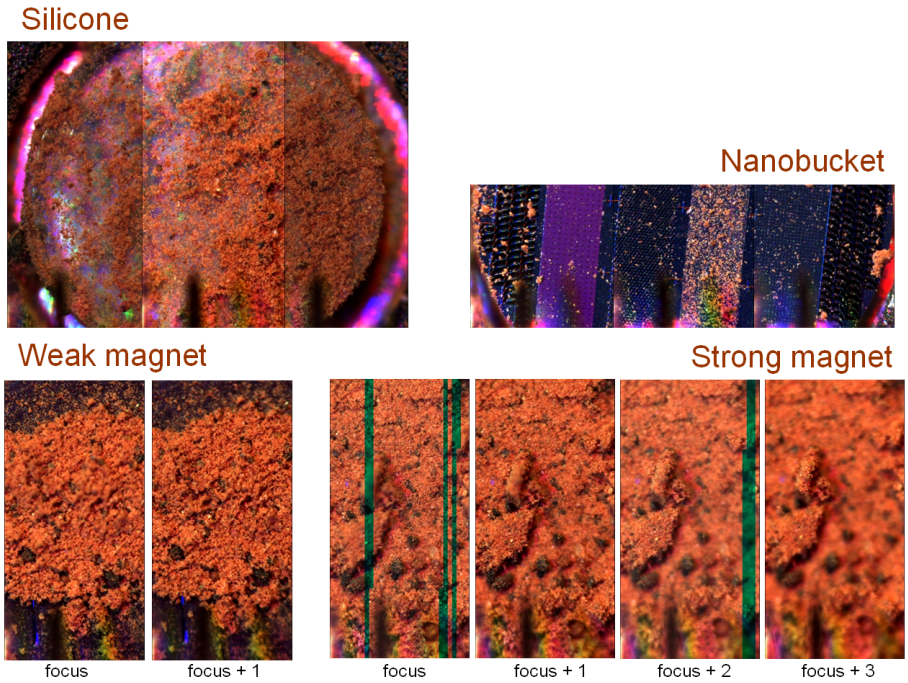


Figure 5.14: The post-delivery images of the Rosy Red sample delivered to MECA on sol 026. The lower portion only of the nanobucket substrate was imaged at a low compression, as this is the portion of the substrate useful for AFM targeting. Through-focus series images of the centres of the magnets were acquired of this sample and the data returned had some lines missing in the red.

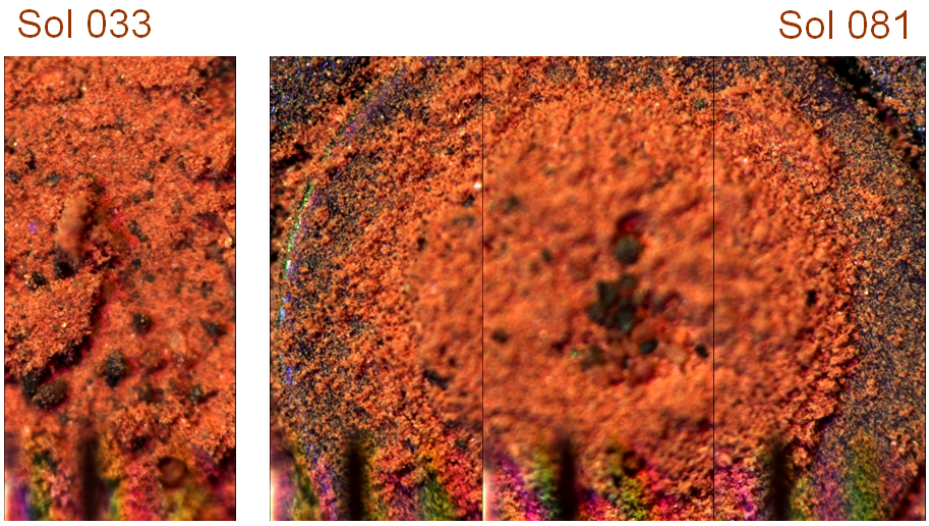


Figure 5.15: Two images of the strong magnet of the Rosy Red sample imaged at different stages of the mission. the Sol 033 image is just of the central portion of the substrate, whereas the mosaic of Sol 081 is of the whole substrate.

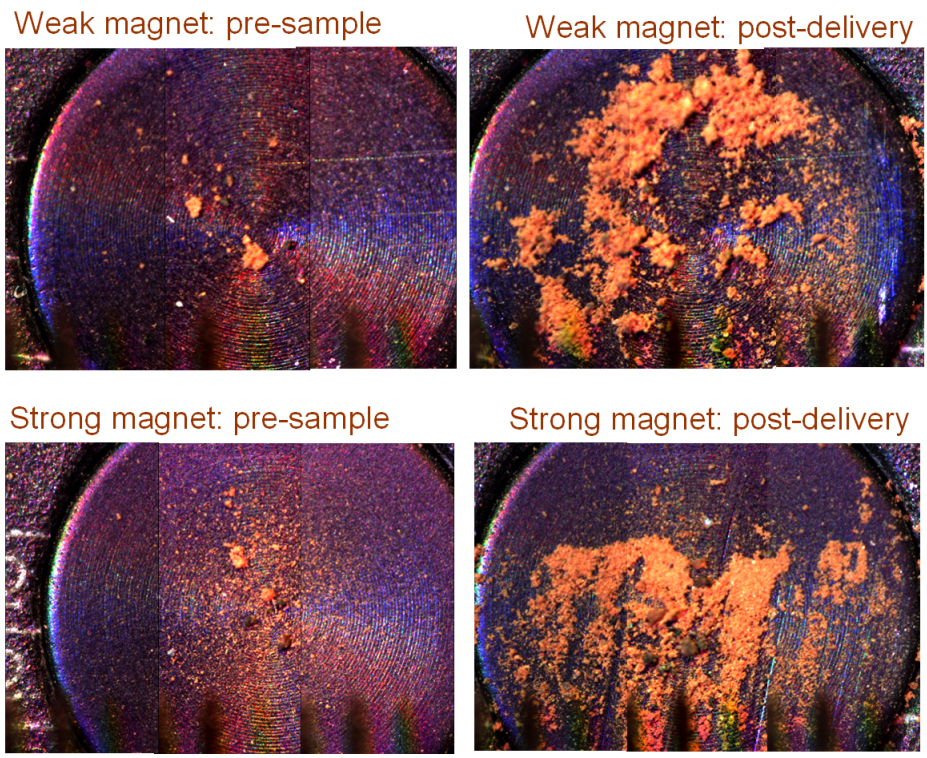


Figure 5.16: Pre- and post- delivery images of the strong magnets of the 'Sorceress' sample.

is no sign of new 'grains' - the larger particle range - and no sign of magnetic segregation.

The lines across the substrate are believed to be scratches as the substrates were drawn into the MECA enclosure under the scraper. On the weak magnet, these scratches are at an angle, suggesting the substrate had rotated by at least 90° since being drawn in. Substrates turning - in particular the magnets - has been observed for other substrate sets during the mission. This occurs as some substrates sit 'loosely' within the hole (unin-

tentionally) and can move when the SWTS is moving, due to the vibration.

5.2.5 Mother Goose

Also very interesting is the presample imaging, of what would soon be the 'Mother Goose' sample set, 058 sols into the mission. The magnetic surface of the strong magnet scavenged many particles from within the MECA enclosure, shown in Fig. 5.17. They appear to be of uniform size - all around 100μm, although they vary in colour from white through to deep red and orange and black.

This may be representative of the Martian material attracted by that magnetic field and thus an integration of all the particles acquired by MECA up to sol 058 and thus close to an equilibrium situation. As the wheel vibrates they are momentarily off the substrate but then almost immediately attracted by the magnetic field. The model would be based in terms of the densities of the particles and their magnetic behaviour.

As the SWTS vibrates, the particles move, clearing the fine layer of small red and white particles also collected. This further suggests that the larger grains are more magnetic than the finer particles making up the bulk of the matrix. It is possible that the finer material is a weathering product of the larger grains and the weathering has resulted in a change in colour and reduction in magnetism.

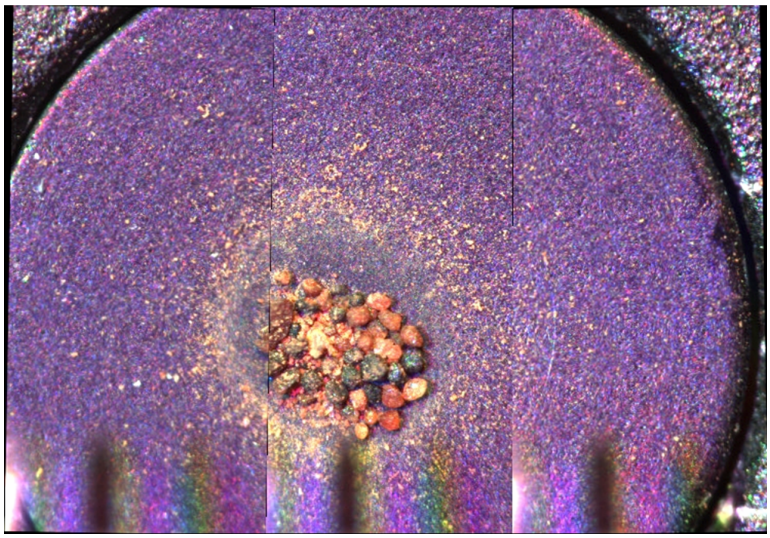


Figure 5.17: Presample image, acquired on sol 058 of the mission, of the strong magnet in the set for 'Mother Goose'. The large particles have collected in the centre and a 'halo' of small particles lie further out as those in the centre have been cleared by the movement of the large particles during the vibration of the wheel.

5.3 AFM Imaging

AFM has proved to be a great success on Mars and has returned many interesting images of great scientific value.

The instrument however got off to a slow start in the mission. Problems were mainly due to thermal drift. After a time of being switched on, some parts of the AFM electronics heated and caused an imbalance in the Wheatstone bridge. As a result, the AFM near signal asserted falsely disabling the stage. To cope with this, the AFM was frequently reinitialized, equilibrating the bridge and stabilizing the switch.

Consequently, through these delays, it was not until sol 044 that the first successful AFM scans were returned.

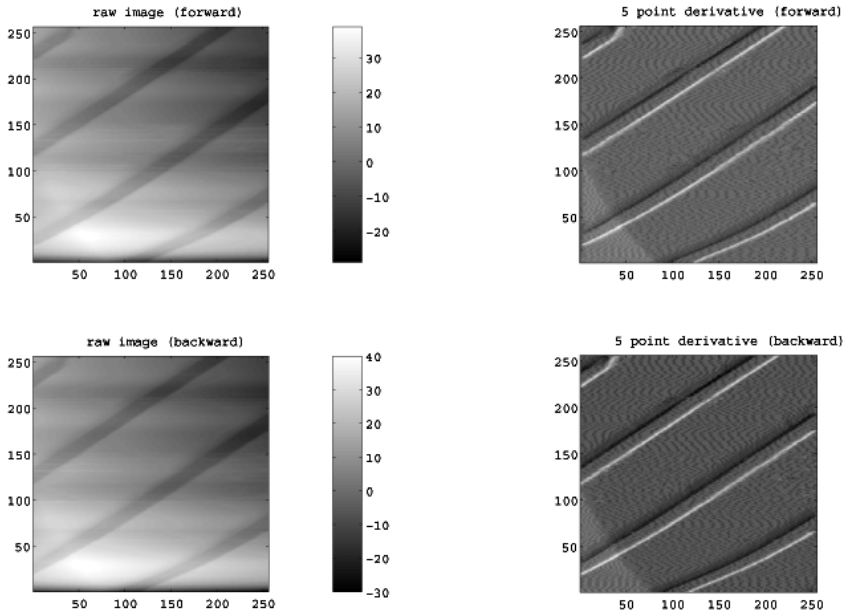
5.3.1 The First Scan

The first scan was performed in static mode, and the result shown in Fig. 5.18. These are the first AFM image from another planet, taking planetary microscopy to a whole new level. The image is of the tip finder tool and shows ridges 300nm tall, 4μm wide with a 6μm pitch. The three-dimensional image is slightly exaggerated in the vertical direction to amplify the features.

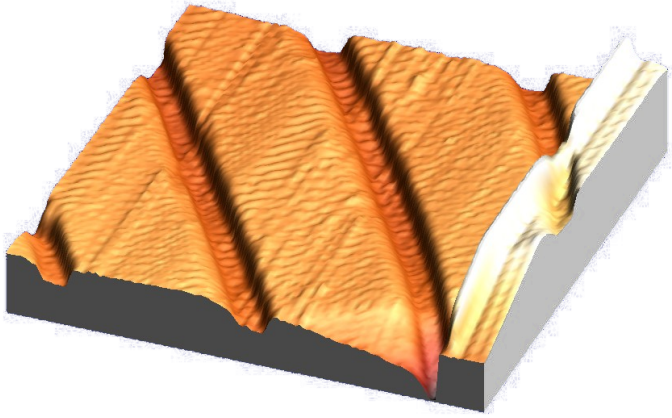
5.3.2 Nanobuckets

The tip finder substrate on the flight wheel was mounted too low to reach the coded region for tip finding. The nanobucket substrates provided the first definitive scan size measurement for the AFM scans on Mars.

Nanobuckets were also frequently used as an engineering check of the



(a)



(b)

Figure 5.18: (a) shows the raw data. 256 by 256 scan. The scan was in fact a $14 \times 14\mu$m scan and the features were 300nm tall. (b) shows a pseudo 3D solid representation of the data.

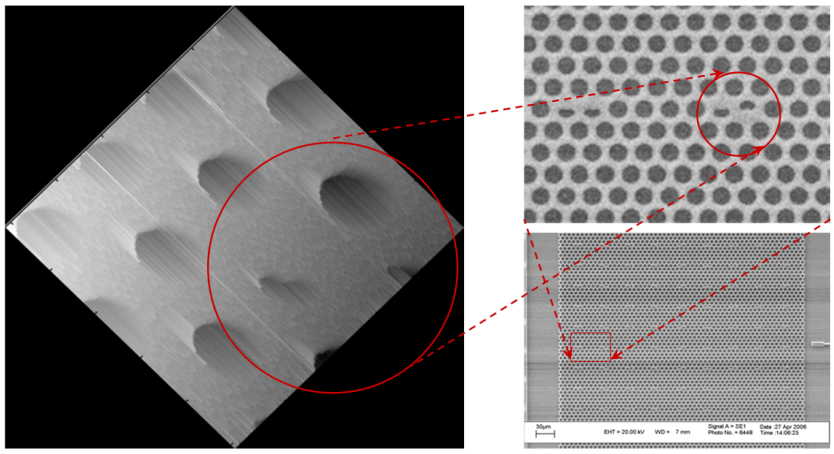


Figure 5.19: The AFM scan has been flipped and rotated into OM frame. The scan area is $20 \times 20\mu$m in size and performed in dynamic mode. The code is identified as the 2nd fiducial from the left edge (or 8th from the right) of the 5μm pit strip.

movements of the SWTS - for OM and AFM data. By scanning the code in the substrates, they provided accurate registration of the AFM scans to the OM region. The AFM scan on sol 109 shown in Fig. 5.19 of the 5μm pits, shows two code markings from which the position of the scan can be identified on the OM image. This position is marked in Fig. 5.20.

5.3.3 Martian Particles

The first scan of a Martian particle occurred on Sol 068. The scan was of the sample 'Sorceress' delivered to the microscope by the RA from the Snow White trench on Sol 038 of the mission. The area imaged was on the 5μm pit region for which the exact position is identified in Fig. 5.21. The scan itself is shown in Fig. 5.22 and shows a particle which is $1.5 \times 1\mu$m in size.

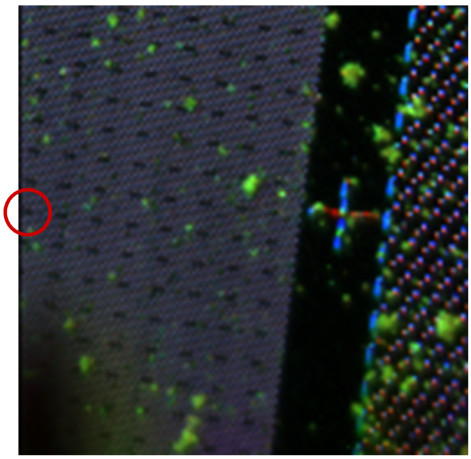


Figure 5.20: An OM context image for the AFM scan acquired without rotation offset. The red circle marks the location of the AFM scan. This corresponds to pixel 2 on the OM image.

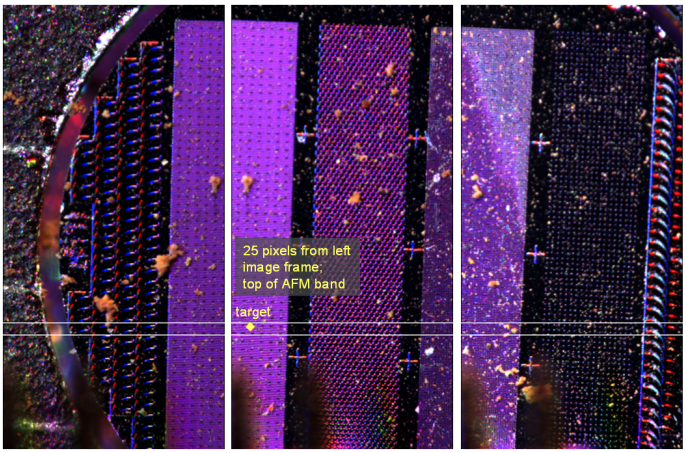


Figure 5.21: The OM images used to target the AFM scanning of Sorceress.

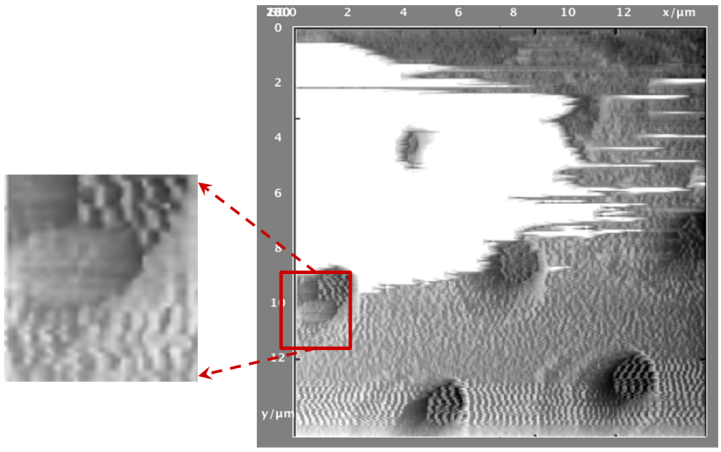


Figure 5.22: An AFM scan of 5μm pits on Sol 068 performed in dynamic mode. The image shows a small particle trapped in a pit. The particle is 1.5 x 1um in size.

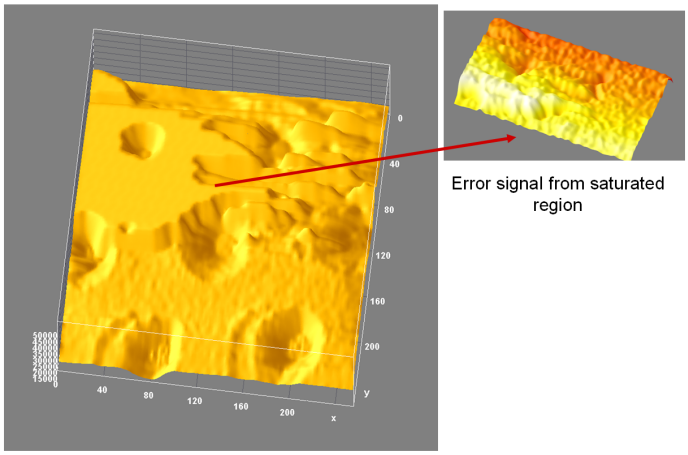


Figure 5.23: A 3D perspective image of the scan containing the particle in a pit performed on sol 068.

Fig. 5.23 is a three-dimensional representation of the scan area and to the right of it the error signal for the saturated region. This demonstrates that in the area where the z-output signal is saturated, the error signal is still changing with the surface shape. This is because even when the limit of what can be corrected in the z-direction is reached, a frequency can still be measured, and thus a frequency shift still recorded.

5.3.4 Identifying Minerals

Overall, the AFM has so far found three possible types of particles which have been recognized. The preliminary investigations show they are all clay-size particles.

One finding is the identification of a plate-like angular particle scanned on sol 074, shown in Fig. 5.24. The shape is very characteristic to a terrestrial material known as denticulated pyroxene - an SEM of which is shown in the same figure.

The angular shape and the smooth surface are consistent with the appearance of the denticular pyroxene mineral, as marked in the images. Marked also is what may be a smectite particle in the same image. As within the SEM scan also, it is not unusual for the two to be found close together yet separated by a pore space as denticulated pyroxene is a precursor of smectite.

On Sol 112 images were acquired from the silicone substrate OM54 with a sample from Mother Goose, as shown in Fig. 5.25. Although the particles move around a little in the image, in areas where the particles are stable, clear features can be identified. These are very similar to the structure of

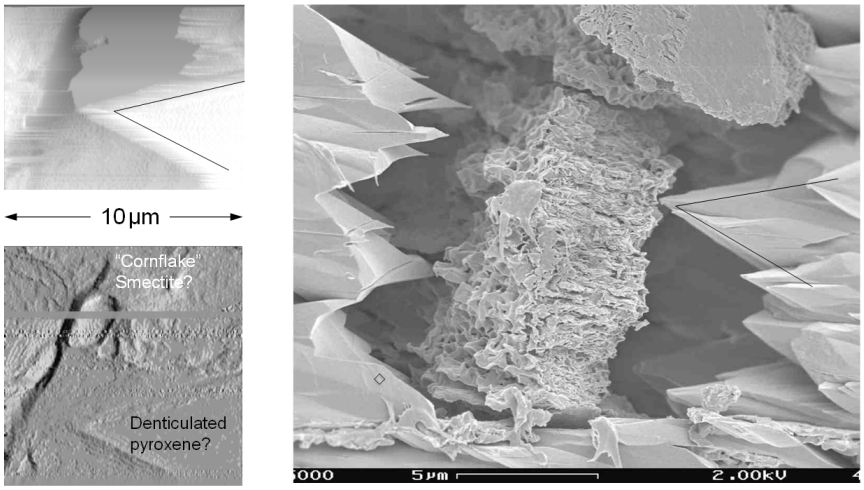


Figure 5.24: On the left are two views of an AFM scan on Sol 074. The top scan is the bottom section of the z-output signal and the bottom scan shown the error. On the right is an SEM image of Denticulated pyroxene and Smectite. Marked are some characteristic angles for this mineral seen within the images. SEM image courtesy of Michael Velbel (Michigan State University) and William Barker, (University of Wisconsin-Madison). From the image database of the Clay Minerals Society and the Mineralogical Society of Great Britain and Ireland at http://www.minersoc.org/pages/gallery/claypix/index.html.

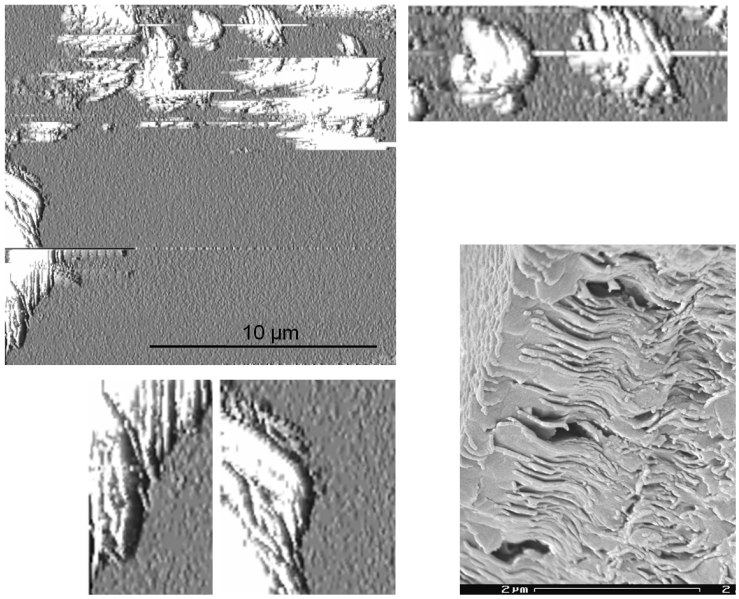


Figure 5.25: To the left and top are Sol 112 AFM scans of OM 54 Mother Goose sample on a silicone substrate some of which show enlarged areas. On the bottom right is an SEM scan of Notronic smectite showing very similar features. Image from the image database of the Clay Minerals Society and the Mineralogical Society of Great Britain and Ireland at http://www.minersoc.org/pages/gallery/claypix/index.html.

notronic smectite.

Another possible mineral match is the identification of hexagonally angled particles characteristic of kaolinite. Scans performed on Sol 085 of the atmospheric dustfall material on silicone substrate OM 24 show such features, as shown in Fig. 5.26.

Finally, Fig. 5.27 shows a section from recent CRISM data published in nature which has some interesting findings relevant to this work. Some parts of the work have been highlighted in bold to show the relevance to the Mars data.

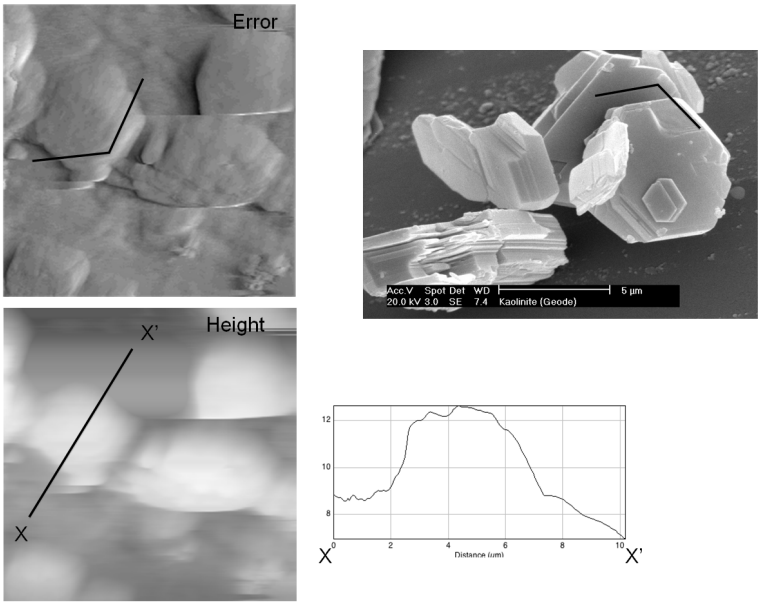


Figure 5.26: On the left of the figure are an error and height scan of the AFM imaging of the atmospheric dustfall on Sol 085. To the right is an SEM scan of a sample of kaolinite. Also shown is a line scan showing the height data across the imaged grain. SEM image from the image database of the Clay Minerals Society and the Mineralogical Society of Great Britain and Ireland at http://www.minersoc.org/pages/gallery/claypix/index.html.

Hydrated silicate minerals on Mars observed by the Mars Reconnaissance Orbiter CRISM instrument
Nature 454, 305-309 (17 July 2008)
Mustard et al.

Phyllosilicates, a class of hydrous mineral first definitively identified on Mars by the OMEGA (Observatoire pour la Mineralogie, L'Eau, les Glaces et l'Activitié) instrument preserve a record of the interaction of water with rocks on Mars. Global mapping showed that phyllosilicates are widespread but are apparently restricted to ancient terrains and a relatively narrow range of mineralogy (Fe/Mg and Al smectite clays). This was interpreted to indicate that phyllosilicate formation occurred during the Noachian (the earliest geological era of Mars), and that the conditions necessary for phyllosilicate formation (moderate to high pH and high water activity were specific to surface environments during the earliest era of Mars's history. Here we report results from the Compact Reconnaissance Imaging Spectrometer for Mars (CRISM) of phyllosilicate-rich regions. We expand the diversity of phyllosilicate mineralogy with the identification of **kaolinite**, chlorite and illite or muscovite, and a new class of hydrated silicate (hydrated silica). We observe diverse Fe/Mg-OH phyllosilicates and find that **smectites** such as **nontronite** and saponite are the most common, but chlorites are also present in some locations. Stratigraphic relationships in the Nili Fossae region show olivine-rich materials overlying phyllosilicate-bearing units, indicating the cessation of aqueous alteration before emplacement of the olivine-bearing unit. Hundreds of detections of Fe/Mg phyllosilicate in rims, ejecta and central peaks of craters in the southern highland Noachian cratered terrain indicate excavation of altered crust from depth. We also find phyllosilicate in sedimentary deposits clearly laid by water. These results point to a rich diversity of Noachian environments conducive to habitability.

Figure 5.27: An abstract of recently published CRISM data.

5.4 Conclusions from MECA microscopy

The OM imaging shows the Martian soil at the Phoenix site is made up of two major and one minor component.

- **Fine particles (majority component.)** Fine, orange particles appear to form cohesive clumps smaller than 20μm in size, with a mean around 10μm. The presence of fine particles is confirmed by the AFM to below 1μm (Krumbein > 6, (Drevin and Vincent, 2002)). This type of material appears to be weakly magnetic.

- **Larger multi-coloured grains (majority component.)** These are 50 to 100μm in diameter (Krumbein <5) and are strongly magnetic and subrounded. They contribute to approximately 20% of the total sample by volume, although this may be more by mass as orange fines appear somewhat 'fluffy'.

- **White particles (minority component.)** These are approximately 10μm in size and attribute to 1% by volume or less of the total sample.

AFM imaging of loose particles of this size was expected to be technically challenging. However, results show the successful imaging of individual grains from the soil. The particles shapes that the AFM has identified are from features too fine to be visible in the OM. The AFM is providing scientific information at a resolution 100$\times$ better than any previous instrument, and together with OM is capable of giving information on both the composition and formation of the Martian soil.

Chapter 6

Conclusions and Further Work

6.1 Contributions of this thesis

This work has been critical to image with a resolution 100× better than any other instrument sent to Mars. Importantly, it has led to some initial identifications of some clay particles.

Prior to this work, scanning loose particles with an AFM was only possible by gluing them down and with close monitoring from the user. In order to scan with an AFM successfully on Mars, a new technique was presented with the particular element of novelty to be the mechanical trapping of the sample.

This thesis has provided an understanding of the lateral forces acting on a sample from the tip during scanning with an AFM. The magnitude and direction of the force was determined for the Mars AFM system and put in

the context of the particles the AFM is scanning on Mars. In the complex field of particle adhesion, the work presents a theoretical discussion of the forces acting on a single particle so as to explain the difficulties of imaging such particles with an AFM.

The work in this thesis demonstrates how etched silicon substrates with a selection of features facilitate the sorting and gripping of particles to allow AFM scanning. Certain features - namely arrays of tiny pits and pillars - were successful at isolating and immobilizing particles allowing both the individual particles, aggregates and small areas of large particles to be scanned, giving information on sizes, shapes and surface morphologies. Patterns which gave selections of particles thought to be of interest to Phoenix were identified and selected for the Mars substrate design and their effectiveness tested - on Earth and on Mars.

6.2 Thesis Objectives Revisited

The objectives set out at the beginning of this thesis called for the design of new substrates to stabilize particles for safe AFM scanning of material on Mars, in the form of micromachined silicon substrates known as 'nanobuckets'.

This involved the study of lateral forces from an AFM tip during scanning - an area of great interest but previously explored to a limited extent only - which was achieved on a quantitative level by identifying the nature of the forces and their magnitude.

The testbed at Imperial College, which contains a copy of the flight

microscopy station within an environmental chamber, was successfully set up and used to investigate the materials in preparation for observations on Mars; this included testing the effectiveness of the designed nanobuckets and assessment of how they would be useful on Mars.

In summary, the objectives of this thesis were achieved through the design, manufacture, delivery, implementation and use of the substrates for the Phoenix mission.

6.3 The objectives of the Phoenix Microscopy Station

The MECA Microscopy station has met its official full mission success criteria to acquire 'Samples of the surface soil and two depths to MECA' and also to 'Use MECA to analyze 3 samples in its microscopy station.' This has allowed the characterization of the dust and soil grain particles from the atmosphere and the surface of Mars, the result of which will help understand the climate and history of the planet.

Having acquired over 2,300 OM images and many AFM scans, the microscopy station will continue to obtain data from Mars for as long as the conditions of the Martian Arctic allow.

6.4 Conclusions

The particles are difficult to stabilize and the forces acting on them are hard to measure. The lateral forces from the AFM tip acting on a particle, even

when scanning in the dynamic mode, are not insignificant when compared to the adhesive forces keeping the particle on the substrate.

Micromachined features have been shown to be successful for stabilizing particles for AFM scanning and provide a new method to investigate loose particles.

6.5 Further Work

This section highlights some of the areas which in the author's view would benefit from further research:

- Understanding the lateral forces involved in AFM scanning is important for applications beyond scanning of particles. For example, AFM is often used to image very sensitive samples, especially in the field of biology; or AFM can be used to push nanoparticles as in the field of nanomanipulation. The lateral force model could usefully be extended to cover the more general application and to other microscopy systems.

- To understand the particle shapes identified by the AFM on Mars, further work will be carried out on the Imperial College system to image some of the clay candidate particles and confirm the features recognized on Mars. This is important work in the ongoing quest to determine the presence of liquid water on Mars.

Bibliography

MM Abbas, D. Tankosic, PD Craven, JF Spann, A. LeClair, EA West, JC Weingartner, A. Tielens, JA Nuth, RP Camata, et al. Photoelectric Emission Measurements on the Analogs of Individual Cosmic Dust Grains. *The Astrophysical Journal*, 645(1):324–336, 2006.

Inc. Advanced Surface Microscopy, date accessed: July 2008. URL `http://www.asmicro.com/Equipment/MultiModeAFM.htm`.

L. Aeschimann, F. Goericke, J. Polesel-Maris, A. Meister, T. Akiyama, B. Chui, U. Staufer, R. Pugin, H. Heinzelmann, NF de Rooij, et al. Piezoresistive scanning probe arrays for operation in liquids. In *Journal of Physics: Conference Series*, volume 61, pages 6–10. Institute of Physics Publishing, 2007.

Co. Agilent Technologies, date accessed: May 2008. URL `http://nano.tm.agilent.com/index.cgi?CONTENT_ID=253`.

SJ Ahn, YK Jang, SA Kim, H. Lee, and H. Lee. AFM nanolithography on a mixed LB film of hexadecylamine and palmitic acid. *Ultramicroscopy*, 91(1-4):171–6, 2002.

T. Akiyama, S. Gautsch, NF de Rooij, U. Staufer, P. Niedermann, L. Howald, D. Müller, A. Tonin, H.R. Hidber, WT Pike, et al. Atomic force microscope for planetary applications. *Sensors & Actuators: A. Physical*, 91(3):321–325, 2001.

TR Albrecht and CF Quate. Atomic resolution imaging of a nonconductor by atomic force microscopy. *Journal of Applied Physics*, 62:2599, 1987.

S. Alexander, L. Hellemans, O. Marti, J. Schneir, V. Elings, PK Hansma, M. Longmire, and J. Gurley. An atomic-resolution atomic-force microscope implemented using an optical lever. *Journal of Applied Physics*, 65: 164, 1989.

C.C. Allen, K.M. Jager, R.V. Morris, D.J. Lindstrom, M.M. Lindstrom, and J.P. Lockwood. JSC Mars-1: A Martian Soil Simulant. 1998a.

CC Allen, KM Jager, RV Morris, DJ Lindstrom, MM Lindstrom, and JP Lockwood. Martian soil simulant available for scientific, educational study. *EOS Trans. Am. Geophys. Union*, 79:405, 1998b.

N.M. Amer, A. Skumanich, and D. Ripple. Photothermal modulation of the gap distance in scanning tunneling microscopy. *Applied Physics Letters*, 49:137, 1986.

B. Anczykowski, D. Kruger, KL Babcock, and H. Fuchs. Basic properties of dynamic force spectroscopy with the scanning force microscope in experiment and simulation. *Ultramicroscopy*, 66(3-4):251–259, 1996.

Y. Ando. Development of three-dimensional electrostatic stages for scanning

probe microscope. *Sensors & Actuators: A. Physical*, 114(2-3):285–291, 2004.

T. Arai, D. Aoki, Y. Okabe, and M. Fujihira. Analysis of surface forces on oxides in aqueous solutions using AFM. *Thin Solid Films*, 273(1-2): 322–326, 1996.

V. Arunachalam, WH Marlow, and JX Lu. Development of a picture of the van der Waals interaction energy between clusters of nanometer-range particles. *Physical Review E*, 58(3):3451–3457, 1998.

Z. Barkay, A. Teller, E. Ganor, Z. Levin, and Y. Shapira. Atomic Force and Scanning Electron Microscopy of Atmospheric Particles. *MICROSCOPY RESEARCH AND TECHNIQUE*, 68(2):107, 2005.

JF Bell, HY McSween, JA Crisp, RV Morris, SL Murchie, NT Bridges, JR Johnson, DT Britt, MP Golombek, HJ Moore, et al. Mineralogic and compositional properties of Martian soil and dust: Results from Mars Pathfinder. *Journal of Geophysical Research*, 105(E1), 2000.

J.F Bell III, H.M Arneson, W. H. Farrand, and W. Goetz. Large Multispectral And Albedo Panoramas Acquired By The Pancam Instruments On The Mars Exploration Rovers Spirit and Opportunity. *36th Lunar and Planetary Science Conferenc*, 2005.

JF Bell III, SW Squyres, KE Herkenhoff, JN Maki, HM Arneson, D. Brown, SA Collins, A. Dingizian, ST Elliot, EC Hagerott, et al. Mars Exploration Rover Athena Panoramic Camera (Pancam) investigation. *J. Geophys. Res*, 108(E12):8063, 2003.

G. Benford. Roving Mars: Spirit, Opportunity, and the Exploration of the Red Planet by Steve Squyres. *NATURE-LONDON-*, 7052:777, 2005.

R. Berger. Cantilever Sensors. *Development of Methods*, date accessed: July 2007. URL `http://www.mpip-mainz.mpg.de/documents/forschungsprojekte/f17.pdf`.

P. Bertelsen, W. Goetz, MB Madsen, KM Kinch, SF Hviid, JM Knudsen, HP Gunnlaugsson, J. Merrison, P. Nornberg, SW Squyres, et al. Magnetic Properties Experiments on the Mars Exploration Rover Spirit at Gusev Crater, 2004.

C. Beuret. *Development of a Double Molding Technique for the Microfabrication of Diamond Scanning Probe Tips*. PhD thesis, 1999.

B. Bhushan. *Micro/Nanotribology and Its Applications*. Kluwer Academic Pub, 1997.

B. Bhushan, T. Kasai, CV Nguyen, and M. Meyyappan. Multi-walled carbon nanotube AFM probes for surface characterization of micro/nanostructures. *Microsystem Technologies*, 10(8):633–639, 2004.

M. Binggeli and CM Mate. Influence of capillary condensation of water on nanotribology studied by force microscopy. *Applied Physics Letters*, 65: 415, 1994.

B.P. Binks. *Modern Characterization Methods of Surfactant Systems*. CRC Press, 1999.

G. Binnig, CF Quate, and C. Gerber. Atomic Force Microscope. *Physical Review Letters*, 56(9):930–933, 1986.

G. Binnig and H. Rohrer. The Scanning tunneling microscope. *Scientific American*, 253:50, 1985.

N. Blanc, J. Brugger, NF De Rooij, and U. Duerig. Scanning force microscopy in the dynamic mode using microfabricated capacitive sensors. *Journal of Vacuum Science and Technology B Microelectronics and Nanometer Structure*, 14:901–905, 1996.

R.A. Bowling. A theoretical review of particle adhesion. *Particles on Surfaces*, 1:129–142, 1988.

WV Boynton, WC Feldman, SW Squyres, TH Prettyman, J. Bruckner, LG Evans, RC Reedy, R. Starr, JR Arnold, DM Drake, et al. Distribution of Hydrogen in the Near Surface of Mars: Evidence for Subsurface Ice Deposits, 2002.

RS Bradley. The cohesive force between solid surfaces and the surface energy of solids. *Phil. Mag*, 13:853–862, 1932.

F. Braet, C. Rotsch, E. Wisse, and M. Radmacher. Comparison of fixed and living liver endothelial cells by atomic force microscopy. *Applied Physics A: Materials Science & Processing*, 66:575–578, 1998.

R.W. Carpick, N. Agrait, DF Ogletree, and M. Salmeron. Measurement of interfacial shear (friction) with an ultrahigh vacuum atomic force micro-

scope. *Journal of Vacuum Science and Technology B Microelectronics and Nanometer Structure*, 14:1289–1295, 1996.

D.C. Catling. Twin studies on Mars. *Nature(London)*, 436(7047):42–43, 2005.

M. Chikazawa, T. Kanazawa, and T. Yamaguchi. The role of adsorbed water on adhesion force of powder particles. *KONA*, 2:54–61, 1984.

J. Chu, T. Itoh, C. Lee, T. Suga, and K. Watanabe. Novel high vacuum scanning force microscope using a piezoelectric cantilever and the phase detection method. *Journal of Vacuum Science & Technology B: Microelectronics and Nanometer Structures*, 15:1551, 1997.

RT Clancy, SW Lee, GR Gladstone, WW McMillan, and T. Rousch. A new model for Mars atmospheric dust based upon analysis of ultraviolet through infrared observations from Mariner 9, Viking, and PHOBOS. *Journal of Geophysical Research (ISSN 0148-0227)*, 100(E3), 1995.

JAS Cleaver and JWG Tyrrell. The Influence of Relative Humidity on Particle Adhesion–a Review of Previous Work and the Anomalous Behaviour of Soda-lime Glass. *KONA*, 22:9, 2004.

PA Clerc, L. Dellmann, F. Gretillat, MA Gretillat, PF Indermuehle, S. Jeanneret, P. Luginbuhl, C. Marxer, TL Pfeffer, GA Racine, et al. Advanced deep reactive ion etching: a versatile tool for microelectromechanical systems. *JOURNAL OF MICROMECHANICS AND MICROENGINEERING*, 8:272–278, 1998.

Delta Mask Co., date accessed: March 2008. URL `http://deltamask.nl/`.

K. Cooper, A. Gupta, and S. Beaudoin. Simulation of the Adhesion of Particles to Surfaces. *Journal of Colloid And Interface Science*, 234(2): 284–292, 2001.

J.W. Cross. Material Science and Scanning Probe Microscopy, date accessed: May 2008. URL `http://www.physics.mun.ca/beaulieu_lab/research.htm`.

B. Derjaguin. Kolloid Z. 69, 155 (1934). *Acta Physicochem. URSS*, 10:333, 1939.

BV Derjaguin, V. Muller, and Y. Toporov. On different approaches to the contact mechanics. J. Colloid. *J. Colloid Interface Sci*, 73(1):293, 1980.

BV Derjaguin, VM Muller, and YP Toporov. Role of molecular forces in contact deformations (critical remarks concerning Dr. Tabor's report). *J. Colloid. Interface Sci*, 67(2):378–379, 1978.

BV Derjaguin, VM Muller, and Yu Toprov. Effect of contact deformation on the adhesion of particles [J]. *Journal of Colloid and Interface Science*, 53(2):314–326, 1975.

T.P. Dolley. DIATOMITE. *USGS Minerals Yearbook p*, pages 24–1, 2001.

GR Drevin and L. Vincent. Granulometric Determination of Sedimentary Rock Particle Roundness. In *Mathematical Morphology: Proceedings of the VIth International Symposium–ISMM 2002: Sydney, 3-5 April, 2002.* CSIRO Publishing, 2002.

S. Eichenlaub, A. Gelb, and S. Beaudoin. Roughness models for particle adhesion. *Journal of Colloid And Interface Science*, 280(2):289–298, 2004.

DA Erie, G. Yang, HC Schultz, and C. Bustamante. DNA bending by Cro protein in specific and nonspecific complexes: implications for protein site recognition and specificity. *Science*, 266(5190):1562–1566, 1994.

WC Feldman, WV Boynton, RL Tokar, TH Prettyman, O. Gasnault, SW Squyres, RC Elphic, DJ Lawrence, SL Lawson, S. Maurice, et al. Global Distribution of Neutrons from Mars: Results from Mars Odyssey, 2002.

LR Fisher and JN Israelachvili. Experimental Studies on the Applicability of the Kelvin Equation to Highly Curved Concave Menisci. *J. Colloid Interface Sci*, 80(2):528–541, 1981.

Flinn. Scientific results of the Viking Project. *Journal of geophysical research - planets*, 82:0148–0227, 1977.

T. Fujita, R. Ito, C. Tokoro, J. Sadaki, G. Dodbiba, R. Tsukamoto, H. Okuda, and H. Yamane. Classification of submicron Ni particles by heterocoagulation. *Powder Technology*, 173(1):19–28, 2007.

G.P. Fulton. *Diatomaceous Earth Filtration for Safe Drinking Water*. Amer Society of Civil Engineers, 2000.

R. García and A. San Paulo. Attractive and repulsive tip-sample interaction regimes in tapping-mode atomic force microscopy. *Physical Review B*, 60 (7):4961–4967, 1999.

S. Gautsch. *Development of an Atomic Force Microscope and Measurement Concepts for Characterizing Martian Dust and Soil Particles.* UFO, Atelier für Gestaltung und Verlag, 2002.

S. Gautsch, T. Akiyama, R. Imer, NF de Rooij, U. Staufer, P. Niedermann, L. Howald, D. Braendlin, A. Tonin, HR Hidber, et al. Measurement of quartz particles by means of an atomic force microscope for planetary exploration. *Surface and Interface Analysis*, 33(2):163–167, 2002.

P Gierasch and R Goody. A study of the thermal and dynamical structure of the martian lower atmosphere. *Planetary and Space Science*, 16:615–646, 1968.

F.J. Giessibl. Atomic Resolution of the Silicon (111)-(7x7) Surface by Atomic Force Microscopy. *Science*, 267(5194):68–71, 1995.

EN Glezer and E. Mazur. Ultrafast-laser driven micro-explosions in transparent materials. *Applied Physics Letters*, 71:882, 1997.

M. Göken and M. Kempf. Microstructural properties of superalloys investigated by nanoindentations in an atomic force microscope. *Acta Materialia*, 47(3):1043–1052, 1999.

F.B. Gross. JSC Mars-1 Martian Regolith Simulant particle-charging experiments in the presence of AC and DC corona fields. *Journal of Electrostatics*, 58(1-2):147–156, 2003.

F.B. Gross, S.B. Grek, C.I. Calle, and R.U. Lee. JSC Mars-1 Martian

Regolith simulant particle charging experiments in a low pressure environment. *Journal of Electrostatics*, 53(4):257–266, 2001.

HC Hamaker. The London-van der Waals' attraction between spheroid particles. *Physica*, 4:1058, 1937.

HG Hansma, RL Sinsheimer, J. Groppe, TC Bruice, V. Elings, G. Gurley, M. Bezanilla, IA Mastrangelo, PV Hough, and PK Hansma. Recent advances in atomic force microscopy of DNA. *Scanning*, 15(5):296–9, 1993.

HG Hansma, J. Vesenka, C. Siegerist, G. Kelderman, H. Morrett, RL Sinsheimer, V. Elings, C. Bustamante, and PK Hansma. Reproducible Imaging and Dissection of Plasmid DNA Under Liquid with the Atomic Force Microscope, 1992.

P.K. Hansma and R. Sonnenfeld. High resolution atomic force microscope, January 24 1989. US Patent 4,800,274.

JA Harkey and TW Kenny. 1/f noise considerations for the design and process optimization of piezoresistive cantilevers. *Microelectromechanical Systems, Journal of*, 9(2):226–235, 2000.

G. Haugstad, W.L. Gladfelter, and E.B. Weberg. Friction Force Microscopy of AgBr Crystals: Agˆ 0 Rods and Adsorbed Gelatin Films. *LANGMUIR*, 9:3717–3717, 1993.

M. Hecht. Microscopy, Electrochemistry and Conductivity Analyzer (MECA) Non-imaging Experiment Data Record (EDR) SIS, Feb 2008.

MH Hecht. The Microscopy, Electrochemistry, and Conductivity Analyzer (MECA) on the 2007 Phoenix Mars Lander. *JPL*, 2006.

K. Henjest. The traction force in magnetic separators. *Measurement Science and Technology*, 5(9):1105–1108, 1994.

H. Hertz. Uber die Beruhrung fester elastischer Korper. J. f. Reine u. *Angew. Math*, 92:156, 1881.

S.L. Hess, R.M. Henry, C.B. Leovy, and et al. Scientific results of the Viking Project - Viking 1 and 2. *Transactions - American Geophysical Union*, 58:827–827, 1977.

W. Hillmann, O. Kranz, and K. Eckolt. Reliability of roughness measurements using contact stylus instruments with particular reference to results of recent research at the Physikalisch-Technische Bundesanstalt. *Wear*, 97(1):27–43, 1984.

A.M. Howatson, Lund P.G., and J.D. Todd. *Engineering Tables and Data.* Chapman and Hall, 1972.

A. Hubert and R. Schäfer. *Magnetic Domains: The Analysis of Magnetic Microstructures.* Springer, 1998.

SF Hviid, MB Madsen, HP Gunnlaugsson, W. Goetz, JM Knudsen, RB Hargraves, P. Smith, D. Britt, AR Dinesen, CT Mogensen, et al. Magnetic Properties Experiments on the Mars Pathfinder Lander: Preliminary Results. *Science*, 278(5344):1768, 1997.

TH Ibrahim, TR Burk, FM Etzler, and RD Neuman. Direct adhesion measurements of pharmaceutical particles to gelatin capsule surfaces. *Journal of Adhesion Science and Technology*, 14(10):1225–1242, 2000.

PF Indermuehle, C. Linder, J. Brugger, VP Jaecklin, and NF de Rooij. Design and fabrication of an overhanging xy-microactuator with integrated tip for scanning surface profiling. *Sensors and Actuators A*, 43:346–350, 1994.

P.F. Indermühle, VP Jaecklin, J. Brugger, C. Linder, NF De Rooij, and M. Bingeli. AFM imaging with an xy-micropositioner with integrated tip. *Sensors and actuators. A, Physical*, 47(1-3):562–565, 1995.

J.N. Israelachvili. *Intermolecular and surface forces*. Academic Press London, 1992.

S.S. Iyer, A.J. Auberton-Hervé, and Institution of Electrical Engineers. *Silicon Wafer Bonding Technology: For VLSI and MEMS Applications*. Institution of Electrical Engineers, 2002.

B.M. Jakosky, K.H. Nealson, C. Bakermans, R.E. Ley, and M.T. Mellon. Subfreezing Activity of Microorganisms and the Potential Habitability of Mars' Polar Regions. *Astrobiology*, 3(2):343–350, 2003.

N. Jalili and K. Laxminarayana. A review of atomic force microscopy imaging systems: application to molecular metrology and biological sciences. *Mechatronics*, 14(8):907–945, 2004.

KL Johnson, K. Kendall, and AD Roberts. Surface Energy and the Con-

tact of Elastic Solids. *Proceedings of the Royal Society of London. Series A, Mathematical and Physical Sciences (1934-1990)*, 324(1558):301–313, 1971.

R. Jones, H.M. Pollock, J.A.S. Cleaver, and C.S. Hodges. Adhesion Forces between Glass and Silicon Surfaces in Air Studied by AFM: Effects of Relative Humidity, Particle Size, Roughness, and Surface Treatment. *LANGMUIR*, 18(21):8045–8055, 2002.

T. Junno, K. Deppert, L. Montelius, and L. Samuelson. Controlled manipulation of nanoparticles with an atomic force microscope. *Applied Physics Letters*, 66:3627, 1995.

RA Kahn, TZ Martin, RW Zurek, and SW Lee. The martian dust cycle. *Mars*, 1992.

HU Keller, WJ Markiewicz, S. Hviid, MT Lemmon, PH Smith, RV Morris, et al. The Robotic Arm Camera (RAC). *Fourth International Conference on Mars Polar Science and Exploration, October 2-6, 2006, Davos, Switzerland. LPI Contribution No. 1323, p. 8042*, 2006.

A. Kempe, F. Jamitzky, W. Altermann, B. Baisch, T. Markert, and W.M. Heckl. Discrimination of Aqueous and Aeolian Paleoenvironments by Atomic Force Microscopy-A Database for the Characterization of Martian Sediments. *Astrobiology*, 4(1):51–64, 2004.

M. Kempf, M. Göken, and H. Vehoff. Nanohardness measurements for studying local mechanical properties of metals. *Applied Physics A: Materials Science & Processing*, 66:843–846, 1998.

W. Kern. The Evolution of Silicon Wafer Cleaning Technology. *Journal of The Electrochemical Society*, 137:1887, 1990.

W. Kern. *Handbook of Semiconductor Wafer Cleaning Technology: Science, Technology, and Applications.* Noyes Publications, 1993.

H.P. Klein, J. Lederberg, A. Rich, N.H. Horowitz, V.I. Oyama, and G.V. Levin. The Viking mission and the search for life on Mars. *Nature*, 262 (5563):24–27, 1976.

JE Kogel. Industrial Minerals & Rocks: Commodities.

V.N. Koinkar and B. Bhushan. Microtribological studies of unlubricated and lubricated surfaces using atomic force/friction force microscopy. *Journal of Vacuum Science & Technology A: Vacuum, Surfaces, and Films*, 14: 2378, 1996.

CE Krauss, M. Hor nyi, and S. Robertson. Experimental evidence for electrostatic discharging of dust near the surface of Mars. *New Journal of Physics*, 5(1):70, 2003.

H. Krupp. *Particle Adhesion: Theory and Experiment.* Elsevier, 1967.

J. Kucharczyk, M. Moseley, and A.J. Barkovich. *Magnetic Resonance Neuroimaging.* CRC Press, 1994.

F. Laermer and A. Schilp. Method of anisotropically etching silicon, March 26 1996. US Patent 5,501,893.

LD Landau, EM Lifshitz, and LP Pitaevskii. Electrodynamics of Continuous Media, 1984.

D. Langbein. Retarded Dispersion Energy between Macroscopic Bodies. *Physical Review B*, 2(8):3371–3383, 1970.

D.W. Lee, T. Ono, and M. Esashi. High-speed imaging by electromagnetically actuated probe with dual spring. *Journal of microelectromechanical systems*, 9(4):419–424, 2000.

GU Lee, LA Chrisey, and RJ Colton. Direct measurement of the forces between complementary strands of DNA. *Science*, 266(5186):771, 1994.

MH Lee and J. Ayala. Adhesion of toner to photoconductor. *Journal of imaging technology*, 11(6):279–284, 1985.

EM Lifshitz. The theory of molecular attractive forces between solids. *Sov. Phys. JETP*, 2(1), 1956.

J. Lowell and AC Rose-Innes. Contact electrification. *Advances in Physics*, 29(6):947–1023, 1980.

M. Ludwig, M. Rief, L. Schmidt, H. Li, F. Oesterhelt, M. Gautel, and HE Gaub. AFM, a tool for single-molecule experiments. *Applied Physics A Materials Science & Processing*, 68(2):173–176, 1999.

J. Mahanty and BW Ninham. Dispersion Forces (Academic Press, London, 1976).

B. Mailhot, K. Komvopoulos, B. Ward, Y. Tian, and GA Somorjai. Mechanical and friction properties of thermoplastic polyurethanes determined by scanning force microscopy. *Journal of Applied Physics*, 89:5712, 2001.

SR Manalis, SC Minne, A. Atalar, and CF Quate. Interdigital cantilevers for atomic force microscopy. *Applied Physics Letters*, 69:3944, 1996.

GM McClelland and JN Glosli. Friction at the Atomic Scale. *Fundamentals of Friction: Macroscopic and Microscopic Processes*, pages 405–422, 1992.

JS McFarlane and D. Tabor. Adhesion of Solids and the Effect of Surface Films. *Proceedings of the Royal Society of London. Series A, Mathematical and Physical Sciences (1934-1990)*, 202(1069):224–243, 1950.

M. Mellon and B. Jakosky. Geographic variations in the thermal and diffusive stability of ground ice on Mars. *Journal of Geophysical Research*, 98: 3345–3364, 1993.

VB Menon, LD Michaels, RP Donovan, and DS Ensor. EFFECTS OF PARTICULATE SIZE, COMPOSITION, AND MEDIUM ON SILICON WAFER CLEANING. *Solid State Technol*, 32(3):7–12, 1989.

J. Merrison, J. Jensen, K. Kinch, R. Mugford, and P. Nørnberg. The electrical properties of Mars analogue dust. *Planetary and Space Science*, 52 (4):279–290, 2004.

E. Meyer, H.J. Hug, and R. Bennewitz. *Scanning Probe Microscopy: The Lab on a Tip*. Springer, 2004.

G. Meyer and N.M. Amer. Novel optical approach to atomic force microscopy. *Applied Physics Letters*, 53:1045, 1988.

VM Muller, VS Yushchenko, and BV Derjaguin. On the influence of molec-

ular forces on the deformation of an elastic sphere and its sticking to a rigid plane. *J. Colloid Interface Sci*, 77(1):91–101, 1980.

VM Muller, VS Yushchenko, and BV Derjaguin. General theoretical consideration of the influence of surface forces on contact deformations and the reciprocal adhesion of elastic spherical particles. *J. Colloid Interface Sci*, 92(1):92–101, 1983.

N. Nagashima, S. Matsuoka, and K. Miyahara. Nanoscopic Hardness Measurement by Atomic Force Microscope. *JSME international journal. Series A, Solid mechanics and material engineering*, 39.

Nanosurf. http://www.nanosurf.com/, date accessed: March 2008.

NASA Mars Envorinmental Rover, date accessed: August 2008. URL `http://marsrovers.jpl.nasa.gov/home/`.

MA Olmstead, NM Amer, S. Kohn, D. Fournier, and AC Boccara. Photothermal displacement spectroscopy: An optical probe for solids and surfaces. *Applied Physics A: Materials Science & Processing*, 32(3):141–154, 1983.

RM Pashley. The van der Waals Interaction for Liquid Water: A Comparison of the Oscillator Model Approximation and Use of the Kramers-Kronig Equation with Full Spectral Data. *J. Colloid Interface Sci.*, 62(2):344–347, 1977.

W. T. Pike. Imaging of unconsolidated material in the MECA AFM. *JPL document*, 2000.

F. Podczeck. *Particle-Particle Adhesion in Pharmaceutical Powder Handling*. Imperial College Press, 1998.

JB Pollack, D. Colburn, J. Hunter, and C. Van. Properties of aerosols in the Martian atmosphere, as inferred from Viking Lander imaging data. *Journal of Geophysical Research*, 82:4479–4496, 1977.

J.B. Pollack, DS Colburn, FM Flasar, R. Kahn, CE Carlson, and D. Pidek. Properties and effects of dust particles suspended in the Martian atmosphere. *Journal of Geophysical Research*, 84(B6):2929–2945, 1979.

C.A.J. Putman, K.O. Van der Werf, B.G. De Grooth, N.F. Van Hulst, and J. Greve. Tapping mode atomic force microscopy in liquid. *Applied Physics Letters*, 64:2454, 1994.

MW Reeks and D. Hall. Deposition and reentrainment of gas-borne particles in recirculating turbulent flows. *J. Fluids Eng*, 110:165–171, 1988.

RS Ridley Sr, C. Strate, J. Cumbo, T. Grebs, and C. Gasser. The implementation of AFM for process monitoring and metrology in trench MOSFET device manufacturing. *Advanced Semiconductor Manufacturing 2002 IEEE/SEMI Conference and Workshop*, pages 408–414, 2002.

R. Rieder, T. Economou, H. Wanke, A. Turkevich, J. Crisp, J. Bruckner, G. Dreibus, and HY McSween Jr. The Chemical Composition of Martian Soil and Rocks Returned by the Mobile Alpha Proton X-ray Spectrometer: Preliminary Results from the X-ray Mode. *Science*, 278(5344):1771, 1997.

W. Riedler, K. Torkar, F. Rüdenauer, M. Fehringer, R. Schmidt, H. Arends,

RJL Grard, EK Jessberger, R. Kassing, H.S.C. Alleyne, et al. The MIDAS experiment for the Rosetta mission. *Advances in Space Research*, 21(11): 1547–1556, 1998.

D. Rugar, HJ Mamin, and P. Guethner. Improved fiber-optic interferometer for atomic force microscopy. *Applied Physics Letters*, 55:2588, 1989.

J.E. Sader. Susceptibility of atomic force microscope cantilevers to lateral forces. *Review of Scientific Instruments*, 74:2438, 2003.

DM Schaefer, R. Reifenberger, A. Patil, and RP Andres. Fabrication of two-dimensional arrays of nanometer-size clusters with the atomic force microscope. *Applied Physics Letters*, 66:1012, 1995.

TE Schäffer, JP Cleveland, F. Ohnesorge, DA Walters, and PK Hansma. Studies of vibrating atomic force microscope cantilevers in liquid. *Journal of Applied Physics*, 80:3622, 1996.

A. Schirmeisen, H. Hölscher, B. Anczykowski, D. Weiner, MM Schäfer, and H. Fuchs. Dynamic force spectroscopy using the constant-excitation and constant-amplitude modes. *Nanotechnology*, 16(3):S13–S17, 2005.

J.A. Schwarz, C.I. Contescu, and K. Putyera. *Dekker Encyclopedia of Nanoscience and Nanotechnology*. Marcel Dekker, 2004.

R. Sharma, DW Clark, PK Srirama, and MK Mazumder. Tribocharging Characteristics of the Mars Dust Simulant (JSC Mars-1). *Industry Applications, IEEE Transactions on*, 44(1):32–39, 2008.

M.I. Shin'ichi Kitamura. High-resolution imaging of contact potential difference with ultrahigh vacuum noncontact atomic force microscope. *Applied Physics Letters*, 72:3154, 1998.

A. Sickafoose, JE Colwell, M. Horányi, and S. Robertson. Experimental investigations on photoelectric and triboelectric charging of dust. *Journal of Geophysical Research*, 106(A5):8343–8356, 2001.

Co. Sigma-Aldrich. 97% fe, 4.5-5.2μm mean particle size, date accessed: January 2008. URL `http://www.sigmaaldrich.com/catalog/search/ProductDetail/SIAL/C3518`.

Co. Sigma Aldrich, date accessed: March 2008. URL `http://www.sigmaaldrich.com/`.

M. Sitti. Atomic force microscope probe based controlled pushing for nanotribological characterization. *Mechatronics, IEEE/ASME Transactions on*, 9(2):343–349, 2004.

PH Smith, JF Bell III, NT Bridges, DT Britt, L. Gaddis, F. Gliem, R. Greeley, HU Keller, KE Herkenhoff, S. Hviid, et al. Results from the Mars Pathfinder Camera. *Science*, 278(5344):1758, 1997.

WR Smythe. Static and Dynamic Electricity, 3rd cd, 1968.

LA Soderblom, RC Anderson, RE Arvidson, JF Bell, NA Cabrol, W. Calvin, PR Christensen, BC Clark, T. Economou, BL Ehlmann, et al. Soils of Eagle Crater and Meridiani Planum at the Opportunity Rover Landing Site, 2004.

M. Soltani and G. Ahmadi. On particle resuspension mechanisms in turbulent flows. *Report no. MAE-264*, 1993.

RW Stark, S. Thalhammer, J. Wienberg, and WM Heckl. The AFM as a tool for chromosomal dissection-the influence of physical parameters. *Applied Physics A: Materials Science & Processing*, 66:579–584, 1998.

A. Steele, D. Goddard, IB Beech, RC Tapper, D. Stapleton, and JR Smith. Atomic force microscopy imaging of fragments from the Martian meteorite ALH84001. *Journal of Microscopy*, 189(Pt 1):2–7, 1998.

Z. Sternovsky, S. Robertson, A. Sickafoose, J. Colwell, and M. Horanyi. Contact charging of lunar and Martian dust simulants. *Journal of Geophysical Research. E. Planets*, 107:15–1, 2002.

W. Stone. Some phenomena of the contact of solids. *Phil. Mag*, 9:610–620, 1930.

CD Stow. Dust and sand storm electrification. *Weather*, 24(4):134–140, 1969.

Y. Sugawara, M. Ohta, T. Konishi, S. Morita, M. Suzuki, and Y. Enomoto. Effects of humidity and tip radius on the adhesive force measured with atomic force microscopy. *Wear*, 168(1-2):13–16, 1993.

S. Sundararajan and B. Bhushan. Topography-induced contributions to friction forces measured using an atomic force/friction force microscope. *Journal of Applied Physics*, 88:4825, 2000.

Surface Technology Systems plc, date accessed: March 2008. URL `http://www.stsystems.com/`.

U.S.G. Survey. History and Overview of the US Diatomite Mining Industry, with Emphasis on the Western United States.

D. Tabor. Surface forces and surface interactions. *J. Colloid Interface Sci*, 58(2), 1977.

D. Tabor. Role of molecular forces in contact deformations. *J. Colloid Interface Sci*, 67:378, 1978.

N. Tas, T. Sonnenberg, H. Jansen, R. Legtenberg, and M. Elwenspoek. Stiction in surface micromachining. *JOURNAL OF MICROMECHANICS AND MICROENGINEERING*, 6:385–397, 1996.

R. Team. Characterization of the Martian Surface Deposits by the Mars Pathfinder Rover, Sojourner. *Science*, 278(5344):1765, 1997.

Computer Simulation Technology. Cst microwave studio, date accessed: April 2008. URL `http://www.cst.com/`.

MG Tomasko, LR Doose, M. Lemmon, PH Smith, and E. Wegryn. Properties of dust in the Martian atmosphere from the Imager on Mars Pathfinder. *JGR-Planets*, 104(E4):8987, 1998.

O.B. Toon, J. B. Pollack, and C. Sagan. Physical properties of the particles composing the Martian dust storm of 1971–1972. *Icarus*, 30(4):663–696, 1977.

MC Towner, MR Patel, TJ Ringrose, JC Zarnecki, D. Pullan, MR Sims, S. Haapanala, A.M. Harri, J. Polkko, CF Wilson, et al. The Beagle 2 environmental sensors: science goals and instrument description. *Planetary and Space Science*, 52(13):1141–1156, 2004.

Vectorworks, date accessed: April 2008. URL `http://www.asmicro.com/Equipment/MultiModeAFM.htm`.

Veeco, date accessed: May 2008. URL `http://www.veeco.com/default.aspx`.

S. Vijendran, H. Sykulska, and WT Pike. AFM investigation of Martian soil simulants on micromachined Si substrates. *Journal of Microscopy*, 227(3): 236–245, 2007.

J. Visser. IN Surface and Colloid Science Vol. 8 (E. MATIJEVIC, ed.). 1976.

H.C. Wang. Effects of Inceptive Motion on Particle Detachment from Surfaces. *Aerosol Science and Technology*, 13(3):386–393, 1990.

C.K. Wentworth. A scale of grade and class terms for clastic sediments. *Journal of Geology*, 30(5):377–392, 1922.

KL Westra and DJ Thomson. The microstructure of thin films observed using atomic force microscopy. *Thin Solid Films*, 257(1):15–21, 1995.

P.A. Withey and J.A. Nuth. Formation of Single-Magnetic-Domain Iron Particles via Vapor-Phase Nucleation: Implications for the Solar Nebula. *Icarus*, 139(2):367–373, 1999.

O. Wolter, T. Bayer, and J. Greschner. Micromachined silicon sensors for scanning force microscopy. *Journal of Vacuum Science & Technology B: Microelectronics and Nanometer Structures*, 9:1353, 1991.

A. Yamamoto, A. Watanabe, H. Tsubakino, and S. Fukumoto. AFM Observations of Microstructures of Deposited Magnesium on Magnesium Alloys. *Magnesium Alloys*, 350-3:241–246, 2000.

Y. Yang, H. Wang, and D.A. Erie. Quantitative characterization of biomolecular assemblies and interactions using atomic force microscopy. *Methods*, 29(2):175–187, 2003.

Bart Van Zeghbroeck. Principles of semiconductor devices, date accessed: November 2008. URL {`http://ece-www.colorado.edu/~bart/book/book/chapter2/ch2_4.htm`}.

X.G. Zhang. *Electrochemistry of Silicon and Its Oxide*. Kluwer Academic Pub, 2001.

AD Zimon. Adhesion ofDust and Powder. *Consultant Bureau, New York*, 1982.

G. Ziskind, M. Fichman, and C. Gutfinger. Resuspension of particulates from surfaces to turbulent flows-Review and analysis. *Journal of Aerosol Science*, 26(4):613–644, 1995.

G. Ziskind, M. Fichman, and C. Gutfinger. Adhesion moment model for estimating particle detachment from a surface. *Journal of Aerosol Science*, 28(4):623–634, 1997.

Declaration by Candidate

I hereby declare that this thesis is my own work and effort and that it has not been submitted anywhere for any award. Where other sources of information have been used, they have been acknowledged.

Signature

Date